University of Nottingham
UK | CHINA | MALAYSIA

Towards naturalistic scanning environments for wearable magnetoencephalography

by

Molly Rea, M.Sci.

Thesis by published works submitted to the University of Nottingham

for the degree of Doctor of Philosophy

September 2022

Contents

Abstract

Magnetoencephalography (MEG) is a neuroimaging technique that probes human brain function, by measuring the magnetic fields generated at the scalp by current flow in assemblies of neurons. A direct measure of neural activity, MEG offers high spatiotemporal resolution, but limitations imposed by superconducting sensor technologies impede its clinical utility. Specifically, neuromagnetic fields are up to a billion times smaller than that of the Earth, meaning MEG must be performed inside a magnetically shielded room (MSR), which is typically expensive, heavy, and difficult to site. Furthermore, current MEG systems employ superconducting quantum interference devices (SQUIDs) to detect these tiny magnetic fields, however, these sensors require cryogenic cooling with liquid helium. Consequently, scanners are bulky, expensive, and the SQUIDs must be arranged in a fixed, one-size-fits-all array. Any movement relative to the fixed sensors impacts data quality, meaning participant movement in MEG is severely restricted. The development of technology to enable a wearable MEG system allowing free participant movement would generate a step change for the field.

Optically-pumped magnetometers (OPMs) are an alternative magnetic field detector recently developed with sufficient sensitivity for MEG measurements. Operating at body temperature, in a small and lightweight sensor package, OPMs offer the potential for a wearable MEG scanner that allows participant movement, with sensors mounted on the scalp in a helmet or cap. However, OPMs operate around a zero-field resonance, resulting in a narrow dynamic range that may be easily exceeded by movement of the sensor within a background magnetic field. Enabling a full range of participant motion during an OPM-MEG scan therefore presents a significant challenge, requiring precise control of the background magnetic field.

This thesis describes the development of techniques to better control the magnetic environment for OPM-MEG. This includes greater reduction of background magnetic fields over a fixed region to minimise motion artefacts and facilitate larger movements, and the application of novel, multi-coil active magnetic shielding systems to enable flexibility in participant positioning within the MSR. We outline a new approach to map background magnetic fields more accurately, reducing the remnant magnetic field to <300 pT and yielding a five-fold reduction in motion artefact, to allow detection of a visual steady-state evoked response during continuous head motion. Employing state-of-the-art, triaxial OPMs alongside this precision magnetic field control technique, we map motor function during a handwriting task involving naturalistic head movements and investigate the advantages of triaxial sensitivity for MEG data analysis. Using multi-coil active magnetic shielding, we map motor function consistently in the same participant when seated and standing, and demonstrate the first OPM-MEG hyperscanning experiments. Finally, we outline how the integration of a multi-coil system into the walls of a lightweight MSR, when coupled with field control over a larger volume, provides an open scanning environment. In sum, these developments represent a significant step towards realising the full potential of OPM-MEG as a wearable functional neuroimaging technology.

Acknowledgements

First, I would like to thank my supervisors, Professor Matt Brookes and Professor Richard Bowtell, for your help, support and guidance throughout my postgraduate study. I feel incredibly lucky to have had the chance to work on such exciting, impactful, and cutting-edge research, as well as the amazing opportunities afforded to me by working on this project; visiting SickKids in Toronto, testing the first triaxial OPM, and giving a talk next to Loch Lomond, to name but a few! I will be forever grateful for this experience. Thank you for enabling me to be a part of it.

A huge thank you to Neil – sorry, *Niall* – who made the content of this thesis possible in many, many ways. Working with you has been an absolute joy, and your help and guidance (and coils) have been invaluable. Gracias Elena, for starting it all. None of us would be doing the wonderful things we do without you and I'm excited to start working with/for you at Cerca very soon. Thanks to Ryan, for having a MATLAB script for everything, and for lending me Maia the Lab whenever I fancied a walk. A general, heartfelt thank you goes to the UoN MEG team and all at the SPMIC, for being so welcoming and making the last three and a half years so enjoyable.

I'd also like to thank our collaborators, Dr. Vishal Shah and QuSpin Inc., and the teams at Magnetic Shields Ltd. and Cerca Magnetics Ltd., for the endless innovation and enthusiasm.

To Natalie, Lucy and Izzy, thank you for putting up with me both at work and at home. I wish you the very best of luck in your Ph.Ds! Thank you to the 2018 ONBI cohort for the best six months in Oxford I could have hoped for, and to BlowSoc Concert Band for always brightening my Wednesdays. To Jess, Scarlett, Jo, Lucy and Hetty, thank you for your unwavering friendship and support over the last thirteen years – here's to many more!

Thank you to Michelle, for being my unofficial mentor and always giving excellent advice. I hope I become as good a friend and role model to your boys as you have been to me.

Finally, thank you to my family for keeping me going through eight years of university life. To Grandma and Grandad and Nanny Rita, for being the most kind-hearted and generous grandparents anyone could wish for. Thank you, Mom, Dad, and Miles, for your never-ending support, advice, and encouragement, despite the fact I didn't become a vet! Thank you for ferrying me back and forth to countless piano lessons and clarinet concerts as a kid, and for helping me access a great education, even if it was on the other side of Birmingham. I'm sure I wouldn't be here, on the cusp of a Ph.D. in Physics, without it. And of course, thank you Sammy, for always welcoming me home with an excited bark and a wagging tail.

Introduction

Over the past fifty years, our knowledge and understanding of the human brain in health and disease has expanded dramatically, in part due to advances in non-invasive, *in vivo* medical imaging techniques. These neuroimaging methods can be broadly categorised as either **structural** techniques – such as x-ray computed tomography (CT) (Hounsfield, 1973) and magnetic resonance imaging (MRI) (Lauterbur, 1973; Mansfield and Grannell, 1973), which generate detailed images of brain structure – or **functional** techniques – such as electroencephalography (Berger, 1929) or functional MRI (Ogawa et al., 1990), which measure moment-to-moment changes in brain function. While structural imaging offers high quality (1 mm spatial resolution or better) images of the composition of the brain, including structural abnormalities such as tumours or lesions, little insight into the working brain can be gleaned from such images. In cases where brain function is affected but structure appears normal, as may be the case in epilepsy or mental health conditions, for example, assessment of brain activity via functional imaging is required.

Functional neuroimaging

Brain function is mediated by electrical currents that flow along neurons. Thus, direct measurement of these neuronal currents, or indirect measurement of associated metabolic changes, allows us to develop an understanding of brain activity and its modulation by tasks. Five non-invasive, functional imaging techniques have become commonplace in research and clinical institutions, which can be categorised as direct, or indirect measures.

Indirect measures of brain function

- **Functional magnetic resonance imaging (fMRI)** – MRI uses strong magnetic fields to image the distribution of water in the body. Functional MRI further exploits differences in the magnetic properties of oxygenated and deoxygenated blood, known as blood-oxygen level dependent (BOLD) contrast, to measure a haemodynamic response to brain activity (Ogawa et al., 1990). Specifically, when a particular region of the brain is active and many neuronal currents are firing, blood flow, volume, and the cerebral metabolic rate of oxygen in the region increase, combining to generate a BOLD response that can be measured via fMRI. This forms an indirect measure of brain function. Since this haemodynamic response is tightly coupled to the active cellular assemblies, the spatial resolution of fMRI is good, however, the temporal precision of fMRI is limited due to the ~6 s timescale of blood flow to the brain, meaning fast neural processes cannot be resolved. In addition, participants are required to lie inside an enclosed scanner and remain still throughout, making this modality unsuitable for many participant cohorts of interest, such as children and people with movement disorders. For structural imaging alone, these participants can be sedated, but this does not provide an appropriate solution when aiming to study brain function.

- **Positron emission tomography (PET)** – In PET (Fox and Raichle, 1984; Ter-Pogossian et al., 1975), biological molecules used in organ and tissue function are tagged with a proton-rich, radioactive isotope such as Fluorine-18 or Oxygen-15, and injected into the bloodstream. Increased blood flow to an active region of the brain causes the radioactive tracer to accumulate in the area. These radioactive nuclei are unstable and will decay via emission of a positron, which annihilates upon interaction with an electron in the surrounding tissue. A pair of gamma photons are generated, travelling in opposite directions, and are detected by sensors that surround the participant. The location of the annihilation event can then be determined by back-projection reconstruction and overlaid onto a structural image (e.g., Kinahan and Rogers, 1989), thus identifying brain regions with large oxygen uptake. Again, the participant is enclosed within the scanner and must remain still. Like fMRI, PET is an indirect measure of

brain function with limited temporal resolution, with the added disadvantage that ionising radiation is required.

- **Functional near-infrared spectroscopy (fNIRS)** – The absorption of near-infrared light by haemoglobin changes with blood flow, volume, and oxygenation. Hence, characterising the absorption spectra at different locations in the brain yields another indirect measure of brain activity (Jöbsis, 1977). The near-infrared light can be transmitted and detected at the scalp (having passed through the skull), meaning the imaging system can be easily deployed as a wearable helmet or cap. This has advantages for imaging cohorts of participants that would struggle to remain still in other scanners (e.g., children), however, fNIRS has poor temporal and spatial resolution – the latter due to scattering of the light in the surrounding tissue.

Direct measures of brain function

- **Electroencephalography (EEG)** – Electrical potentials generated by current flow in assemblies of neurons can be measured using electrodes at the scalp placed in electrical contact with the skin (Berger, 1929). This forms a direct measure of brain function with excellent (millisecond) temporal resolution, and the scalp electrodes can be deployed in a wearable cap, meaning EEG has found extensive use in the clinic due to its portability, adaptability, and low cost. However, the spatial resolution of EEG is poor, due to the electrical impedance of the skull distorting the electrical potentials. Furthermore, EEG is highly susceptible to muscle artefact (Muthukumaraswamy, 2013), meaning that despite the wearable approach, participants have to remain fairly still to maintain a reasonable data quality.

- **Magnetoencephalography (MEG)** – In contrast, the accompanying magnetic fields generated by current flow in neuronal assemblies pass through the skull mostly unimpeded, meaning the assessment of magnetic fields at the scalp can obtain high spatial, as well as temporal, resolution (Cohen, 1968; Hämäläinen et al., 1993). However, the magnetic fields generated by the brain are tiny, and so to gain sufficient sensitivity conventional MEG systems employ cryogenically cooled, superconducting sensors. This requirement for cryogenics makes scanners cumbersome and expensive. Furthermore, the detectors are arranged in a fixed helmet array, therefore the system cannot adapt to different head sizes and shapes, and the participant must remain still throughout the scan, which limits clinical utility.

Thesis aim

As a direct measure of neural activity that provides millisecond temporal resolution and excellent spatial resolution (typically ~5 mm), MEG is arguably the leading modality for high quality functional neuroimaging. At present, there are approximately one hundred and fifty conventional MEG systems in use across the globe, but wider uptake of MEG – particularly in clinical settings – is hindered by several fundamental limitations of the existing technology. The neuromagnetic fields of interest in MEG are approximately one billion times smaller than the Earth's magnetic field (Hämäläinen et al., 1993), meaning MEG must be performed inside a magnetically shielded enclosure, which is usually large, heavy and expensive, and imposes siting restrictions. Furthermore, the superconducting sensors require constant cooling with liquid helium, which is a dwindling resource and thus increases maintenance costs. This also necessitates a 2—5 cm separation between the sensors and the scalp, which, combined with the fixed nature of the sensor array, impacts the maximum signal-to-noise ratio that can be achieved. Furthermore, unless the participant's head fits the helmet perfectly, the separation between the scalp and the sensors varies with position, leading to inhomogeneous coverage (most often, participants rest their head at the back of the helmet, leading to poor sensitivity in frontal brain regions). This is true for all participants, but especially those with smaller heads, such as children. Altogether, these shortcomings limit the accessibility of MEG for widespread use in the clinic or research.

In recent years, however, advancements in sensor technologies, commercialisation and miniaturisation have led to the development of a new generation of magnetic field sensor called optically-pumped magnetometers (OPMs). OPMs are suitable for MEG measurements (Shah and Wakai, 2013) and, unlike the conventional superconducting sensors, are small, lightweight and operate at body temperature, enabling the potential for a wearable, OPM-based MEG system (Boto et al., 2017). Such a system allows placement of the sensors at the scalp and is adaptable to any head shape or size, akin to EEG and fNIRS, while providing superior spatiotemporal resolution. In addition, the lightweight nature of the sensors allows them to move with the head when worn, notionally allowing free participant movement. Removing the requirement for cryogenics also reduces overall running costs. Hence, OPM-MEG is an emerging modality that shows great promise for translation to widespread clinical use.

Despite this promise, a particular challenge in OPM-MEG is realising the potential for free participant movement. Commercially available OPMs have a narrow operating range of ±5 nT (Osborne et al., 2018), outside of which the sensor output saturates. Movement of an OPM through a background magnetic field generates a measurable change in magnetic field that has the potential to saturate the sensor output and cause loss of MEG data. If the sensor remains within operating range, these motion artefacts manifest as low frequency interference much larger in amplitude than the neuromagnetic signals of interest. Therefore, accurate compensation and control of the background magnetic field experienced by the OPM array is required to enable participant motion and preserve data quality.

Previous work developed a wearable OPM-MEG system (Boto et al., 2018) with whole-head coverage (Hill et al., 2020) that enabled head movements of ~30° and 10 cm by reducing the background magnetic field inside a magnetically shielded room (MSR). A bi-planar electromagnetic coil system was designed and constructed to generate equal and opposing magnetic field components that cancel the remnant field across the OPM array, which was determined using reference measurements. This approach reduced the background magnetic field to <1 nT, thus minimising motion artefacts and keeping the OPMs within their operating range (Holmes et al., 2018). However, the accuracy with which the background magnetic field could be mapped was limited and the permitted range of movement relatively small, restricted to within a fixed volume over which the background magnetic field could be controlled. This thesis aims to build upon that work, to further improve the scanning environment for wearable MEG by developing techniques to expand the range of motion possible and perform more naturalistic experimental paradigms. There are two primary aims to this:

1. **To develop techniques to more accurately map and compensate the background magnetic field inside a MSR, using existing coil systems for active magnetic shielding.**

Greater control of the strength and spatial variation of the background magnetic field across an OPM array is required to enable larger participant motion while maintaining sensor operation and good data quality. Further reduction of the ambient magnetic field below the nT level will minimise motion artefacts and thus improve MEG data quality at low frequencies that are typically challenging to measure with OPMs, such as the delta and theta bands (1—8 Hz). This is also especially relevant for imaging children, as neural oscillations during childhood occur at lower frequencies than the adult equivalent (Saby and Marshall, 2012).

2. **To demonstrate new, multi-coil active magnetic shielding systems that enable flexibility in participant positioning within the MSR.**

To fully realise the potential for OPM-MEG, we aim to allow the full range of ambulatory motion, allowing a participant to walk around the room during a scan. This would open up new possibilities for research to further develop our understanding of human brain function in health and disease, for example by studying a patient with Parkinson's disease as they stand from a chair, or a child as they learn to walk. To do this, the region over which the background magnetic field is compensated must be adaptable, such that the participant can be positioned anywhere within the MSR, for example standing, seated, or lying down. This requires the use of new, multi-coil designs for active magnetic shielding, that use individually controllable coil currents to allow the generated magnetic field distribution to be reconfigured.

If these two aims can be met, the capability and utility of OPM-MEG will be fundamentally changed.

Thesis outline

This thesis is structured in the style of a thesis by published works. To begin, three chapters describing the theory underpinning MEG, OPMs and magnetic shielding techniques are presented. Four experimental chapters then follow, each comprising a published research article to which my contribution was substantial. Finally, an overall discussion of the work presented in this thesis is made, and possible future directions for the research are considered.

Theory

- **Chapter 1** – An overview of MEG is given, beginning with the origins of the MEG signal, followed by data collection and analysis techniques that enable determination of underlying neuronal activity. The OPM is briefly introduced as an alternative sensor technology for MEG.
- **Chapter 2** – OPMs are explored in detail, including the physics that underpins their operation. A summary of the implementation of commercially available OPMs for MEG at the University of Nottingham is given, followed by an overview of the evolution of this OPM-MEG system to date.
- **Chapter 3** – Passive and active shielding techniques to screen interfering magnetic fields are introduced. Since OPM operation requires additional compensation of the background magnetic field inside a shielded enclosure, electromagnetic coil designs for active magnetic shielding are explored, and the remaining challenges presented.

Experimental work

- **Chapter 4** – A new approach for sampling the background magnetic field for compensation in OPM-MEG is presented, which uses optical tracking and a moving array of OPMs to determine the coefficients of the magnetic field as defined by a spherical harmonic model. Improved magnetic field compensation is achieved by applying the corresponding cancellation field with the bi-planar coil system, and a steady-state visual evoked response MEG experiment is performed during head movement, to validate the approach.
- **Chapter 5** – Utilising this improved magnetic field modelling and control technique, in combination with newly available triaxial OPMs, a handwriting study involving naturalistic head movement is conducted with OPM-MEG. We assess differences in neural activity when writing with the dominant vs. non-dominant hand, and experimentally demonstrate the benefits of triaxial sensitivity for interference rejection in MEG data analysis.

- **Chapter 6** – So far, our background magnetic field control only permits movement within a fixed central volume, which in turn limits scanning to a single participant. Here, a bi-planar multi-coil system made up of a series of small, unit coils with individually controllable currents is demonstrated for use in OPM-MEG. This enables flexibility in participant positioning, allowing assessment of motor function with a single participant seated or standing, and of two interacting participants simultaneously.

- **Chapter 7** – Finally, a lightweight MSR with integrated, multi-coil active magnetic shielding is presented. Here, the coils are built into the walls of the room to provide an open scanning environment, and we develop our background magnetic field mapping technique to enable accurate magnetic field compensation over a larger, 1 m^3 central volume. This combination of lightweight shielding and an open scanning environment works towards addressing two substantial barriers to the widespread deployment of OPM-MEG.

Summary and outlook

- Finally, a discussion of the work presented in the experimental chapters is made, to contextualise each publication within the aims of the thesis. To conclude, a summary of the original contribution to knowledge made by this research is given and possible future directions considered.

Author contributions to experimental chapters

- **Chapter 4 – Precision magnetic field modelling and control for wearable MEG.** My contributions to this chapter were in conceptualisation of the approach, development of software to implement the magnetic field model, all data collection and analysis.

- **Chapter 5 – A 90-channel triaxial MEG system using OPMs.** In this chapter, I contributed to conceptualisation of the study, performed all data collection and analysed the background magnetic field compensation and participant movement data, as well as constructing the pseudo-Ŧ-statistical maps, amplitude envelopes and performing the neural fingerprinting analyses.

- **Chapter 6 – Naturalistic hyperscanning with wearable MEG.** My contributions to this chapter were in conceptualisation, data collection and analysis of the MEG demonstrations.

- **Chapter 7 – A lightweight MSR with active shielding.** In this chapter, my contributions were to design of the magnetic field mapping technique and development of software to implement magnetic field control over a larger volume. I also contributed to data collection and analysis for the window coil performance and repeatability measurements and OPM verification.

Chapter 1

Magnetoencephalography

In this chapter, the electrophysiological origins of the MEG signal are examined, along with the resulting measurable effects we aim to detect. An overview of the conventional MEG scanner, which relies on cryogenically cooled, superconducting sensors, is given and the resulting limitations discussed. We then briefly review emerging alternative sensor technologies that may alleviate some of these constraints. Techniques for collection and analysis of MEG data are investigated, and the solutions to the forward and inverse problems used in subsequent experimental work are presented.

1.1. The origin of the MEG signal

The adult human brain constitutes approximately two per cent of total body mass, yet accounts for a fifth of the body's energy uptake (Raichle and Gusnard, 2002). The majority of this energy is used for functional processes in neurons (Attwell and Laughlin, 2001), the cellular building blocks of the brain that facilitate processing and transfer of electrical signals. These signals comprise ionic currents that propagate along the neurons, generating an associated magnetic field that can be detected at the scalp via MEG. Subsequent processing of these magnetic fields can generate three-dimensional (3D) images showing moment-to-moment changes in electrical brain activity.

1.1.1. Neurons

The human brain, arguably the most complex structure in the known universe, contains approximately one hundred billion neurons within its outermost layer, the cerebral cortex (Hämäläinen et al., 1993). Each neuron is connected to around ten thousand other neurons, in an extremely complex network that facilitates all human behaviour. A single neuron consists of three parts (see Figure 1.1A):

1. The soma (or cell body) contains the nucleus and is responsible for cell metabolism.
2. The dendrites are thread-like extensions to the soma that receive electrochemical stimuli from other neurons.
3. The axon is a fibre that extends away from the soma and carries electrical impulses to other cells.

The dendrites and soma make up the grey matter of the brain, whilst the axons extend into the white matter, to facilitate electrochemical transfer to cells in other regions of the brain and throughout the central nervous system. The distribution of the dendrites around the soma of each cortical neuron determines its classification: **stellate** neurons (see Figure 1.1B) have a symmetric distribution of dendrites around the soma, whereas in **pyramidal** neurons, the dendrites extend parallel to each other and perpendicular to the cortical surface (Figure 1.1C). This is of significance for MEG, since the current flow within the cell is directed along the dendrites. The symmetric distribution of dendrites in stellate cells largely results in a net cancellation of the induced electromagnetic fields, while the elongated structure of pyramidal neurons results in coherent propagation of currents along the axis of the cell, perpendicular to the surface of the cortex. The resulting fields interfere constructively, therefore it is these pyramidal neurons whose induced magnetic fields contribute most to the MEG signal.

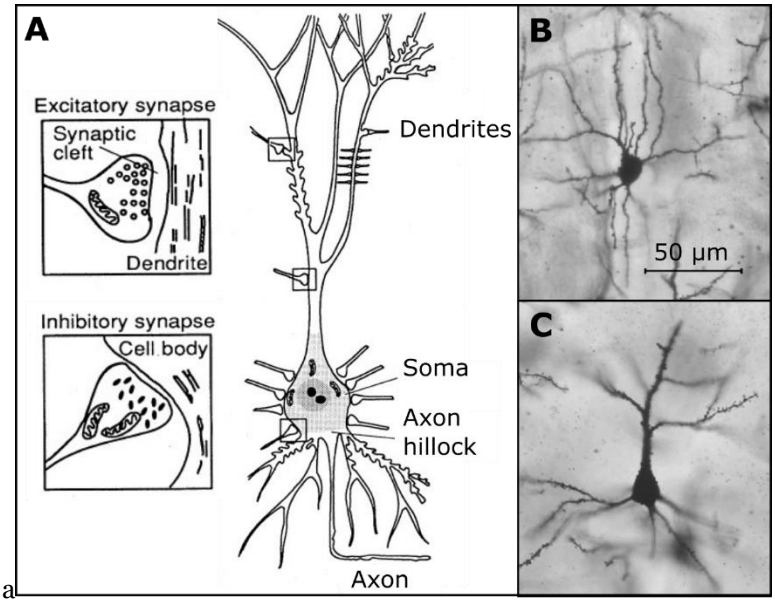

Figure 1.1 – The neuron. *A) Diagram of the neuron. (Adapted from Hämäläinen et al., 1993) B & C) Images of stellate (B) and pyramidal (C) neurons after Golgi staining. (Adapted from Churchill et al., 2004)*

Like most cells, neurons are surrounded by a phospholipid bilayer membrane, which defines the intracellular and extracellular regions. At rest, these regions have different concentrations of ions (mainly sodium (Na^+), potassium (K^+) and chlorine (Cl^-)), creating a potential difference across the cell membrane of −70 mV, measured inside the cell relative to the outside (Goldman, 1943). To increase or decrease the likelihood of a neuron firing, this potential is altered by electrochemical transfer from other neurons, via connections between cells known as synapses.

When the potential at the axon hillock (where the axon meets the soma) of the pre-synaptic cell reaches a threshold of −55 mV, the neurons 'fires', and an electrical impulse propagates along the axon towards other cells. This is known as an action potential. When the pulse arrives at the post-synaptic neuron, neurotransmitter molecules are released at the synapse, diffuse across the synaptic cleft between the two cells and trigger receptors on the post-synaptic neuron to open ion channels in the membrane. This causes an influx of charge that alters the membrane potential, known as a post-synaptic potential.

Depending on the ion channels that are opened by neurotransmission, the effect on the post-synaptic cell can be either excitatory or inhibitory (see Section 1.1.1.2), and it is the sum of these events that determine whether the threshold is reached. In general, many excitatory post-synaptic potentials are required for a neuron to fire an action potential. Excitatory synapses typically attach to the dendrites (see Figure 1.1A) and facilitate an increase in the intracellular potential, making the neuron more likely to fire. In contrast, inhibitory synapses attach to the soma and decrease the intracellular potential, making the neuron less likely to fire. Both action potentials and post-synaptic potentials constitute neuronal current flow, and therefore induce magnetic fields, but their respective contributions to the overall, measurable MEG signal requires further investigation.

1.1.1.1. Action potentials

As an action potential propagates along an axon, it can be described by a leading edge of depolarisation, followed by a trail of repolarisation (see Figure 1.2A). This is facilitated by the opening of potassium and sodium ion channels that line the cell membrane of the axon. Once the potential at the axon hillock exceeds the −55 mV threshold, the voltage-gated sodium channels nearest the cell body open and an influx of Na^+ ions depolarise the cell further, to +40 mV in 1–2 ms. This rapid change in potential difference also triggers the sodium channels to open in the neighbouring region of the membrane, allowing unattenuated propagation of the action potential along the length of the axon. At +40 mV, the sodium ion channels are deactivated, and potassium channels opened to enable an efflux of K^+ ions from the cell. A brief period of hyperpolarisation before the potassium channels close prevents the action potential from propagating back towards the soma. Following this, both the sodium and potassium ions are actively pumped against their concentration gradients (out of and into the cell, respectively) for repolarisation of the intracellular potential back to rest.

An action potential can therefore be modelled as a current quadrupole (Hämäläinen et al., 1993) – two opposing current dipoles separated by a small distance (Figure 1.2B). The leading depolarisation is characterised by a current dipole oriented away from the soma, while the repolarising tail is characterised by an equivalent dipole a short distance behind, oriented towards the soma. The strength of the magnetic field induced by a current quadrupole varies as the inverse cube of distance, r. This $1/r^3$ dependence, combined with the short (1–2 ms) timescale of current flow due to action potentials, would result in weak, short-lived extracranial magnetic fields unlikely to occur synchronously in many neurons. Consequently, action potentials are unlikely to be the dominant source of the MEG signal.

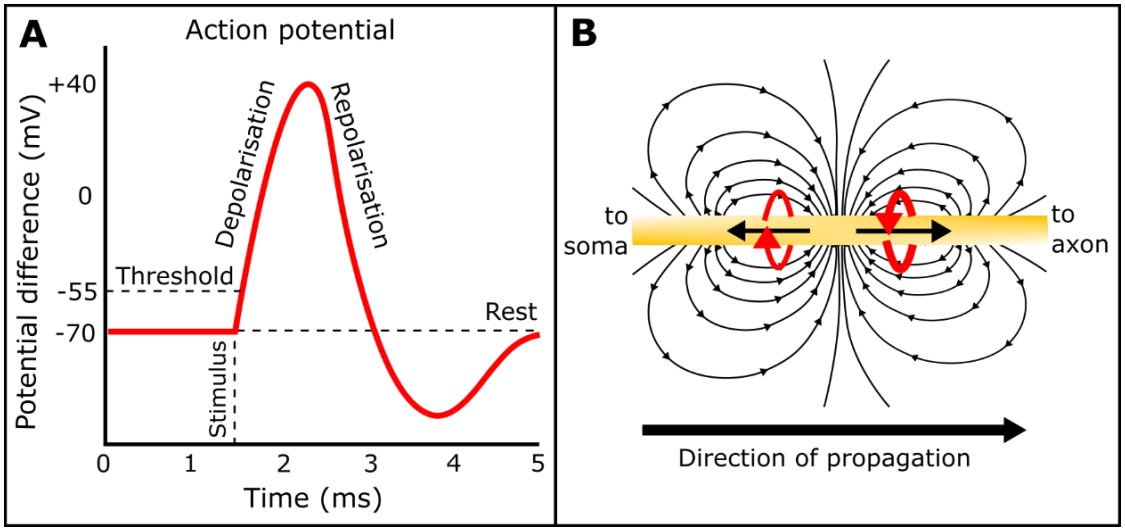

Figure 1.2 – Action potential. *A) Representation of an action potential as a function of intracellular potential difference over time. (Adapted from Hill, 2020). B) An action potential can be modelled as a current quadrupole. The direction of the magnetic fields that result from the opposing dipoles are shown in red.*

1.1.1.2. Post-synaptic potentials

Post-synaptic potentials occur due to excitatory or inhibitory neurotransmission. Excitatory post-synaptic potentials cause current to flow into the cell, along the axis of the pyramidal neuron from the dendrites towards the soma. This is known as the primary current. Extracellular currents (known as volume currents) occur due to repolarisation of the cell to the resting potential. The mechanism of repolarisation is the same as for the axon, via ion pumps working against the concentration gradient to actively pump Na^+ ions across the membrane and back into the extracellular region. An electric field is induced between the expulsion point of the ions and the excitatory synapse, causing a volume current to flow in the opposite direction to the primary current that is dependent on the conductivity of the extracellular tissue (see Figure 1.3A).

In contrast to the current quadrupole generated by an action potential, the primary current due to a post-synaptic potential can be modelled as a current dipole (Figure 1.3B). The magnetic field induced by a current dipole varies as the inverse square of distance ($1/r^2$ dependence), increasing the likelihood of magnetic fields due to post-synaptic potentials being measured at the scalp. In addition to this, the longevity of post-synaptic potentials (approximately 10 ms duration) compared to short-lived (1–2 ms) action potentials, increases the probability that simultaneous post-synaptic events will occur in neighbouring neurons. The induced magnetic fields will sum constructively, therefore synchronised primary currents occurring in assemblies of pyramidal neurons are most likely the dominant source of the MEG signal.

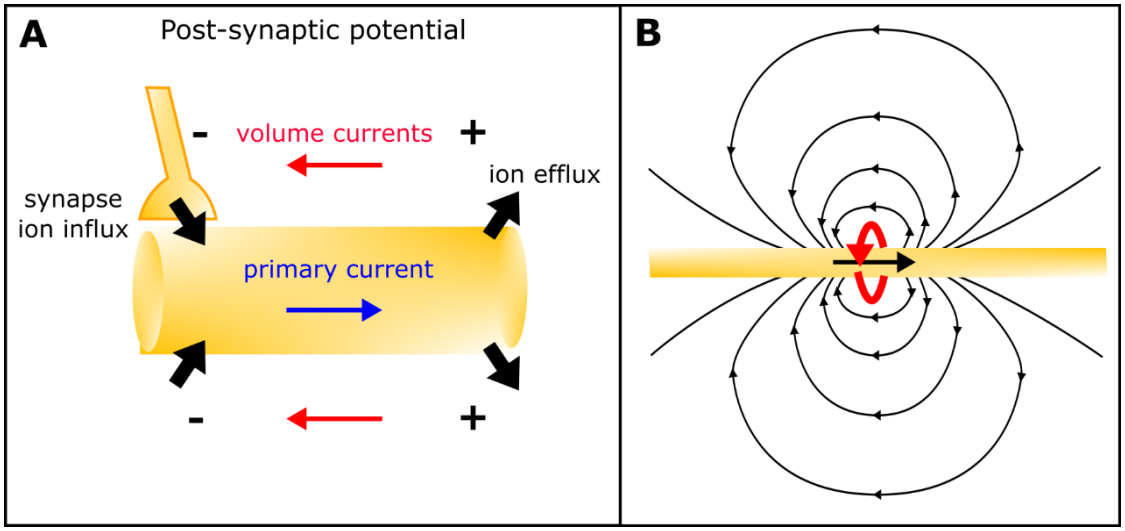

Figure 1.3 – Post-synaptic potential. *A) Schematic of the excitatory post-synaptic potential. The primary current flows along the neuron from the synapse towards the soma, while volume currents flow outside the cell in the opposite direction, due to repolarisation. B) The primary current can be modelled as a current dipole. Again, the direction of the resulting magnetic field is shown in red.*

1.1.2. Measurable effects

MEG data are rich in spatiotemporal information, which is key to developing our understanding of human brain function. However, the information gleaned from MEG data will be influenced by the type of recording made and the methods of data analysis employed. The neuroelectric effects measured in MEG can be broadly categorised as spontaneous rhythms, induced responses, or evoked responses.

1.1.2.1. Spontaneous rhythms

There is electrical activity occurring in the brain at all times, meaning brain function can be measured even while a participant is 'at rest' or asleep. Such spontaneous neural activity was first measured in humans via EEG almost one hundred years ago, by Hans Berger. Berger recorded an 8–13 Hz neural oscillation at the back of the head, which could be modulated by opening and closing the eyes (Berger, 1929). This is known as the alpha rhythm, and further work has led to the classification of spontaneous activity into the following frequency bands (Mandal et al., 2018; Saby and Marshall, 2012):

- **Delta oscillations <4 Hz** – associated with relaxation, restorative sleep, and unconscious tasks.
- **Theta oscillations 4–8 Hz** – associated with sleep and meditation, as well as memory, learning and intuition. Abnormalities in both delta and theta oscillations have been observed following mild traumatic brain injury (mTBI) (Huang et al., 2009; Kaltiainen et al., 2018) and in patients with mild cognitive impairment (López et al., 2014).
- **Alpha oscillations 8–13 Hz** – resting state activity associated with attention and modulated by visual and sensory stimulation. Alpha oscillations are believed to gate inhibition (Jensen and Mazaheri, 2010) and information transfer between visual and frontal brain regions (Zumer et al., 2014).
- **Beta oscillations 13–30 Hz** – often associated with movement (and therefore the sensorimotor cortices), thought to relate to inhibition during tasks. Recent work has developed our understanding of beta activity as transient 'bursts', rather than sustained oscillations (Jones, 2016; Shin et al., 2017; van Ede et al., 2018) and models have been developed to interpret how these bursts are generated (Neymotin et al., 2020).
- **Gamma oscillations >30 Hz** – thought to relate to cognitive processing, often associated with the visual cortex but also occur elsewhere in the brain. Gamma oscillations have been implicated in attention and memory (Jensen et al., 2007) and shown to be highly repeatable within individuals (Muthukumaraswamy et al., 2010).

Most MEG studies therefore require femtotesla sensitivity in the 1–100 Hz range (Lopes da Silva, 2013), however there is evidence of much higher frequency neural oscillations, up to 1 kHz (Cimatti et al., 2007; Fedele et al., 2015), that are of particular interest in the study of epilepsy (Engel and Lopes da Silva, 2012).

1.1.2.2. Induced responses

Changes in the amplitude, but not frequency, of the spontaneous rhythms described above can be generated using external stimuli (Pfurtscheller and Lopes da Silva, 1999). These 'induced' responses are time-locked to the stimulus, but their phase is incoherent across multiple events. As a result, induced responses in MEG data must be analysed in the frequency domain, first filtering the time series data to the frequency band of interest, then calculating the amplitude or power envelope. By averaging these envelopes over multiple trials, the changes in oscillatory power in the chosen frequency band induced by the stimulus can be observed.

A well-characterised example of an induced response is the change in oscillatory power in the beta-band related to movement (see Figure 1.4). During voluntary movement, such as a finger abduction, the amplitude envelope of beta oscillations in the sensorimotor cortices decrease, known as an event-related beta desynchronisation. This is followed by an increase above baseline following movement cessation – the post-movement beta rebound (Pfurtscheller et al., 1996). Study of the post-movement beta rebound alone has shown variation in a number of neurological disorders when compared to healthy controls, including schizophrenia (Gascoyne et al., 2021; Robson et al., 2016), autism (Gaetz et al., 2020) and multiple sclerosis (Barratt et al., 2017).

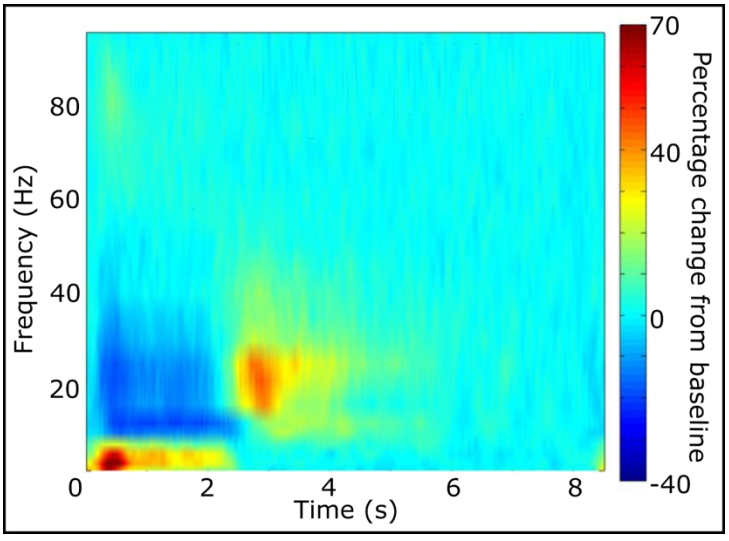

Figure 1.4 – Induced response in beta-band. *Time-frequency spectrum showing the movement-related beta desynchronisation and post-movement beta rebound associated with a finger abduction task. (Adapted from Robson et al., 2016).*

1.1.2.3. Evoked responses

Evoked responses occur due to the presentation of external stimuli but, in contrast to induced effects, are both time-locked and phase-locked to the stimulus. This allows evoked responses to be analysed by averaging across trials in the time domain, without altering the signal magnitude or morphology due to phase differences. Averaging across trials also poses an advantage for noise rejection, since fluctuations due to background brain activity or external interference in individual trials are not phase-locked to the stimulus and will therefore be attenuated as the number of trials increases (see Figure 1.5). Assuming Gaussian random noise, this reduction is characterised as approximately $\sqrt{N}$, where N is the number of trials being averaged.

Evoked responses can occur as a result of auditory (Mäkelä and Hari, 1987), visual (Ahlfors et al., 1992) and somatosensory stimuli (Hari et al., 1993), the latter including median-nerve stimulation, which has been well-characterised in MEG (Korvenoja et al., 1995). Delays in the auditory evoked response present a promising biomarker for autism spectrum disorder (Roberts et al., 2010), and a reduced mismatch negativity component of the auditory evoked potential has been observed in schizophrenia (Umbricht and Krljesb, 2005).

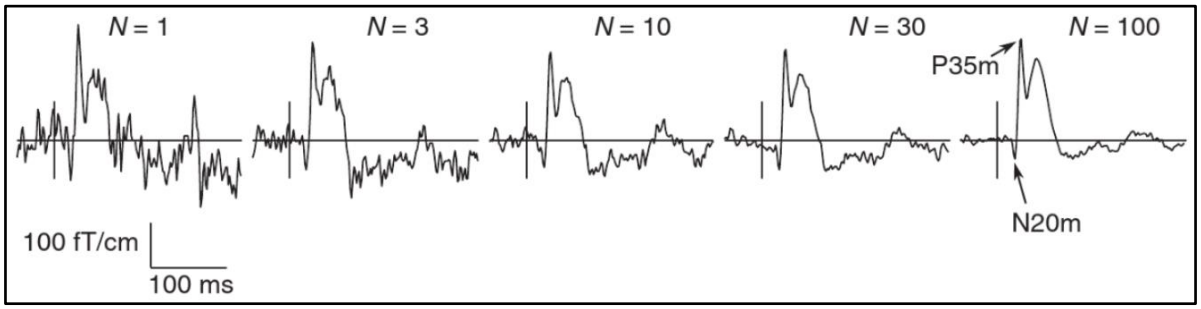

Figure 1.5 – Evoked response. *The effect of averaging across trials (number of trials increasing from left to right) is demonstrated, revealing the evoked response as a result of median-nerve stimulation (Taken from Hansen et al., 2010).*

1.1.2.4. Functional connectivity

So far, neural oscillations have been discussed in the context of localisation to specific areas of the brain e.g., beta oscillations in the motor cortex. However, formation and dissolution of functional networks between different brain regions is required for healthy cognition; for example, interaction between the language network and motor cortex to enable handwriting. We measure such communication via functional connectivity, which identifies brain regions that are spatially separated but whose activity shows a statistical interdependency. The first functional connectivity study was performed using fMRI and identified connections between the left and right motor cortices during the resting state (Biswal et al., 1995), while task-based connectivity has also been shown (Bassett et al., 2015; Hermundstad et al., 2013).

One approach to measuring functional connectivity in EEG and MEG is via assessment of the phase relation between neural oscillations of different brain regions (Breakspear et al., 2004; Nolte et al., 2004). It follows that the oscillations of spatially separate neural networks must be coherent for successful communication between regions to occur, known as the 'communication by coherence' hypothesis (Fries, 2005). An alternative measure of functional connectivity is amplitude envelope correlation, where the amplitude or power envelopes of signals from different regions of the brain are compared to distinguish networks of connectivity (Engel et al., 2013). Use of this approach in MEG has identified many of the same functional networks as other imaging modalities (Boto et al., 2021; Brookes et al., 2011; De Pasquale et al., 2010; Luckhoo et al., 2012) with improved temporal resolution, enabling assessment of network dynamics in greater detail (e.g., Baker et al., 2014).

In summary, the rich spatiotemporal information obtained by MEG enables detailed measurement of neural oscillations due to external stimuli and in the resting state, as well as assessment of evoked responses and connectivity between distinct brain regions. Next, the methods of data acquisition in MEG will be explored.

1.2. Data collection: MEG hardware

The extracranial magnetic fields measured in MEG are incredibly small, typically tens to hundreds of femtotesla in magnitude. For comparison, the Earth's geomagnetic field is approximately fifty microtesla, up to a billion times larger than the neuromagnetic fields of interest (Hämäläinen et al., 1993). Magnetic interference due to vehicles, electrical power lines and other aspects of the urban environment is also much larger than the neuromagnetic field. In addition, the femtotesla signals of interest from the brain are several orders of magnitude smaller than other magnetic fields from the body, such as those generated by the heart, and movement of the eyes and muscles. As a result, MEG devices require extremely sensitive magnetic field sensors with sufficient dynamic range to handle environmental magnetic noise, as well as techniques to reduce external interference, in order to distinguish neuromagnetic fields.

1.2.1. Conventional MEG systems

To reduce the impact of the geomagnetic field and interfering magnetic fields from external sources, MEG devices are usually housed inside a MSR. The walls of the MSR are made from multiple layers of material with a high magnetic permeability, interspersed with layers of high conductivity metal, to reduce DC (0—10 Hz) magnetic fields and interfering fields from AC (>10 Hz) sources, respectively. The origins of such magnetic shielding and its implementation for MEG will be explored in further detail in Chapter 3. Inside the enclosure, typical MSRs have a remnant static magnetic field on the order of tens of nanotesla, with shielding factors of 100–1000 up to 1 Hz and 100—10,000 in the 1—100 Hz frequency range.

1.2.1.1. SQUIDs

The first MEG recording was made inside a three layer MSR by David Cohen in 1968, using a single magnetic field detector comprising 1-million turns of copper wire (Cohen, 1968, 1967). This approach, while proving the existence of neuromagnetic fields, was highly impractical, and a more compact detector with femtotesla sensitivity desired. Fortuitously, such sensors were already in development (Jaklevic et al., 1964; Zimmerman et al., 1970), and in 1972, Cohen carried out the first MEG measurements using superconducting quantum interference devices, or SQUIDs (Cohen, 1972), which remain the state-of-the-art sensors for MEG to this day.

The dc SQUID is the most common building block of a MEG system and is made from a superconducting ring interrupted by two Josephson junctions (thin layers of insulating material, see Figure 1.6A). Superconductivity describes the state in which certain materials have no electrical resistance when cooled below their critical temperature, T_c. According to BCS theory, at $T < T_c$, the electrons inside the superconductor couple together to act as a boson (rather than two fermions) forming so-called 'Cooper pairs', many of which can occupy the same quantum state and thus can be described by a single wavefunction (Bardeen et al., 1957). These pairs are able to tunnel through the insulating gap – known as the Josephson effect (Josephson, 1962) – allowing current to flow through the SQUID.

Magnetic flux that passes through the superconducting ring is quantised (due to the continuous wavefunction of the Cooper pairs) and induces a 'shielding' current in the ring that maintains constant flux. The Josephson junctions enable this current to flow through the ring, giving rise to a flux-dependence resistance across the SQUID. A bias current is then applied such that the voltage across the ring becomes a measure of changes in magnetic flux. However, this relationship between voltage and flux is periodic, and the measurement of magnetic flux therefore ambiguous (see Figure 1.6B). To combat this, SQUIDs are operated in a 'negative feedback' mode, where additional flux through the ring is generated artificially, to oppose the changes in flux due to external sources. The magnitude of this feedback voltage is therefore the negative of the flux through the SQUID, thus providing a quantitative measure of magnetic field (Hämäläinen et al., 1993).

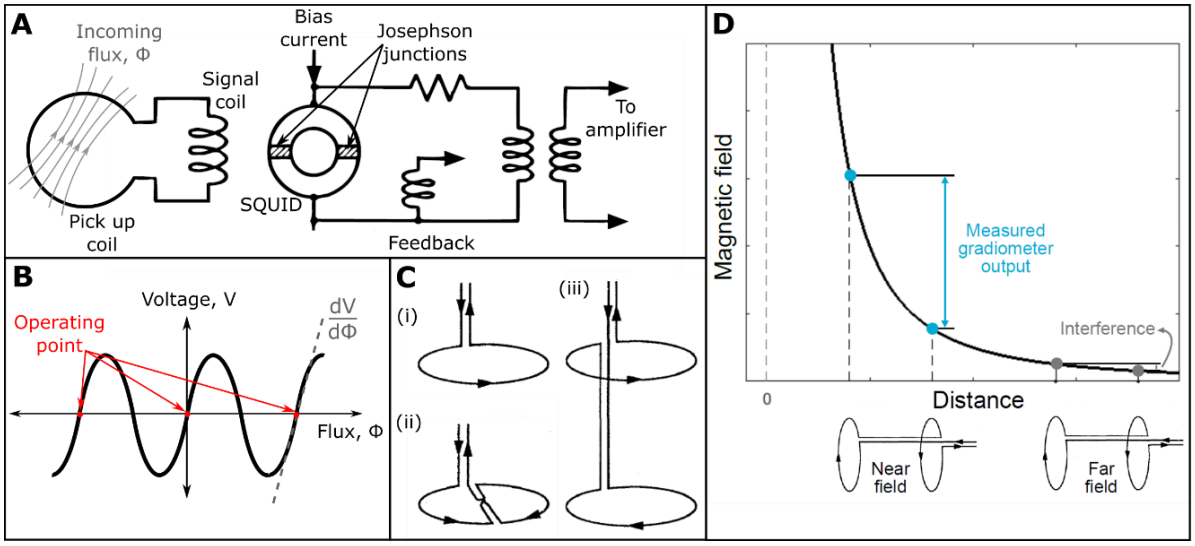

Figure 1.6 – Operation of a SQUID. *A) Schematic diagram of dc SQUID operation. (Adapted from Vrba and Robinson, 2001) B) Voltage to flux response function for a SQUID. The relationship is periodic, therefore negative feedback holds the SQUID at an operating point, where the gradient is steepest. C) Diagrams of (i) magnetometer, (ii) planar gradiometer and (iii) axial gradiometer pick-up coil configurations. (Adapted from Hämäläinen et al., 1993) D) Graph to show the advantage of axial gradiometers for reducing interference for distant sources (Taken from Boto, 2019).*

To enhance their sensitivity to magnetic fields, SQUIDs are coupled to flux transformers, which feature coils with a larger diameter (1–2 cm) than a SQUID (1 mm). Flux transformers are formed from a signal coil and a pick-up coil, the latter can be configured as a magnetometer or gradiometer (see Figure 1.6C). The use of gradiometers allows measurement of the change in magnetic field between two coil loops, which attenuates external interference while retaining signals close to the gradiometer (e.g., the neuromagnetic field), since the rate of change of magnetic field decreases with distance from the source (Vrba and Robinson, 2001).

1.2.1.1. Limitations

Current, state-of-the-art, SQUID-based MEG systems employ approximately three hundred channels spread evenly around the head, measuring the component of magnetic field approximately radial to the head surface with sensitivities of 2–10 fT/√Hz (Vrba, 2000). To maintain superconductivity, the SQUIDs and pick-up coils are immersed in liquid helium at 4 K (–269 °C), and held in a fixed, one-size-fits-all helmet arrangement inside the dewar (see Figure 1.7). The dewar must be refilled periodically as the liquid helium boils off over time, resulting in high running costs. Helium recycling units can be fitted to cryogenic MEG systems to limit these ongoing costs but require an initial investment and an ongoing maintenance contract.

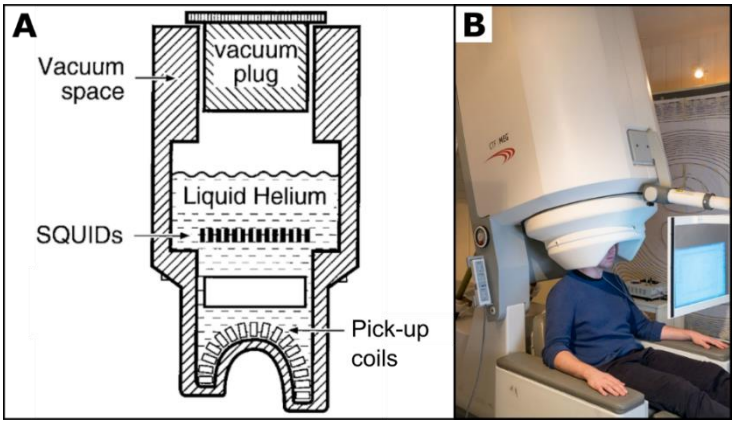

Figure 1.7 – Cryogenic MEG system. *A) Schematic diagram of a cryogenic MEG dewar, where the SQUIDs and pick-up coils are immersed in liquid helium and arranged in a one-size-fits-all helmet. (Adapted from Vrba and Robinson, 2001) B) Photograph of the CTF MEG system at the Sir Peter Mansfield Imaging Centre, University of Nottingham.*

A vacuum is maintained between the sensors and the inner surface of the helmet, where the participant positions their head for a scan. This provides thermal insulation to protect the participant from the cold temperatures at which the pick-up coils are kept yet limits the proximity of sensors to the head. Since magnetic field strength has an inverse square relationship with increasing distance from the source, this results in reduced signal-to-noise ratio (SNR) and spatial resolution of MEG data, compared to the case where the sensors could be placed directly on the scalp (Boto et al., 2016). This distance between the sensors and the brain also varies between participants due to the one-size-fits-all nature of the helmet, leading to inconsistencies in coverage – typically in the frontal areas, as participants rest their head at the back of the helmet. This problem is exacerbated across the entire brain in participant cohorts with smaller heads, e.g., children, such that the use of a dedicated scanner with a smaller helmet array may be required.

Furthermore, any movement of the participant's head away from the fixed sensor array will degrade data quality due to corresponding changes in signal amplitude, SNR, and field topography. Typically, head movements up to 5 mm are tolerated (Gross et al., 2013) and, while challenging, further movement artefacts can be minimised in post-processing (Nenonen et al., 2012; Taulu et al., 2005; Wehner et al., 2008). Simulations have shown that errors in spatial localisation of MEG data due to participant motion (up to ~2 cm) can be restored to pre-movement levels (Larson and Taulu, 2017), hence such compensation techniques are essential for paediatric MEG and other study cohorts that may find it difficult to remain still throughout a scan. Nevertheless, movement is fundamentally restricted by the fixed helmet array, since moving more than a few centimetres would cause the participant's head to hit the helmet, therefore access to naturalistic experimental paradigms is extremely limited.

1.2.2. Alternative sensor technologies

As a result of the limitations imposed by SQUID-based sensing described above, it is desirable to construct a MEG system from sensors that operate at ambient temperatures, can be flexibly mounted on or near the scalp and easily reconfigured to adapt to different head sizes and shapes. In recent years, technological advances have led to the development of several highly sensitive magnetic field detectors that may be suitable for MEG, while also alleviating some of the limitations of conventional systems.

1.2.2.1. High-T_c SQUIDs

Using a superconducting material with a higher critical temperature than the conventional SQUID allows for operation of high-T_c SQUIDs at 77 K, rather than 4 K. Cryogenic cooling is still required but can be achieved with liquid nitrogen, which is more readily available than liquid helium, at lower cost. These higher temperatures also enable reduction of the insulating vacuum gap between the sensor and the scalp to ~3 mm (Öisjöen et al., 2012). The substantial limitations imposed by a cryogenic dewar (restricted participant movement and fixed sensor arrays) remain; nevertheless, efforts to develop a multi-channel high-T_c SQUID array are ongoing (Pfeiffer et al., 2019; Riaz et al., 2017).

1.2.2.2. Nitrogen-vacancy centres

Nitrogen-vacancy (NV) centres are formed when a nitrogen atom is substituted into the lattice structure of diamond, with a corresponding vacancy in the lattice occuring at an adjacent site. The electronic spin system of a negatively-charged NV centre can be exploited, using a microwave source and an exciting laser, to measure magnetic fields (Rondin et al., 2014; Taylor et al., 2008). NV centre magnetometry operates at room temperature, thus miniaturised sensors could be mounted at the scalp. However, at present, the ~300 pT/√Hz sensitivity of NV centres is insufficient for MEG measurements (Dale and Morley, 2017; Patel et al., 2020).

1.2.2.3. Optically-pumped magnetometers

OPMs exploit the spin properties of alkali atoms in a vapour to form highly sensitive atomic magnetometers, via a process called optical-pumping (Budker and Romalis, 2007; Happer, 1972). The vapour is heated (to 150 °C for ^{87}Rb) to achieve sufficient spin coherence times for magnetometry (Allred et al., 2002), but the external temperature of the sensor casing remains below 45 °C, at approximately body temperature. This, combined with microfabrication and miniaturisation (Knappe et al., 2010; Sander et al., 2012; Shah and Wakai, 2013), has enabled the construction of multi-channel OPM arrays for MEG, with sensors mounted at the scalp.

The first MEG measurements using a single OPM were performed in 2006, capturing the auditory evoked response (Xia et al., 2006). Since then, the use of OPMs for MEG has increased (e.g., Borna et al., 2017; Boto et al., 2017; Iivanainen et al., 2017; Johnson et al., 2010; Kamada et al., 2015),

particularly, in recent years, due to sensor commercialisation. At the time of writing, several companies across the globe manufacture OPMs suitable for biomedical applications, including QuSpin Inc. (Louisville, CO, U.S.A.), FieldLine Inc. (Boulder, CO, U.S.A.), Twinleaf LLC (Plainsboro, NJ, U.S.A.) and MAG4Health (Grenoble, France). The OPMs used in this work were sourced from QuSpin Inc. (zero-field magnetometer, Osborne et al., 2018), which have sensitivities <15 fT/√Hz in the 1–100 Hz frequency band, a small footprint of 12.4×16.6 mm^2 and 6.5 mm standoff from the scalp (https://quspin.com/products-qzfm/). At the time of writing, such properties make OPMs the most appropriate alternative sensing technology for MEG, and hence form the focus of this thesis. More detailed theory underpinning OPM operation will be examined in Chapter 2.

1.3. Data analysis

Once MEG data have been collected, the challenge becomes how to determine the underlying neuronal currents that generated the magnetic fields measured at the scalp. This is known as the MEG inverse problem and is mathematically ill-posed (Hadamard, 1902), since any given magnetic field distributions could be generated by an infinite number of different current distributions, due to field cancellation. Therefore, we begin by first constructing a model that characterises the magnetic field distribution outside the head from a **known** current source in the brain. This is a mathematically well-defined solution known as the forward model, which can be solved via Maxwell's equations.

1.3.1. The forward problem

The MEG forward problem requires that given a known current distribution in the brain we determine the resulting magnetic fields generated outside the head, at our sensors.

To describe a current density, $\boldsymbol{J}$, we use Maxwell's equations that characterise electric, $\boldsymbol{E}$, and magnetic, $\boldsymbol{B}$, fields:

$$\begin{aligned} \boldsymbol{\nabla} \cdot \boldsymbol{E} &= \frac{\rho}{\epsilon} \\ \boldsymbol{\nabla} \times \boldsymbol{E} &= \frac{-\partial \boldsymbol{B}}{\partial t} \\ \boldsymbol{\nabla} \cdot \boldsymbol{B} &= 0 \\ \boldsymbol{\nabla} \times \boldsymbol{B} &= \mu_0 \left(\boldsymbol{J} + \epsilon \frac{\partial \boldsymbol{E}}{\partial t} \right) \end{aligned} \tag{1.1}$$

where ρ is the charge density of the medium, ϵ is the permittivity and μ_0 is the permeability of free space. We approximate the permeability of biological tissue to be equal to μ_0, and further simplify the equations by making a quasistatic approximation (Hämäläinen et al., 1993); since the electromagnetic

fields from the brain mostly occur at relatively low frequencies (1–100 Hz), the terms in Equations (1.1) that vary with time can be considered negligible, yielding:

$$\begin{aligned} \boldsymbol{\nabla} \times \boldsymbol{E} &= 0 \\ \boldsymbol{\nabla} \times \boldsymbol{B} &= \mu_0 \boldsymbol{J}. \end{aligned} \tag{1.2}$$

The magnetic field generated at position $\boldsymbol{r}$ outside a volume conductor, G, by current density $\boldsymbol{J}$ at position $\boldsymbol{r}'$ inside the conductor, is then given by the Ampère-Laplace law:

$$\boldsymbol{B}(\boldsymbol{r}) = \frac{\mu_0}{4\pi} \int_G \boldsymbol{J}(\boldsymbol{r}') \times \frac{\boldsymbol{r} - \boldsymbol{r}'}{|\boldsymbol{r} - \boldsymbol{r}'|^3} dv'. \tag{1.3}$$

The total current $\boldsymbol{J}(\boldsymbol{r}')$ is characterised by the sum of the primary currents, $\boldsymbol{J_p}$, and volume currents, $\boldsymbol{J_v}$, along a dendrite, as described in Section 1.1.1.2, such that

$$\boldsymbol{J}(\boldsymbol{r}') = \boldsymbol{J_p}(\boldsymbol{r}') + \boldsymbol{J_v}(\boldsymbol{r}'). \tag{1.4}$$

Since volume currents occur as a result of the extracellular electric field, in a medium with uniform conductivity, σ, these currents can be expressed in terms of an electrical potential, V, as $\boldsymbol{E} = -\nabla V$ (Sarvas, 1987), such that

$$\boldsymbol{J}(\boldsymbol{r}') = \boldsymbol{J_p}(\boldsymbol{r}') - \sigma \nabla V(\boldsymbol{r}'). \tag{1.5}$$

By substituting Equation (1.5) into (1.3), the magnetic field can be described by

$$\boldsymbol{B}(\boldsymbol{r}) = \frac{\mu_0}{4\pi} \int_G \boldsymbol{J_p}(\boldsymbol{r}') \times \frac{\boldsymbol{r} - \boldsymbol{r}'}{|\boldsymbol{r} - \boldsymbol{r}'|^3} dV' - \sigma \frac{\mu_0}{4\pi} \int_G \nabla V(\boldsymbol{r}') \times \frac{\boldsymbol{r} - \boldsymbol{r}'}{|\boldsymbol{r} - \boldsymbol{r}'|^3} dV', \tag{1.6}$$

If the conductivity varies within the medium, the volume current can be calculated by summation of the integral computed over any number of 'compartments' (e.g., the brain, skull, and scalp, see Figure 1.8A), G_j, as follows:

$$\boldsymbol{B}(\boldsymbol{r}) = \frac{\mu_0}{4\pi} \left[\int_G \boldsymbol{J_p}(\boldsymbol{r}') \times \frac{\boldsymbol{r} - \boldsymbol{r}'}{|\boldsymbol{r} - \boldsymbol{r}'|^3} dV' - \sum_{j=1}^{n} \sigma_j \int_G \nabla V(\boldsymbol{r}') \times \frac{\boldsymbol{r} - \boldsymbol{r}'}{|\boldsymbol{r} - \boldsymbol{r}'|^3} dV' \right]. \tag{1.7}$$

Isolating the content of the volume current integral, we apply the vector identity $\nabla a \times \nabla b = \nabla \times (a \nabla b)$, such that

$$\nabla V(\boldsymbol{r}') \times \frac{\boldsymbol{r} - \boldsymbol{r}'}{|\boldsymbol{r} - \boldsymbol{r}'|^3} = \nabla \times V(\boldsymbol{r}') \frac{\boldsymbol{r} - \boldsymbol{r}'}{|\boldsymbol{r} - \boldsymbol{r}'|^3}. \tag{1.8}$$

The generalised Stokes' theorem, $\int_G \nabla \times \boldsymbol{X}\, dV' = \int_S \hat{\boldsymbol{n}} \times \boldsymbol{X}\, dS$, can then be applied to convert the volume integral to a surface integral, and thus derive the Geselowitz formula (Geselowitz, 1967):

$$\boldsymbol{B}(\boldsymbol{r}) = \frac{\mu_0}{4\pi}\int_G \boldsymbol{J_p}(\boldsymbol{r}') \times \frac{\boldsymbol{r}-\boldsymbol{r}'}{|\boldsymbol{r}-\boldsymbol{r}'|^3}\, dV' - \frac{\mu_0}{4\pi}\sum_{j=1}^{n}(\sigma_j' - \sigma_j'')\int_{S_j} V(\boldsymbol{r}')\cdot\hat{\boldsymbol{n}}(\boldsymbol{r}') \times \frac{\boldsymbol{r}-\boldsymbol{r}'}{|\boldsymbol{r}-\boldsymbol{r}'|^3}\, dS_j, \tag{1.9}$$

where σ' and σ'' are the conductivities in neighbouring compartments, and $\hat{\boldsymbol{n}}(\boldsymbol{r}')$ is the unit vector perpendicular to the surface S_j at $\boldsymbol{r}'$. Note that the first term of Equation (1.9) represents the magnetic fields associated with the primary current within a dendrite, which are unaffected by the conductivity of the medium.

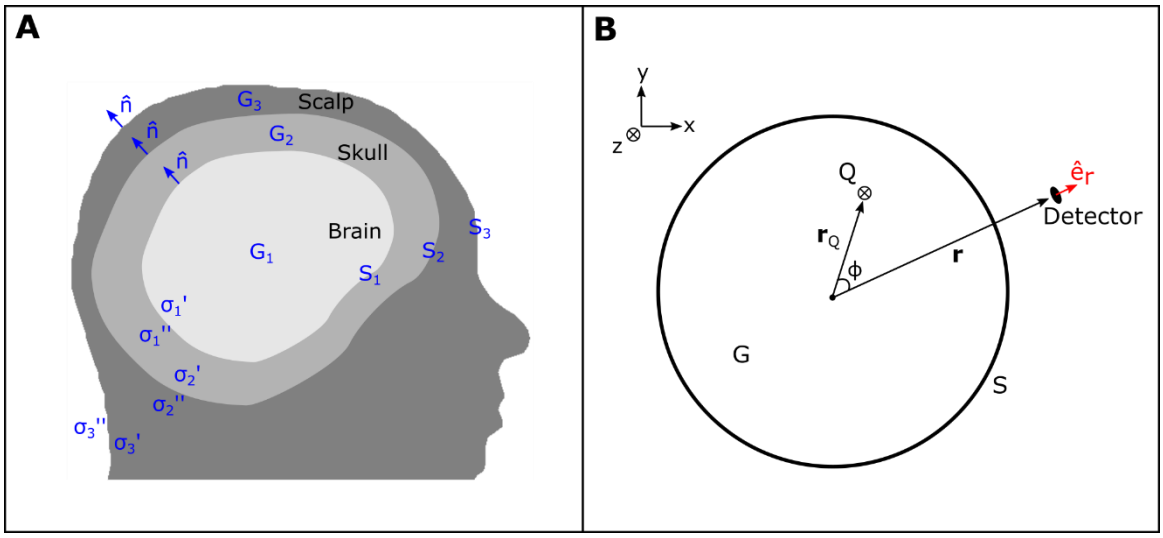

Figure 1.8 – MEG forward model. *A) Schematic diagram showing three head compartments, each with volume G, surface S, surface normal* $\hat{\boldsymbol{n}}$ *and conductivity σ. B) The single sphere forward model, where current dipole Q is oriented along z at position* $\boldsymbol{r_Q}$.

1.3.1.1. Single sphere model

The simplest forward model implemented in MEG is known as the single sphere model, where the brain, skull and scalp are approximated as a spherically symmetric conductor with uniform conductivity. Assuming we measure the component of magnetic field radial to the sphere surface S, using a detector at with orientation $\hat{\boldsymbol{e}}_r$, the measured field $B_r(\boldsymbol{r})$ is given by the dot product $B_r(\boldsymbol{r}) = \boldsymbol{B}(\boldsymbol{r})\cdot\hat{\boldsymbol{e}}_r$, thus

$$B_r(\boldsymbol{r}) = \frac{\mu_0}{4\pi}\left[\int_G \boldsymbol{J_p}(\boldsymbol{r}') \times \frac{\boldsymbol{r}-\boldsymbol{r}'}{|\boldsymbol{r}-\boldsymbol{r}'|^3}\cdot\hat{\boldsymbol{e}}_r\, dV' - \sigma\int_S V(\boldsymbol{r}')\cdot\hat{\boldsymbol{n}}(\boldsymbol{r}') \times \frac{\boldsymbol{r}-\boldsymbol{r}'}{|\boldsymbol{r}-\boldsymbol{r}'|^3}\cdot\hat{\boldsymbol{e}}_r dS\right]. \tag{1.10}$$

By inspection of the second term of Equation (1.10), we note that

$$\hat{\boldsymbol{n}}(\boldsymbol{r}') \times (\boldsymbol{r} - \boldsymbol{r}') \cdot \hat{\boldsymbol{e}}_{\boldsymbol{r}} = (\hat{\boldsymbol{n}}(\boldsymbol{r}') \times \boldsymbol{r} - \hat{\boldsymbol{n}}(\boldsymbol{r}') \times \boldsymbol{r}') \cdot \hat{\boldsymbol{e}}_{\boldsymbol{r}}, \tag{1.11}$$

and considering the geometry shown in Figure 1.8B, we find

$$\begin{gathered} \hat{\boldsymbol{n}}(\boldsymbol{r}') \times \boldsymbol{r}' = 0, \text{since } \hat{\boldsymbol{n}}(\boldsymbol{r}') \parallel \boldsymbol{r}' \\ \hat{\boldsymbol{n}}(\boldsymbol{r}') \times \boldsymbol{r} \cdot \hat{\boldsymbol{e}}_{\boldsymbol{r}} = 0, \text{since } \hat{\boldsymbol{n}}(\boldsymbol{r}') \times \boldsymbol{r} \perp \hat{\boldsymbol{e}}_{\boldsymbol{r}}. \end{gathered} \tag{1.12}$$

The second term of Equation (1.10) therefore tends to zero for the single sphere model, leaving an expression for the magnetic field measured by the sensor that is unaffected by volume currents:

$$B_r(\boldsymbol{r}) = \frac{\mu_0}{4\pi} \int_G \boldsymbol{J_p}(\boldsymbol{r}') \times \frac{\boldsymbol{r} - \boldsymbol{r}'}{|\boldsymbol{r} - \boldsymbol{r}'|^3} \cdot \hat{\boldsymbol{e}}_{\boldsymbol{r}}\, dV'. \tag{1.13}$$

Note that there is no measurable magnetic field outside the head if the direction of current flow is radial, since $\boldsymbol{J}$ is parallel to $\boldsymbol{r}'$, and $\boldsymbol{J} \times \boldsymbol{r}$ is perpendicular to $\hat{\boldsymbol{e}}_{\boldsymbol{r}}$.

1.3.1.2. Current dipole approximation

As discussed previously in Section 1.1.1.2, the primary current can be represented by a current dipole. We therefore approximate the primary current density, $\boldsymbol{J_p}(\boldsymbol{r}')$, as a unidirectional current at a single point, which is expressed mathematically using a Dirac delta function, thus

$$\boldsymbol{J_p}(\boldsymbol{r}') = \boldsymbol{Q}\delta(\boldsymbol{r}' - \boldsymbol{r_Q}), \tag{1.14}$$

where $\boldsymbol{Q}$ is the strength of a current dipole at position $\boldsymbol{r_Q}$. It follows that the measured magnetic field $B_r(\boldsymbol{r})$ is

$$B_r(\boldsymbol{r}) = \frac{\mu_0}{4\pi} \int_G \boldsymbol{Q}\delta(\boldsymbol{r}' - \boldsymbol{r_Q}) \times \frac{\boldsymbol{r} - \boldsymbol{r}'}{|\boldsymbol{r} - \boldsymbol{r}'|^3} \cdot \hat{\boldsymbol{e}}_{\boldsymbol{r}}\, dV', \tag{1.15}$$

which simplifies to

$$B_r(\boldsymbol{r}) = \frac{\mu_0}{4\pi} \frac{\boldsymbol{Q} \times (\boldsymbol{r} - \boldsymbol{r_Q})}{|\boldsymbol{r} - \boldsymbol{r_Q}|^3} \cdot \hat{\boldsymbol{e}}_{\boldsymbol{r}} = \frac{\mu_0}{4\pi} \frac{\boldsymbol{Q} \times \boldsymbol{r_Q}}{|\boldsymbol{r} - \boldsymbol{r_Q}|^3} \cdot \hat{\boldsymbol{e}}_{\boldsymbol{r}}. \tag{1.16}$$

Note that Equation (1.16) gives only the radial component of measured magnetic field. To obtain the total magnetic field generated outside the conductor, G, by a current dipole $\boldsymbol{Q}$ inside the conductor at position $\boldsymbol{r_Q}$, we employ Maxwell's equation $\boldsymbol{\nabla} \times \boldsymbol{B} = \mu_0 \boldsymbol{J}$. This expression tends to zero outside the head, since $\boldsymbol{J} = 0$. Therefore, the total magnetic field can be described in terms of the scalar potential, $U(\boldsymbol{r})$

$$\boldsymbol{B}(\boldsymbol{r}) = -\mu_0 \nabla U(\boldsymbol{r}). \tag{1.17}$$

The formula for $U(\boldsymbol{r})$ was derived by Sarvas via evaluation of a line integral of ∇U along the radius $\boldsymbol{r} + t\hat{\boldsymbol{e}}_r$, where $0 < t < \infty$ and U tends to zero at infinity. The integral is given as

$$\begin{aligned} U(\boldsymbol{r}) &= -\int_0^\infty \nabla U(\boldsymbol{r} + t\hat{\boldsymbol{e}}_r) \cdot \hat{\boldsymbol{e}}_r dt \\ &= \frac{1}{\mu_0}\int_0^\infty \boldsymbol{B}(\boldsymbol{r} + t\hat{\boldsymbol{e}}_r) \cdot \hat{\boldsymbol{e}}_r dt \\ &= \frac{1}{\mu_0}\int_0^\infty B_r(\boldsymbol{r} + t\hat{\boldsymbol{e}}_r)\, dt \\ &= \frac{1}{\mu_0}\int_0^\infty \boldsymbol{B_p}(\boldsymbol{r} + t\hat{\boldsymbol{e}}_r) \cdot \hat{\boldsymbol{e}}_r dt \\ &= \frac{1}{4\pi}\boldsymbol{Q} \times (\boldsymbol{r} - \boldsymbol{r_Q}) \cdot \hat{\boldsymbol{e}}_r \int_0^\infty \frac{dt}{|\boldsymbol{r} + t\hat{\boldsymbol{e}}_r - \boldsymbol{r_Q}|^3}, \end{aligned} \tag{1.18}$$

with solution

$$U(\boldsymbol{r}) = -\frac{1}{4\pi}\frac{\boldsymbol{Q} \times \boldsymbol{r_Q} \cdot \boldsymbol{r}}{F}, \tag{1.19}$$

where $F = a(ar + \boldsymbol{r}^2 - \boldsymbol{r_Q} \cdot \boldsymbol{r})$, $\boldsymbol{a} = \boldsymbol{r} - \boldsymbol{r_Q}$, $a = |\boldsymbol{a}|$ and $r = |\boldsymbol{r}|$ (Sarvas, 1987).

Finally, we obtain an expression for the total magnetic field outside the conductor by substituting Equation (1.19) into (1.17) as follows

$$\boldsymbol{B}(\boldsymbol{r}) = -\frac{\mu_0}{4\pi F^2}\left(F\boldsymbol{Q} \times \boldsymbol{r_Q} - \boldsymbol{Q} \times \boldsymbol{r_Q} \cdot \boldsymbol{r}\nabla F\right). \tag{1.20}$$

1.3.1.3. Other forward models

While the single sphere model allows for more straightforward computation of the extracranial magnetic fields from a known current distribution in the brain, it is an oversimplification of head geometry and conductivity. More accurate forward models have been developed, such as the multiple sphere model (Huang et al., 1999), where the best fitting sphere for each sensor location is chosen, leading to a series of overlapping volumes that better characterise the brain geometry. A multiple sphere forward model is employed in Chapter 6.

Perhaps the most realistic forward model to date is derived using boundary element methods (BEM), where the brain, skull and scalp surfaces are determined from an anatomical MRI and the forward problem (i.e., the Geselowitz formula, Equation (1.9) is solved numerically (Stenroos et al., 2014). The head geometry is therefore known accurately, and such models are computationally expensive. To compromise, single-shell models employ only the inner skull boundary (Hämäläinen and

Sarvas, 1989, 1987), and assume the skull and scalp are insulating such that their contribution to the MEG signal is negligible. As a result, accurate forward models can be achieved with practical computation times. A single-shell forward model is used in Chapter 5, where additional, non-radial components of the neuromagnetic field were measured, thus a more advanced head model required.

1.3.2. Inverse problem

Having generated a forward model that characterises the magnetic fields generated outside the head by a known current dipole inside the brain, we can now work towards solving the inverse problem and determine the underlying neuronal currents that created the magnetic fields captured by our MEG data. Despite being mathematically ill-posed, optimisation approaches exist that allow us to solve the MEG inverse problem, including equivalent current dipole methods, minimum norm estimation and beamformer spatial filters (Brenner et al., 1978; Hämäläinen and Ilmoniemi, 1994; Hari and Salmelin, 2012). Here we focus on the linearly constrained minimum variance (LCMV) beamformer technique, due to its efficacy at reconstructing oscillatory activity and its excellent interference rejection properties (Sekihara et al., 2006).

1.3.2.1. Forward fields

A forward field is given by the solution to the forward problem at each sensor, for a current dipole of unit strength at some predetermined location, and characterises the magnetic field measured by a given sensor at time t. For sensor i of N total channels, the forward field generated by a current dipole at position $\boldsymbol{r}'$ in the brain is given by $l_i(\boldsymbol{r}')$. The measured field, $m_i(t)$, can be calculated via multiplication of the forward field by the true dipole strength $q(\boldsymbol{r}', t)$, and integration over the volume conductor:

$$m_i(t) = \int_V l_i(\boldsymbol{r}') \cdot q(\boldsymbol{r}', t) dV'. \tag{1.21}$$

To evaluate this expression, we discretise the brain volume into $(j = 1,2,3 \dots M)$ cubic voxels, each assumed to contain a single current dipole. Equation (1.21) can then be written as the following summation,

$$m_i(t) = \sum_{j=1}^{M} l_{i,j} \cdot q_j(t). \tag{1.22}$$

Casting this in matrix form, we find

$$\boldsymbol{m}(t) = \boldsymbol{L}\boldsymbol{q}(t), \tag{1.23}$$

where $\boldsymbol{L}$ is the lead field matrix, of dimensions $N \times M$, and $\boldsymbol{q}(t)$ is a vector of length M.

Equation (1.23) is known as the generative model in MEG and allows us to determine the current distribution that best maps to the magnetic fields measured at the sensors, by inversion of the lead field

matrix. This inversion is an underdetermined problem, however, since there are many more current sources than detectors, the matrix $\boldsymbol{L}$ is not square, and its columns are correlated (i.e., it is rank deficient). Hence, the MEG inverse problem is ill-posed, and assumptions are required to determine a solution.

1.3.2.2. Beamforming

Beamformer approaches are used extensively to solve the inverse problem in both EEG and MEG (Van Veen et al., 1997; Vrba and Robinson, 2001), but were first developed and implemented for signal processing in radar and communications (Van Veen and Buckley, 1988). Beamforming aims to determine an estimate, $\hat{q}_{\boldsymbol{\theta}}(t)$, of the true electrical source strength $q_{\boldsymbol{\theta}}(t)$, at a given voxel and orientation $\boldsymbol{\theta}$, via a weighted sum of the sensor measurements (see Figure 1.9). This can be described as follows

$$\hat{q}_{\boldsymbol{\theta}}(t) = \boldsymbol{w}_{\boldsymbol{\theta}}^{\boldsymbol{T}}\boldsymbol{m}(t). \tag{1.24}$$

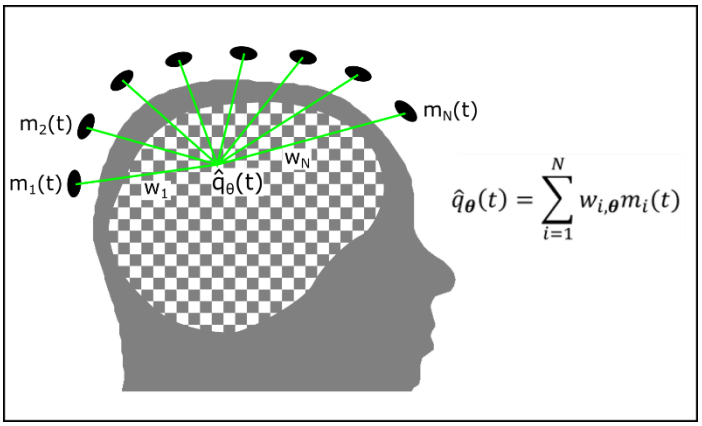

Figure 1.9 – Beamforming. *An estimate $\hat{q}_{\theta}$ of the dipole strength is obtained via a weighted sum of the magnetic field measured by sensors distributed around the head.*

The weighting parameters, $\boldsymbol{w}_{\boldsymbol{\theta}}$, are determined via a power minimisation method, reducing the variance in $\hat{q}_{\boldsymbol{\theta}}(t)$ with the linear constraint that signal originating from $\boldsymbol{\theta}$ is retained. Consequently, all other signals, including magnetic interference from external sources, are minimised. Mathematically this is expressed as

$$\min_{\boldsymbol{w}_{\boldsymbol{\theta}}} \left|\langle \hat{q}_{\boldsymbol{\theta}}{}^2(t)\rangle\right|, \text{ subject to } \boldsymbol{w}_{\boldsymbol{\theta}}^{\boldsymbol{T}}\boldsymbol{l}_{\boldsymbol{\theta}} = 1, \tag{1.25}$$

where $\langle x\rangle$ denotes the expectation value of x, and $\boldsymbol{l}_{\boldsymbol{\theta}}$ contains the lead fields generated at all N sensors by a current dipole of unit strength at location $\boldsymbol{\theta}$ (i.e., $\boldsymbol{l}_{\boldsymbol{\theta}}$ is a column of $\boldsymbol{L}$).

Using Equation (1.24) we evaluate $\langle \hat{q}_{\boldsymbol{\theta}}{}^2(t) \rangle$ such that

$$\begin{aligned} \langle \hat{q}_{\boldsymbol{\theta}}{}^2(t) \rangle &= \langle \boldsymbol{w}_{\boldsymbol{\theta}}^{\boldsymbol{T}} \boldsymbol{m}(t) \rangle \langle \boldsymbol{w}_{\boldsymbol{\theta}}^{\boldsymbol{T}} \boldsymbol{m}(t) \rangle \\ &= \boldsymbol{w}_{\boldsymbol{\theta}}^{\boldsymbol{T}} \langle \boldsymbol{m}(t) \boldsymbol{m}^{\boldsymbol{T}}(t) \rangle \boldsymbol{w}_{\boldsymbol{\theta}} \\ &\approx \boldsymbol{w}_{\boldsymbol{\theta}}^{\boldsymbol{T}} \boldsymbol{C} \boldsymbol{w}_{\boldsymbol{\theta}}, \end{aligned} \tag{1.26}$$

where $\boldsymbol{C}$ is an estimate of the covariance matrix of the MEG data, with dimensions $N \times N$. As such the ij^{th} element of $\boldsymbol{C}$ is the covariance of the data measured by sensor channels i and j.

The solution to Equation (1.25) is found analytically using a Lagrange multiplier (Van Veen et al., 1997), and the weights given by

$$\boldsymbol{w}_{\boldsymbol{\theta}}^{\boldsymbol{T}} = \frac{\boldsymbol{l}_{\boldsymbol{\theta}}^{\boldsymbol{T}} \boldsymbol{C}^{-\mathbf{1}}}{\boldsymbol{l}_{\boldsymbol{\theta}}^{\boldsymbol{T}} \boldsymbol{C}^{-\mathbf{1}} \boldsymbol{l}_{\boldsymbol{\theta}}}. \tag{1.27}$$

The data covariance is calculated over the total number of time points, P, as follows:

$$C_{ij} = \frac{1}{P} \sum_{p=1}^{P} m_i(t_p) m_j(t_p). \tag{1.28}$$

Regularisation techniques, such as the Tikhonov method, may be required if the matrix $\boldsymbol{C}$ is close to singular. For Tikhonov regularisation, the regularised matrix is calculated as $\boldsymbol{C}_{\boldsymbol{r}} = \boldsymbol{C} + \mu \boldsymbol{I}$, where μ is typically a small percentage of the maximum eigenvalue of $\boldsymbol{C}$, and $\boldsymbol{I}$ is the identity matrix.

So far, we have assumed the position and orientation of the current dipole is known and contained within the vector $\boldsymbol{\theta}$, however, in practise this must be calculated. This is achieved by determining the dipole orientation that generates maximum SNR, which can be simplified given that MEG is insensitive to radially oriented dipoles. Thus, the computation is constrained to the polar-azimuthal plane, such that $0 < \varphi < \pi$. The angle, φ, that maximises the SNR can be calculated by optimising either the pseudo-Z-statistic,

$$\mathrm{Z}_{\boldsymbol{r},\boldsymbol{\varphi}} = \frac{\boldsymbol{w}_{\boldsymbol{r},\varphi}^{T} \boldsymbol{C} \boldsymbol{w}_{\boldsymbol{r},\varphi}}{\boldsymbol{w}_{\boldsymbol{r},\varphi}^{T} \sum \boldsymbol{w}_{\boldsymbol{r},\varphi}}, \tag{1.29}$$

or the power at each voxel, where the power is equivalent to the numerator of Equation (1.29). This can be achieved via an exhaustive search or by first reconstructing a vector beamformer and applying principle component analysis (PCA).

As a measure of neural activity, the pseudo-Ŧ statistic can be computed at each voxel, which contrasts MEG data obtained during active and control time windows determined by the task. This is given by

$$Ŧ = \frac{Q_a - Q_c}{2Q_c}. \tag{1.30}$$

where $Q_a = \boldsymbol{w^T C_a}$ and $Q_C = \boldsymbol{w^T C_c}$ represent power during the active and control periods, respectively (Vrba and Robinson, 2001). By evaluating the pseudo-Ŧ statistic at every voxel in the brain, a volumetric functional image is obtained, highlighting areas of neural activation. Figure 1.10 shows an example pseudo-Ŧ-statistical image obtained when writing with the right hand; neural activity is localised to the contralateral motor cortex. To perform source reconstruction analyses and construct such images, the location and orientation of all detectors in the MEG array must be determined relative to brain anatomy, known as co-registration (see Section 2.5.4.1).

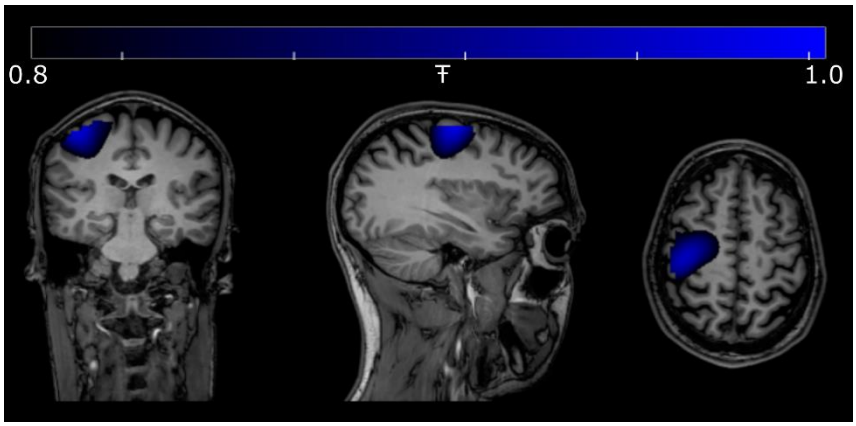

Figure 1.10 – Pseudo-T-statistical image. *A 3D functional image characterising brain activity is obtained via computation of the pseudo-T statistic at each voxel in the brain. These values are thresholded at 80% of the maximum and overlaid onto the anatomical MRI for visualisation. In this example the participant performed a handwriting task with their right hand, thus the activity is localised to the left motor cortex.*

Chapter 2

Optically-pumped magnetometers

In this chapter, a brief history of OPMs is presented, before shifting focus to the commercially available QuSpin OPM that is used throughout this thesis. The principle of operation of a QuSpin OPM is explored in detail, including the mechanisms of optical pumping and the spin-exchange relaxation free regime, upon which these sensors rely. The resulting signal equations are defined, and we examine how they manifest in the output of our OPM. Finally, the approaches taken to implement OPMs for MEG at the Sir Peter Mansfield Imaging Centre, University of Nottingham are described, to characterise the evolution of our OPM-MEG system to date.

2.1. Introduction

OPMs rely on the manipulation of a quantum property known as spin, which characterises the intrinsic angular momentum of atoms and governs how they interact with magnetic fields (Gerlach and Stern, 1922; Rabi et al., 1938; Uhlenbeck and Goudsmit, 1926). As introduced in the previous chapter, optically-pumped magnetometry is performed by illuminating atomic species with resonant light tuned to specific atomic transitions (Kastler, 1951). This was first achieved around the 1960s (Bell and Bloom, 1961, 1957), however the required optics equipment meant that experiments were confined to the laboratory bench for the remainder of the 20th century.

Nevertheless, once sensitivities suitable for biomagnetic recordings were obtained (Dang et al., 2010; Kominis et al., 2003), MEG measurements were undertaken, mapping the auditory evoked response (Xia et al., 2006). The development of microfabrication techniques transformed bench top OPMs into a lightweight sensor package (Griffith et al., 2010; Knappe et al., 2010; Mhaskar et al., 2012; Schwindt et al., 2007; Shah et al., 2007; Shah and Wakai, 2013; Sheng et al., 2017; see Figure 2.1). enabling mounting on the scalp and consequently, multi-channel recordings. OPMs have since been used to map most measurable neuromagnetic effects of interest, including evoked responses to auditory (Borna et al., 2020; Johnson et al., 2010, 2013; Kowalczyk et al., 2021) and somatosensory stimulation (Borna et al., 2017; Boto et al., 2017; Iivanainen et al., 2019; Sander et al., 2012), as well as neural oscillations in the alpha (Coussens et al., 2021; Roberts et al., 2019; R. Zhang et al., 2020; X. Zhang et al., 2020), beta (Boto et al., 2018; Tierney et al., 2018) and gamma bands (Hill et al., 2020) and functional connectivity (Boto et al., 2021). The flexibility in sensor placement afforded by OPMs has also allowed the measurement of deep brain structures, such as the hippocampus and cerebellum (Lin et al., 2019; Tierney et al., 2021). OPMs have also been employed to measure biomagnetic signals beyond the brain, such as those from the adult (Bison et al., 2003; Kamada et al., 2015) and fetal heart (Alem et al., 2015; Batie et al., 2018), muscles (Broser et al., 2018; Elzenheimer et al., 2020; Marquetand et al., 2021) and the retina (Westner et al., 2021).

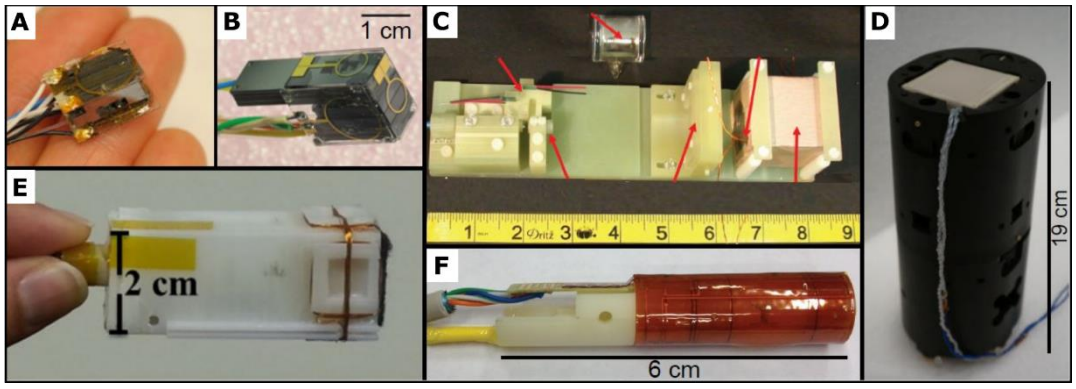

Figure 2.1 - The first compact OPMs. *A) Sander et al., 2012. B) Mhaskar et al., 2012. C) Johnson et al., 2013. D) Kamada et al., 2015. E) Shah and Wakai, 2013. F) Sheng et al., 2017. (Adapted from Boto, 2019).*

Many of these studies were made possible by the commercialisation of OPM technologies into 'off-the-shelf' sensors for biomagnetism, facilitating the construction of modular OPM systems that can be added to as required, to increase channel count over time while spreading the cost. As discussed in Section 1.2.2.3, four companies currently manufacture OPMs (QuSpin Inc., FieldLine Inc., Twinleaf LLC, and MAG4Health). At the time of writing, Mag4Health have developed a Helium-based OPM (Fourcault et al., 2021) due to be made commercially available by the end of 2022, and no MEG studies using Twinleaf magnetometers have yet been published. The first studies involving FieldLine sensors did not occur until 2019 (Nardelli et al., 2019), and since work began on developing an OPM-MEG system at the University of Nottingham in 2016, this thesis describes work undertaken using QuSpin Zero-Field Magnetometers (QZFM), which were the first commercially available OPMs with sufficient sensitivity for MEG. Three generations of QZFM are employed throughout this work that all follow the same principle of operation.

2.1.1. Principle of operation

For each generation of QZFM, their working principle is as follows:

- The glass cell is heated to 150 °C using resistive coils, to form a rubidium-87 vapour of high atomic density.
- The atomic spin ensemble is prepared in a magnetically sensitive quantum state via optical pumping, where absorption of light drives a transition between atomic energy levels in ^{87}Rb. A 795 nm, circularly polarised laser is passed through the cell to facilitate this (see Figure 2.2).
- A photodetector measures the intensity of the laser light transmitted through the cell. Optical pumping drives the spins into a 'dark state', where they no longer interact with the laser light, absorption ceases and the intensity at the photodetector is maximised.
- An external magnetic field will interact with the spin ensemble, allowing reabsorption of laser light, which reduces the light intensity reaching the photodetector. Thus, the intensity of laser light transmitted through the cell becomes a sensitive measure of magnetic field.

Since the spins interact with external magnetic fields, to first optically pump the rubidium atoms into the dark state the magnetic field across the vapour cell must be zero. Three pairs of orthogonal electromagnetic coils therefore surround the cell to compensate magnetic fields up to 50 nT, in an automated 'field-zeroing' procedure (Shah and Hughes, 2015). A modulation signal is later applied via these coils to obtain directional sensitivity (see Section 2.4).

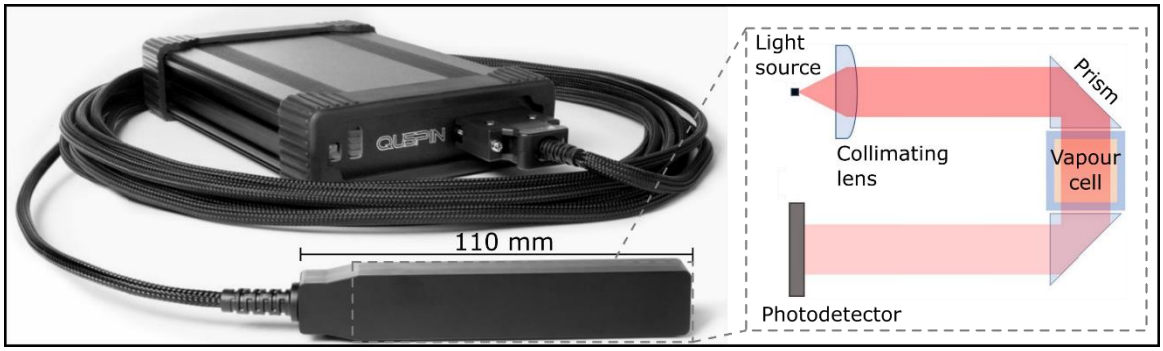

Figure 2.2 – The QZFM. *Gen-1 QZFM and associated electronics. Inset: schematic of components inside QZFM, including a laser, vapour cell and photodetector. (Adapted from Osborne et al., 2018 and http://quspin.com/).*

2.2. Optical pumping

Optical pumping describes the process of transferring energy and angular momentum of incident light to an atomic species, such that almost all the atoms in the sample occupy the same energy level (Happer, 1972). Alkali metals, like ^{87}Rb, have a single valence electron in their outer shell, which makes them well suited to optical pumping for precise control of the atomic spin ensemble.

The total angular momentum, $\boldsymbol{F}$, of an atom is characterised by the sum of the electron angular momentum, $\boldsymbol{I}$, and the nuclear angular momentum, $\boldsymbol{J}$:

$$\boldsymbol{F} = \boldsymbol{J} + \boldsymbol{I}. \tag{2.1}$$

The nuclear spin quantum number for ^{87}Rb is $I = {}^{3}/_{2}$, and the electron angular momentum is a sum of its orbital angular momentum $\boldsymbol{L}$ and its spin $\boldsymbol{S}$:

$$\boldsymbol{J} = \boldsymbol{L} + \boldsymbol{S}. \tag{2.2}$$

The valence electron of a ^{87}Rb atom has spin quantum number $S = {}^{1}/_{2}$, the orbital angular momentum quantum number of the ground state is $L = 0$, and the first excited state has $L = 1$.

2.2.1. Fine structure

Due to interaction between the spin and orbital angular momentum of the electron, splitting of the orbital structure into additional energy levels occurs, known as the fine structure. These energy levels occur in integer steps defined by the quantum number J, which can take values in the range $|L - S| \leq J \leq |L + S|$. Considering this, we find that the ground state has one fine structure level, at $J = {}^{1}/_{2}$, while the first excited state is split into two energy levels, defined by $J = {}^{1}/_{2}$ and $J = {}^{3}/_{2}$. This fine structure is shown in Figure 2.3.

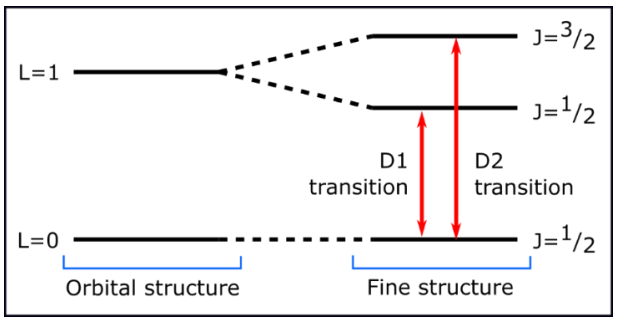

Figure 2.3 – Fine structure of Rubidium-87. *Interaction between spin and angular momentum causes splitting of the excited state into two energy levels.*

Consequently, two transitions are possible between the ground and excited states: the D1 transition to the first excited state $\left(L = 1,\ J = {}^{1}/_{2}\right)$, and the D2 transition to the second excited state $\left(L = 1,\ J = {}^{3}/_{2}\right)$. These transitions occur when the electron absorbs the energy of a photon of laser light that is equal to the energy difference between the two states. Since the energy of a photon is described by

$$E = h\upsilon = \frac{hc}{\lambda} \tag{2.3}$$

(where h is Planck's constant, c is the speed of light in a vacuum and υ and λ are the frequency and wavelength of the incident light, respectively), it follows that a particular transition can be driven by selecting the frequency of the laser light. For the D1 transition of ^{87}Rb, this corresponds to a laser with wavelength 795 nm.

2.2.2. Hyperfine structure

Further splitting of the fine structure occurs due to interactions between the nuclear and electron spins. The resulting hyperfine structure is defined by the total angular momentum $\boldsymbol{F} = \boldsymbol{I} \pm \boldsymbol{J}$. Considering the D1 transition of ^{87}Rb alone, where $J = {}^{1}/_{2}$ and $I = {}^{3}/_{2}$, the ground and first excited states are each split into two energy levels where $F = 1$ and $F = 2$ (see Figure 2.4).

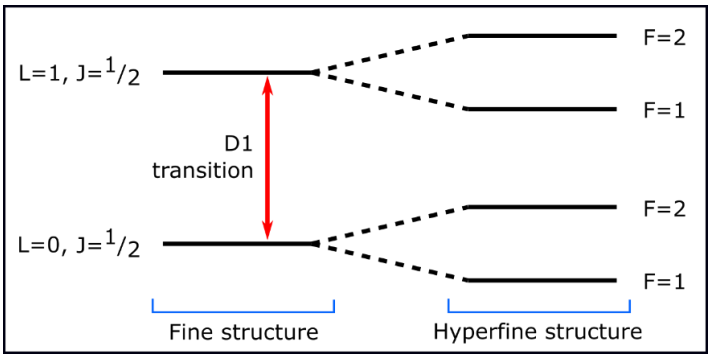

Figure 2.4 – Hyperfine structure of Rubidium-87. *The ground and first excited states are each split into two energy levels defined by F=1 and F=2.*

2.2.3. Zeeman splitting

The final occurrence of energy level splitting is due to interaction of the atom with an external magnetic field. Zeeman splitting of the hyperfine structure occurs along a quantisation axis, which in the absence of magnetic field is along the direction of propagation of the laser beam through the atomic sample. The projection of Zeeman sublevels is given by $m_F = [-F, -F+1, \dots, F-1, F]$, thus is dependent on the atomic angular momentum. For the $F = 1$ hyperfine state, $m_F = [-1, 0, 1]$, and for the $F = 2$ state, $m_F = [-2, -1, 0, 1, 2]$ as shown in Figure 2.5.

The difference in energy between Zeeman sublevels is described as

$$\Delta E = g_F \mu_B B, \tag{2.4}$$

where g_F is the hyperfine Lande g-factor, μ_B is the Bohr magneton and B is the magnetic field strength. Note that at zero-field, the states are degenerate and have the same energy. In an external magnetic field, the spins will precess at the Larmor frequency, ω:

$$\omega = \gamma B, \tag{2.5}$$

where γ is the gyromagnetic ratio of the atomic species, which for the valence electron in ^{87}Rb is given by

$$\frac{\gamma_F}{2\pi} = \frac{g_F \mu_B}{\hbar}. \tag{2.6}$$

For the $F = 1$ state, $g_F = -1/2$, and for the $F = 2$ state $g_F = +1/2$. The opposite signs of g_F indicate precession in opposite directions for the two states, with

$$\left|\frac{\gamma_F}{2\pi}\right| = 7 \text{ Hz nT}^{-1}. \tag{2.7}$$

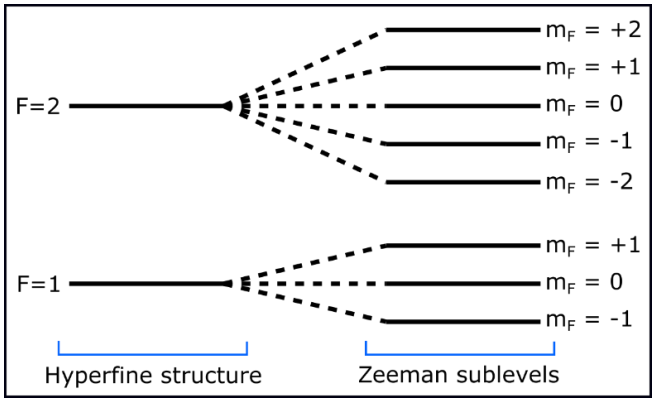

Figure 2.5 – Zeeman splitting in Rubidium-87. *The hyperfine states are further split into additional energy levels, governed by* $m_F = [-F, -F+1, \dots, F-1, F]$.

When the valence electron is illuminated by a 795 nm laser, the D1 transition can be driven. If the light is right-hand circularly polarised, all photons have +1 angular momentum along the direction of propagation of the laser beam. This angular momentum can then be transferred to the atom according to the selection rule $\Delta m_F = m_{F_{final}} - m_{F_{initial}} = +1$. Absorption of a photon excites the atom into its first excited state, from which it returns to the ground state via spontaneous emission of a randomly polarised resonant photon. This emitted photon may go on to be absorbed by another atom in the sample. The atom may be repolarised by absorption of another photon if permitted by the selection rule.

In combination, D1 transition pumping and spontaneous emission drive the ^{87}Rb atoms into the state with lowest energy (ground state, $L = 0$) and highest angular momentum ($F = 2, m_F = 2$). This is known as the 'dark state', since no more photons can be absorbed by the atoms in accordance with the selection rule, as no energy levels exist with $m_F > 2$. The atoms therefore become 'transparent' to the laser light and no longer interact, maximising the intensity of light measured at the photodetector. This process constitutes optical pumping and is shown in Figure 2.6.

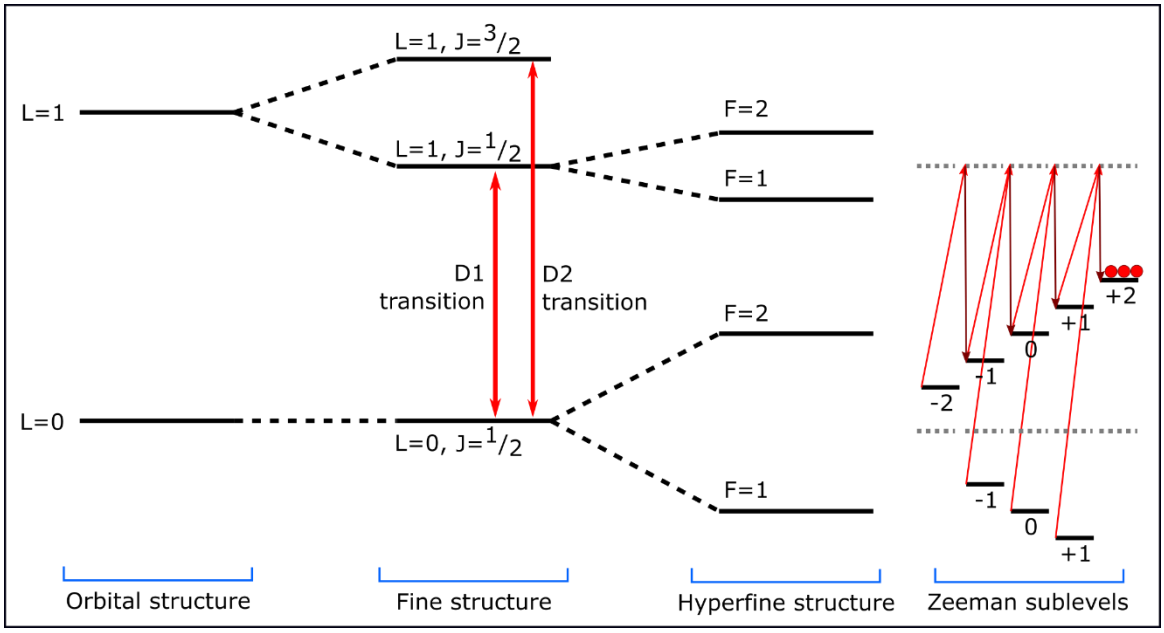

Figure 2.6 – The mechanism of optical pumping. *The ^{87}Rb atoms are optically pumped until they occupy a state (F=2, m_F=2) where there are no remaining transitions with $\Delta m_F = +1$. At zero-field, the states are degenerate, indicated by grey dashed lines.*

2.3. Spin-exchange relaxation free regime

As the rubidium atoms are optically pumped into the dark state, a strong net magnetisation occurs along the direction of propagation of the laser beam. This is described as spin polarisation and represents the magnetically sensitive state of the sample. However, the coherence of the spins must be maintained over sufficient timescales for practical use as a magnetometer. The atoms can be depolarised and spin coherence destroyed in a number of ways, including spin-exchange and spin-destruction collisions, collisions with the walls of the cell and interactions with the laser. Fortunately, we can reduce the impact of these relaxation effects by adjusting experimental parameters, such as the composition of the vapour cell and pumping rate of the laser (Kornack, 2005). At high atomic densities, such as that inside the vapour cell of our OPM, spin-exchange collisions are considered the dominant relaxation mechanism at play.

A spin-exchange collision between two ^{87}Rb atoms preserves the total angular momentum but may alter the hyperfine states of the atoms, as shown in Figure 2.7A. Before the collision, the spins are coherent and occupy the same F-state, but after the collision, the electron spin orientation of one of the atoms is reversed and it occupies a different hyperfine state. As a result, the spins of the two atoms now precess in opposite directions, due to the change in sign of g_F for the $F = 1$ and $F = 2$ states (see Equations (2.6) and (2.7)). Thus, spin-exchange collisions contribute to decoherence of the spin ensemble. The relaxation rate R due to spin-exchange collisions is given by

$$R_{SE} = \frac{1}{T_{SE}}, \tag{2.8}$$

where T_{SE} is the time between collisions.

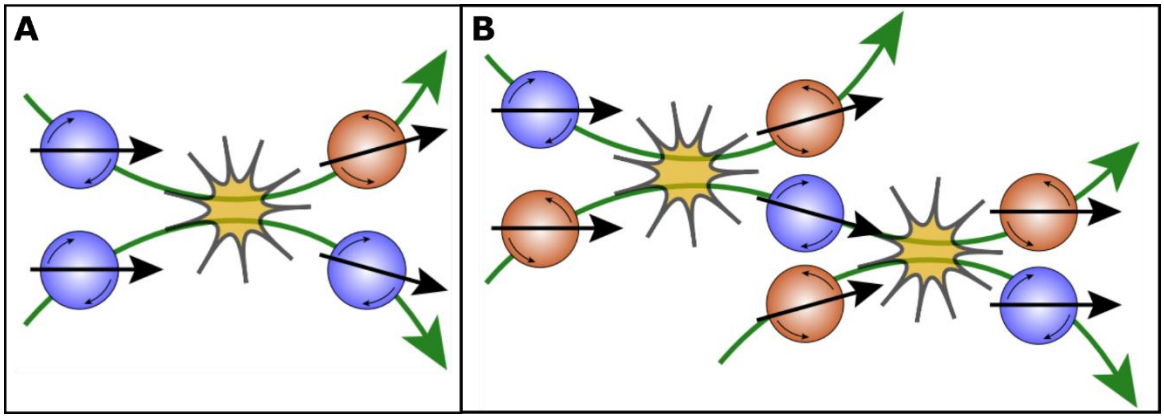

Figure 2.7 – Spin-exchange relaxation. *A) Spin-exchange collisions alter the hyperfine state of an atom (blue) such that its spin precesses in the opposite direction (red), causing decoherence. B) In the SERF regime, collisions occur at a much higher rate and give rise to a net polarisation at a slower frequency of precession. (Adapted from Seltzer, 2008).*

In an environment with sufficiently low magnetic field and high atomic density, however, the spin-exchange relaxation rate increases such that $R_{SE} \gg \gamma B$. At such a high rate of collisions, relaxation is minimised as the atoms switch rapidly between the $F = 1$ and $F = 2$ hyperfine states, in which they precess in opposite directions (Figure 2.7B). There are more Zeeman sublevels with $F = 2$, however, which results in a net positive, albeit slower coherent spin precession, described by

$$\omega_0 = \frac{\gamma B}{Q(P)}. \tag{2.9}$$

Here $Q(P)$ represents the nuclear slowing down factor, which quantifies the decrease in the frequency of precession as a result of this spin-exchange relaxation free (SERF) regime. $Q(P)$ is a function of the total polarisation, P, of the sample, as follows (Seltzer, 2008):

$$Q(P) = \frac{6 + 2P^2}{1 + P^2}. \tag{2.10}$$

If the sample is fully polarised (i.e., all atoms in the $F = 2,\ m_F = 2$ hyperfine state), spin-exchange collisions cannot redistribute the spins among the hyperfine states, since no other m_F levels can accommodate the high angular momentum. If the degree of polarisation in the sample decreases, the value of $Q(P)$ increases, as the atoms switch rapidly between the two hyperfine states and reduce the overall frequency of precession in the spin ensemble. As such, $Q(P = 0) = 6$ for an unpolarised sample, and for a fully polarised sample $Q(P = 1) = 4$.

So-called SERF magnetometers make use of this regime, as suppression of spin-exchange collisions substantially extends the timescale over which spin coherence is maintained (Allred et al., 2002). The high atomic density enabled by the SERF regime also gives rise to greater measured signal.

2.4. Signal equations

As mentioned previously, the spin polarisation, $\boldsymbol{P}$, established following optical pumping in the SERF regime is oriented along the direction of propagation of the laser beam through the cell, which we define here as the z-axis. The response of the polarisation to external magnetic fields can be described by the Bloch equations (Bloch, 1953, 1946), akin to MRI. The rate of change of polarisation in the sample over time is given by:

$$\frac{d\boldsymbol{P}}{dt} = \frac{1}{Q(P)}\left[\gamma \boldsymbol{P} \times \boldsymbol{B} - (\boldsymbol{P} - P_0\hat{\boldsymbol{z}})\frac{1}{T}\right], \tag{2.11}$$

where $Q(P)$ is the nuclear slowing down factor, γ is the gyromagnetic ratio of the valence electron and P_0 is the equilibrium polarisation achieved at zero-field following optical pumping (Shah and Romalis,

2009). The time constant T incorporates the optical pumping rate, R, and the relaxation time, T_2, of the sample, expressed as $T = (R + {}^{1}/_{T_2})^{-1}$.

Since the direction of propagation of laser light is along the z-axis, the light transmitted through the cell is sensitive to the P_z component of polarisation only. In the steady state (i.e., $\frac{d\boldsymbol{P}}{dt} = 0$), the vector components of polarisation are described by

$$P_x = \frac{\frac{B_y}{(\gamma T)} + B_x B_z}{\frac{1}{(\gamma T)^2} + {B_x}^2 + {B_y}^2 + {B_z}^2} P_0'$$

$$P_y = \frac{\frac{-B_x}{(\gamma T)} + B_y B_z}{\frac{1}{(\gamma T)^2} + {B_x}^2 + {B_y}^2 + {B_z}^2} P_0' \qquad (2.12)$$

$$P_z = \frac{\frac{1}{(\gamma T)^2} + {B_z}^2}{\frac{1}{(\gamma T)^2} + {B_x}^2 + {B_y}^2 + {B_z}^2} P_0',$$

where $P_0' = P_0 R T$. If we construct the magnetometer such that it measures magnetic field perpendicular to the axis of the laser, for example B_x, then the B_y and B_z terms become zero, thus simplifying Equations (2.12) as follows:

$$P_x = 0$$
$$P_y = \frac{-\gamma T B_x}{1 + (\gamma T B_x)^2} P_0' \qquad (2.13)$$
$$P_z = \frac{1}{1 + (\gamma T B_x)^2} P_0'.$$

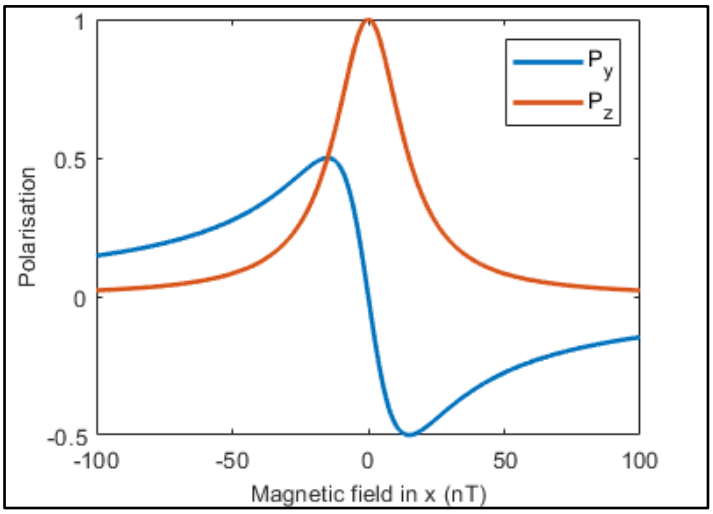

Figure 2.8 – Steady state solution to the Bloch equations. *In the y-direction, polarisation takes the form of a dispersion curve. In the z-direction, it forms a Lorentzian line shape known as zero-field resonance. To give an accurate representation of the QZFM,* $2/\gamma T$=30 nT.

Evaluating Equations (2.13) as a function of B_x, the z-component of polarisation follows a Lorentzian line shape, known as the zero-field resonance of the sample. The full width at half maximum is given as $^2/_{\gamma T}$, which is ~30 nT for the QZFM. In contrast, polarisation in the y-direction follows a dispersion curve. These response curves are shown in Figure 2.8, both of which are sensitive to 1/f noise (Osborne et al., 2018). At this stage, a measurement of magnetic field would be ambiguous, due to the symmetric nature of the zero-field resonance (i.e., a positive or negative magnetic field of equal magnitude yields the same degree of polarisation). To distinguish between positive and negative measured fields, an oscillating magnetic field, known as the modulation field, is applied in the direction of desired sensitivity (in this example, B_x) (Cohen-Tannoudji et al., 1970; Dupont-Roc et al., 1969; Kastler, 1973). The modulation signal is applied at a much higher frequency (932 Hz for the QZFM) than the relaxation rate of the atomic sample. The relaxation rate for the QZFM is of the order 100 Hz, which also determines the bandwidth of the sensor. An oscillating current is applied to the on-sensor coils that surround the glass cell to generate the modulation signal, and thus our expression for rate of change of polarisation must be updated to incorporate a modulation term, $b_x \cos(\omega t)$:

$$\frac{d\boldsymbol{P}}{dt} = \frac{1}{Q(P)}\left[\gamma \boldsymbol{P} \times [\boldsymbol{B} + b_x \cos(\omega t)\,\hat{\boldsymbol{x}}] - (\boldsymbol{P} - P_0\hat{\boldsymbol{z}})\frac{1}{T}\right], \tag{2.14}$$

where b_x is the amplitude of the modulation field, with frequency ω. The steady state solutions given by Equations (2.12) and (2.13) no longer apply, since the modulation term varies in time. Hence, we re-evaluate for P_z, again assuming $B_y = B_z = 0$, to find

$$P_z = \left(\frac{\gamma T B_x}{1 + (\gamma T B_x)^2}\right) J_0\left(\frac{\gamma b_x}{Q(P)\omega}\right) J_1\left(\frac{\gamma b_x}{Q(P)\omega}\right) P_0' \sin(\omega t), \tag{2.15}$$

where J_n are Bessel functions of the first kind (Shah and Romalis, 2009; Tierney et al., 2019). These functions can be evaluated to a constant term, dependent on the ratio of $^{\gamma b_x}/_{Q(P)}$ to ω, and all constants subsequently combined into a single constant of proportionality, yielding

$$P_z \propto \frac{\gamma T B_x}{1 + (\gamma T B_x)^2} P_0'. \tag{2.16}$$

Using a lock-in amplifier, the amplitude of the oscillating signal can be obtained while also rejecting background interference at other frequencies. This is achieved by multiplication of the input by the modulation signal, as a reference, and applying an adjustable low-pass filter. Lock-in detection of the voltage from the photodetector inside our OPM provides a final signal output of the form

$$V \propto \frac{\gamma T B_x}{1 + (\gamma T B_x)^2}. \tag{2.17}$$

Evaluating this expression as a function of B_x generates the dispersion curve shown in Figure 2.9, which enables us to distinguish between positive and negative changes in magnetic field. For small changes in magnetic field, where $\gamma T B_x \ll 1$, we employ the Taylor expansion of $V(B_x)$ to obtain a linear relationship:

$$V \propto \gamma T B_x. \tag{2.18}$$

Thus, the change in magnetic field measured by an OPM is computed simply as the field per unit voltage. Since this is an approximation, the larger the measured changes in magnetic field, the less accurate the assumption of linearity becomes. For the QZFM, the linear approximation is valid in the region of ±5 nT (see Figure 2.9). Magnetic field changes greater than this induce up to 10 % changes in sensor gain (Osborne et al., 2018), with 5 % gain changes occurring at ±3.4 nT (Hill et al., 2022).

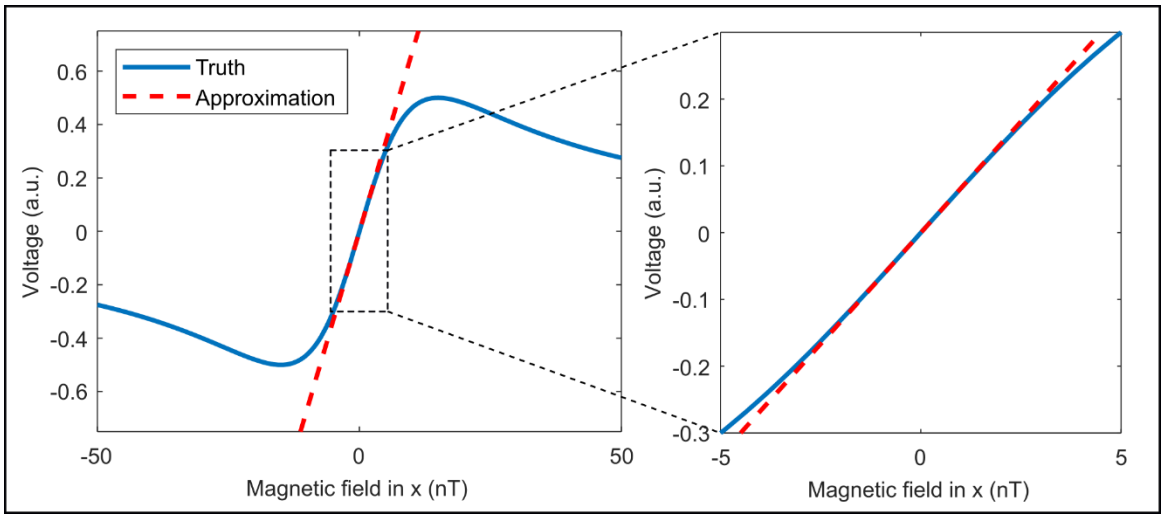

Figure 2.9 – Voltage output of an OPM. *Using lock-in detection at the modulation frequency, a dispersion curve is obtained to distinguish positive and negative changes in magnetic field. For the QZFM a linear approximation is reasonable between ±5 nT.*

2.5. Implementation for MEG

2.5.1. The QuSpin OPM

The first generation of QZFM (Gen-1) became available commercially in 2016, had external dimensions 13×19×110 mm^3 and contained a glass cell with internal dimensions 3×3×3 mm^3, housing a rubidium-87 vapour and located 6 mm from the end face of the sensor casing. A dual-axis magnetometer, the Gen-1 OPM was sensitive to magnetic fields in two orthogonal directions either independently or simultaneously – along the axis of the sensor and one tangential orientation (see Figure 2.10A). Each OPM is connected to its dedicated electronics by a 6.5 m cable. While Gen-1 QZFMs have sufficient sensitivity for MEG measurements and have been used as such in the past (e.g., Boto et al., 2017), these sensors were large and the cabling reasonably heavy, making them difficult to deploy

for MEG, particularly in children. Here Gen-1 OPMs were used in Chapters 4 and 5 as reference sensors for measuring fluctuations in the background magnetic field.

The second generation of QZFM (Gen-2) became available in 2018; a smaller, more lightweight sensor package with dimensions 12.4×16.6×24.4 mm^3, these OPMs were better suited for use in wearable sensor arrays (see Figure 2.10B). In Gen-2 OPMs, the vapour cell is housed at 6.5 mm from the sensor casing, and the sensor head is connected to an initial length (60 cm) of lightweight flex cable, reducing the weight of an OPM-MEG system worn on the head. A limitation of these sensors, however, was that the cable was directly attached to internal components of the OPM, meaning any pulling on the cables, particularly during movement, could compromise sensor operation. Here, Gen-2 QZFMs were used for MEG measurements in Chapters 4 and 6.

The third generation of QZFM (Gen-3) maintains the lightweight cabling and compact sensor package of Gen-2, with the development that the Gen-3 sensor head can be detached from its cable and associated electronics (Figure 2.10C). This improves the ease of use of QZFMs in reconfigurable sensor arrays and prevents movement of the cables affecting the internal components of the sensor. Gen-3 became available in both dual-axis and triaxial variants in 2021. Triaxial Gen-3 QZFMs were employed for MEG measurements in Chapter 5, and an array of dual-axis Gen-3 sensors was used to obtain a noise recording inside a novel MSR in Chapter 7.

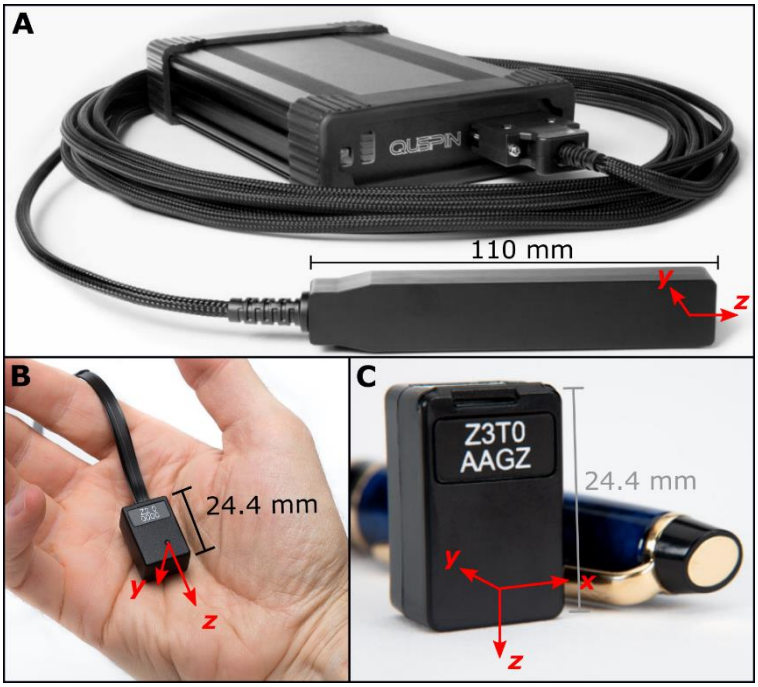

Figure 2.10 – Three generations of QZFM. *A) Gen-1 QZFM and associated electronics. Arrows indicate the orientations of sensitive axes. B) Gen-2 QZFM and lightweight flex cable. C) Detachable Gen-3 triaxial QZFM sensor head. (Adapted from http://quspin.com/).*

2.5.1.1. The triaxial QZFM

OPMs are sensitive to magnetic fields in two orthogonal orientations, each perpendicular to the direction of propagation of the laser beam, hence the first two generations of QZFM forming dual-axis magnetometers. To facilitate measurement in all three orthogonal orientations and thus capture the full magnetic field vector at each sensor, a second, perpendicular laser beam is transmitted through the vapour cell, using a beam splitter (Figure 2.11A). If we define the directions of propagation of these laser beams as x and z respectively, the first beam (x) facilitates measurement of the magnetic fields oriented in y and z, while the second beam (z) facilitates measurements in x and y (Shah et al., 2020). Since triaxial detection essentially requires two measurements in the same vapour cell (with the same atomic density), the sensitivity of the triaxial QZFM is somewhat worsened in comparison to its dual-axis equivalent: 13.5 ± 0.8 fT/√Hz in x, 9.9 ± 1.4 fT/√Hz in y (note the y-axis is measured twice in the triaxial QZFM, resulting in some noise suppression) and 14.9 ± 2.0 fT/√Hz in z, compared to 11.3 ± 1.5 fT/√Hz in y and 13.8 ± 1.1 fT/√Hz in z (Boto et al., 2022). Regardless, such sensitivities remain sufficient for MEG measurements.

The advantages of a triaxial OPM array for MEG have been evaluated in simulation, revealing substantial improvements for rejection of external interference (see Figure 2.11B). Following beamforming, a 50-sensor (150-channel) triaxial OPM-MEG array was shown to better reconstruct an underlying current distribution in the presence of external interference (Gaussian noise) than both 50- and 150-channel radial systems (Brookes et al., 2021). It has also been shown that external interference characterised by up to 3rd order spherical harmonics (defined using the Signal Space Separation method) can be regressed from simulated OPM-MEG data with only 2 dB attenuation of neuronal signals when using a 90-channel triaxial system, in comparison to 15 dB attenuation with 90 radial channels (Tierney et al., 2022).

Furthermore, simulations have shown that a triaxial OPM-MEG array offers improvements in coverage across the cortex. In children, there is a reduced separation between the brain and the scalp surface, which results in hot- and cold-spots in coverage when using only single-axis OPMs (Boto et al., 2022, see Figure 2.11C). It follows that sparse arrays employing triaxial OPMs could be used as an alternative to increasing the number of radial-only sensors on the head, to capture the same amount of neural information.

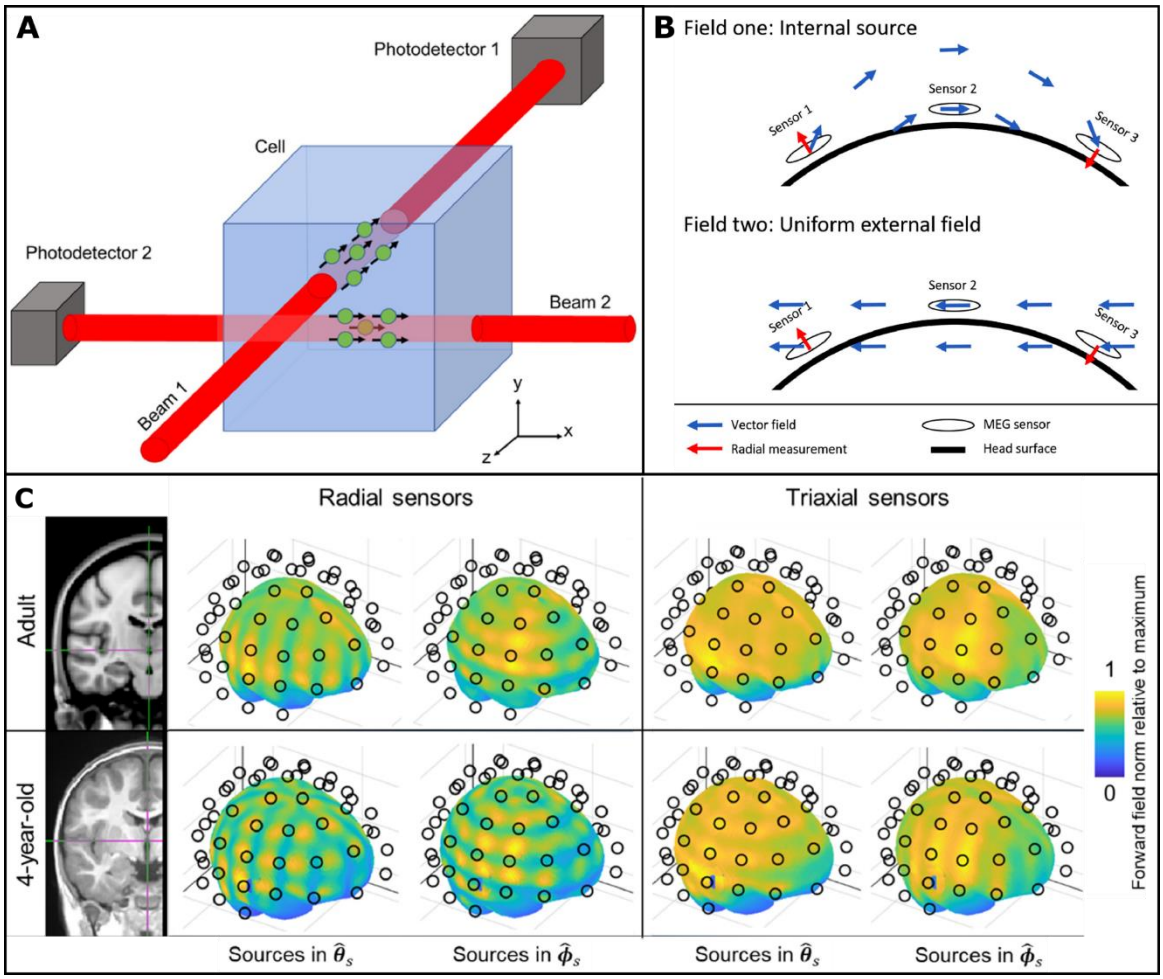

Figure 2.11 – The triaxial QZFM. *A) Schematic diagram of the arrangement inside a triaxial QZFM. A beam splitter directs two perpendicular laser beams through the vapour cell, that each independently facilitate optical pumping. (Taken from Boto et al., 2022). B) Diagram to demonstrate how triaxial measurements can improve characterisation of external interference. Information contained within a tangential measurement would enable the distinction between internal and external magnetic fields that appear similar in radial-only approaches. (Adapted from Brookes et al., 2021). C) Comparing coverage across the brain when using radial and triaxial OPM arrays. More even coverage is achieved using triaxial measurements, especially in children. (Adapted from Boto et al., 2022).*

2.5.2. OPM operation in practice

The electronics unit attached to each QZFM facilitates control and readout of the sensor via proprietary software, interfacing with each unit via a USB connection. This software is used to perform three initialisation tasks, before a magnetic field measurement can be made. First, current is applied to the on-sensor coils that surround the glass cell, to resistively heat the vapour to 150 °C, achieving a high atomic density and facilitating the SERF regime. Second, the laser is initiated and stabilised to the appropriate frequency to drive the D1 transition of ^{87}Rb for optical pumping. Finally, the on-sensor coils are used to generate the modulation signal for lock-in detection.

Once the sensor is operational, current is applied to the on-sensor coils to cancel the magnetic field across the vapour cell. For open-loop operation of the QZFM, these 'field-zeroing' currents are fixed prior to starting a MEG recording and remain unchanged throughout the experiment. This operational mode is used throughout this thesis, where the voltage from the photodetector gives the measure of external magnetic field. Alternatively, closed-loop operation maintains the zero-field environment across the vapour cell by updating the currents applied to the coils, thus operating the sensor with negative feedback (Nardelli et al., 2020). When using closed-loop, these currents yield the measurement of external magnetic field.

Data from the OPM can be recorded using either digital or analogue output. The digital output is obtained via the USB connection, with a sampling rate of 200 Hz. The analogue output, however, can be recorded at a much higher rate using an analogue-to-digital converter. In this work, data were recorded using the analogue output at a sampling frequency of 1,200 Hz.

The 1–100 Hz bandwidth of the QZFM is determined by the susceptibility of the system to 1/f noise and the relaxation rate of ^{87}Rb in the SERF regime. Fortunately, most neural activity studied in MEG occurs within this frequency range (Baillet, 2017; Lopes da Silva, 2013). Nevertheless, some high (>100 Hz) frequency effects are of interest; neural oscillations up to 1 kHz may be of importance in the study of epilepsy (as discussed in Section 1.1.2.1), and in magnetospinography, the signals that propagate along nerves in the spine occur at frequencies up to 1.5 kHz (Curio, 1995; MacKert et al., 1998).

2.5.3. Multi-channel arrays

For MEG, a multi-channel array of several OPMs positioned around the head is required to simultaneously measure the neuromagnetic field across the brain. To achieve this with QZFMs, the modulation signal and heater frequency should be common to all sensors, generated by a 'master' electronics unit and transmitted to all other units in the array. Otherwise, small differences in phase, frequency or amplitude of individual signals introduce beat frequencies that affect the recordings.

The magnetic field per unit voltage calculation must also be consistent across multiple sensors. This is achieved by application of a known magnetic field to the on-sensor coils, enabling calibration of the

sensor outputs. For the triaxial QZFM, an orthogonalisation step is performed following calibration of each sensitive axis. The analogue output of the QZFM has three gain settings, the standard setting yields a conversion factor of 2.7 V nT^{-1}, operating within the ±1.5 nT range. A ×3 gain setting has conversion factor 8.1 V nT^{-1} in the ±0.5 nT range, and a ×0.33 gain setting has conversion factor 0.9 V nT^{-1} in the ±4.5 nT range.

Operating multiple OPMs in close proximity can give rise to interference between sensors, when the modulation signal generated at one OPM is detected by another nearby. Such 'cross-talk' impacts both the sensor gain and the orientation of the sensitive axis (Boto et al., 2018; Tierney et al., 2019). It is possible to model the effects of cross-talk using measured data, and optimise coil designs to decrease the generated interference (Nardelli et al., 2019), however, cross-talk was not found to be a significant obstacle in the measurements undertaken for this work. We note that this issue is addressed in the triaxial QZFM by application of the orthogonalisation step.

2.5.4. OPM-MEG helmets

Multi-channel OPM arrays require a method of mounting many sensors as close to the scalp as possible, whilst allowing for variation between participant head shapes and sizes. In general, two approaches have been taken to create wearable OPM-MEG helmets that facilitate participant comfort and movement. The first technique uses a participant's anatomical MRI to design a bespoke head cast that is then 3D printed (Boto et al., 2017; Holmes et al., 2018; Tierney et al., 2018). The result allows OPMs to be placed with minimal standoff from the scalp (maximising the measured signal) and facilitates accurate knowledge of sensor positions and orientations relative to the brain, necessary for source reconstruction of MEG data (see Section 1.3). However, the cast is unique to the individual's head shape and cannot be used by multiple participants, thus scaling up this approach to generate several bespoke head casts for a study cohort would be costly.

Generic helmets designed to encompass a variety of head shapes and sizes were therefore pursued; Figure 2.12 shows examples of such OPM-MEG helmets developed at the Sir Peter Mansfield Imaging Centre, University of Nottingham. In 2019, OPMs were held near the scalp using adapted bicycle helmets, in both adult and child sizes. The resulting helmets were lightweight and improved the scanning experience for younger participants, and a 3D digitisation of the helmet design enabled accurate knowledge of the sensor positions and orientations within the helmet (Hill et al., 2019). Co-registration methods were then required to match the helmet position on the head to an anatomical MRI, using markers and facial features (see Section 2.5.4.1).

Further developments saw the use of flexible, 'EEG-like' caps to mount Gen-2 OPMs closer to the scalp while still adapting to various head shapes, however determination of sensor locations relative to the brain proved challenging; random errors in sensor positions and orientations across the array that

arose when using the flexible cap impacted co-registration and reconstruction analyses more strongly than the systematic errors experienced with rigid helmets (Hill et al., 2020). Therefore, 3D printed generic helmets are now in use, which house up to sixty-four OPMs, enable accurate co-registration and are available in increasing sizes from 2-year-old to adult, to capture a large range of participant cohorts (see Figure 2.12). These helmets also incorporate cable management techniques into their design, to minimise interactions between overlapping cables affecting recordings (see Discussion in Chapter 4) and neaten the overall appearance of the wearable OPM-MEG system.

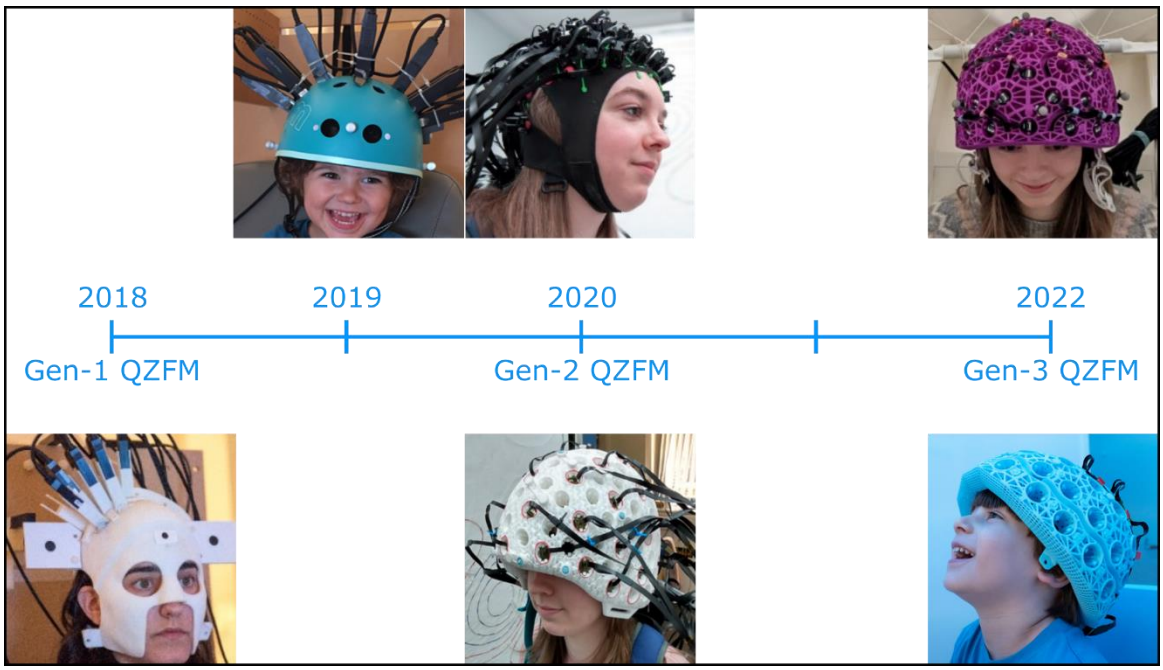

Figure 2.12 - OPM helmet designs at the University of Nottingham. *In 2018, the first multi-channel array (Gen-1 QZFM) was mounted in a bespoke 3D printed head cast. In 2019, sensors were mounted in adapted bicycle helmets to fit multiple participants. In 2020, both flexible caps and generic 3D printed helmets were used to house Gen-2 QZFM. In 2022, 3D-printed generic helmets that fit both Gen-2 and 3 QZFM are available in different sizes, to scan participants from 2 years old (5-year-old and large adult helmets pictured).*

2.5.4.1. Co-registration

To reconstruct the underlying neuronal current distribution from our OPM data, accurate knowledge of the position of the sensitive volume (i.e., the vapour cell) and the orientation of sensitive axes of each OPM is required, relative to brain anatomy. When using 3D-printed, rigid helmets as described above, the sensor locations within the helmet geometry are defined accurately during the design process. Therefore, we simply require a technique to determine the position of the helmet on the head, which can then be co-registered to an anatomical MRI.

To do this, a 3D digitisation of the participant's head and the wearable OPM array is generated before the helmet is removed following a MEG scan. This may be achieved using structured-light or laser scanners (such as the Structure Core, Occipital Inc., CA, U.S.A. and HandySCAN, Creaform Inc., Levis, Canada), or an electromagnetic digitiser (e.g. FASTRAK, Polhemus, VT, U.S.A.) (Cao et al., 2021; Gu et al., 2021). An additional digitisation of the participant's head is obtained with the helmet removed, to ascertain facial features and head shape (a cap may be worn to provide a smoother head surface by flattening hair). In this work, we employed a structured-light scanner for our co-registration approaches.

The resulting surface meshes that characterise the participant's head shape and helmet location are co-registered to one another, to an anatomical MRI and to the helmet geometry known from the design process (see Figure 2.13) in software. This is achieved using facial features or markers, which can be attached to the face for the digitisation or built into the helmet design at known locations to aid co-registration efforts (Hill et al., 2020; Zetter et al., 2019). As a result, the position and orientation of each OPM in the array is determined relative to the brain, enabling source reconstruction analysis e.g., via beamforming.

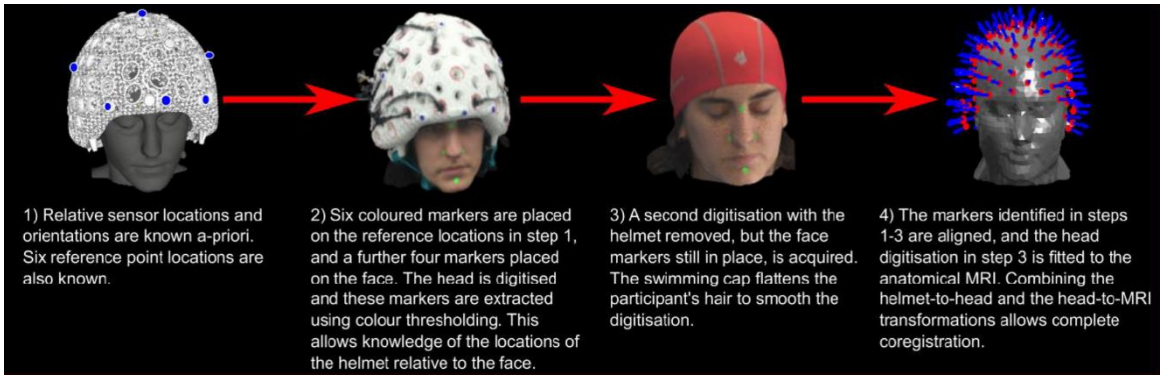

Figure 2.13 – Co-registration pipeline. *Sensor locations within the helmet are known from the design process. 3D digitisations of the participant's head with and without the helmet are obtained and co-registered to an anatomical MRI to determine OPM positions and orientations relative to the brain. (Adapted from Hill et al., 2020).*

Chapter 3

Magnetic shielding

In this chapter, the stringent magnetic shielding requirements for OPM-MEG are first discussed before examining approaches to screen magnetic interference. The use of high permeability materials for shielding of low frequency magnetic fields via flux shunting is explored, along with de-magnetisation of these materials to further improve shielding performance. Screening of AC sources via eddy current cancellation is also reviewed. Methods of active shielding using electromagnetic coils are then explored, from simple Helmholtz coil designs to the more complex windings of a bi-planar coil system that was designed for OPM-MEG.

3.1. OPM zero-field requirement

To maximise the potential of wearable MEG and access new experimental paradigms, we aim to enable free participant movement within our MSR. However, the zero-field resonance around which the QZFM operates presents a challenge. The on-sensor coils used to cancel the magnetic field across the vapour cell can only compensate up to 50 nT in magnitude, thus the background magnetic field inside the MSR must be within this range. Furthermore, when operating the QZFM in open-loop, these 'field zeroing' currents are set prior to starting a MEG recording and remain unchanged throughout. Movement of a sensor through the background magnetic field during a recording, and changes in this magnetic field over time, will therefore induce sensor gain changes and may saturate the output.

Previously, when deriving the OPM signal equation (Equation (2.15)), for simplicity we assumed that the magnetic field components B_y and B_z orthogonal to the measurement direction, x, were zero. In reality, this is not the case, and the full signal equation takes the form (Zhang et al., 2022)

$$V \propto -J_0\left(\frac{\gamma b_x}{Q(P)\omega}\right)J_1\left(\frac{\gamma b_x}{Q(P)\omega}\right)\frac{\frac{1}{T}\gamma B_x + \gamma^2 {J_0}^2\left(\frac{\gamma b_x}{Q(P)\omega}\right)B_y B_z}{\frac{1}{T^2} + \gamma^2 {B_x}^2 + {J_0}^2\left(\frac{\gamma b_x}{Q(P)\omega}\right)\gamma^2 {B_y}^2 + {J_0}^2\left(\frac{\gamma b_x}{Q(P)\omega}\right)\gamma^2 {B_z}^2}, \tag{3.1}$$

where V is the sensor output and B_x the magnetic field we wish to measure. The sensor gain is given by the gradient of the resulting response curve for the instantaneous values of B_x, B_y and B_z. Hence, changes in the magnetic field experienced by the cell will alter the sensor gain and affect the measured field. This can be summarised by the following three effects:

- We assume a constant sensor gain, given by the slope of the response curve at $B_x = 0$, however, a change in the background magnetic field along the measurement direction changes the value of B_x. This alters the position on the curve at which the OPM is operating, and hence the sensor gain. Furthermore, a large change in magnitude of B_x will exceed the approximately linear region of the response curve, and thus render the OPM inoperable.
- Changes in the background magnetic field components along the y- and z-directions are reflected in the values of B_y and B_z, which alter the shape of the response curve (see Figure 3.1), further impacting sensor gain. If both B_y and B_z are non-zero, the zero-crossing of the curve, as well as its slope, is affected.
- For a constant B_x, fluctuations in the values of B_y and B_z cause apparent changes in the measured field. These are known as cross-axis projection errors (CAPE) (Borna et al., 2022).

If we consider the impact of this on beamformer analysis of OPM-MEG data as described in Section 1.3.2.2, in the presence of gain changes the lead fields will become a function of time. It follows that modulation of the envelopes of reconstructed signals would occur, and averaging over time (e.g., to compare active and control windows) will therefore lead to a reduction in projected power and SNR.

It is therefore crucial that the magnetic field across the vapour cell be maintained as close to zero-field as possible throughout an OPM-MEG recording, especially during movement, to minimise gain changes and CAPE. This could be achieved by operating each OPM in closed-loop, though it follows from Equation (3.1) that viable closed-loop operation requires sensitivity to all three orthogonal components of magnetic field simultaneously. If the on-sensor coil currents are fixed, however, the magnetic field across the entire OPM array must be reduced, which can be achieved using a combination of magnetic shielding techniques.

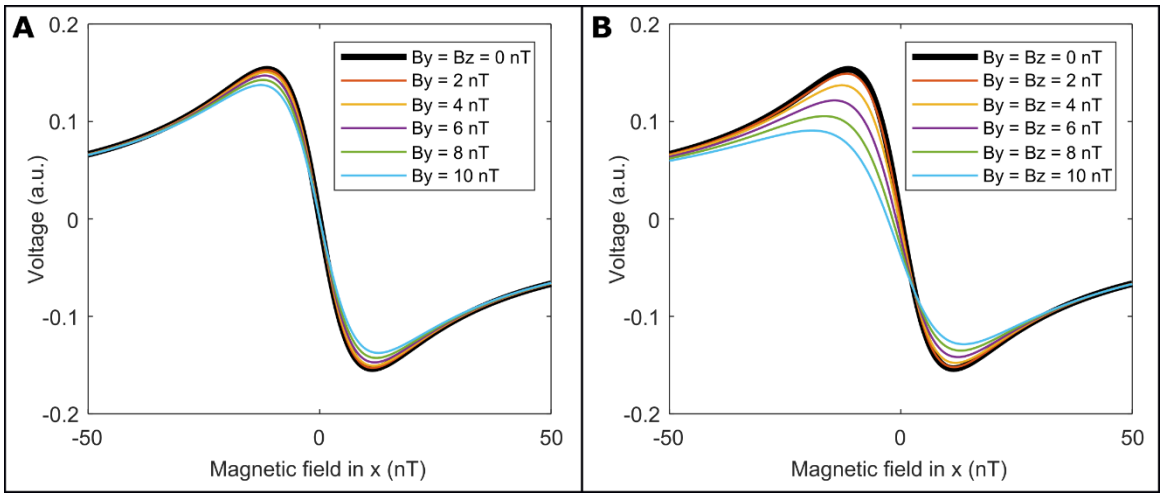

Figure 3.1 – Magnetic fields orthogonal to the measurement direction alter the OPM response curve. *A) Graph to show how magnetic fields up to 10 nT in the y-direction affect the response to fields in the x-direction, and hence the sensor gain, calculated using values* ${}^{\gamma}/_{2\pi} = 28\ rad\ s^{-1}\ nT^{-1}$, $b_x = 200\ nT$, $Q(P) = 4$, ${}^{\omega}/_{2\pi} = 1000\ rad\ s^{-1}$, $T = 5 \times 10^{-4}\ s$. *B) Further gain changes are induced, and the zero-crossing altered, if both* B_y *and* B_z *are non-zero.*

3.2. Passive magnetic shielding

Techniques to screen extraneous magnetic fields were first required to protect radio-receiver equipment and have only become more necessary in the modern world, as the use of electronics and computers has become commonplace. In particular, the use of magnetic shielding increased with the advent of cathode ray tube displays, but nowadays it is primarily employed to protect sensitive equipment and for measurements that require a stable magnetic environment, such as MEG. Both static and time-varying magnetic fields must be shielded; the static magnetic field occurs due to the Earth's geomagnetic field, as well as the magnetisation of nearby ferromagnetic materials, while changes in the

magnetic field over time (<1 kHz) typically result from AC sources, such as power lines, and passing vehicles.

Passive magnetic screening involves enclosing the region that needs shielding in one or more layers of material with properties that facilitate attenuation of DC or AC magnetic fields. To assess the performance of a passive shield, a quantitative measure of the shielding factor is obtained via the ratio of the magnetic field measured in the absence of shielding, $|\boldsymbol{B_0}|$, and the same magnetic field measured inside the shielded enclosure, $|\boldsymbol{B_S}|$:

$$SF = \frac{|\boldsymbol{B_0}|}{|\boldsymbol{B_S}|}. \tag{3.2}$$

Therefore, a large shielding factor indicates good shielding performance, while values approaching unity indicate poor shielding. This quantity can also be expressed in decibels, known as the shielding effectiveness, as follows:

$$SE = 20\log_{10}\frac{|\boldsymbol{B_0}|}{|\boldsymbol{B_S}|}. \tag{3.3}$$

3.2.1. Flux shunting

The dominant mechanism for screening low frequency (0—10 Hz, known as DC) magnetic fields is flux shunting, which involves the use of a material with high magnetic permeability. At the boundary between the surface of the material and air, the behaviour of the magnetic field and flux is governed by two conditions:

1. Ampere's Law states that the tangential component of the magnetic field, $\boldsymbol{H}$, must be continuous across the boundary.
2. Gauss' Law states that the normal component of magnetic flux density, $\boldsymbol{B}$, must also be continuous across the boundary.

In air, $\boldsymbol{B} = \mu_0\boldsymbol{H}$, while in the material, $\boldsymbol{B} = \mu_0\mu_r\boldsymbol{H}$, and since the relative permeabilities (μ_r) of typical shielding materials are on the order of 10^4 or higher, to satisfy both conditions simultaneously the magnetic field and flux must change direction abruptly at the interface (Hoburg, 1995). As a result, on the side of the interface in air the magnetic field and flux lines are almost normal to the surface, whereas on the other side of the interface, inside the material, the field and flux are almost parallel to the surface (Mager, 1970). In essence, the magnetic field is pulled towards the shielding material perpendicular to its surface, diverted through the material, then released into the air (see Figure 3.2). A common shielding material for flux shunting is known as MuMetal, a nickel-iron alloy with relative permeability that can be as high as 470,000 (https://magneticshields.co.uk/technical/material-technical-data).

In addition to the value of μ_r, the performance of such a shield is also impacted by its geometry. If we consider a spherical shield, the area over which magnetic flux is diverted into the material is determined by the diameter of the sphere. The magnetic flux density that results inside the enclosure depends upon both the shield diameter and the thickness of the shielding material, meaning more flux leakage occurs if a large volume is enclosed by a thin shield. In such cases, it follows that increasing the relative permeability of the shielding material would reduce flux leakage.

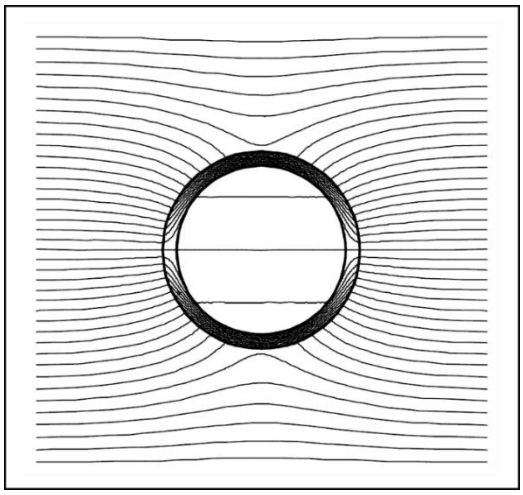

Figure 3.2 – Flux shunting. *Diagram to demonstrate the mechanism of flux shunting, shown for the cross-section of a cylindrical shield. Magnetic flux is drawn to the high permeability material and thus diverted around the enclosure. (Taken from Celozzi et al., 2008).*

Assuming a constant value of μ_r for a spherical shield with inner radius a, and outer radius b, the shielding factor inside the enclosure will be uniform given a uniform incident magnetic field. This shielding factor is described as follows (Hoburg, 1995):

$$SF = \frac{(\mu_r + 2)(2\mu_r + 1) - 2\frac{a^3}{b^3}(\mu_r - 1)^2}{9\mu_r}. \tag{3.4}$$

If the value of μ_r is large and the material thickness, $\Delta = b - a$, small in comparison to the inner radius, then the condition $\mu_r \frac{\Delta}{a} \gg 1$ is met, and Equation (3.4) can be simplified to (Hoburg, 1995; Mager, 1970)

$$SF \approx \frac{2}{3}\mu_r \frac{\Delta}{a} + 1. \tag{3.5}$$

Increasing both the ratio of material thickness to inner diameter and the value of μ_r will thus improve shielding performance, as shown in Figure 3.3A.

To further enhance the shielding factor obtained, multiple layers of shielding material can be employed, where the spacing between layers becomes an important factor in determining the shielding performance, in addition to the thickness-to-diameter ratio (Schweizer, 1962). The shielding factor of a two-layer spherical shield can be approximated as follows (Mager, 1970)

$$SF \approx S_i S_o \left(1 - \frac{{d_i}^3}{{d_o}^3}\right) + S_i + S_o + 1, \tag{3.6}$$

where S_i and S_o are the shielding factors and d_i and d_o the diameters of the inner and outer layers, respectively. Figure 3.3B compares the shielding factor achieved for a single layer versus a two-layer MuMetal spherical shield, with thickness 1.5 mm and layer spacing 0.2 m.

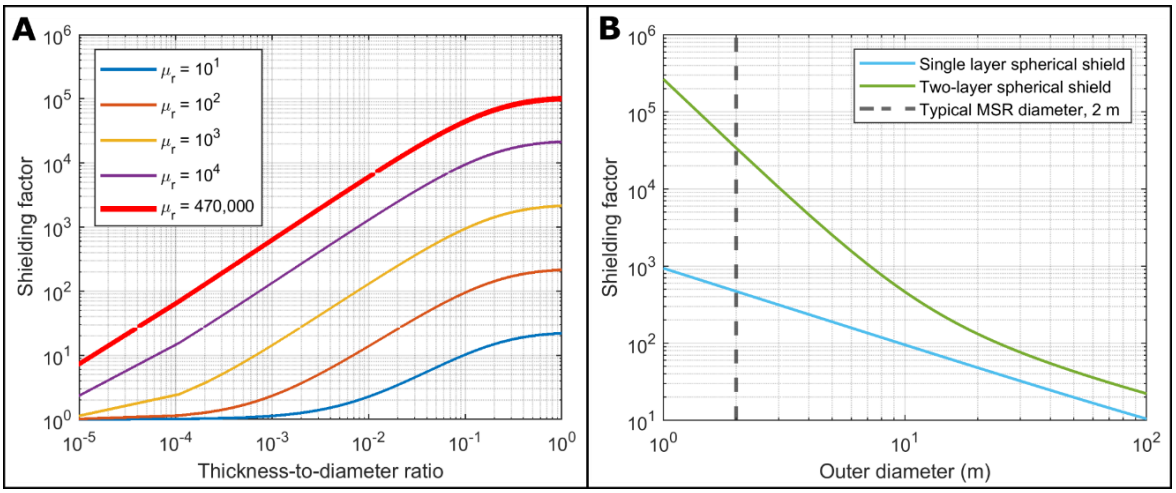

Figure 3.3 – Assessing shielding performance. *A) Shielding factor as a function of the thickness-to-diameter ratio for a spherical shield. Results are shown for a range of relative permeabilities, including a typical value from a manufacturer of MuMetal, μ_r = 470,000. B) Shielding factor as a function of outer diameter for a single layer and two-layer MuMetal (μ_r = 470,000) spherical shield with thickness 1.5 mm and layer spacing 0.2 m. Note that for typical MSR diameters (~2 m) shielding performance is much improved by using a two-layer shield.*

3.2.2. Eddy current cancellation

When a time-varying magnetic field $\boldsymbol{B}(t)$ is incident upon a material, an electric field $\boldsymbol{E}(t)$ is induced within the material, according to Faraday's law:

$$\boldsymbol{\nabla} \times \boldsymbol{E}(t) = -\frac{\partial \boldsymbol{B}(t)}{\partial t}, \tag{3.7}$$

Furthermore, Lenz's law states that if the material has an electrical conductivity σ, a current density is also induced, which in turn generates magnetic flux that opposes the impinging magnetic field. Superposition of the incident and induced flux results in a net screening of magnetic field away from the enclosure by the conductive material (see Figure 3.4A). This is known as eddy current cancellation and is the dominant magnetic shielding mechanism for AC (>10 Hz) magnetic fields (Hoburg, 1995).

The current density induced by a time-varying magnetic field decays exponentially in the material with distance from the surface, a characteristic known as the 'skin depth', δ. This value depends upon the frequency of the incident AC magnetic field, as well as the relative permeability and electrical conductivity of the material, as follows

$$\delta = \sqrt{\frac{2}{\omega \mu_0 \mu_r \sigma}}, \tag{3.8}$$

for an incident magnetic field of angular frequency $\omega = 2\pi f$ (Hoburg, 1995). It follows then that good shielding performance is achieved when the skin depth is smaller than the material thickness ($\delta \ll \Delta$).

Highly conductive materials such as copper and aluminium are commonly employed for eddy current shielding, as their relative permeability $\mu_r \approx 1$. For a 60 Hz AC source (e.g., the American power line frequency) the skin depths of copper and aluminium are 8.5 mm and 11.8 mm, respectively. In such cases, the skin depth is larger than the thickness of the shield (typically 1—4 mm), however, good shielding performance can still be achieved by increasing the outer dimensions of the shield. This allows eddy currents to circulate over a larger area, inducing greater flux densities for shielding.

The shielding factor achieved by eddy current cancellation varies across space and is a complex number. For a given position, the magnitude of the shielding factor describes the ratio of the magnitude of shielded to unshielded magnetic field, and the phase of the shielding factor describes the difference in phase between the shielded and unshielded fields. For a spherical shield with $\mu_r = 1$, $\delta \gg \Delta$ and $\Delta \ll a$, the shielding factor is described as (Hoburg, 1995)

$$SF = 1 + i\omega \frac{\mu_0 \sigma a \Delta}{3}. \tag{3.9}$$

Hence, shielding performance can be improved by increasing the conductivity and thickness of the material, as well as the dimensions of the shield. These characteristics are summarised in a property known as the magnetic diffusion time of the material, $\tau = \mu_0 \sigma a \Delta$, and Figure 3.4B shows how the shielding factor varies with the product of the angular frequency and the magnetic diffusion time.

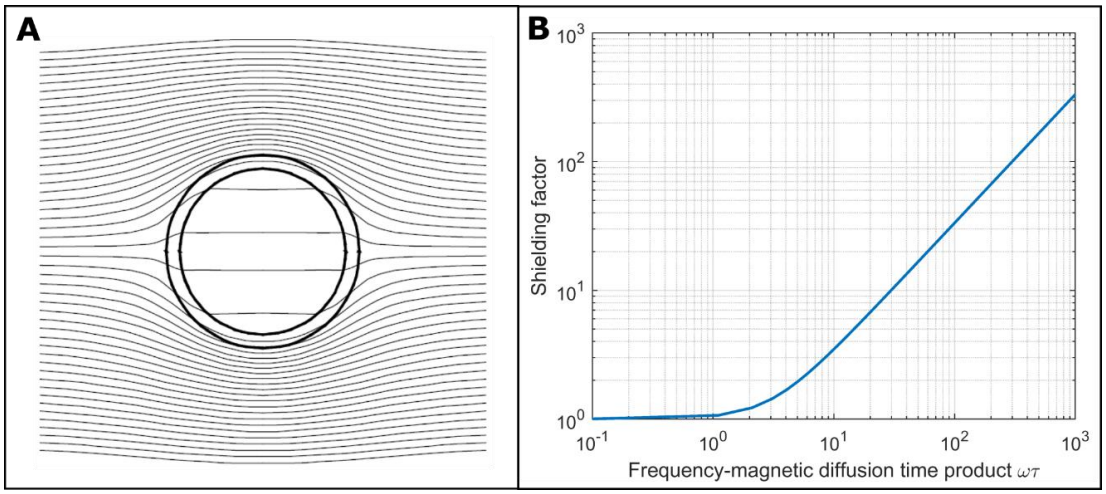

Figure 3.4 – Eddy current cancellation. *A) Diagram of the mechanism of eddy current shielding. Current density induced in materials with high electrical conductivity by time-varying magnetic fields generates magnetic flux that opposes the incident flux, screening the enclosure (Taken from Celozzi et al., 2008). B) Shielding factor as a function of the frequency-diffusion time product,* $\omega\tau = \omega\mu_0\sigma a\Delta$ *assuming* $\mu_r = 1$.

3.2.3. De-magnetisation

The materials with high permeability used for passive magnetic shielding are often also ferromagnetic, meaning that exposure of these materials to magnetic fields (e.g., movement of the material through the Earth's magnetic field) leaves a remnant magnetisation in the walls of the enclosure. Upon exposure to a magnetic field, the magnetic domains within the ferromagnetic material start to align with the external magnetic field, increasing the flux density until it reaches a saturation point – for MuMetal this value is 0.75 T (https://magneticshields.co.uk/technical/b-h-curves-mumetal-50-nife). Fortunately, such remnant magnetisation can be reduced via a process known as de-magnetisation or de-gaussing.

De-magnetisation of metals was first performed on the steel hulls of ships during World War II, to evade detection by naval mines (Kelly, 1946). Electrical wires are wrapped around the material to administer a sinusoidally decaying, alternating current, driving the metal around its $\boldsymbol{B}(\boldsymbol{H})$ hysteresis curve to minimise the remnant magnetisation (see Figure 3.5). When applied to a passive magnetic shield, de-gaussing can also improve shielding performance by a factor of ten or more (Voigt et al., 2013). However, detailed modelling of the shield and de-gaussing system, in addition to specialised equipment, is required to obtain reproducible results (Sun et al., 2016; Thiel et al., 2007).

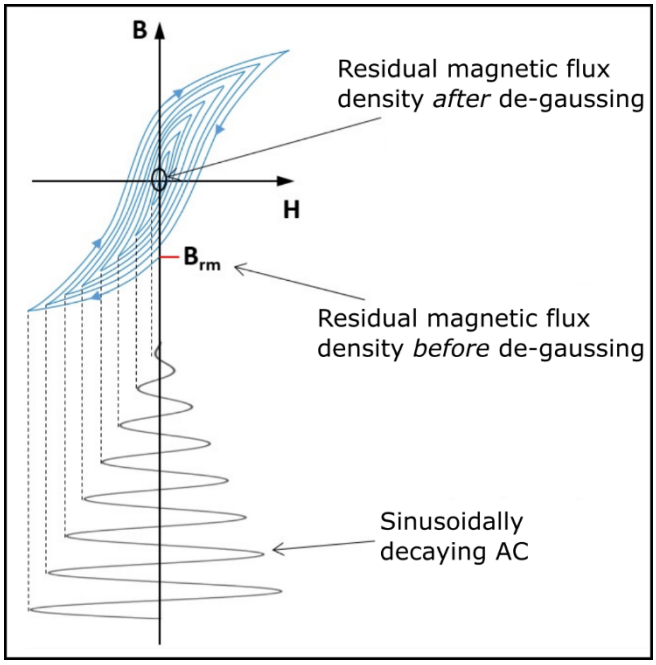

Figure 3.5 – De-gaussing. *A sinusoidally decaying, alternating current is applied to the ferromagnetic material, driving the metal around its hysteresis curve to minimise remnant magnetisation. (Adapted from https://cestriom.com/en/technology/demagnetization-basics/)*

3.2.4. Magnetically shielded rooms for MEG

So far, we have considered the performance of a spherical passive magnetic shield, however, utilisation of spherical shields is impractical and presents a significant engineering challenge. For MEG, cuboidal MSRs with large internal dimensions are typically used, to house the cryogenic dewar and enable access and comfort for participants and scanner operators. While a cuboidal structure is simpler to manufacture, a comparatively reduced shielding performance results, for several reasons:

1. Due to the large dimensions of a MSR, the walls are constructed from multiple panels of material and the small gaps between panels lead to discontinuities in μ_r.
2. Variation in the permeability of each of these panels leads to inconsistent shielding, resulting in spatial variation of the remnant magnetic field inside the enclosure.
3. Further discontinuities in the material occur due to the need for access doors and holes for feed-through of equipment.
4. Substantial flux leakage occurs in the corners of a MSR, since magnetic flux cannot flow continuously across the junction.
5. De-magnetisation equipment can be expensive and requires good flux linkage. The de-gaussing wires must be in contact with the high-permeability material in the MSR walls, often between different layers, and are therefore difficult to retro-fit to existing MSRs.

Consequently, the remnant magnetic field inside a MSR is typically a few tens of nT in magnitude, which also varies with position inside the enclosure (Holmes et al., 2018; Iivanainen et al., 2019).

While the effects of flux shunting and eddy current cancellation on shielding performance can be evaluated analytically for simple geometries such as spheres, cylinders, and infinite planes, more complex modelling is required for cuboidal and realistic structures. Specialised software, such as Ansys (Ansys Inc., Canonsburg, PA, U.S.A.) or COMSOL (COMSOL Inc., Stockholm, Sweden), is a vital tool to optimise the design and performance of bespoke magnetic shields. These software packages use finite element modelling (FEM) to incorporate complex geometries, variation in permeability between panels and saturation effects into computation of the magnetic field profile inside an enclosure.

High performance MSRs have thus been designed and constructed to achieve extremely high shielding factors. For example, the Physikalisch Technische Bundesanstalt (PTB) institute in Berlin features a MSR with seven layers of MuMetal and one layer of aluminium, yielding a shielding factor of 75,000 at 0.01 Hz (Bork et al., 2001). A remnant static magnetic field of 700 pT (with gradients ~300 pTm^{-1}) was achieved with two layers of MuMetal and one layer of aluminium at the Technische Universität München (Altarev et al., 2014). Both of these shields employ de-gaussing coils for de-magnetisation of the MuMetal panels.

While conventional MEG systems require large MSRs to house the cryogenic dewar, OPM-MEG systems can be housed in person-sized, cylindrical shields, akin to the bore of an MRI scanner. Such a shield, designed to accommodate a fixed, 20-channel OPM array for MEG and equipped with de-gaussing coils, achieved ~1 nT static magnetic field in the region containing the OPMs (Borna et al., 2017). Due to their smaller footprint, cylindrical shields are easier to site than traditional MSRs and reduce material and construction costs, however, participant comfort and movement are restricted, thus the full potential of OPM-MEG cannot be exploited.

In 2019, an OPM-optimised MSR was installed at the University of Nottingham (MuRoom, Magnetic Shields Ltd. Kent, U.K.), featuring four layers of MuMetal and one layer of copper, with de-gaussing coils attached to the innermost layer (Hill et al., 2020). This shield has large internal dimensions (3 x 2.4 x 3 m^3), with the aim to allow a large range of participant motion during future MEG studies, and achieves a remnant magnetic field inside the enclosure of approximately 2 nT over the central cubic metre, with gradients <2 nTm^{-1}.

While SQUID-based MEG systems are insensitive to the remnant magnetic field inside a MSR – due to their sinusoidal response function (see Section 1.2.1.1) and negative feedback operation – in contrast, OPMs are extremely sensitive to their magnetic environment. As a result, further reduction of this magnetic field is required to facilitate participant movement without impacting data quality.

3.3. Active magnetic shielding

Compensation of the remnant magnetic field inside a shielded enclosure can be achieved by using electromagnetic coils to generate an equal and opposite magnetic field. We revisit Maxwell's equations to describe the behaviour of the magnetic field as follows:

$$\begin{aligned} \nabla \cdot \boldsymbol{B} &= 0 \\ \nabla \times \boldsymbol{H} &= \boldsymbol{J}, \end{aligned} \tag{3.10}$$

where $\boldsymbol{J}$ is the current density. Inside the enclosure there is no current flow and $\mu_r \approx 1$, and since $\boldsymbol{B} = \mu_0 \mu_r \boldsymbol{H}$, we determine that

$$\nabla \times \boldsymbol{B} = 0. \tag{3.11}$$

Upon evaluation of these equations in the Cartesian coordinate system, the magnetic field inside the enclosure can be described by three vector components, B_x, B_y and B_z. These components each obey Laplace's equation, meaning they can be represented as a series of spherical harmonics. The lowest order terms in the series describe the spatially uniform magnetic field components, and the linear magnetic field gradient components, respectively. Evaluating Equations (3.10) and (3.11) reveals symmetry between these gradient terms, as

$$\frac{\partial B_x}{\partial z} = \frac{\partial B_z}{\partial x}$$

$$\frac{\partial B_y}{\partial z} = \frac{\partial B_z}{\partial y}$$

$$\frac{\partial B_x}{\partial y} = \frac{\partial B_y}{\partial x} \tag{3.12}$$

$$\frac{\partial B_x}{\partial x} + \frac{\partial B_y}{\partial y} + \frac{\partial B_z}{\partial z} = 0.$$

As a result, the static magnetic field and its gradients that correspond to linear field variation with position can be described by a total of eight components (three uniform and five spatially varying). Higher order terms (e.g., with dependence on the square of position) can also be modelled (see Chapter 7). If we measure the magnetic field inside the MSR corresponding to these components, an equal and opposing magnetic field distribution can be generated by passing current through appropriately designed electromagnetic coils.

3.3.1. Electromagnetic coils

The magnetic field generated by a current carrying wire is described by the Biot-Savart law. Assuming a constant current I, the magnetic field generated at position $\boldsymbol{r}(x, y, z)$ can be determined by evaluating the following line integral over all elements $d\boldsymbol{l}$ of the current path C:

$$\boldsymbol{B}(\boldsymbol{r}) = \frac{\boldsymbol{\mu_0}}{4\pi} \int_C \frac{I d\boldsymbol{l} \times \boldsymbol{r}'}{|\boldsymbol{r}'|^3}, \tag{3.13}$$

where $\boldsymbol{r}'$ is the vector separating a given line element and the position $\boldsymbol{r}$. Hence, a loop of wire driven with a constant current can be used to generate a magnetic field.

For compensation of multiple components of the magnetic field, as required here, a dedicated coil is designed to generate each component (i.e., to compensate eight components of magnetic field we require eight different coils). Each coil is driven with an independent current, such that the magnitude of the magnetic field generated in each component can be controlled by the amount of applied current through each coil.

3.3.1.1. Discrete coils

Coils can be designed from basic building blocks, such as arcs and loops (Golay, 1958; Roméo and Hoult, 1984). The simplest design is a Helmholtz coil, which consists of two circular current loops of radius a. If we position the two loops symmetrically in the x—y plane, separated by the distance equal to their radius, and drive both loops with the same constant current, then the magnetic field B_z is highly homogeneous at the centre of the coil (see Figure 3.6A). This is due to superposition of the magnetic

fields generated by each current loop. Rotating this arrangement to position the loops in the y—z or x—z plane will equivalently produce a homogeneous magnetic field in B_x or B_y, respectively. Combining these current loops to generate all three spatially uniform components of magnetic field simultaneously is known as a Helmholtz cage.

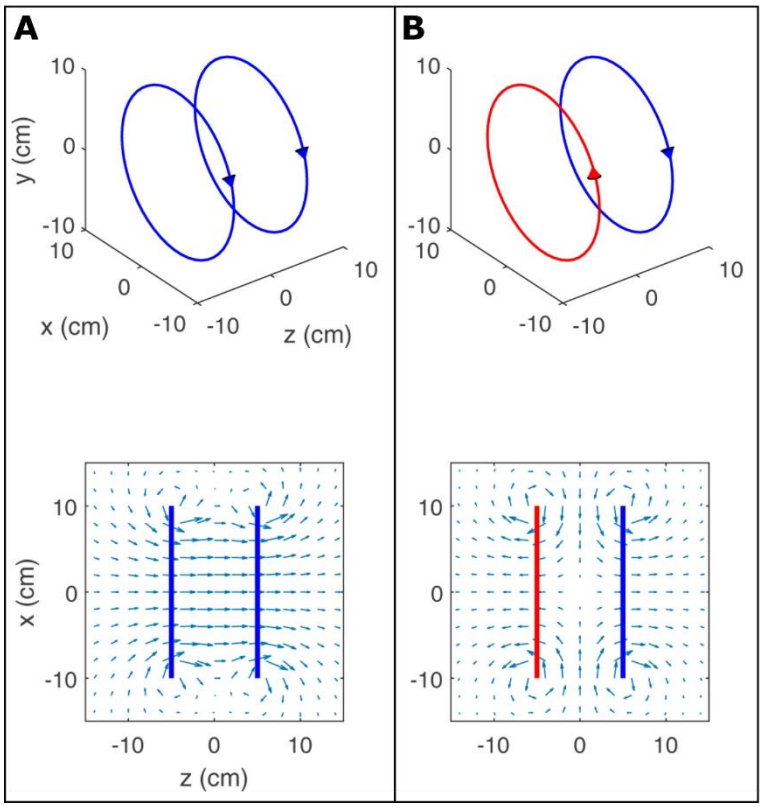

Figure 3.6 – Helmholtz coil. *A) The magnetic field at the centre of two identical, co-axial current loops separated by the distance equal to their radius is spatially uniform. B) Reversing the current flow in one of these loops generates a longitudinal gradient. (Adapted from Holmes et al., 2019).*

A Helmholtz-type coil can also be used to generate a longitudinal magnetic field gradient, where a given magnetic field component varies with position along the same direction, i.e., $\frac{\partial B_x}{\partial x}$, $\frac{\partial B_y}{\partial y}$ and $\frac{\partial B_z}{\partial z}$. To achieve this, the current applied to one of the current loops is reversed. The resulting superposition of magnetic fields generated by each current loop yields a value of zero at the centre of the coil, with the field increasing or decreasing linearly with distance towards each current loop (see Figure 3.6B). The strength of the gradient can be modulated by scaling the current applied to each loop. As before, rotating the Helmholtz arrangement to lie along each Cartesian axis will enable generation of each longitudinal gradient component. The remaining components, $\frac{\partial B_x}{\partial y}$, $\frac{\partial B_x}{\partial z}$ and $\frac{\partial B_y}{\partial z}$, are referred to as transverse magnetic field gradients, and more complex wire paths are required to generate these (Golay, 1958; Roméo and Hoult, 1984).

For use in OPM-MEG, an active shielding system of eight square coils arranged akin to a Helmholtz cage (see Figure 3.7) was developed at Aalto University in Finland. Deployed inside a MSR, compensation of both static and time-varying magnetic field and gradient was implemented via feedback control (to be discussed in Section 3.3.2), using the outputs of OPMs held in a fixed helmet array. The magnitude of the background magnetic field was reduced from 70 nT to <1 nT, while the magnetic field drift over time was reduced to below 400 pT (Iivanainen et al., 2019).

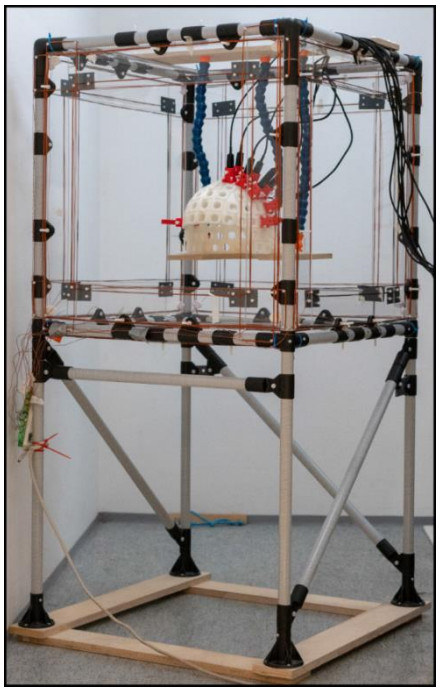

Figure 3.7 – Active magnetic shielding system for OPM-MEG. *A series of eight rectangular coils in a cage arrangement enable compensation of static and time-varying magnetic fields across the OPM array (Taken from Iivanainen et al., 2019).*

3.3.1.2. Distributed coils

In MRI, magnetic field gradients facilitate spatial encoding of the signal and enable formation of an image, since the precession frequency of nuclei within this magnetic field will vary with position. Much expertise in coil design was therefore established in the development of MRI gradient coils that generate highly homogeneous magnetic field gradients, as this leads to the best image quality. Coils with distributed windings were developed, where intricate wire paths are arranged across a surface, to generate homogeneous gradients over larger volumes (Hidalgo-Tobon, 2010). These designs are also known as 'fingerprint' coils, due to the resemblance (see Figure 3.8). Optimisation approaches are often incorporated into the design process of such coils, to minimise power dissipation (i.e., use as little current as possible) and inductance (to enable rapid gradient switching and minimise scan times), and balance any torque on the coil due to the large B_0 field of the scanner (Carlson et al., 1992; Turner, 1993).

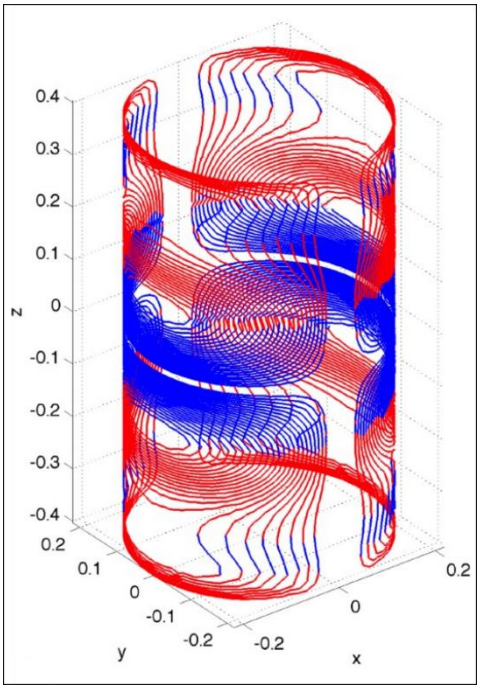

Figure 3.8 – Cylindrical gradient coil for MRI. *A head insert gradient coil designed and optimised by Handler et al., 2014.*

3.3.1.3. Bi-planar coil active shielding system

These methods can be readily applied to the design of electromagnetic coils for active magnetic shielding. Planar coil designs (Yoda, 1990) are particularly relevant due to the cuboidal geometries of most MSRs for MEG, and aim to optimise the homogeneity of a single magnetic field component; thus eight dedicated coils can be designed that generate one of the three spatially uniform magnetic field components, B_x, B_y or B_z, or the following five gradient components:

$$G_{xz} = \frac{\partial B_x}{\partial z} = \frac{\partial B_z}{\partial x}$$

$$G_{yz} = \frac{\partial B_y}{\partial z} = \frac{\partial B_z}{\partial y}$$

$$G_{zz} = \frac{\partial B_z}{\partial z} = -2\frac{\partial B_x}{\partial x} = -2\frac{\partial B_y}{\partial y} \tag{3.14}$$

$$G_{xy} = \frac{\partial B_x}{\partial y} = \frac{\partial B_y}{\partial x}$$

$$G_{xx} = \frac{\partial B_x}{\partial x} = -\frac{\partial B_y}{\partial y} - \frac{\partial B_z}{\partial z}.$$

For active shielding of the OPM-MEG system at the University of Nottingham, a bi-planar coil system was designed and constructed, with the distributed windings mounted on two 1.6 m^2 planes, separated by 1.5 m (Holmes et al., 2018). During MEG recordings, the participant would be seated such

that the head mounted OPM array is within the central volume of the coils (Figure 3.9), the region over which the magnetic fields generated by the coils is most homogeneous. This approach avoids enclosing the participant within any hardware that would limit movement, instead creating an access corridor for participants and scanner operators. However, the participant's head must remain within the central volume during a scan, for optimal performance.

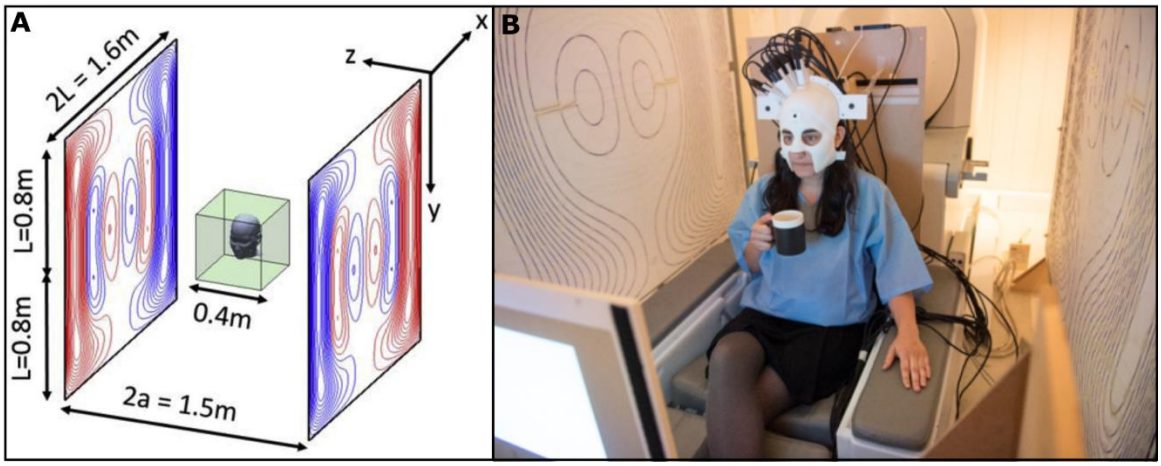

Figure 3.9 – Bi-planar coil system. *A) Two square planes of side length 1.6 m are placed 1.5 m apart. Each coil produces a homogeneous magnetic field or gradient (to within ±5%) inside a 40 cm³ volume highlighted by the green cube (Taken from Holmes et al., 2018). B) Photograph of the constructed coils and OPM-MEG participant.*

To design the coils, mathematics from MRI planar coil design (Yoda, 1990) were incorporated into a harmonic minimisation approach (Carlson et al., 1992), which aims to minimise spatial variation of the generated magnetic field component from the desired field, using the functional:

$$F = \sum_{i=1}^{I} |B(\boldsymbol{r}_i) - b(\boldsymbol{r}_i)|^2, \tag{3.15}$$

where $B(\boldsymbol{r}_i)$ is the desired field at position $\boldsymbol{r}_i$, and $b(\boldsymbol{r}_i)$ is the calculated field at $\boldsymbol{r}_i$. The position vector $\boldsymbol{r}_i$ defines a set of target points within the volume over which magnetic field or gradient homogeneity is required. Here, each coil pair was designed to optimise homogeneity over the central 40 cm³ volume of the coils.

However, the coil that results from this calculation would likely be formed of extremely complex windings that are difficult to implement in practice. Therefore, a power dissipation term, P, was included in the functional, along with a tuneable factor ω, as follows:

$$F = \sum_{i=1}^{I} |B(\boldsymbol{r}_i) - b(\boldsymbol{r}_i)|^2 + \omega P. \tag{3.16}$$

High values of ω result in simpler wire paths, at the expense of field homogeneity. Here, the value of ω was set to the minimum value that produced <5 % spatial deviation of the required magnetic field or gradient over the target volume (Holmes et al., 2018). Note that since these coils are not operated in a large magnetic field and we do not require gradient switching as in MRI, minimisation of inductance and torque balancing in the system were not necessary. The resulting eight coil designs are shown in Figure 3.10, where red and blue lines indicate opposing current flow. This bi-planar active magnetic shielding system is employed in experimental work described by Chapters 4 and 5.

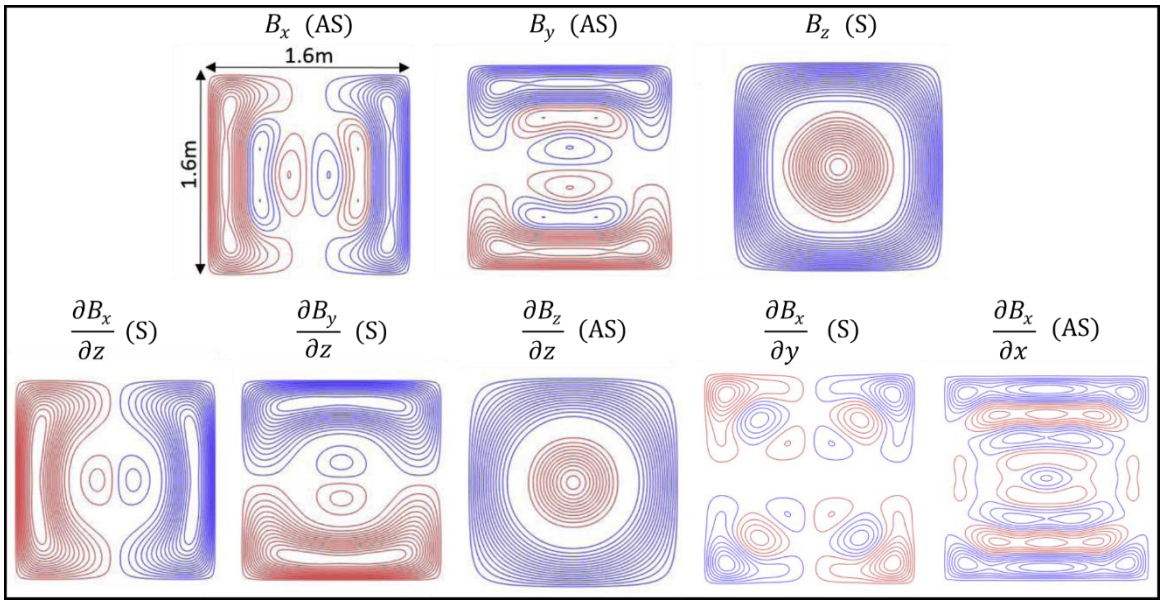

Figure 3.10 – Bi-planar coil windings. *Wire paths for the eight coils, each generating one component of magnetic field or magnetic field gradient. Red and blue lines indicate wires with opposing current flow; (S) or (AS) indicates whether current flow on the opposite plane is symmetric or anti-symmetric, respectively.*

3.3.2. Feedback control

Having designed and constructed a system of electromagnetic coils for active shielding, an approach to automate control of the applied magnetic fields was required. For compensation of the spatially uniform magnetic field components, B_x, B_y and B_z, triaxial measurement of the remnant magnetic field at one position inside the MSR is used for feedback control. These measurements inform the applied coil currents using prior knowledge of the magnetic field generated by a unit of applied current in each coil, known as the coil efficiency. Using a series of measurements at multiple positions inside the MSR gives an estimate of the spatial variation of the remnant magnetic field, hence the outputs of a series of magnetometers at known locations can be used to inform currents applied to the gradient coils in a similar manner.

A more advanced method of automating feedback control is the widely used proportional integral derivative (PID) controller, which is particularly effective for complex systems. For active magnetic

shielding, the PID controller applies current to each coil based upon both the corresponding measurement and the history of the system. A user-defined 'setpoint' specifies the desired measurement value to be reached, which in this case is zero magnetic field. The difference between the measurement $b(t)$ and the setpoint s is described as the error in the system $e(t)$, computed as follows (Åström and Hägglund, 1995):

$$e(t) = b(t) - s. \tag{3.17}$$

The current $I(t)$ applied to each coil is computed by the PID controller as the sum of three terms; the first term is proportional to the error, the second term varies with the integral of the error over time, and the third term varies with the derivative of the error. Each term is modulated by a gain value, K, which is adjusted to achieve stability in the system (Åström and Hägglund, 1995).

$$I(t) = K_p e(t) + K_i \int_0^t e(\tau) d\tau + K_d \frac{de(t)}{dt}. \tag{3.18}$$

While inclusion of the derivative term theoretically helps to stabilise the controller, in practice the third term can often amplify noise in the system (Ang et al., 2005), therefore PI controllers are also common.

A PID controller was implemented alongside the bi-planar coils described previously, to enable magnetic field and gradient compensation over the central volume of the coils. Four dual-axis QZFMs (Gen-1) were used to sample the remnant magnetic field, operated in their field-zeroing mode to allow measurement of magnetic fields up to 50 nT in magnitude (Osborne et al., 2018). These reference sensors were positioned behind the participant's head, and arranged such that two measurements of B_x, B_y and B_z were made at a separation of 30 cm in the z-direction (see Figure 3.11A), enabling feedback control of the uniform magnetic field components and gradients that vary in z (Holmes et al., 2018). Estimates of the magnetic field (taken from a single OPM output or the mean of the two measurements in each direction) and gradients (subtraction of the two measurements in each direction) were input to the PID controller, which varied the current applied to each coil to drive these values to zero. Once this field nulling step was completed, the PID controllers were deactivated and the coil currents fixed, ready to begin to an OPM-MEG recording.

Use of this technique inside a MSR for conventional MEG resulted in a reduction of the magnitude of the magnetic field from 28 nT to 0.74 nT, and its spatial variation was reduced by a factor of 4. This enabled head movements of up to ~30° and 10 cm, without exceeding the operating range of the QZFM (Holmes et al., 2018). The approach was later extended to allow dynamic compensation of changes in the remnant magnetic field over time, reducing fluctuations in the background field to less than 200 pT over a ten minute period (Holmes et al., 2019).

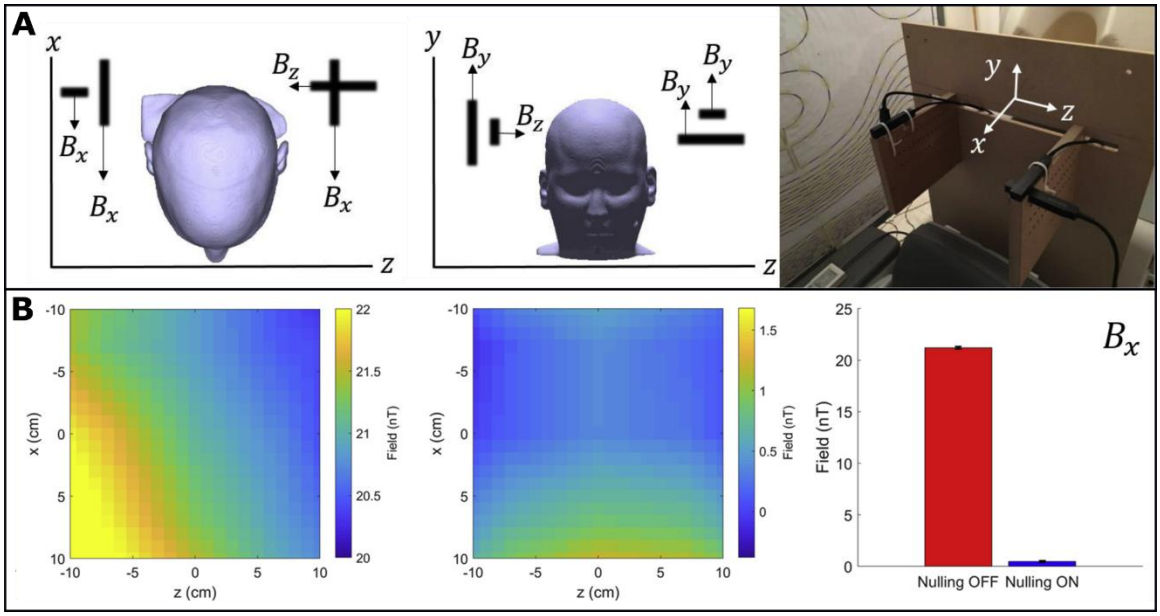

Figure 3.11 – Implementing active magnetic shielding for OPM-MEG. *A) A reference array of four OPMs positioned behind the participant's head facilitates feedback control of the coils. B) Mapping of the uniform magnetic field component B_x, before and after nulling with the bi-planar coils. Left panel shows the strength and spatial variation of the remnant field over a 20 cm² plane. Bar chart shows the strength of the component before and after nulling. (Adapted from Holmes et al., 2018)*

3.3.3. Multi-coil approaches

The size and location of the volume over which the bi-planar coil system generates homogeneous magnetic field distributions is determined during the design process and restricted by the fixed wire paths. Therefore, the strength of the magnetic field generated by each coil can be modulated by the applied current, but its pattern of spatial variation remains unchanged. To enable more flexibility, adjustable currents could be applied to a series of smaller coils, and thus generate a variety of magnetic field distributions. Simple rectangular or square coil geometries are perhaps the most appropriate, as they are comparatively easier to manufacture than distributed coils.

Multi-coil approaches have been utilised in MRI for shimming, a process in which local magnetic field distributions are generated to counteract distortions in the B_0 field that impact image quality (Gruetter, 1993). For example, accurate imaging of the prefrontal cortex of the brain is challenging, due to large differences in susceptibility between the air-filled cavities, tissues and bones around the sinuses causing localised distortions (Juchem et al., 2010), shown in Figure 3.12. For active shimming using a multi-coil array, the inhomogeneities in magnetic field over the region of interest are mapped, such that the optimal coil currents to reduce these distortions can be calculated. In practice, shimming is performed prior to starting a scan, with the coil currents fixed throughout, or applied dynamically during acquisition. Hence, active shimming coils present an adaptable approach that can be easily translated for use in active magnetic shielding.

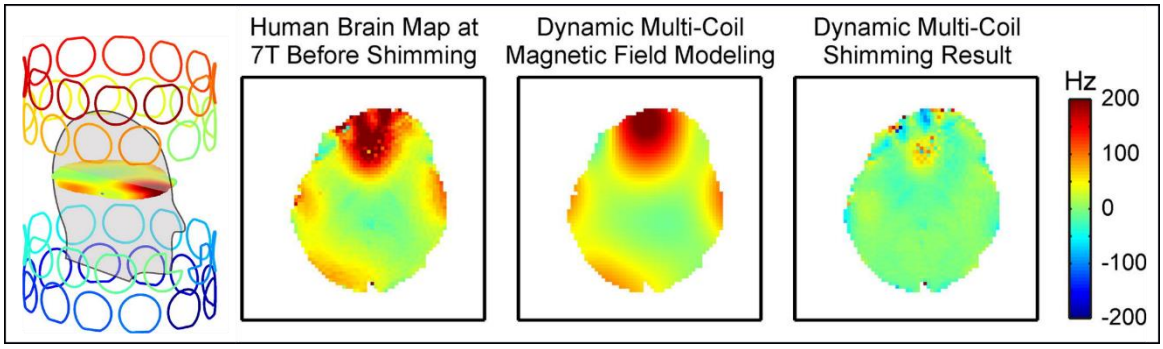

Figure 3.12 – Multi-coil active shimming for MRI. *Susceptibility differences around the sinuses distort the magnetic field profile and degrade image quality. A 48-coil active shimming system was used to counteract these inhomogeneities (Taken from Juchem et al., 2011).*

The person-sized cylindrical shield for OPM-MEG discussed previously also features a multi-coil active shielding system, consisting of eighteen coils designed to control the uniform magnetic field and first- and second-order gradients over the fixed region that contains the OPM array (Borna et al., 2017). Fluxgate magnetometers were used to sample the ambient magnetic field, and a transfer function computed to generate the required cancellation field using the multi-coil system. As a result, the remnant magnetic field was reduced to <0.3 nT across the OPM array (Borna et al., 2020).

3.4. Limitations and challenges

Despite the combination of passive and active magnetic shielding techniques proving effective at reducing the magnetic interference experienced by an array of OPMs, and even enabling some degree of participant movement, a few substantial challenges remain. First, the required high permeability and high conductivity shielding materials make typical MSRs heavy, expensive, and difficult to site. While cylindrical shields for OPM-MEG may alleviate some of these constraints, participant movement is then extremely limited.

Use of the bi-planar coil active shielding system described above provides a reasonably open scanning environment and easy access to the participant, however the region over which the background magnetic field can be accurately controlled is limited to a fixed, 40 cm^3 central volume. This region is defined at the design stage and can only later be moved by physically translating the coils. Since the OPM array needs to be positioned within this region for optimal performance, multiple participants cannot be scanned simultaneously using this approach.

The coil planes themselves are large, occupying space in the MSR, and the distributed windings are challenging to manufacture. In addition, interactions between the magnetic fields generated by the coils with the high-permeability walls of the MSR will occur, which affect the effective field per unit current and distort the spatial variation of the magnetic fields generated by the coils (Hammond, 1960; Roshen, 1990). These effects were not taken into account when designing the bi-planar coil system, but recent

work has shown that the interactions can be modelled and incorporated into coil designs to generate more accurate field profiles (Hobson et al., 2022; Kutschka et al., 2021; Packer et al., 2020; Zetter et al., 2020). Conceivably, a multi-coil system of simpler geometries that could be mounted nearer to the walls of a MSR would optimise the scanning environment for participant comfort and movement, and enable flexibility in their positioning, since the region over which background magnetic fields are controlled could be reconfigured by adjusting the coil currents. Interactions between the generated magnetic fields and the MuMetal walls could be readily considered for such wall-mounted multi-coil systems.

Finally, coil control has so far been facilitated using a fixed reference measurements and feedback control. The reference array must be positioned close to the volume over which we wish to cancel the remnant magnetic field, but not directly on the participant's head (to avoid cancelling any magnetic fields of interest from the brain). Hence, the use of a reference array also restricts scanning to a fixed region. For the bi-planar coil system, the reference sensors were operated in field-zeroing mode, to obtain a measure of the ambient magnetic field inside the MSR. The magnetisation of internal components of each OPM leads to a small DC offset (usually <5 nT for a QZFM), meaning the zero magnetic field point of the sensor does not reflect a true zero remnant field in the MSR. Although these offsets can be measured and accounted for, they add inaccuracies to reference array-based field nulling approaches. In addition, only the magnetic field gradients that vary in z were able to be accurately compensated, as the reference OPMs could be spatially separated in the z-direction without impinging on the participant. For full compensation of all gradients, including those that vary with position in the x- and y- directions, additional reference measurements extended in the remaining directions would be required, thus occupying more space and further surrounding the participant. Regardless, sampling of the background magnetic field in this way is limited to a small number of fixed locations, thus it follows that improved magnetic field compensation could be achieved if the remnant magnetic field could be more accurately mapped.

Chapter 4

Precision magnetic field modelling and control for wearable MEG

NeuroImage, Volume 241, 2021, 118401

NeuroImage 241 (2021) 118401

Contents lists available at ScienceDirect

NeuroImage

journal homepage: www.elsevier.com/locate/neuroimage

Precision magnetic field modelling and control for wearable magnetoencephalography

Molly Rea[a,*], Niall Holmes[a,*,+], Ryan M. Hill[a], Elena Boto[a], James Leggett[a], Lucy J. Edwards[a], David Woolger[b], Eliot Dawson[b], Vishal Shah[c], James Osborne[c], Richard Bowtell[a], Matthew J. Brookes[a]

[a] Sir Peter Mansfield Imaging Centre, School of Physics and Astronomy, University of Nottingham, University Park, Nottingham, NG7 2RD, UK
[b] Magnetic Shields Limited, Headcorn Road, Staplehurst, Tonbridge, Kent, TN12 0DS, UK
[c] QuSpin Inc., 331 South 104th Street, Suite 130, Louisville, 80027, Colorado, USA

ARTICLE INFO

Keywords:
Optically-pumped magnetometer
OPM
Magnetoencephalography
MEG
Magnetic field
Nulling

ABSTRACT

Optically-pumped magnetometers (OPMs) are highly sensitive, compact magnetic field sensors, which offer a viable alternative to cryogenic sensors (superconducting quantum interference devices – SQUIDs) for magnetoencephalography (MEG). With the promise of a wearable system that offers lifespan compliance, enables movement during scanning, and provides higher quality data, OPMs could drive a step change in MEG instrumentation. However, this potential can only be realised if background magnetic fields are appropriately controlled, via a combination of optimised passive magnetic screening (i.e. enclosing the system in layers of high-permeability materials), and electromagnetic coils to further null the remnant magnetic field. In this work, we show that even in an OPM-optimised passive shield with extremely low (<2 nT) remnant magnetic field, head movement generates significant artefacts in MEG data that manifest as low-frequency interference. To counter this effect we introduce a magnetic field mapping technique, in which the participant moves their head to sample the background magnetic field using a wearable sensor array; resulting data are compared to a model to derive coefficients representing three uniform magnetic field components and five magnetic field gradient components inside the passive shield. We show that this technique accurately reconstructs the magnitude of known magnetic fields. Moreover, by feeding the obtained coefficients into a bi-planar electromagnetic coil system, we were able to reduce the uniform magnetic field experienced by the array from a magnitude of 1.3 ± 0.3 nT to 0.29 ± 0.07 nT. Most importantly, we show that this field compensation generates a five-fold reduction in motion artefact at 0–2 Hz, in a visual steady-state evoked response experiment using 6 Hz stimulation. We suggest that this technique could be used in future OPM-MEG experiments to improve the quality of data, especially in paradigms seeking to measure low-frequency oscillations, or in experiments where head movement is encouraged.

1. Introduction

Magnetoencephalography (MEG) (Cohen, 1968) measures magnetic fields generated above the scalp by neuronal current flow in the brain. Mathematical modelling of these fields (or source reconstruction) forms 3D images showing moment-to-moment changes in brain electrophysiology. MEG offers a high spatial and temporal resolution assessment of neural activity (Baillet, 2017; Hämäläinen et al., 1993) in which the formation and dissolution of networks can be tracked in real time (Baker et al., 2014). Human brain dysfunction in neurological and psychiatric disorders can also be assessed, potentially offering powerful biomarkers of disease.

Despite its utility, the current generation of MEG systems is limited due to the use of superconducting quantum interference devices (SQUIDs) to detect the neuromagnetic field (Cohen, 1972). Whilst extremely sensitive, these cryogenic sensors must be fixed rigidly in position inside a liquid helium dewar, and the requisite thermally insulating vacuum space makes it difficult to position sensors closer than ~2 cm to the scalp. This reduces the strength of the MEG signal at the detectors (in accordance with an inverse square law), an effect which becomes further pronounced when scanning people with small heads (e.g. infants).

[+] Corresponding author at: Sir Peter Mansfield Imaging Centre, School of Physics and Astronomy, University of Nottingham, University Park, Nottingham, NG7 2RD.
E-mail address: niall.holmes@nottingham.ac.uk (N. Holmes).
[*] These authors contributed equally to this work

https://doi.org/10.1016/j.neuroimage.2021.118401.
Received 4 December 2020; Received in revised form 30 June 2021; Accepted 13 July 2021
Available online 15 July 2021.

It also limits our ability to sample the highest spatial frequencies of the magnetic field pattern (since field patterns become more spatially diffuse with distance). This, in turn, limits spatial resolution (Boto et al., 2016; Iivanainen et al., 2017). The fixed nature of the array also means that motion of a participant during a scan is restricted to less than 5 mm (Gross et al., 2013). Although small head motion (up to a few centimetres) inside the helmet can be algorithmically corrected (Nenonen et al., 2012; Taulu et al., 2005), large movements cannot be made, and no algorithms can correct for changing signal-to-noise ratio when a participant gets closer to or further from the sensors. This requirement to keep still over lengthy scans makes MEG inaccessible to many interesting study groups, and these confounds mean MEG has remained primarily a research tool, despite its clinical advantages over techniques such as electroencephalography (EEG) (Baillet, 2017; Boto et al., 2019).

Recent advances in quantum sensing have allowed the construction of 'wearable' or 'on-scalp' MEG systems where magnetic field sensors are placed either directly onto, or held near to the scalp. Optically-pumped magnetometers (OPMs) have emerged as the stand-out sensor technology in this area (Borna et al., 2020; Boto et al., 2021; Hill et al., 2020; Iivanainen et al., 2019), although arrays of High-Tc SQUIDs, which operate at liquid nitrogen temperatures, also offer great promise (Pfeiffer et al., 2019). Briefly (see Tierney et al., 2019 for a review), OPMs comprise a small, heated cell containing a vapour of alkali metal (e.g. rubidium) that is optically-pumped into a magnetically-sensitive state using laser light (Happer, 1972). Once prepared, the optical properties of the system (e.g. the transparency of the cell to the pumping laser) can be used to infer the magnetic field experienced by the atoms in the cell (Bell and Bloom, 1961, 1957; Dupont-Roc et al., 1969). For OPMs to attain sufficient sensitivity to detect changes in the neuromagnetic field, they are operated around a zero-field resonance in the spin-exchange relaxation free (SERF) regime (Allred et al., 2002). The ability of OPMs to measure neuromagnetic fields – first shown by Xia et al. (2006) – is now well established (e.g. (Boto et al., 2017; Johnson et al., 2010; Kamada et al., 2015; Sander et al., 2012)) and sensor miniaturisation and commercialisation (Allred et al., 2002; Johnson et al., 2013; Kamada et al., 2015; Kominis et al., 2003; Mhaskar et al., 2012; Sander et al., 2012; Schwindt et al., 2007; Shah and Wakai, 2013; Sheng et al., 2017) means that robust, small, and lightweight OPMs can now be mounted on the scalp surface. This allows for the introduction of wearable systems where the lightweight sensor array, mounted in a helmet, can be adapted to different head shapes/sizes and moves with the head during a scan (Boto et al., 2018; Hill et al., 2020). Given this, alongside lower overall cost, it is likely that OPMs will lift the significant limitations associated with cryogenic MEG systems. Challenges remain, however, before OPMs can replace SQUIDs as the fundamental building block of MEG instrumentation.

One of the biggest challenges in operationalising OPM-MEG is generating a well-controlled magnetic field environment. MEG systems (based on SQUIDs and OPMs) are housed inside magnetically-shielded rooms (MSRs). These are typically constructed from multiple layers of high magnetic permeability metal (e.g. mu-metal) to exclude low-frequency (DC to ~10 Hz) magnetic fields, and a layer of a metal with a high electrical conductivity (such as copper or aluminium) to attenuate higher-frequency (>10 Hz) magnetic fields (Hoburg, 1995). These 'passively' shielded enclosures provide screening of external sources of interference, which improve the signal-to-noise ratio of MEG data. However, the ferromagnetic properties of the high-permeability materials used in MSR construction often result in a 'remnant' DC (i.e. temporally static) magnetic field. SQUIDs are insensitive to such DC fields, but OPMs (being *zero-field* magnetometers) are very sensitive to background magnetic fields and fail to operate in fields larger than a few nT. For this reason, OPMs typically come equipped with on-board electromagnetic coils that null the local magnetic field vector experienced by the cell. In open-loop mode, currents in these coils are set at the beginning of an experiment, meaning that sensors can be rendered inoperable by field changes produced when the OPMs move during acquisition (i.e. if head movement occurs when using a wearable system). For example, in a 30 nT background magnetic field, a rotation of ~4° would generate sufficient change in field to take an OPM outside its ±1.5 nT dynamic range (defined here as a 5% gain error) (Boto et al., 2018; Iivanainen et al., 2019). Even if the sensor were to remain working, the resulting magnetic artefact would be much larger in amplitude than the neuromagnetic field. For these reasons, suppressing background static magnetic field – even beyond what is achieved with passive shielding – is critical for OPM-MEG.

In previous work (Holmes et al., 2019, 2018), we designed and constructed a bi-planar electromagnetic coil system that contains multiple coil elements, each designed to produce a distinct, homogeneous, component of either magnetic field or magnetic field gradient over a $40 \times 40 \times 40$ cm^3 volume at the centre of the two planes. The remnant magnetic field inside a MSR was compensated by computing estimates of the magnetic field (and its gradients) using a fixed OPM reference array. These estimates were fed into independent feedback controllers to automatically drive field estimates to zero by varying the currents in the bi-planar coil elements. Field mapping before and after the cancellation revealed a reduction in the magnitude of the magnetic field from 28 nT to 0.74 nT. This, in turn, enabled participant movements (Holmes et al., 2018). Dynamic compensation of large sources of interference below 1 Hz has also been demonstrated using a high-speed feedback controller to modulate the coil currents (Holmes et al., 2019). These bi-planar coil systems have proved effective, allowing OPM-MEG studies to be carried out in freely moving participants (e.g. (Hill et al., 2019; Roberts et al., 2019)). However, accurate assessment of the background magnetic fields is limited by the geometry of the reference array, and significant improvements could be made if we were able to more accurately model the remnant magnetic field that informs the optimal coil currents.

Recently, a new MSR dedicated to OPM measurements has been installed at the Sir Peter Mansfield Imaging Centre, University of Nottingham. This room comprises four layers of mu-metal and one layer of copper, and features demagnetisation (or 'degaussing') coils wound around the mu-metal panels (MuRoom, Magnetic Shields Ltd., Kent, U.K.). When driven with a linearly decaying sinusoidal current, these coils force the mu-metal around its hysteresis curve towards a point of zero magnetisation (Altarev et al., 2015, 2014; Voigt et al., 2013). However, the effect of joints between mu-metal panels, the need for access apertures, and variations in the permeability of the mu-metal mean that a remnant magnetic field of around 2 nT still remains. Nevertheless, this is a significant improvement over the ~30 nT remnant magnetic field present within another MSR at our institution that houses a cryogenic MEG system (for comparison, this room consists of two layers of mu-metal, one layer of aluminium and does not feature degaussing coils (Vacuumschmelze, Hanau, Germany)). A remnant magnetic field of 2 nT allows OPMs to operate with minimal compensation currents applied to their on-sensor coils. Despite this improvement, full rotation of the head (e.g. during ambulatory motions) would produce a field shift that would render an OPM inoperable. Smaller movements that do not saturate OPM outputs will still generate magnetic field artefacts in MEG data that would mask brain activity (particularly at low frequency). For these reasons, integrating field compensation coils with the new generation of MSR remains of critical importance.

In this paper, we propose a new approach to using bi-planar coils in an OPM-optimised MSR. Starting with a magnetic field of <2 nT, we combine optical tracking of the movements of an OPM-array worn by a participant with synchronised recording of magnetometer data to generate a model of the remnant magnetic field inside the MSR. Compared to our previous approach using a reference array (Holmes et al., 2018), this model increases the number of components of magnetic field and field gradient that can be measured from six to eight, without surrounding the participant with additional reference sensors. A map of the magnetic field in the full volume of the head-mounted OPM array is produced, rather than at a limited number of sample points located a

small distance from the participant. By combining the model with dynamic compensation of low-frequency interference and appropriate coil calibration, we were able to accurately null the background magnetic field inside the MSR. We begin by outlining the theory underlying the new field nulling method and describing our implementation. We then investigate the ability of this method to map known magnetic fields, and assess its performance when compensating the remnant magnetic field within our MSR. Finally, we present a MEG demonstration featuring continuous head-movements and compare sensor-level data analysis with and without magnetic field compensation.

2. Theory

We begin by assuming that the area inside the MSR is a current-free space and consequently we model the remnant magnetic field, $\boldsymbol{B}(x, y, z)$ using a magnetic scalar potential $\Phi(x, y, z)$, thus

$$\boldsymbol{B}(x, y, z) = -\nabla\Phi(x, y, z). \tag{1}$$

We set

$$\nabla^2\Phi(x, y, z) = 0, \tag{2}$$

in order to ensure that the magnetic field obeys Maxwell's equations for magnetostatics in a current-free region; i.e.

$$\nabla \cdot \boldsymbol{B}(x, y, z) = 0, \tag{3}$$

$$\nabla \times \boldsymbol{B}(x, y, z) = 0. \tag{4}$$

As the scalar potential obeys Laplace's equation, its solutions can be represented as the real spherical harmonics, where n^{th} order terms in the scalar potential generate $(n\text{-}1)^{th}$ order terms in the magnetic field. We assume, for simplicity, that the local magnetic field at a position in or around the centre of the MSR, which is far from any sources of magnetic field, can be approximated as the sum of three spatially uniform components $\boldsymbol{B_U}$, and five (linearly) spatially dependent magnetic field gradient components $\boldsymbol{B_G}$, thus

$$\boldsymbol{B}_{local}(x, y, z) = \boldsymbol{B_U} + \boldsymbol{B_G}(x, y, z). \tag{5}$$

In the spherical harmonic field model, the 1st order terms in the scalar potential describe the three spatially uniform magnetic field components:

$$\text{uniform field components} \begin{cases} \boldsymbol{B_x} = \alpha_1\hat{\boldsymbol{x}}, \ \{B_x\} \\ \boldsymbol{B_y} = \alpha_2\hat{\boldsymbol{y}}, \ \{B_y\} \\ \boldsymbol{B_z} = \alpha_3\hat{\boldsymbol{z}}, \ \{B_z\}, \end{cases}$$

and the 2nd order terms of the scalar potential describe the five magnetic field gradient components:

$$\begin{cases} \boldsymbol{G_{xy}} = \alpha_4(y\hat{\boldsymbol{x}} + x\hat{\boldsymbol{y}}), \left\{ \frac{dB_x}{dy} = \frac{dB_y}{dx} \right\} \\ \boldsymbol{G_{xz}} = \alpha_5(z\hat{\boldsymbol{x}} + x\hat{\boldsymbol{z}}), \left\{ \frac{dB_x}{dz} = \frac{dB_z}{dx} \right\} \\ \boldsymbol{G_{yz}} = \alpha_6(z\hat{\boldsymbol{y}} + y\hat{\boldsymbol{z}}), \left\{ \frac{dB_y}{dz} = \frac{dB_z}{dy} \right\}, \\ \boldsymbol{G_{zz}} = \alpha_7(-x\hat{\boldsymbol{x}} - y\hat{\boldsymbol{y}} + 2z\hat{\boldsymbol{z}}), \left\{ 2\frac{dB_z}{dz} = -\frac{dB_x}{dx} - \frac{dB_y}{dy} \right\} \\ \boldsymbol{G_{xx}} = \alpha_8(x\hat{\boldsymbol{x}} - y\hat{\boldsymbol{y}}), \left\{ \frac{dB_x}{dx} = -\frac{dB_y}{dy} \right\} \end{cases}$$

where the coefficient, α_n, describes the strength of the nth component and $\hat{\boldsymbol{x}}$, $\hat{\boldsymbol{y}}$ and $\hat{\boldsymbol{z}}$ are the Cartesian unit vectors. The equivalent magnetic field or magnetic field gradient for each term is shown in brackets. We then re-write Eq. (5) in terms of the α_n coefficients,

$$\boldsymbol{B}_{local}(x, y, z) = \boldsymbol{\alpha}_U + \mathbf{G}(x, y, z)\boldsymbol{\alpha}_G, \tag{6}$$

where $\boldsymbol{\alpha}_U$ contains the three uniform field coefficients, $\boldsymbol{\alpha}_G$ contains the five field gradient coefficients and $\boldsymbol{G}(x, y, z)$ is a gradient characterisation matrix. Incorporating the expressions from the above model and using a column vector to represent the field, Eq. (6) becomes

$$\boldsymbol{B}_{local}(x, y, z) = \begin{pmatrix} B_x(x, y, z) \\ B_y(x, y, z) \\ B_z(x, y, z) \end{pmatrix} = \begin{pmatrix} \alpha_1 \\ \alpha_2 \\ \alpha_3 \end{pmatrix} + \begin{pmatrix} y & z & 0 & -x & x \\ x & 0 & z & -y & y \\ 0 & x & y & 2z & 0 \end{pmatrix} \begin{pmatrix} \alpha_4 \\ \alpha_5 \\ \alpha_6 \\ \alpha_7 \\ \alpha_8 \end{pmatrix}. \tag{7}$$

OPMs used in MEG are vector (as distinct from scalar, or total field) magnetometers that measure the magnetic field component along at least one sensitive axis. The component of magnetic field measured by an OPM at position (x, y, z) can be calculated as

$$b_e(x, y, z) = \boldsymbol{B}_{local}(x, y, z) \cdot \boldsymbol{e}, \tag{8}$$

where $\boldsymbol{e}$ is a unit vector characterising the orientation of the sensitive axis of the magnetometer with respect to the MSR (i.e. $\boldsymbol{e} = e_x\hat{\boldsymbol{x}} + e_y\hat{\boldsymbol{y}} + e_z\hat{\boldsymbol{z}}$ and $|\boldsymbol{e}| = 1$). From Eqs. (7) and 8 we note that rotation of a magnetometer about $\hat{\boldsymbol{x}}$, $\hat{\boldsymbol{y}}$ and $\hat{\boldsymbol{z}}$ will generate a change in the measured field due to the uniform field components. Similarly, translations (and rotations) of the sensor will generate a change in the measured field due to the spatially dependent field gradient components.

By recording the initial positions and orientations of an array of OPMs, and then measuring changes in these positions and orientations as the array is rotated about all axes and translated in all directions, we can use Eqs. (7) and 8 to simulate the change in magnetic field that would be measured by the array, if the remnant magnetic field in the MSR through which the array was moved comprised a unit (e.g. 1 nT or 1 nTm^{-1}) contribution of one of the eight coefficients. This can be repeated for all coefficients, and through comparing the simulated sensor time-courses with magnetic field data recorded simultaneously with the movement data, we can recover the coefficients that best approximate the remnant magnetic field. Mathematically, we generate a linear matrix equation:

$$\mathbf{B}_{\text{mat}}\boldsymbol{\alpha} = \boldsymbol{b}, \tag{9}$$

where $\boldsymbol{\alpha}$ is a column vector that contains all eight coefficients, $\mathbf{B}_{\text{mat}}$ is a matrix characterising the fields that would be produced over the array of N OPMs by the eight unit-weighted field components, based on the sensor positions and orientations measured at each of T time-points (see Appendix A). $\mathbf{B}_{\text{mat}}$ has 8 columns (one for each field component) and $T \cdot N$ rows (one row for each sensor at each time-point at which the magnetic field and the sensor positions and orientations were measured). The target field column vector $\boldsymbol{b}$ contains the magnetic fields measured by each of the N OPMs at T time-points, at the same positions and orientations as in $\mathbf{B}_{\text{mat}}$. The coefficients $\boldsymbol{\alpha}$ that produce the best fit to $\boldsymbol{b}$ can be obtained by identification of a pseudo-inverse matrix, or similar process.

In order to use the field model to then compensate the remnant magnetic field, currents need to be chosen in a series of electromagnetic coils, which produce an equal and opposite magnetic field to that found by the model. We assume, for now, that our coil system features eight distinct coils that each produce a single, spatially homogeneous component of the magnetic field or magnetic field gradient over the region in which the field was mapped. The magnetic or magnetic field gradient strength produced per unit of applied current can be matched to the negative of the model coefficients to generate appropriate currents. Note here that this argument necessarily assumes that the magnetic field inside the MSR is temporally stable. In practice, particularly for the low magnetic fields inside the OPM-optimised shield, this is unlikely to be the case due to external sources of interference, or slow temperature changes affecting the magnetisation of the mu-metal used to construct the MSR. For this reason, implementing high-speed dynamic stabilisation of the remnant field prior to the mapping procedure is crucial to enable accurate field mapping and compensation.

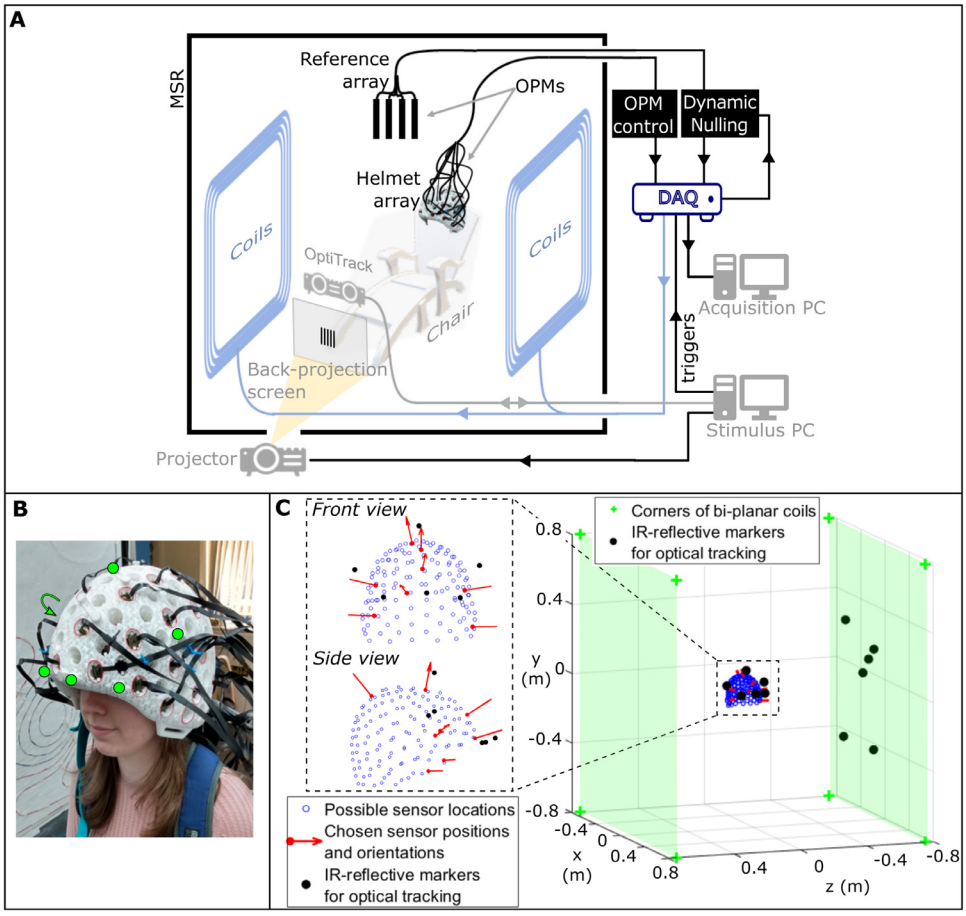

Fig. 1. System overview. A) A schematic diagram of the OPM-MEG system at the University of Nottingham. B) The additively-manufactured rigid helmet used to mount the OPM sensors close to the scalp. Six IR-reflective markers are attached to the helmet at known locations to facilitate 6-DoF optical tracking (marked in the photograph with the green circles (an arrow indicates the sixth marker is positioned on the side of the helmet not visible here)). C) Location of the helmet between the bi-planar coils. The coils are shown by the green shading; the coil corners by the green crosses. The blue markers show OPM locations and the black dots show OptiTrack markers (on the helmet and coils). Inset, the helmet is shown with the location and sensitive orientation of the 8 OPMs used for collecting the data to fit to the field model. (For interpretation of the references to colour in this figure legend, the reader is referred to the web version of this article.)

3. Experimental implementation

3.1. System overview

To perform field mapping, we used an OPM-MEG device developed at the University of Nottingham and described in detail by Hill et al., 2020 (see Fig. 1A). In brief, the system comprises an array of up to fifty second-generation QuSpin Inc. (Louisville, Colorado, U.S.A.) zero-field magnetometers (Osborne et al., 2018) housed within a custom-built, additively manufactured helmet (Added Scientific Ltd., Nottingham, U.K.) (Fig. 1B). The additive manufacturing process means that the OPM locations and the orientations of the sensitive axes, relative to the helmet, are known accurately. Whilst in principle each OPM provides two sensitive axes, only fields orientated (approximately) radial to the head were measured. The magnetometer data were recorded using a National Instruments (NI, Austin, Texas, U.S.A.) digital acquisition system (DAQ), controlled using LabVIEW (NI, Austin, Texas, U.S.A.) at 16-bit resolution and a sampling rate of 1200 Hz. The system is housed within an OPM-optimised MSR (MuRoom, Magnetic Shields Ltd., Kent, U.K.), which provides an open scanning environment. The participant was positioned such that their head was within the central region of the room, where the remnant magnetic field and magnetic field gradient are <2 nT and <2 nTm^{-1} following degaussing (Altarev et al., 2015; Hill et al., 2020).

Bi-planar coils

The two planes of the bi-planar coil system (Holmes et al., 2018) were placed on either side of the participant (Fig. 1C). The system in use consists of seven distinct coil elements each designed to generate one of α_1 to α_7 in the magnetic field model (note that a coil corresponding to the eighth component in our model, i.e. α_8, was unavailable at the time of these experiments). The coil planes are separated by 1.5 m, such that the head is located within the central volume. Coil currents are controlled using a voltage generated by a 16-bit digital-to-analogue converter interfaced with the DAQ via LabVIEW. These voltages are passed through a series of low-noise coil drivers provided by QuSpin (http://quspin.com/low-noise-coil-driver/) before being sent to the bi-planar coils. A resistor is added in series with the coils to ensure the magnetic field generated per unit voltage is within an appropriate range of approximately ±1 nTV^{-1}. This gives rise to ~0.25 fT magnetic field noise, to which the OPMs are insensitive.

Dynamic stabilisation

A reference array, comprising three, first-generation QuSpin OPMs, was placed in a fixed, orthogonal arrangement behind the participant's head, more than 10 cm from the helmet to prevent any collisions during mapping movements (see Figure B1A). In previous work, this reference array was used to map the remnant magnetic field; however, this method was limited in terms of the number of spatial field components that could be calculated, and the accuracy of the resulting values. Here, instead, we used the reference array for dynamic stabilisation of changes in the uniform components of the remnant magnetic field. Outputs of the reference magnetometers were input to a high-speed (60 Hz), PI controller implemented in LabVIEW, which calculates compensation currents that are fed back to the bi-planar coils. This, in turn, generates temporally changing fields that dynamically compensate <3 Hz changes in the three uniform components of the magnetic field (Holmes et al., 2019). In practice, the user specifies a desired 'set-point' at which the OPM outputs are held. This is unlikely to be zero-field, but the process acts to stabilise the uniform background magnetic field to prevent low-frequency changes that would otherwise cause the field to 'drift' over time, and so reduce the accuracy of our mapping and degrade the quality of the nulling (see Appendix B).

Head tracking

Tracking of participants' head motion was performed using an OptiTrack V120:Duo camera (NaturalPoint Inc., Corvallis, Oregon, U.S.A.), which facilitates six degrees of freedom (6-DoF) tracking of the centre of mass of a series of infra-red (IR) reflective markers, to sub-millimetre and sub-degree precision at a frame rate of 120 Hz. Motion tracking data were recorded using the NaturalPoint Motive software platform. Control of Motive from MATLAB (MathWorks Inc., Natick, Massachusetts, U.S.A.) was facilitated by the NaturalPoint NatNet SDK software. Six IR-reflective markers were attached to known locations on the OPM-MEG helmet to facilitate tracking of head movements and, by extension, sensor movements (since the locations of the sensors relative to the helmet are known from the additive manufacturing process). Six additional markers were added to one of the bi-planar coils to construct a stationary plane of reference (see Fig. 1C). The OptiTrack camera was positioned such that all twelve markers were visible when the participant was facing the camera. These two groups of six markers were then used to form rigid bodies, enabling tracking. During participant movement, the helmet rigid body could be accurately tracked by the Motive software provided at least three of the six markers were visible.

Data collection

Eight, head-mounted sensors, roughly positioned at the front, left, right, and top of the helmet (see inset diagram of Fig. 1C), were chosen to sample the background magnetic field. These OPMs were 'field-zeroed' (the process in which the on-sensor coils within each OPM are used to zero the field across its vapour cell) and calibrated after dynamic stabilisation of the background magnetic field had been initiated.

The participant was instructed to move their head for 60 s in order to rotate and translate the head-mounted sensors about and along three orthogonal axes, to ensure comprehensive sampling of each of the magnetic field components. The magnetometer and motion tracking data were simultaneously collected and synchronised using a DAQ trigger channel controlled by MATLAB, to indicate that Motive had started recording.

Two participants took part in this study. Both gave written informed consent, and the study was approved by the University of Nottingham Medical School Research Ethics Committee. Data are available upon reasonable request from the corresponding author.

3.2. Field characterisation using the model

The above process results in two separate (synchronised) datasets; magnetic field data recorded by the OPMs, and the movement data recorded by the OptiTrack camera. We used an affine transform to define the location and movement of the helmet in the coordinate frame of the bi-planar coils (which itself was made possible by the markers on the coil plane). The field model was also generated in this same frame of reference. In the motion data, there were a small number of frames in which the cameras failed to record the position of the helmet. Since a minimum of three markers must be visible to enable optical tracking, if the cameras lost sight of four of the six helmet markers due to the limited field of view of the OptiTrack Duo within the MSR, the rigid body position could not be tracked and an 'empty frame' was recorded in the motion data. In such empty frames, missing data were replaced by equivalent data from the previous frame.

Magnetometer field measurements were defined relative to the value measured at the start of the experiment (i.e. we subtracted the magnetic fields measured at the first time point from all subsequent time points). This was to ensure that the measured data represent the change in magnetic field due to the measured motion. Magnetometer data were down-sampled to 120 Hz to match the sampling frequency of the motion data. Both the magnetometer and motion datasets were then low-pass filtered using a finite impulse response filter of order 500, with a cut-off frequency of 10 Hz. (We assumed that motion would be in the 0–10 Hz range.)

Once processed, the magnetometer and motion data were used to construct the linear matrix equation characterised by Eq. (9). The motion data were used in Eqs. (7) and (8) to calculate $\mathbf{B}_{\text{mat}}$, which contains the simulated change in magnetic fields from unit-weighted field components over time caused by the changes in position and orientation. The processed magnetometer data were used to form the target field vector $\boldsymbol{b}$, and the coefficients of the magnetic field model, $\boldsymbol{\alpha}$, that best map $\mathbf{B}_{\text{mat}}$ to $\boldsymbol{b}$ were obtained by calculation of the pseudo-inverse of $\mathbf{B}_{\text{mat}}$. All calculations were implemented using bespoke code in MATLAB. The resulting parameters completely describe the spatially uniform and linear gradient terms of the temporally static (i.e. DC) magnetic field. Recall that any drift (over time) is already accounted for by the dynamic stabilisation process, meaning that removal of this DC component should leave the system sitting in a zero magnetic field environment.

3.3. Field nulling

In order to null the remnant magnetic field, we need to feed the corresponding coefficients, calculated using the model, into the bi-planar coil system to generate a magnetic field equal and opposite to that measured. In theory, appropriate coil currents could simply be estimated from the known coil efficiencies. However, in practice, the presence of high-permeability materials used in the walls of the MSR distort the spatial variation of the fields produced by the coils and a failure to take this into account would lead to sub-optimal nulling. For this reason, we used a data-driven approach in which the strength and spatial profile of the (distorted) magnetic field patterns produced by the coils, over the array of OPMs, was measured. This was then used to inform our choice of coil currents.

We defined a coil calibration matrix $\boldsymbol{C}$, formed of 7 columns (one column per coil element) and 8 rows (one row per magnetic field component, α_1 through α_8). The elements of this matrix characterise the amount of each of the eight components of magnetic field that is generated by a unit current applied to each coil. The coil calibration matrix was defined *a priori*, using 47 OPMs to measure the change in magnetic field produced by a series of known currents applied to the seven coil elements. The OPMs were positioned within the rigid helmet to provide comprehensive coverage, and the helmet itself was placed within the central volume of the coils and MSR, where the head of the participant would be located. As before, the position of the helmet relative to the bi-planar coils was recorded using the OptiTrack camera. The measured magnetic field data at the known, fixed, sensor positions and orientations generated by coil currents were then fitted to our magnetic field model to calculate the elements of $\boldsymbol{C}$.

Following calculation of the coil calibration matrix and the identification of the remnant magnetic field coefficients via the field mapping process, a linear matrix equation

$$\boldsymbol{C}\boldsymbol{i} = -\boldsymbol{\alpha}_t, \tag{10}$$

is generated to find optimal coil currents for nulling. Here, $\boldsymbol{i}$ is a column vector containing the 7 coil currents and $\boldsymbol{\alpha}_t$ is a column vector containing the 8 coefficients found following field mapping. Coil currents that best produce the required magnetic field components are found by identifying the pseudo-inverse of the matrix $\boldsymbol{C}$. Note that we have an underdetermined system since our coil array is missing one element; in order to ensure optimal compensation of the 7 components for which we do have a distinct element, we artificially set the value of α_8 in $\boldsymbol{\alpha}_t$ to zero (in order to avoid small contributions to α_8 from each coil element impacting the calculation). To null the remnant magnetic field, dynamic stabilisation was briefly paused and coil currents held at the final value computed by the controller. The currents calculated via Eq. (10) were then added to the dynamic stabilisation currents to remove the DC component. Dynamic stabilisation was then reinitiated. This process takes <1 s and so field drift in this short time-window was minimal.

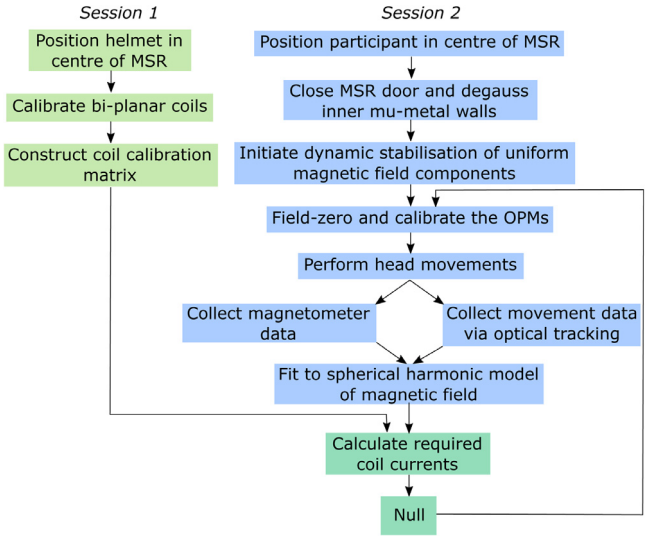

Fig. 2. Schematic overview of the field nulling process.

3.4. Overview

An overview of the entire process is given in Fig. 2. The field nulling procedure itself takes approximately 4 min to carry out, including 1 min to record the data, and a further 3 min to complete the fit and feed the resulting data back to the bi-planar coils.

4. Mapping known fields

In our first experimental demonstration, we aimed to determine whether the model could accurately compute the known magnitude of a background field change that was deliberately applied inside the MSR.

4.1. Method

A single participant took part in this experiment. The additively manufactured helmet containing 40 OPMs was mounted on the head. All sensors were switched on and functioning, though only eight OPMs were involved in the field mapping process (as described in Section 3.1), as this was sufficient to map the remnant magnetic field comprehensively while minimising the time taken to compute model coefficients. The participant was seated with their head positioned approximately centrally in the MSR and at the isocentre of the bi-planar coils. The MSR door was closed and the internal mu-metal walls of the MSR degaussed. Dynamic stabilisation was applied and the background magnetic field was mapped via the procedure outlined in Section 3. To sample the background magnetic field, the participant moved their head such that they completed rotations about each Cartesian axis in turn, followed by translations along each axis. This series of movements was performed twice within the 60 s recording. Once the sequence of movements had been completed, the coefficients that described the remnant magnetic field and its linear gradients were calculated.

Following the initial field map, an offset magnetic field or magnetic field gradient was applied using a single element of the bi-planar coils: the coil current required to generate the desired magnetic field, or magnetic field gradient, was calculated using the appropriate diagonal element of the coil calibration matrix $\boldsymbol{C}$. Once the offset had been applied, the field mapping procedure was repeated. This process was repeated for each of the seven components in the field model for which we have dedicated coils, using offsets of 0.5 and 1 nT or nTm^{-1}. For each component, and field strength, we repeated the experiment three times. Field offsets were determined by subtraction of the model coefficients calculated before and after the offset was applied. All values were averaged over the three repeat runs and the standard deviation computed.

4.2. Results

Data for a single representative run are shown in Fig. 3A. Here, the line plots show magnetometer data (in blue) measured during the sequence of participant movements. The fit to these fields, based on the motion tracking data and field model, is shown in red. Notice that in this case the model fits well to the data, suggesting that the magnetometer data are dominated by field changes due to movement (as distinct from other low-frequency magnetic artefacts (see Discussion)). The three inset plots show the locations of the OPM array (in blue) relative to its location at the start of the experiment (in grey), at three different timepoints during the sequence.

Fig. 3B shows the coil calibration matrix $\boldsymbol{C}$, in units of nTV^{-1} or $\mathrm{nTm}^{-1}\mathrm{V}^{-1}$ (note that in the matrix, for visualisation, different scales are used for components of the matrix that relate to uniform magnetic fields and magnetic field gradients). The matrix depicts the field generated at the helmet by pulsing a coil with a unit voltage generated by the DAQ. As expected, each coil maps almost exclusively to a different component in our field model, but with some small, off-diagonal elements that are likely caused by field interactions with the MSR (Holmes et al., 2019).

Fig. 3C and D show results of mapping known field offsets via our head movement-based mapping procedure. Fig. 3C shows results for a field of 0.5 nT or gradient of 0.5 nTm^{-1}. Fig. 3D shows results for a field of 1 nT or gradient of 1 nTm^{-1}. In both cases, the diagonal elements of the matrices are broadly consistent with the expected size of the applied magnetic field, showcasing the accuracy of the mapping procedure. In general, the accuracy of the uniform field components was higher than the accuracy of the gradients; this, we believe, is due to the scale of the applied fields. For example, a uniform magnetic field of 0.5 nT would generate a measured OPM signal change of order ~0.1 nT for the scale of motion carried out by the participant (e.g. a 10° head rotation). However, a magnetic field gradient of 0.5 nTm^{-1}, would only produce a signal change of ~0.01 nT over the scale of motion carried out (e.g. a head translation of 2 cm). This means that field gradients are likely harder to fit. Nevertheless, the fitted values for the gradient fields remain reasonable. Data for all three repeats are shown in Supplementary Material Figure S1.

5. Magnetic field compensation

In our second demonstration, the aim was to show that we could not only accurately measure the amplitude of a DC magnetic field and its field gradient using the model, but also that we could feedback these fitted data to the bi-planar coils and consequently null the measured field; this would enable suppression of artefacts caused by head movement.

5.1. Method

The participant sat inside the MSR wearing the additively manufactured rigid helmet containing 40 OPMs, and the internal walls of the room were degaussed. Following this, dynamic stabilisation was activated. The unknown remnant DC magnetic field inside the MSR was then mapped, again with the participant completing a sequence of rotations and translations of the head to sample the field variation. Once the field had been mapped, and coefficients calculated, the seven coil currents required to best produce the equal and opposing magnetic field were found using the coil calibration matrix. These currents were then applied to the bi-planar coils, as outlined in Section 3.3.

After this first nulling process was completed, the magnetic field that remained was then mapped again, the coefficients calculated and updated currents applied to the coils to test whether this field could be further reduced. Finally, field mapping was performed once more to determine the coefficients of the magnetic field achieved by this further

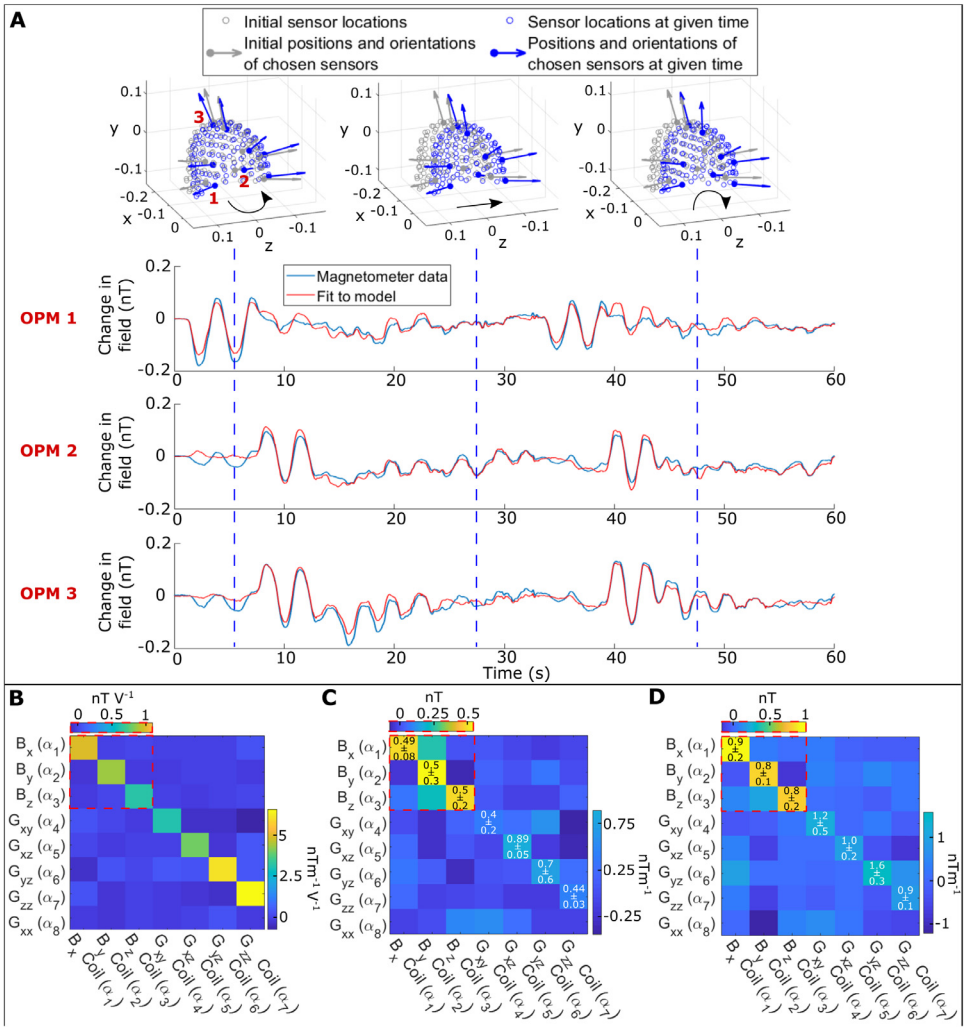

Fig. 3. Mapping known fields. A) Representative data taken from three OPMs during a sequence of head movements. The blue line shows the magnetometer data. The red line shows the model fit. The three inset images show the position of the sensors (blue) relative to their initial position (grey) at three moments in time during the sequence of movements. B) Coil calibration matrix. Values represent the effect of pulsing each of the 7 available coils with a unit voltage. Notice that for visualisation, values for uniform magnetic field and field gradient are shown on different scales. As expected, each coil largely affects a single component of the model. C) The results of mapping known fields: a known magnetic field of 0.5 nT, or a field gradient of 0.5 nTm^{-1} was generated by each coil. The values in the matrix show the model fit to those fields. The numbers show how accurate the model fit was in terms of mean and standard deviation across runs (i.e. numbers along the diagonal should be close to 0.5). D) Equivalent to (C) but for known fields/gradients of 1 nT and 1 nTm^{-1} (numbers along the diagonal should be close to 1). See also Supplementary Material Figure S1. (For interpretation of the references to colour in this figure legend, the reader is referred to the web version of this article.)

compensation. Two participants took part in the experiment and each completed five independent experimental runs.

In order to assess whether or not the remnant magnetic field had been reduced, we employed two summary measures. The first was simply the magnitude of the fitted coefficients of magnetic field before and after the nulling procedure; we expected these to decrease. To provide simple representative values, we calculated both the Euclidean norm of the uniform field vector and the Euclidean norm of the field gradient coefficients. The second measure was the standard deviation of the measured magnetometer data. Here we reasoned that, assuming head movements were similar before and after nulling, and that the measured fields were dominated by the movement artefact, the standard deviation of the measured fields should be reduced following nulling. Standard deviation of the measured field variation was calculated for the eight OPMs involved in field mapping, and the result averaged across sensors.

We also calculated the Pearson correlation coefficient between the measured magnetometer data and the model fit; note that values close to 1 represent high confidence that the model was fitting the data accurately, and consequently that the magnetometer data were dominated by the motion artefact. Finally, we took data from the OptiTrack camera and calculated the standard deviation of the motion parameters (3 rotation and 3 translation) in order to summarise the extent to which the two participants moved, and the similarity of that movement across experimental runs.

5.2. Results

Fig. 4A shows an example data set; data acquired during movement are shown from 3 representative OPMs, with their locations in the helmet given in the central panel. The blue, orange and yellow lines respectively, show data prior to nulling, after the first nulling currents were applied, and after the second, updated currents were applied. As expected, the variance of the measured signal decreases, suggesting that the nulling procedure is reducing the effect of movement in a background magnetic field. In this single example, the fitted uniform magnetic field magnitudes were 1.42 nT before nulling, 0.46 nT after the first null and 0.27 nT after the second null. The norm of the magnetic field gradients was estimated as 1.79 nTm^{-1} before nulling, 1.52 nTm^{-1} after the first null and 0.84 nTm^{-1} after the second null.

Fig. 4B and C show the results across all five runs for participants 1 and 2, respectively. In both Fig. 4B and C, the upper left bar chart shows the Euclidean norm of the three uniform magnetic field components before and after nulling, averaged over experimental runs (individual data points for each experiment are given as black crosses). The average norm of the magnetic field gradient components (not including α_8) is shown in the upper right bar chart. For participant 1, the Euclidean norm of the uniform field was reduced from $1.3(+0.5, -0.2)$ nT to $0.27(+0.09, -0.08)$ nT (mean and range of measured data), representing a 13 dB reduction. For participant 2, the uniform field was reduced from $1.4(+0.2, -0.3)$ nT to $0.31(+0.11, -0.05)$ nT; also a 13 dB reduction. Reduction of the gradi-

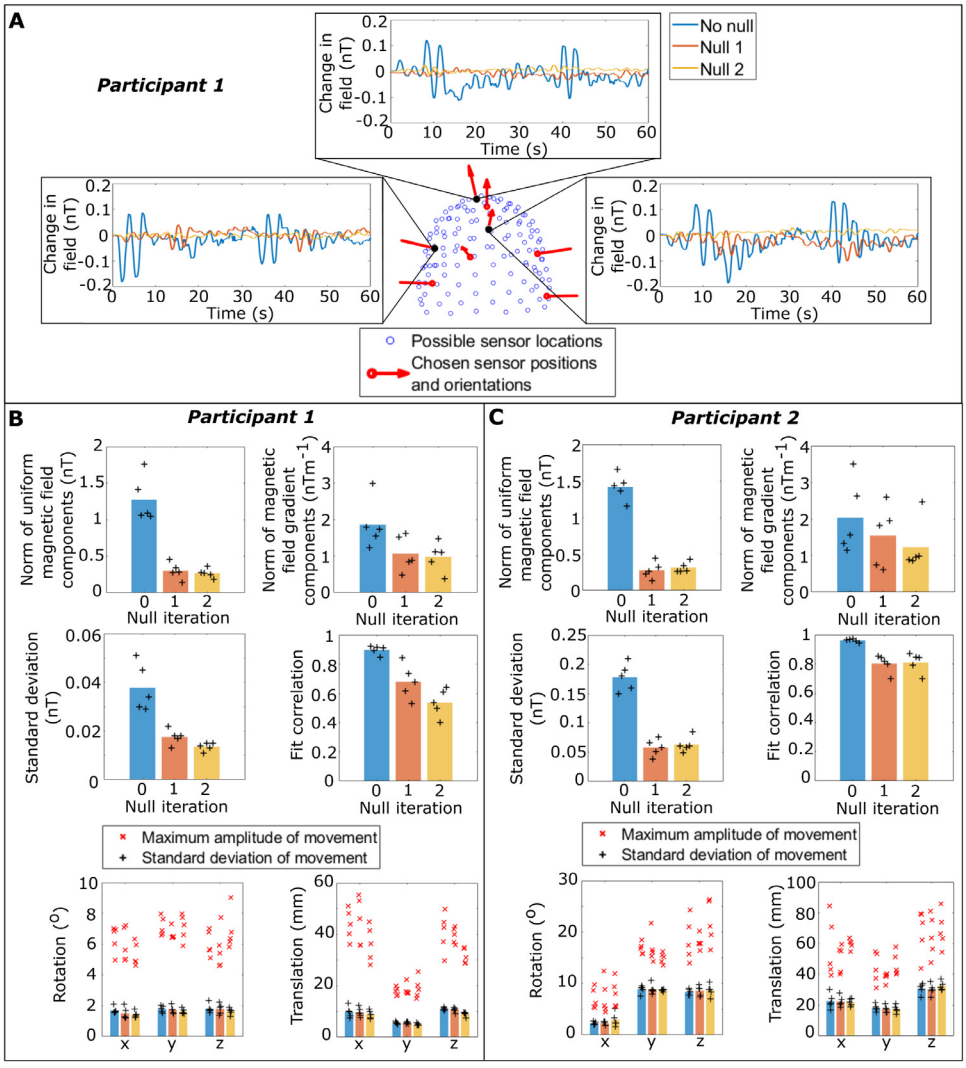

Fig. 4. Field nulling A) Example magnetic field data measured from three selected OPMs during head motion. The OPM locations are shown on the central panel in black; red arrows show sensor orientations. In the field plots, measured fields prior to nulling are in blue. Fields after one null are shown in orange and after two nulls are shown in yellow. Deflections in these data are largely the result of movement in the background field. Notice how this movement artefact is diminished after nulling. B) Summary of results for participant 1: The upper panel shows the norm of the uniform magnetic field (left), and norm of the magnetic field gradients (right) before and after nulling. The bars represent the mean value across five repeat experiments, and the individual data points are shown as black crosses (+). The centre panel shows the standard deviation of the field measurements (left) and correlation to the model fit (right) again before and after nulling. Finally, the lower panels show movement parameters (left and right panels show rotation and translation, respectively). Here, the black crosses show the standard deviation of movement from the equilibrium (mean) position in each experiment, and the mean value is given by the bars. The red crosses (x) show the maximum movement recorded in each experiment. C) Equivalent to (B) for participant 2. (For interpretation of the references to colour in this figure legend, the reader is referred to the web version of this article.)

ents was less dramatic: we estimated that the norm of the gradient fell from $1.9(+1.1, -0.6)$ nTm^{-1} to $1.0(+0.5, -0.6)$ nTm^{-1} after two nulls in participant 1, and from $2.0(+1.5, -0.9)$ nTm^{-1} to $1.2(+1.2, -0.37)$ nTm^{-1} in participant 2.

In agreement with these data, we saw a similar drop in the standard deviation of the time-courses of the magnetometer data. The centre left panels of Fig. 4B and C show the standard deviation averaged across sensors (given by the crosses) and then across experimental runs (given by the bars), before and after nulling for each participant. The average standard deviation of the artefact was reduced from $38(+13, -9)$ pT to $14(+2, -3)$ pT after two nulls for participant 1 and $178(+32, -28)$ pT to $63(+22, -14)$ pT for participant 2 (note here that movement was more extensive for participant 2, hence the larger recorded artefact).

The centre right bar charts in Fig. 4B and C show the correlation to the magnetic field model; values close to 1 indicate high confidence in the fit. These values were averaged across sensors (shown by the crosses), and then across runs (shown by the bars). As might be expected, we observe a decrease in correlation as the field is nulled; this likely reflects the fact that the magnetometer data is becoming dominated by sources of artefact other than movement. Finally, the lower panels in Fig. 4B and C show the range of rotations and translations performed by the participant during each field mapping procedure. The bars show the standard deviation averaged across the five experiments; the red crosses show the maximum movement in each experiment. Importantly, whilst the two participants carried out different movements, those movements were similar across repeats for the individual participants.

6. MEG demonstration

The final experimental demonstration aimed to show that, in a real MEG experiment, our nulling process would reduce the effect of motion artefact and therefore improve the quality of MEG data recorded in the presence of participant movement. To this end, we undertook a visual steady-state evoked response experiment.

6.1. Method

Two participants took part in the experiment. The participant was seated inside the MSR, ~80 cm from a back-projection screen. The visual stimulus comprised a centrally-located green square on a black background, which was presented by projection, with a visual angle of 9° In a single trial, the square flashed at 6 Hz for 10 s, preceded by a 10 s rest period in which only a black screen was shown. This was repeated 25 times giving a total experimental length of 500 s. We expected to measure a driven, 6 Hz steady-state response in occipital sensors during the active periods.

Again, the participant wore the additively manufactured helmet containing 40 OPMs. Once the helmet was mounted, the MSR door was

closed and the internal walls degaussed. During the recording, the participant was instructed to focus on the square whilst performing head movements, such as nods and shakes of the head. The experiment was first performed without background magnetic field compensation (the norm of the uniform magnetic field components was 1.25 nT for participant 1 and 1.40 nT for participant 2). Our nulling procedure was then applied, and the experiment repeated (participant 1: 0.13 nT, participant 2: 0.46 nT). Participant movements were monitored throughout using the OptiTrack camera, in order to assess the equivalency of movement during the first and second (pre- and post-nulling) runs.

We expected the magnetic field artefacts generated by continuous head movements to manifest at low frequencies, with the majority of the interference between 0 and 2 Hz. A 6 Hz flicker frequency was chosen such that the response would not be masked by movement artefact in the case where no field nulling was applied. This would enable comparison of the magnitude of the low frequency movement artefact with and without our field mapping and nulling method. We also hypothesised that the 6 Hz peak would have a larger SNR when data were recorded with the field nulling procedure applied.

Raw OPM data, collected at 1200 Hz, were filtered by a low-pass, finite impulse response filter of order 50 with a 10 Hz cut-off frequency. These time-series data were segmented into individual trials and then averaged in the time domain, prior to computation of the fast Fourier transform (FFT) of this averaged trial. The absolute value of the FFT was taken (1/10s = 0.1 Hz frequency resolution) and scaled to units of femtotesla to produce amplitude spectra. Separate spectra were derived for the stimulus 'on' and 'off' periods; this analysis was applied to each channel separately and an estimate of the SNR (defined as the height of the 6 Hz peak during the on period, divided by the height of the 6 Hz peak during the off period) was calculated for all channels.

6.2. Results

Fig. 5A shows results for the first participant, and Fig. 5B shows equivalent results for the second participant. In both cases, the upper panel shows the amplitude spectra computed for the active and rest periods separately, taken from the OPM that exhibited the largest, and most consistent, 6 Hz peak (the location of this sensor is marked on the inset diagram). Plot i) shows the case with no field nulling and ii) shows data with the bi-planar coils activated. Notice that significant artefacts are observed in both cases that manifest at very low (<2 Hz) frequency. However, these artefacts show a marked reduction in the case where field nulling was applied – providing evidence that they are generated by head movement in the background field. In the 0–2 Hz band, these data suggest that nulling affords a five-fold reduction of interference for participant 1, and a four-fold reduction for participant 2 (in both cases calculated as the integral of the signal without nulling between 0 and 2 Hz, divided by the equivalent integral with nulling). This is consistent with the decrease in field that we might expect from Fig. 4.

The two inset Figures in the upper panel show a zoomed-in plot of the 6 Hz peak. This peak is observable in all cases, but becomes more prominent after field nulling. Quantitatively, the SNR of the 6 Hz peak increased from 1.2 to 9.9 in participant 1, and from 1.6 to 11.0 in participant 2. We note, however, that the amplitude spectra corresponding to the experiments without field nulling feature a higher baseline, which increases the amplitude of the 6 Hz peak compared to the case with nulling applied. Specifically, linear trends present in the average trial time-course of the magnetometer data were also present in the average trial time-course of the motion data for each participant, suggesting these trends result from movement of the sensor through a non-zero magnetic field. The Fourier transform of these linear trends produce a 1/frequency contribution that interferes constructively with the 6 Hz neuronal peak and raises the baseline of the measurement (see Supplementary Material). Our field nulling technique does not affect the physiological signal strength at 6 Hz, but reduces the motion artefact that causes this constructive interference.

The data in the upper panel are from a single sensor. In order to get a more global picture of the improvement in data quality, the central panel shows sensor-space topographies detailing the difference in the magnitude of the 6 Hz peak between the active and rest periods, for all sensors. Given the nature of the stimulus, we would expect this difference to be most prominent in sensors covering the occipital lobe. This is largely the case, however a more focal response is observed in the case where field nulling is employed, suggesting that the spatial topography of the 6 Hz response is being degraded by the presence of the movement artefacts in the data.

Finally, the lower panels show the power spectral density (PSD) of the rotations (left) and translations (right) of the helmet recorded by the OptiTrack camera. The case with no field nulling is shown in blue and the case with field nulling is shown in orange. In participant 1, the data show similarly sized movements, with largely equivalent power spectra with and without nulling. For participant 2, whilst the magnitude of movement was largely similar, the frequency components post-nulling were missing the large peak at ~1.7 Hz. This is a potential confound since the participant clearly did not carry out the same movements in the two experiments.

7. Discussion

Recent years have shown that OPMs have the potential to revolutionise MEG as an imaging technology, with the promise of a wearable system that adapts to any head shape (Hill et al., 2019), enables movement during scanning (Boto et al., 2018), and provides higher sensitivity (Boto et al., 2017) with improved spatial resolution (Boto et al., 2019). However, this potential can only be realised if background magnetic fields can be appropriately controlled, and this proves a significant challenge. In this work, we have shown that even in an OPM-optimised MSR with extremely low (<2 nT) remnant fields, head movement generates significant artefacts, which manifest as low-frequency interference that obfuscates the MEG signal. To counter this effect we have introduced a field mapping technique in which participants move their head to sample background magnetic fields using scalp-mounted OPM sensors; resulting data are compared to simulations in order to derive coefficients representing the three uniform magnetic field components and five magnetic field gradient components in the vicinity of the head inside the MSR. We were able to show that this technique accurately reconstructed the magnitude of known offset fields. Moreover, by feeding these coefficients into a bi-planar coil system (Holmes et al., 2019, 2018) via a coil calibration matrix, we were able to reduce the uniform magnetic field from a magnitude of 1.3 ± 0.3 nT, to 0.29 ± 0.07 nT (mean ± standard deviation across both participants). This extremely low field is similar to other high performance magnetically-shielded environments (Altarev et al., 2014; Bork et al., 2001). Most importantly, we have shown that this magnetic field compensation, which was readily implemented in combination with dynamic stabilisation of temporal variations of the uniform field components, significantly reduces the motion artefact present in OPM-MEG data. Low-frequency artefact (0—2 Hz) was found to be reduced by a factor of five in a visual steady-state evoked response experiment using 6 Hz stimulation. We therefore suggest that this technique could be used in future OPM-MEG experiments to significantly improve the quality of data, especially in paradigms that encourage head movement.

Our previous OPM-MEG studies involving substantial participant movement (Boto et al., 2018; Hill et al., 2019; Roberts et al., 2019) were performed within a MSR that has a remnant magnetic field of ~30 nT (Vacuumschmelze, Hanau, Germany), and houses a cryogenic MEG system. The efficacy of coil systems to reduce MSR background magnetic fields in the range of 20–70 nT to <1 nT has been reported in previous papers (Borna et al., 2019; Holmes et al., 2019; Iivanainen et al., 2019). However, a MSR was recently installed at our institution with a comparatively lower remnant magnetic field of <2 nT, which is achieved by regular use of integrated degaussing coils (MuRoom, Magnetic Shields

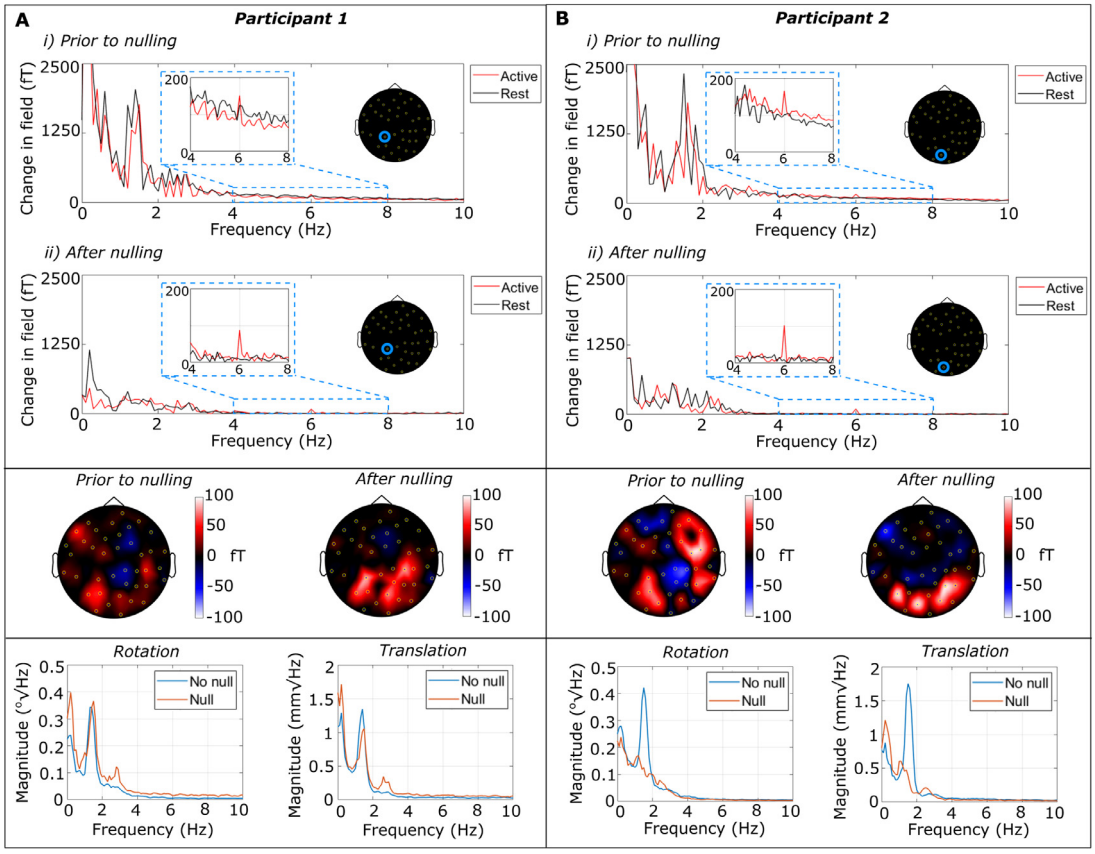

Fig. 5. . **MEG demonstration.** A) MEG data from participant 1. B) Equivalent data from participant 2. In both cases: upper panel – amplitude spectral density derived from trial-averaged data taken from the single channel with the most consistent 6 Hz response. Data from the active segment of the trial (i.e. when the stimulus is flashing) are in red and data from the resting segment are shown in black. Plot i) shows the case with no nulling applied and ii) shows the case with nulling. Notice the overall drop in low-frequency artefacts. The inset graphs show the same data, but focussing on the 4–8 Hz range (i.e. where we expect to see a 6 Hz neural response to the stimulus). In all cases the response is clear, but is more prominent when field nulling is applied. Centre panel – spatial topography of the difference in 6 Hz signal strength between stimulus on and off, plotted for all sensors. Note that we expect the strongest response in sensors covering the visual areas. Lower panel – power spectra of movement data showing rotations (left) and translations (right). Data without nulling shown in blue, and with nulling in orange. (For interpretation of the references to colour in this figure legend, the reader is referred to the web version of this article.)

Ltd., Kent, U.K.). Equivalent demagnetisation of the walls of a more conventional MEG MSR may achieve a similarly low remnant magnetic field (Voigt et al., 2013), however the required coils are not typically included during MSR installation, and fitting such coils to a room that has already been built would pose a significant challenge. Therefore, the commercial availability of a MSR that can readily provide such a low background magnetic field has positive implications for the future of OPM-MEG, however using electromagnetic coil systems to further improve upon this already low background magnetic field becomes more challenging.

In order to further suppress such a low remnant magnetic field, a high accuracy of characterisation of the field and its spatial variation is required. Previously, field mapping for OPM-MEG has been achieved using stationary reference arrays positioned close to (e.g. Borna et al., 2020) or on the head (e.g. Iivanainen et al., 2019). Our previous reference array approach sampled the full vector field at two locations behind the participant's head, yielding measurements of the three uniform magnetic field components and three of the five magnetic field gradients (Holmes et al., 2018). Increasing the number of reference sensors and sampling at more locations would improve this method, however it would also further enclose the scanning environment and so reduce the volume available for participant movement. Our new technique for mapping the remnant magnetic field via head movement has two distinct advantages: firstly, head-mounted OPMs sample the background magnetic field, meaning that the mapping is performed in the precise region encompassing the participant's head (rather than behind the head at the location of the reference array, for example). This makes the nulling more accurate. Secondly, in order to sample the remnant field, the OPMs are not required to measure an absolute field, but rather movement-induced field change. This leads to a more accurate characterisation, since measurement of absolute field by an OPM (or indeed any magnetometer) is often distorted, for example by small amounts of magnetisation in the sensor itself, which can lead to field offsets. The improvement of our present approach over our reference array findings can be quantified; in our previous approach, we achieved a magnetic field of 0.74 nT: rotation of a magnetometer by 10° in this field will generate an artefact of amplitude 0.14 nT. Rotation by the same amount in the magnetic field of 0.29 nT achieved here will generate a change of 0.055 nT – a reduction in artefact size by a factor of 2.5.

Despite offering improved characterisation of the remnant magnetic field for OPM-MEG, our head-movement based sampling technique does pose some disadvantages that should be considered. Firstly, we have assumed that the measurements made by the OPMs during the head movement procedure are dominated by motion artefacts. Theoretically, this should be the case (e.g. brain activity is much smaller (and typically higher frequency) than the movement artefact and so should not impact the fitted data). However, at the time of writing there is a known problem with interference due to the cables used in the QuSpin sensors – specifically that relative movement of the OPM cables generates low-frequency artefacts that correlate with the movement data. Whilst this

problem will be corrected in future revisions of the cables, at present it is a source of error that likely contributes to inaccuracies in the fit coefficients (and consequently the efficacy of the nulling procedure). Second, the field nulling process is extremely sensitive to the accuracy of the measured sensor positions and orientations. Here, we employed an OptiTrack Duo camera placed in front of the participant, and tracked the movement of six markers on the front of the helmet relative to six markers that were placed on the coils. Whilst this approach works well, it is possible that improved motion tracking would yield more accurate data. Specifically, since the OptiTrack Duo has only two cameras, the field of view was limited to markers on the front of the helmet. Any inaccuracy in characterisation of these markers at the front of the head would likely be amplified at the back of the head, resulting in degradation of the quality of the fit to data acquired towards the rear of the head. Additionally, the limited field of view meant that reference points could only be placed on a single coil. Any slight inaccuracy in coil placement could then generate a systematic error in reconstructed head position. These inaccuracies in head tracking may have led to errors in the obtained coefficients of magnetic field. An improved optical tracking system with multiple cameras placed around the participant would expand the field of view, enabling tracking of markers more evenly spread across the helmet as well as additional stationary reference points. This would likely lead to an improved accuracy of field characterisation and consequently improved field nulling.

The significant problem of field drift was ameliorated by the use of dynamic stabilisation. Specifically, a reference array was used to measure temporal changes in the three uniform magnetic field components. These dynamic changes were then fed back to the coils in order to generate equal and opposite field shifts. This allowed us to 'lock' the fields such that field drift over the course of an experiment, and the remnant DC field inside the MSR, could be separated. In other words, it allowed us to remove temporal field variation prior to mapping, and nulling the DC field. This was an essential step in order to achieve the low fields shown in Fig. 4, and the reduction of motion artefact in MEG data shown in Fig. 5. Our dynamic stabilisation procedure is effective: it allows magnetic fields to remain stable to within 0.2 nT over a time period of 20 min (see Appendix B). Again, however, there is some room for improvement in future iterations of the technique. Specifically, in the present work we only dynamically stabilised the three uniform magnetic field components; if we were to also dynamically stabilise magnetic field gradients, this would likely lead to more accurate characterisation of the parameters in the model relating to gradient fields, and consequently lead to more accurate nulling. Possibly the use of a more extensive reference array might be of some benefit, or even incorporating the dynamic stabilisation into the sensors on the helmet (Iivanainen et al., 2019) (though this would require separation of the field change due to movement, and that due to drift).

Despite some of the problems mentioned above, the final remnant magnetic fields that we were able to achieve using this method were extremely low. This resulted in MEG data in which motion artefact was reduced five-fold by application of our technique. This, we believe, will be of significant importance if we are to move forward and realise the potential of a wearable MEG system. Head movement typically manifests at low frequency, and so the technique reported is likely to become important in studies of either sustained responses (DC field shifts for the duration of stimulation), delta, or theta oscillations. Given the apparently important role of frontal midline theta oscillations in cognition (e.g. (Brookes et al., 2011)), and the purported clinical relevance of delta oscillations in, for example, patients with mild traumatic brain injury (Huang et al., 2017), it is likely that removal of head movement artefacts will become increasingly important for OPM-MEG. In addition, whilst in healthy participants head movement artefacts may be low-frequency, in patients (e.g. an epilepsy patient suffering a seizure) or in specific participant groups (e.g. infants or patients with movement disorders), it is conceivable that head movement may begin to manifest at higher frequency, where it could overlap with alpha or beta oscillations, for example. Here again, the importance of suppressing this effect at source by optimally minimising the background magnetic field will be of great importance.

Finally, there are other refinements that could be made to improve this technique. Firstly, we have concentrated on spatially-uniform magnetic field and linear magnetic field gradient terms, but there is no reason why the model cannot be extended to fit higher-order spherical harmonics. Here, we limited the fit because our coil array was confined to only generating uniform magnetic fields and magnetic field gradients. However, new types of coil design and the inclusion of higher-order terms have the potential to offer significant improvements. Secondly, the method of coil calibration that we used was somewhat limited to a data-driven approach. However, if the interactions between the magnetic fields generated by our coils and the mu-metal walls of the MSR are properly taken into account (e.g. via appropriate evaluation of the boundary conditions imposed on the magnetic field by high-permeability materials (Holmes et al., 2019; Packer et al., 2020; Zetter et al., 2020)) it is possible that improved coil calibration may make nulling more effective. Finally, from a practical point of view, the nulling procedure could be made quicker via the use of less data, and by more detailed instructions of how to carry out the head motion. This may become important, particularly for some participant groups who may find it difficult to carry out the series of head translations and rotations required.

8. Conclusion

In this paper we present a new way to map background magnetic field and magnetic field gradient, using data sampled by an on-scalp sensor array as a participant moves their head through the remnant magnetic field. By feeding back the fit coefficients of magnetic field to an electromagnetic coil array, we were able to effectively minimise this magnetic field. Results show that we can null the field inside an OPM-optimised MSR to a level of <0.3 nT. This, in turn, offers a marked reduction in the motion artefact present in OPM-MEG data. This method will be important in future studies where OPM-MEG is used, particularly when measuring neuromagnetic effects at low frequency, and also in cases where natural head movement is encouraged.

Declaration of Competing Interest

V.S. is the founding director of QuSpin Inc. QuSpin built the sensors used here and advised on the system design and operation, but played no part in the subsequent measurements or data analysis. This work was funded by a Wellcome award, which involves a collaboration agreement with QuSpin. E.B., D.W. and M.J.B. are directors of Cerca Magnetics Ltd., a newly established spin-out company whose aim is to commercialise aspects of OPM-MEG technology. D.W. is the managing director of Magnetic Shields Ltd. Bi-planar coils for field nulling are available as a product from Cerca Magnetics Ltd., sold under license from the University of Nottingham.

Credit authorship contribution statement

Molly Rea: Conceptualization, Methodology, Software, Formal analysis, Data curation, Writing – original draft. **Niall Holmes:** Conceptualization, Methodology, Software, Formal analysis, Data curation, Writing – original draft. **Ryan M. Hill:** Conceptualization, Methodology, Software, Writing – review & editing. **Elena Boto:** Conceptualization, Methodology, Writing – review & editing. **James Leggett:** Conceptualization, Methodology, Writing – review & editing. **Lucy J. Edwards:** Methodology, Writing – review & editing. **David Woolger:** Methodology, Writing – review & editing. **Eliot Dawson:** Methodology, Writing – review & editing. **Vishal Shah:** Methodology, Writing – review & editing. **James Osborne:** Methodology, Writing – review & editing. **Richard Bowtell:** Conceptualization, Methodology, Software, Formal

analysis, Writing – review & editing, Supervision, Funding acquisition. **Matthew J. Brookes:** Conceptualization, Methodology, Software, Formal analysis, Writing – review & editing, Supervision, Funding acquisition.

Data and code availability

Data are available from the corresponding author on request, under a data sharing agreement. Some aspects of code are commercially sensitive, they can be shared with academic partners under a non-disclosure agreement.

Acknowledgements

We express our thanks to Benjamin Wittevrongel from the Department of Neurosciences at K.U. Leuven, Belgium, for providing the paradigm used here in the MEG demonstration. This work was supported by the UK Quantum Technology Hub in Sensing and Timing, funded by the Engineering and Physical Sciences Research Council (EPSRC) [EP/T001046/1], and a Wellcome Collaborative Award in Science [203257/Z/16/Z and 203257/B/16/Z] awarded to Gareth R. Barnes, R.B. and M.J.B. For the purpose of open access, the author has applied a CC BY public copyright licence to any Author Accepted Manuscript version arising from this submission. Funding from the EPSRC and the Medical Research Council (MRC) [EP/L016052/1] provided a Ph.D. studentship for M.R. via the Oxford Nottingham Biomedical Imaging Centre for Doctoral Training.

Supplementary materials

Supplementary material associated with this article can be found, in the online version, at doi:10.1016/j.neuroimage.2021.118401.

Appendix A. B_{mat} matrix

The matrix, $\mathbf{B}_{mat}$, was constructed to characterise the change in magnetic field predicted by our model due to movement through a 1 nT or 1 nTm^{-1} magnetic field or magnetic field gradient in each component, respectively. By evaluation of the pseudo-inverse of this matrix, the coefficients that best characterised the remnant magnetic field inside our MSR could be determined in accordance with the following equation:

$$\mathbf{B}_{mat}\boldsymbol{\alpha} = \boldsymbol{b}, \tag{A1}$$

where $\boldsymbol{\alpha}$ is a column vector containing the eight coefficients of magnetic field and $\boldsymbol{b}$ is the target field column vector, which contains the magnetic fields measured by the OPM array. Here we describe the construction of $\mathbf{B}_{mat}$ in more detail.

Using the rotation and translation data for each sensor obtained during the field mapping process Fig. A1A), we simulate the change in magnetic field measured by each sensor as it moves through a background magnetic field consisting of a unit contribution in one component of our model. The measured field is calculated by evaluating Eqs. (7) and ((8) for each sensor at each time-point, using the measured sensor position, (x, y, z), and orientation, $\boldsymbol{e}$. This is repeated for each of the eight components in our model.

We construct the matrix, $\mathbf{B}_{mat}$, such that it has eight columns, each corresponding to a component of magnetic field or magnetic field gradient in our model. Each row corresponds to one sensor at one time-point, and contains the modelled change in magnetic field for each component. In the case of a single sensor, each column of $\mathbf{B}_{mat}$ forms a modelled sensor time-course, which characterises the change in measured field experienced by that sensor due to its movement through the corresponding unit magnetic field or field gradient component, as shown in Fig. A1B. The corresponding $\mathbf{B}_{mat}$ for this sensor is shown in Fig. A1C.

For an array of N OPMs whose movements are measured over T time-points, $\mathbf{B}_{mat}$ has $T \cdot N$ rows. The target field column vector, $\boldsymbol{b}$, also has $T \cdot N$ rows while the column vector of coefficients, $\boldsymbol{\alpha}$, is unchanged. These are arranged as follows:

$$\mathbf{B}_{mat} = \begin{pmatrix} B_{1,1,\alpha_1} & \cdots & B_{1,1,\alpha_8} \\ \vdots & \ddots & \vdots \\ B_{1,N,\alpha_1} & \cdots & B_{1,N,\alpha_8} \\ \vdots & \ddots & \vdots \\ B_{T,N,\alpha_1} & \cdots & B_{T,N,\alpha_8} \end{pmatrix}, \quad \boldsymbol{\alpha} = \begin{pmatrix} \alpha_1 \\ \vdots \\ \alpha_8 \end{pmatrix}, \quad \boldsymbol{b} = \begin{pmatrix} b_{1,1} \\ \vdots \\ b_{1,N} \\ \vdots \\ b_{T,N} \end{pmatrix}. \tag{A2}$$

The coefficients of magnetic field were found using the pseudo-inverse of $\mathbf{B}_{mat}$. If the participant made no movements at all then the matrix would be singular, but in practice, with proper instruction, this is very unlikely.

Appendix B. Dynamic stabilisation

In order to ensure accurate mapping of the remnant magnetic field inside the MSR it was necessary to dynamically stabilise the uniform components of the field during experiments. Here we provide a simple demonstration to highlight the importance of dynamic stabilisation.

An array of 40, second-generation QuSpin OPM sensors were placed inside the rigid helmet, which was positioned in the MSR at the centre of the bi-planar coils and close to a reference array containing three OPMs. The position and orientation of the reference sensors with respect to the head and the coils is shown in Fig. B1A. The internal mu-metal walls of the MSR were degaussed and 'empty room' magnetic field data were recorded for 20 min. The experiment was repeated with and without dynamic stabilisation.

Fig. B1B shows sensor time-course data collected from the OPM array when dynamic stabilisation was not used (left), and the equivalent data when dynamic stabilisation was active (right). Figure B1C shows the median value (across sensors) of the power spectral density (PSD, computed by segmenting time-course data into 10 s chunks and applying a flat-top window before taking the fast Fourier transform of each chunk

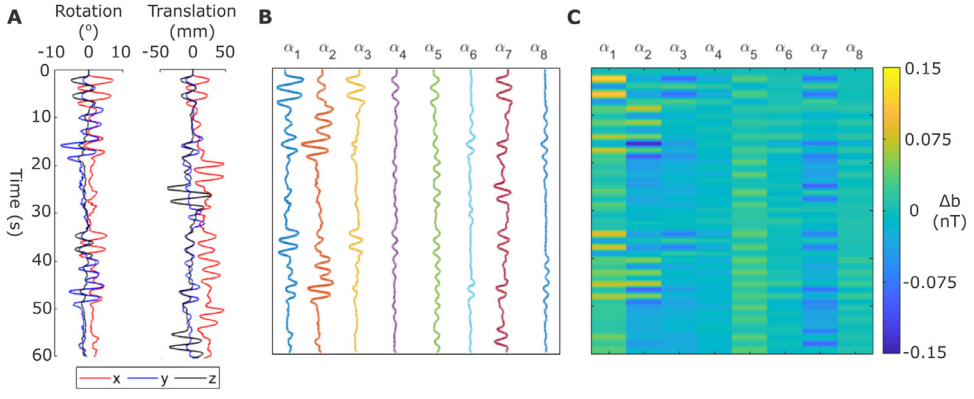

Fig. A1. ***Visualisation of B_{mat} for a single sensor.*** *A) The measured rotations and translations of a single sensor, relative to its initial orientation and position. B) In the case of a single sensor, each column of $\mathbf{B}_{mat}$ corresponds to the change in measured field due to movement through a unit contribution in each of the 8 magnetic field or magnetic field gradient components in our model. C) Image representation of the corresponding matrix, $\mathbf{B}_{mat}$.*

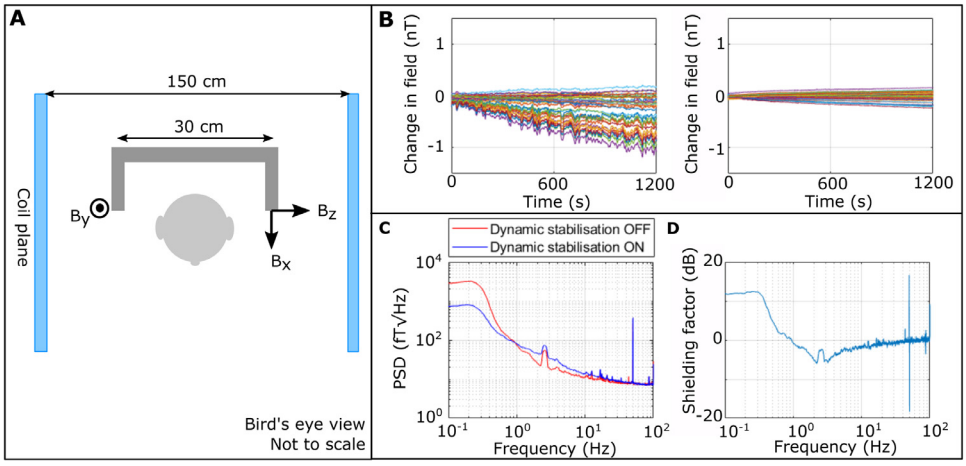

Fig. B1. Demonstration of dynamic stabilisation. A) Experimental set up: The helmet was placed at the isocentre of the coils (and approximately at the centre of the MSR). The reference array is placed slightly off-centre, behind the helmet, to avoid collisions during mapping movements. Reference OPMs used for dynamic nulling are mounted either side of the head and separated by a distance of ~30 cm. B) Time-courses derived from 40 OPMs inside an empty MSR, without dynamic stabilisation (left) and with dynamic stabilisation active (right). C) Median (over sensors) power spectral density with (blue) and without (red) stabilisation. D) Estimated field attenuation of the system as a function of frequency (in decibels). (For interpretation of the references to colour in this figure legend, the reader is referred to the web version of this article.)

and averaging the results). Results are shown with dynamic stabilisation switched off (red) and active (blue). Fig. B1D shows an estimate of the field attenuation of the dynamic stabilisation system as a function of frequency (obtained via division of the two PSDs). The field attenuation is expressed in decibels, where a positive value indicates shielding.

Visual inspection of the data in Fig. B1B shows that the temporal field drift at low frequencies is of the same order as the static background field following degaussing inside the OPM-optimised MSR. More quantitatively, the maximum change in magnetic field over the 20-minute recording was 980 pT; given the expected static background of ~2 nT, this could lead to errors in the magnetic field model of around 50%. A qualitative comparison of the plots in Fig. B1B suggests that temporal variations in the field occurring over timescales of ~10 s are well compensated by the dynamic stabilisation. Indeed, when dynamic stabilisation was switched on, the maximum field change over the 20 min recording was reduced to 214 pT, and consequently the error on nulling would fall to around 10%. This confirms the critical need for dynamic stabilisation.

However, it is also clear from these results that dynamic stabilisation is not perfect. A steady drift in field remains even with dynamic stabilisation, albeit with a shallower temporal gradient. This effect may be due to changing field gradients within the room that are poorly sampled by the reference array and are therefore not compensated by the procedure. Consequently, it seems likely that improved reference arrays and dynamic nulling of field gradients might prove fruitful in improving nulling further. In addition, Figs. B1C and B1D show that, whilst for frequencies <1 Hz the dynamic stabilisation decreases interference, at higher frequencies interference is marginally increased. This is likely due to the bit-depth of the DACs used in the controller, and improved electronics, (e.g. separate controllers for the static and dynamic stabilisation schemes) could be used to reduce this effect.

References

Allred, J.C., Lyman, R.N., Kornack, T.W., Romalis, M.V., 2002. High-sensitivity atomic magnetometer unaffected by spin-exchange relaxation. Phys. Rev. Lett. doi:10.1103/physrevlett.89.130801.

Altarev, I., Babcock, E., Beck, D., Burghoff, M., Chesnevskaya, S., Chupp, T., Degenkolb, S., Fan, I., Fierlinger, P., Frei, A., Gutsmiedl, E., Knappe-Grüneberg, S., Kuchler, F., Lauer, T., Link, P., Lins, T., Marino, M., McAndrew, J., Niessen, B., Paul, S., Petzoldt, G., Schläpfer, U., Schnabel, A., Sharma, S., Singh, J., Stoepler, R., Stuiber, S., Sturm, M., Taubenheim, B., Trahms, L., Voigt, J., Zechlau, T., 2014. A magnetically shielded room with ultra low residual field and gradient. Rev. Sci. Instrum. doi:10.1063/1.4886146.

Altarev, I., Fierlinger, P., Lins, T., Marino, M.G., Nießen, B., Petzoldt, G., Reisner, M., Stuiber, S., Sturm, M., Taggart Singh, J., Taubenheim, B., Rohrer, H.K., Schläpfer, U., 2015. Minimizing magnetic fields for precision experiments. J. Appl. Phys. doi:10.1063/1.4922671.

Baillet, S., 2017. Magnetoencephalography for brain electrophysiology and imaging. Nat. Neurosci. doi:10.1038/nn.4504.

Baker, A.P., Brookes, M.J., Rezek, I.A., Smith, S.M., Behrens, T., Smith, P.J.P., Woolrich, M., 2014. Fast transient networks in spontaneous human brain activity. Elife doi:10.7554/eLife.01867.

Bell, W.E., Bloom, A.L., 1961. Optically driven spin precession. Phys. Rev. Lett. doi:10.1103/PhysRevLett.6.280.

Bell, W.E., Bloom, A.L., 1957. Optical detection of magnetic resonance in alkali metal vapor. Phys. Rev. doi:10.1103/PhysRev.107.1559.

Bork, J., Hahlbohm, H., Klein, R., 2001. The 8-layered magnetically shielded room of the PTB: design and construction.

Borna, A., Carter, T.R., Colombo, A.P., Jau, Y.Y., McKay, J., Weisend, M., Taulu, S., Stephen, J.M., Schwindt, P.D.D., 2020. Non-invasive functional-brain-imaging with an OPM-based magnetoencephalography system. PLoS ONE doi:10.1371/journal.pone.0227684.

Borna, A., Carter, T.R., Derego, P., James, C.D., Schwindt, P.D.D., 2019. Magnetic source imaging using a pulsed optically pumped magnetometer array. IEEE Trans. Instrum. Meas. doi:10.1109/TIM.2018.2851458.

Boto, E., Bowtell, R., Krüger, P., Fromhold, T.M., Morris, P.G., Meyer, S.S., Barnes, G.R., Brookes, M.J., 2016. On the potential of a new generation of magnetometers for MEG: a beamformer simulation study. PLoS ONE 11, 1–24. doi:10.1371/journal.pone.0157655.

Boto, E., Hill, R.M., Rea, M., Holmes, N., Seedat, Z.A., Leggett, J., Shah, V., Osborne, J., Bowtell, R., Brookes, M.J., 2021. Measuring functional connectivity with wearable MEG. Neuroimage doi:10.1016/j.neuroimage.2021.117815.

Boto, E., Holmes, N., Leggett, J., Roberts, G., Shah, V., Meyer, S.S., Muñoz, L.D., Mullinger, K.J., Tierney, T.M., Bestmann, S., Barnes, G.R., Bowtell, R., Brookes, M.J., 2018. Moving magnetoencephalography towards real-world applications with a wearable system. Nature 555, 657–661. doi:10.1038/nature26147.

Boto, E., Meyer, S.S., Shah, V., Alem, O., Knappe, S., Kruger, P., Fromhold, T.M., Lim, M., Glover, P.M., Morris, P.G., Bowtell, R., Barnes, G.R., Brookes, M.J., 2017. A new generation of magnetoencephalography: room temperature measurements using optically-pumped magnetometers. Neuroimage 149, 404–414. doi:10.1016/j.neuroimage.2017.01.034.

Boto, E., Seedat, Z.A., Holmes, N., Leggett, J., Hill, R.M., Roberts, G., Shah, V., Fromhold, T.M., Mullinger, K.J., Tierney, T.M., Barnes, G.R., Bowtell, R., Brookes, M.J., 2019. Wearable neuroimaging: combining and contrasting magnetoencephalography and electroencephalography. Neuroimage 201, 116099. doi:10.1016/j.neuroimage.2019.116099.

Brookes, M.J., Wood, J.R., Stevenson, C.M., Zumer, J.M., White, T.P., Liddle, P.F., Morris, P.G., 2011. Changes in brain network activity during working memory tasks: a magnetoencephalography study. Neuroimage doi:10.1016/j.neuroimage.2010.10.074.

Cohen, D., 1972. Magnetoencephalography: detection of the brain's electrical activity with a superconducting magnetometer. Science 175 (80–.).), 664–666. doi:10.1126/science.175.4022.664.

Cohen, D., 1968. Magnetoencephalography: evidence of magnetic fields produced by alpha-rhythm currents. Science 161, 784–786. doi:10.1126/science.161.3843.784.

Dupont-Roc, J., Haroche, S., Cohen-Tannoudji, C., 1969. Detection of very weak magnetic fields (10−9gauss) by 87Rb zero-field level crossing resonances. Phys. Lett. A 28, 638–639. doi:10.1016/0375-9601(69)90480-0.

Gross, J., Baillet, S., Barnes, G.R., Henson, R.N., Hillebrand, A., Jensen, O., Jerbi, K., Litvak, V., Maess, B., Oostenveld, R., Parkkonen, L., Taylor, J.R., van Wassenhove, V., Wibral, M., Schoffelen, J.M., 2013. Good practice for conducting and reporting MEG research. Neuroimage doi:10.1016/j.neuroimage.2012.10.001.

Hämäläinen, M., Hari, R., Ilmoniemi, R.J., Knuutila, J., Lounasmaa, O.V., 1993. Magnetoencephalography theory, instrumentation, and applications to noninvasive studies of the working human brain. Rev. Mod. Phys. 65, 413–497. doi:10.1103/RevModPhys.65.413.

Happer, W., 1972. Optical pumping. Rev. Mod. Phys. doi:10.1103/RevModPhys.44.169.

Hill, R.M., Boto, E., Holmes, N., Hartley, C., Seedat, Z.A., Leggett, J., Roberts, G., Shah, V., Tierney, T.M., Woolrich, M.W., Stagg, C.J., Barnes, G.R., Bowtell, R.R., Slater, R.,

Brookes, M.J., 2019. A tool for functional brain imaging with lifespan compliance. Nat. Commun. doi:10.1038/s41467-019-12486-x.

Hill, R.M., Boto, E., Rea, M., Holmes, N., Leggett, J., Coles, L.A., Papastavrou, M., Everton, S.K., Hunt, B.A.E., Sims, D., Osborne, J., Shah, V., Bowtell, R., Brookes, M.J., 2020. Multi-channel whole-head OPM-MEG: helmet design and a comparison with a conventional system. Neuroimage doi:10.1016/j.neuroimage.2020.116995.

Hoburg, J.F., 1995. Principles of Quasistatic Magnetic Shielding with Cylindrical and Spherical Shields. IEEE Trans. Electromagn. Compat. doi:10.1109/15.477342.

Holmes, N., Leggett, J., Boto, E., Roberts, G., Hill, R.M., Tierney, T.M., Shah, V., Barnes, G.R., Brookes, M.J., Bowtell, R., 2018. A bi-planar coil system for nulling background magnetic fields in scalp mounted magnetoencephalography. Neuroimage doi:10.1016/j.neuroimage.2018.07.028.

Holmes, N., Tierney, T.M., Leggett, J., Boto, E., Mellor, S., Roberts, G., Hill, R.M., Shah, V., Barnes, G.R., Brookes, M.J., Bowtell, R., 2019. Balanced, bi-planar magnetic field and field gradient coils for field compensation in wearable magnetoencephalography. Sci. Rep. 9. doi:10.1038/s41598-019-50697-w.

Huang, M.X., Swan, A.R., Quinto, A.A., Matthews, S., Harrington, D.L., Nichols, S., Bruder, B.J., Snook, C.C., Huang, C.W., Baker, D.G., Lee, R.R., 2017. A pilot treatment study for mild traumatic brain injury: neuroimaging changes detected by MEG after low-intensity pulse-based transcranial electrical stimulation. Brain Inj doi:10.1080/02699052.2017.1363409.

Iivanainen, J., Stenroos, M., Parkkonen, L., 2017. Measuring MEG closer to the brain: performance of on-scalp sensor arrays. Neuroimage doi:10.1016/j.neuroimage.2016.12.048.

Iivanainen, J., Zetter, R., Grön, M., Hakkarainen, K., Parkkonen, L., 2019. On-scalp MEG system utilizing an actively shielded array of optically-pumped magnetometers. Neuroimage doi:10.1016/j.neuroimage.2019.03.022.

Johnson, C., Schwindt, P.D.D., Weisend, M., 2010. Magnetoencephalography with a two-color pump-probe, fiber-coupled atomic magnetometer. Appl. Phys. Lett. doi:10.1063/1.3522648.

Johnson, C.N., Schwindt, P.D.D., Weisend, M., 2013. Multi-sensor magnetoencephalography with atomic magnetometers. Phys. Med. Biol. doi:10.1088/0031-9155/58/17/6065.

Kamada, K., Sato, D., Ito, Y., Natsukawa, H., Okano, K., Mizutani, N., Kobayashi, T., 2015. Human magnetoencephalogram measurements using newly developed compact module of high-sensitivity atomic magnetometer. Jpn. J. Appl. Phys. doi:10.7567/JJAP.54.026601.

Kominis, I.K., Kornack, T.W., Allred, J.C., Romalis, M.V., 2003. A subfemtotesla multichannel atomic magnetometer. Nature doi:10.1038/nature01484.

Mhaskar, R., Knappe, S., Kitching, J., 2012. A low-power, high-sensitivity micromachined optical magnetometer. Appl. Phys. Lett. doi:10.1063/1.4770361.

Nenonen, J., Nurminen, J., Kičić, D., Bikmullina, R., Lioumis, P., Jousmäki, V., Taulu, S., Parkkonen, L., Putaala, M., Kähkönen, S., 2012. Validation of head movement correction and spatiotemporal signal space separation in magnetoencephalography. Clin. Neurophysiol. 123, 2180–2191. doi:10.1016/j.clinph.2012.03.080.

Osborne, J., Orton, J., Alem, O., Shah, V., 2018. Fully integrated standalone zero field optically pumped magnetometer for biomagnetism. In: Shahriar, S.M., Scheuer, J. (Eds.), Steep Dispersion Engineering and Opto-Atomic Precision Metrology XI. SPIE, pp. 89–95. doi:10.1117/12.2299197.

Packer, M., Hobson, P.J., Holmes, N., Leggett, J., Glover, P., Brookes, M.J., Bowtell, R., Fromhold, T.M., 2020. Optimal inverse design of magnetic field profiles in a magnetically shielded cylinder. Phys. Rev. Appl. doi:10.1103/physrevapplied.14.054004.

Pfeiffer, C., Ruffieux, S., Jonsson, L., Chukharkin, M.L., Kalabukhov, A., Xie, M., Winkler, D., Schneiderman, J.F., 2019. A 7-channel high-T_{c} SQUID-based on-scalp MEG system. IEEE Trans. Biomed. Eng. doi:10.1109/tbme.2019.2938688.

Roberts, G., Holmes, N., Alexander, N., Boto, E., Leggett, J., Hill, R.M., Shah, V., Rea, M., Vaughan, R., Maguire, E.A., Kessler, K., Beebe, S., Fromhold, M., Barnes, G.R., Bowtell, R., Brookes, M.J., 2019. Towards OPM-MEG in a virtual reality environment. Neuroimage doi:10.1016/j.neuroimage.2019.06.010.

Sander, T.H., Preusser, J., Mhaskar, R., Kitching, J., Trahms, L., Knappe, S., 2012. Magnetoencephalography with a chip-scale atomic magnetometer. Biomed. Opt. Express. doi:10.1364/boe.3.000981.

Schwindt, P.D.D., Lindseth, B., Knappe, S., Shah, V., Kitching, J., Liew, L.A., 2007. Chip-scale atomic magnetometer with improved sensitivity by use of the Mx technique. Appl. Phys. Lett. doi:10.1063/1.2709532.

Shah, V.K., Wakai, R.T., 2013. A compact, high performance atomic magnetometer for biomedical applications. Phys. Med. Biol. 58, 8153–8161. doi:10.1088/0031-9155/58/22/8153.

Sheng, D., Perry, A.R., Krzyzewski, S.P., Geller, S., Kitching, J., Knappe, S., 2017. A microfabricated optically-pumped magnetic gradiometer. Appl. Phys. Lett. doi:10.1063/1.4974349.

Taulu, S., Simola, J., Kajola, M., 2005. Applications of the signal space separation method. October 53, 3359–3372. doi:10.1109/TSP.2005.853302.

Tierney, T.M., Holmes, N., Mellor, S., López, J.D., Roberts, G., Hill, R.M., Boto, E., Leggett, J., Shah, V., Brookes, M.J., Bowtell, R., Barnes, G.R., 2019. Optically pumped magnetometers: from quantum origins to multi-channel magnetoencephalography. Neuroimage doi:10.1016/j.neuroimage.2019.05.063.

Voigt, J., Knappe-Grüneberg, S., Schnabel, A., Körber, R., Burghoff, M., 2013. Measures to reduce the residual field and field gradient inside a magnetically shielded room by a factor of more than 10. Metrol. Meas. Syst. doi:10.2478/mms-2013-0021.

Zetter, R., Mäkinen, A.J., Iivanainen, J., Zevenhoven, K.C.J., Ilmoniemi, R.J., Parkkonen, L., 2020. Magnetic field modeling with surface currents. Part II. Implementation and usage of bfieldtools. J. Appl. Phys. doi:10.1063/5.0016087.

Chapter 5

A 90-channel triaxial MEG system using OPMs

Annals of the New York Academy of Sciences, 2022, 14890

DOI: 10.1111/nyas.14890

ORIGINAL ARTICLE

ANNALS OF THE NEW YORK ACADEMY OF SCIENCES

A 90-channel triaxial magnetoencephalography system using optically pumped magnetometers

Molly Rea[1] | Elena Boto[1] | Niall Holmes[1] | Ryan Hill[1] | James Osborne[2] | Natalie Rhodes[1] | James Leggett[1] | Lukas Rier[1] | Richard Bowtell[1] | Vishal Shah[2] | Matthew J. Brookes[1]

[1]Sir Peter Mansfield Imaging Centre, School of Physics and Astronomy, University of Nottingham, Nottingham, UK

[2]QuSpin Inc., Louisville, Colorado, USA

Correspondence
Matthew J. Brookes, Sir Peter Mansfield Imaging Centre, School of Physics and Astronomy, University of Nottingham, University Park, Nottingham NG7 2RD, UK.
Email: matthew.brookes@nottingham.ac.uk

Funding information
Innovate UK, Grant/Award Number: 1003346; Wellcome, Grant/Award Numbers: 203257/B/16/Z, 203257/Z/16/Z; Engineering and Physical Sciences Research Council, Grant/Award Numbers: EP/L016052/1, EP/T001046/1, EP/V047264/1; National Institutes of Health, Grant/Award Numbers: R01EB028772, R44MH110288

Abstract

Magnetoencephalography (MEG) measures the small magnetic fields generated by current flow in neural networks, providing a noninvasive metric of brain function. MEG is well established as a powerful neuroscientific and clinical tool. However, current instrumentation is hampered by cumbersome cryogenic field-sensing technologies. In contrast, MEG using optically pumped magnetometers (OPM-MEG) employs small, lightweight, noncryogenic sensors that provide data with higher sensitivity and spatial resolution, a natural scanning environment (including participant movement), and adaptability to any age. However, OPM-MEG is new and the optimum way to design a system is unknown. Here, we construct a novel, 90-channel triaxial OPM-MEG system and use it to map motor function during a naturalistic handwriting task. Results show that high-precision magnetic field control reduced background fields to ~200 pT, enabling free participant movement. Our triaxial array offered twice the total measured signal and better interference rejection compared to a conventional (single-axis) design. We mapped neural oscillatory activity to the sensorimotor network, demonstrating significant differences in motor network activity and connectivity for left-handed versus right-handed handwriting. Repeatability across scans showed that we can map electrophysiological activity with an accuracy ~4 mm. Overall, our study introduces a novel triaxial OPM-MEG design and confirms its potential for high-performance functional neuroimaging.

KEYWORDS
electrophysiology, human brain imaging, magnetoencephalography, optically pumped magnetometers

INTRODUCTION

Magnetoencephalography using optically pumped magnetometers (OPM-MEG) is a new way to noninvasively assess human brain activity. Like conventional MEG, the technique measures magnetic fields generated above the scalp by current flow in assemblies of neurons.[1–3] These fields, with appropriate mathematical analysis, allow us to infer moment-to-moment changes in electrical brain activity as a participant

carries out a task.[4] However, unlike conventional MEG, which employs a fixed array of cryogenically cooled magnetic field sensors (i.e., superconducting quantum interference devices—SQUIDs), OPM-MEG uses a new generation of sensors (OPMs) that are small and lightweight, do not require cryogenic cooling, and can be mounted flexibly on or near the scalp.[5] The result is a more practical scanner that is free from cryogenics and can, in principle, adapt to different head sizes and shapes, enabling free movement during scanning.[5–9] Since less thermal insulation is required between the sensor and the head, the OPMs are positioned closer to the brain (compared to conventional SQUID-based systems), thereby improving sensitivity and spatial precision.[10–13] The potential of OPM-MEG as a high-performance functional imaging modality is significant, and growing enthusiasm within the neuroscientific and clinical research communities has been seen in recent years. However, OPM-MEG is a nascent technology, and there are significant challenges to the successful implementation of an optimized system, including control of background magnetic fields, the design of OPMs, and implementation of sensor arrays. Here, we bring together new developments in each of these key areas to demonstrate how a novel, 90-channel OPM-MEG instrument can accurately characterize brain function during a naturalistic task.

OPMs rely on the quantum properties of alkali atoms (e.g., ^{87}Rb) to detect magnetic fields.[5] Briefly, an atomic vapor housed in a glass cell is illuminated with a laser. If the wavelength of the laser is resonant with the D1 transition of the atomic species, the atoms absorb photons from the laser and, in an absolute zero magnetic field, are optically pumped into a "dark state". Atoms in a dark state cannot absorb more photons making the vapor transparent to incident light.[14] Alkali atoms possess a magnetic moment and, in the absence of a magnetic field, the effect of pumping is to align those magnetic moments along the direction of the laser. Consequently, the vapor gains a *bulk* magnetic moment (i.e., the sum of all individual magnetic moments pointing in the same direction). Once aligned and because the vapor is transparent, the intensity of laser light passing through the cell is maximized (known as a zero-field resonance). However, in the presence of an external magnetic field, the bulk magnetization is deflected away from alignment. The atoms can once again absorb photons, and the light passing through the cell is reduced. The intensity of light passing through the vapor thus becomes a function of the magnetic field, and the system behaves as a magnetometer.[15] In practice, this mode of operation is complicated by atomic collisions (which reduce bulk magnetization) and by first-order insensitivity of the transparency to field orientation. However, operation in the spin-exchange relaxation-free (SERF) regime[16] and application of a known oscillating field across the cell[17] counteracts these effects—enabling magnetic fields to be sampled accurately with directional sensitivity in two orthogonal orientations, perpendicular to the laser.

OPMs are well established as a successful means to measure the MEG signal; however, this mode of operation offers significant flexibility for OPM design, and the optimal sensor configuration is not yet set. One recent development is the triaxial OPM, which can simultaneously measure magnetic field components along three orthogonal orientations.[30] This is made possible via the use of two laser beams. Specifically (assuming Cartesian coordinates), a beam oriented in *x* enables field measurement in *y* and *z*; a second beam, oriented in *z*, enables field measurement in *x* and *y*. Combining all four measurements allows us to determine the full vector field (Figure 1A). Triaxial measurement of the magnetic field is promising for a number of reasons. First, almost all conventional MEG systems measure a single component of the field vector (radial to the head surface). Triaxial OPMs provide two additional (tangential) metrics and thus three times more measurements. The tangential field components generated by neural sources are smaller in magnitude than the radial components[12,31,32] so they do not equate to three times more signal. Nevertheless, an array containing 50 triaxial sensors is approximately equivalent to an array of 80 conventional (radial) sensors in terms of total signal acquired.[32] Second, theory shows that triaxial measurement is better than radial-only measurements for differentiating fields originating inside the head (i.e., the MEG signal) from fields originating in the environment (i.e., interference). This provides a marked advantage in terms of signal quality since artifacts can be identified and rejected based on the spatial signature of their magnetic field.[32] Third, when the number of sensors is limited (which is usually the case), triaxial measurement offers advantages in terms of the uniformity of coverage—particularly in the case of pediatric measurements.[31,33] Finally, the ability to characterize the complete field vector offers significant advantages for sensor calibration, elimination of crosstalk (both between axes in a single sensor and between adjacent sensors), and the prospect of robust "closed-loop" operation, whereby sensors are operated in a continuous feedback loop to improve dynamic range in all three directions. Evaluation of a small number of triaxial OPMs for MEG has been undertaken,[33] and the sensitivity of these prototypes was similar to the more conventional single- and dual-axis OPMs (triaxial sensitivities of ~9–14 fT/sqrt (Hz) compared to ~7–10 fT/sqrt (Hz)), potentially making triaxial sensors well suited for MEG. However, at the time of writing, to our knowledge, no one has built a large-scale triaxial array.

Aside from OPM and array design, the biggest challenge in OPM-MEG—particularly if free participant movement is to be enabled—is control of the background magnetic field. Magnetic fields from the brain are ~100–1000 fT in amplitude; several orders of magnitude smaller than naturally occurring environmental fields. For this reason, all systems (including cryogenic MEG) are housed within a magnetically shielded environment (MSE) constructed using multiple layers of high magnetic permeability and high electrical conductivity metals. These layers reduce temporally fluctuating environmental fields at low and high frequencies, respectively, to a level where brain activity can be delineated from background fluctuations. However, in such environments, the presence of metal in the walls leaves a remnant static (i.e., constant over time) magnetic field of 20–70 nT. This field does not affect cryogenic sensors; however, it is too large for an OPM to achieve its zero-field resonance and OPMs will not function. Once in operation, the dynamic range of an OPM (i.e., the range of magnetic field it can accurately measure) is small (~±3 nT for gain errors less than 5%), meaning that movement of the sensor with respect to the static field causes a measurable change in the field that may exceed its dynamic

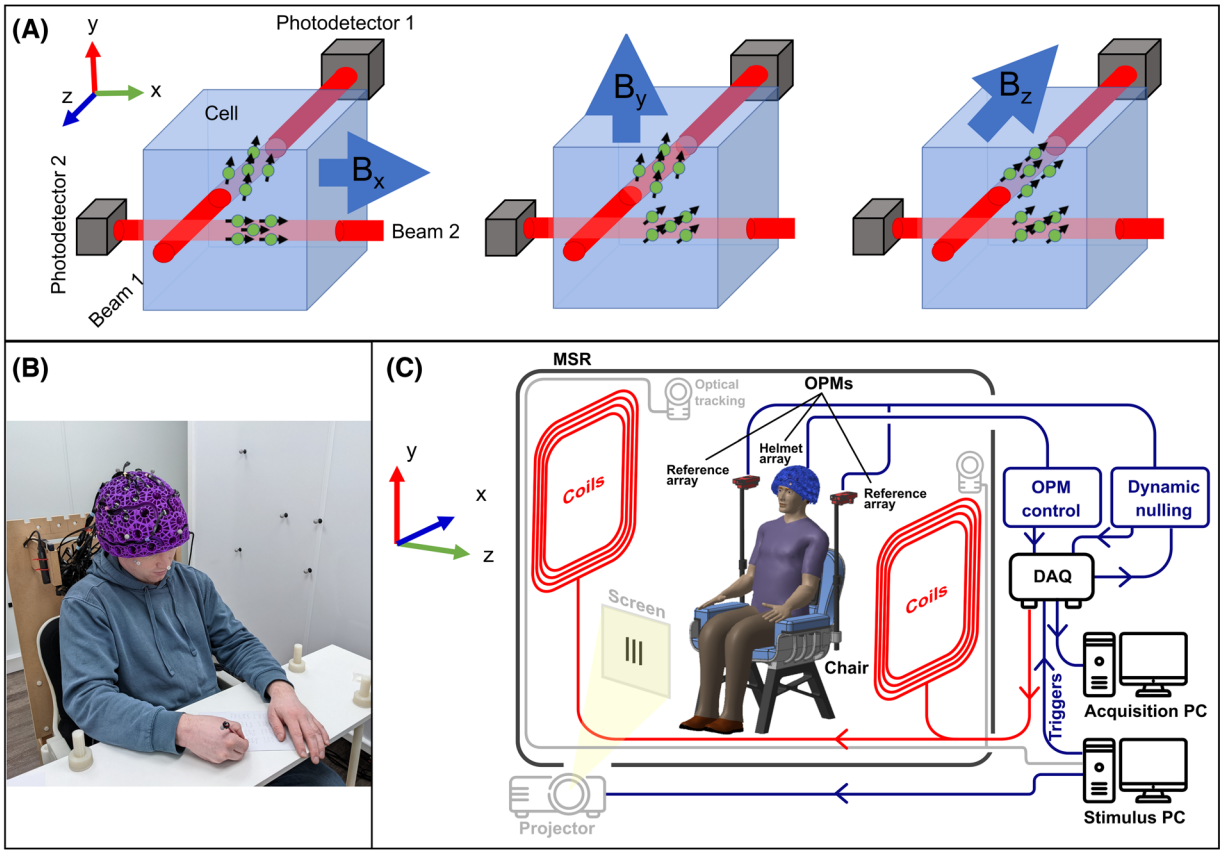

FIGURE 1 System overview. (A) Schematic diagrams of a triaxial OPM. Two independent laser beams are projected through the vapor cell. The beam oriented in *z* allows measurements of the field components B_x and B_y. The beam oriented in *x* allows measurements of the field components B_z and B_y. These four measurements can be combined to determine the full vector magnetic field. Note, however, that B_y is measured twice and thus has marginally lower noise. (B) Photograph of a participant wearing the OPM-MEG helmet, taking part in the handwriting paradigm. (C) A schematic diagram of the OPM-MEG system. The participant is placed in a magnetically shielded enclosure (in this case, a room of internal dimension $3 \times 2.4 \times 3\ m^3$, whose walls comprise four layers of mu-metal and a single layer of copper). Biplanar coils are placed on either side of the participant for background field control. Data acquisition and storage, as well as coil control, are implemented via digital acquisition systems coupled to a PC. A second PC controls the experimental paradigm and motion tracking.

range. This is a key consideration given that one of the major advantages of OPM-MEG is free participant movement. For these reasons, both the static magnetic field and temporally fluctuating fields must be controlled in OPM-MEG.

In practice, electromagnetic coils can be placed inside each OPM to cancel the static magnetic field at each sensor. Energizing these *on-sensor* coils at the start of a MEG experiment will enable operation if the OPM remains stationary.[10] However, if the participant moves, the OPM measures a change in the magnetic field that may exceed its dynamic range (e.g., a 4° rotation in a 30 nT field would be sufficient to prevent the OPM working). There are two solutions to this. The sensor can be operated in a *closed-loop* configuration, whereby the on-sensor coils are continually updated based on the sensor read-out in order to keep the field within the OPM close to zero.[34] In principle, this would allow the OPM to operate even if it were moving through a large magnetic field. However, closed-loop sensing preserves artifacts generated by movement, causes sensors in close proximity to interfere with one another,[34] and introduces implementation challenges because the shape of the zero-field resonance is strongly affected by fields in all three orientations. An alternative solution is to remove the static field entirely by using reference sensors inside the MSE in conjunction with large electromagnetic coils situated around the participant. A feedback loop, alongside judicious coil design, enables both spatially uniform magnetic fields and linear field gradients to be compensated across the entire head.[35–37] Removal of the field in this way not only ensures OPMs remain operational when moving but also reduces movement artifacts. Such systems have proved effective—enabling the construction of a wearable system where participants have been able to move during a scan.[6,9,35,38] However, some degree of remnant magnetic field remains, and it is not yet known whether a genuine zero-field could be achieved with such a system.

In this paper, we bring together novel triaxial OPMs with newly developed magnetic shielding techniques to demonstrate a 90-channel OPM-MEG system operating in a close-to-zero-field environment. To demonstrate effectiveness, we employ an experimental paradigm in which participants write down a word shown on a screen with either their left or right hand. Using this task, we elicit known effects associated with movement (specifically the event-related beta decrease,

the postmovement beta rebound,[39,40] and their modulation with left- and right-handed movements). We hypothesized that these well-characterized effects could be measured with high fidelity using our system, despite the natural, large-scale head movements required to perform the task.

To assess repeatability between scans, we measure both neural oscillatory modulation and electrophysiological functional connectivity in the same participants multiple times. We localize the maximum amplitude modulation in the beta-band for each task condition and quantitatively assess repeatability by comparing this localization across repeat experiments. To further assess system robustness, we exploit a phenomenon known as *neural fingerprinting*, where it has been shown[41–43] that brain activity is unique to an individual (e.g., a fingerprint). We measure the correlation between repeat experiments for functional images and connectome graphs, and we hypothesize that assuming our system provides high-fidelity data in moving participants, within-participant correlations should be higher than between-participant correlations. Finally, we test the extent to which background magnetic fields can be suppressed using a field nulling system and analyze the advantages of MEG reconstruction using a triaxial array.

METHODS

System overview

Thirty OPMs with triaxial sensitivity[30,33] (QuSpin Inc., Louisville, CO, USA) were operated in a single array. The sensors were housed in a 3D-printed helmet (Cerca Magnetics Ltd., Nottingham, UK) worn by the participant (Figure 1B). This helmet can house up to 64 OPMs; the 30 sensors available were arranged to provide coverage of the left and right sensorimotor cortices. The participant was seated at the center of a $3 \times 2.4 \times 3$ m^3 (internal dimensions) magnetically shielded room (MuRoom, Magnetic Shields Ltd., Kent, UK), and between a set of biplanar electromagnetic coils (Cerca Magnetics Ltd.) that were used for background magnetic field control. The participant's head is positioned in the central volume between the coil planes. The coils themselves are 1.6×1.6 m^2 in area, with a separation of 1.5 m. Four additional OPMs (first generation, dual-axis, QuSpin Inc.) were placed behind the participant to measure field fluctuation inside the MSE. A set of six infra-red (IR) cameras (OptiTrack Flex 13, NaturalPoint Inc., Corvallis, OR, USA) were placed around the participant and used to optically track the position of IR-retroreflective markers, attached to the OPM-MEG helmet and biplanar coils. A schematic diagram of the system is shown in Figure 1C. The outputs of OPMs in both the helmet and reference arrays are fed into a digital acquisition (DAQ) system (National Instruments, Austin, TX, USA) and recorded by a computer. An additional DAQ is used to control the currents through each of the electromagnetic coils via a set of low-noise current drivers (QuSpin Inc.). A single PC controlled the OPMs, coils, data acquisition, and storage, while a separate PC controlled the experimental paradigm (i.e., what the participant sees throughout the experiment) and the motion tracking cameras.

Paradigm

Two participants took part in the study. Both gave written, informed consent, and the study was approved by the University of Nottingham Medical School Research Ethics Committee. The participants (henceforth termed 1 and 2) were 42 and 27 years old; both were male and right-handed (both scored 100 on the Edinburgh handedness test).

The paradigm was implemented using custom code written in Presentation (Neurobehavioral Systems Inc., Berkeley, CA, USA). A single experiment comprised two blocks of 20 trials. In a single trial, a randomly selected five-letter word was presented on a screen for 5 s; this was followed by a 7 s rest period (indicated by a blank screen). Upon stimulus presentation, the participant wrote down the word shown using a pencil and paper. In one block of trials, the participant used their left hand to complete the task, and in the other block, they used their right hand. An instruction telling the participant which hand to use was shown on the screen at the start of each block. The words were selected at random from a database of 200. Within a single experiment, the words, and the order in which they were presented, were the same for both blocks (i.e., participants wrote the same words, in the same order, with their left and right hand). However, the words differed between experiments. Both participants undertook this experiment eight times, and the order in which the left- and right-handed blocks were presented was alternated between runs.

Background magnetic field compensation

For each of the 16 experiments, compensation of both static and time-varying magnetic fields in the region containing the OPM-MEG helmet was undertaken based on a technique originally described by Rea et al.[37] Compensation fields were generated using the biplanar coils shown in Figure 1C. This coil system is designed to output the three homogeneous magnetic field components and all five independent (linear in space) field gradient components. All coils had previously been calibrated to determine the magnetic field (or field gradient) per unit current generated by each coil. The procedure of magnetic field compensation was as follows.

Immediately following the positioning of the participant in the center of the MSE and coils, the MSE door was closed and the inner mu-metal panels in the walls demagnetized.[44] This optimizes the performance of passive shielding, leaving (on average) around a 3–5 nT spatially homogeneous field in the center of the room with field gradients of order 2–4 nTm^{-1}. This procedure takes approximately a minute to complete.

Following demagnetization, we aimed to compensate for any (slow) drift in the magnetic field over time using dynamic stabilization.[36] Such drift can result from, for example, temperature variations causing small changes in the spatial dimensions of the MSE. The OPM reference array was used to sample changes in the magnetic field over time. The outputs of these sensors were low-pass filtered at 3 Hz and input to a high-speed (60 Hz) proportional integral controller, implemented in LabVIEW (National Instruments), and used to determine compensation currents, which were applied dynamically to the biplanar coils. This

approach stabilizes <3 Hz changes in the three uniform components of the magnetic field, and the three gradients that vary in *z*. (Note: the reference sensors were separated by ∼40 cm in *z*, but had similar *x*- and *y*-coordinates so dynamic stabilization of gradients varying in the *x*- and *y*-directions was not possible using this arrangement.)

Having applied dynamic stabilization, the background magnetic field was held constant over time; however, the temporally static offset field (i.e., the spatially homogenous field and associated gradients that exist following demagnetization) remained. This was sampled by moving the helmet through the background field and simultaneously recording the resulting change in magnetic field measured at the OPMs along with the helmet location. Specifically, the participant was asked to complete a series of head movements for 60 s—rotating and translating their head about each of the three Cartesian axes to sample the magnetic field and its spatial variation, comprehensively. Throughout this process, the location and orientation of the rigid helmet with respect to the coils were tracked using the six optical tracking cameras. This was achieved by attaching five markers to known positions on the helmet and five markers to one coil plane as a stationary reference. The locations and orientations of the sensors, relative to the helmet, were known as a result of the 3D printing process. The magnetometer and corresponding motion data derived from this procedure were then fit to a spherical harmonic model comprising the eight components of the magnetic field (i.e., three spatially uniform magnetic field components and five field gradient components) that can be generated by the coils. This modeling, combined with the coil calibration data, enabled us to apply DC currents to the coils such that an equal and opposing magnetic field was generated to cancel the remnant field. Having applied the currents, the final magnetic field should be close to zero across the volume occupied by the OPM helmet. Dynamic stabilization remains active through data acquisition to compensate for changes in the background field over time.

The process of field mapping, which included calculation and application of nulling currents, was performed twice to optimize the static magnetic field compensation for each experiment. The field mapping procedure was then undertaken a third time to capture the final field in which the helmet was situated. This procedure takes approximately 10 min. To simplify the fitting procedure and minimize scan time, triaxial measurements from only five of the 30 OPMs were used to fit the background magnetic field. These OPMs were positioned at the front, back, top, left, and right of the helmet (Figure 2A).

Data acquisition

Ninety channels of OPM data were recorded throughout the handwriting paradigm, at 16-bit resolution and a sampling rate of 1200 Hz.

The optical tracking system was used to measure both participant head motion and the location of the pencil throughout all experiments with six degrees of freedom. These data were recorded using the NaturalPoint Motive software platform at a sampling rate of 120 Hz. Control of Motive from MATLAB (MathWorks Inc., Natick, MA, USA) was facilitated by the NaturalPoint NatNet SDK software.

Synchronization of the magnetometer and motion data was achieved using a trigger channel controlled via MATLAB and recorded using the DAQ to indicate when the motion recording began. Additional triggers were recorded upon stimulus onset and presentation of the left- and right-hand instructions in order to enable data segmentation.

Upon completion of the paradigm, the position of each OPM and the orientations of its sensitive axes were determined relative to the participant's brain anatomy by a coregistration procedure.[45,46] Three-dimensional (3D) structured light scans (Structure Core, Occipital Inc., Boulder, CO, USA) were acquired, showing the location of the helmet relative to the participant's facial features. These data were aligned with the participant's anatomical MRI (acquired using a Phillips 3T Ingenia MRI scanner, at 1 mm isotropic resolution) and the known structure of the OPM-MEG helmet (from 3D printing) in order to generate a complete, 3D registration of the sensor locations and orientations relative to the brain anatomy (Figure 2A).

The eight repeat experiments for each participant were conducted across 3 days and each run was distinct. Runs consisted of not only separate data acquisitions, but the participant also removed the helmet and left the room. Furthermore, the MSE walls were demagnetized, and separate coregistration procedures were undertaken.

Data preprocessing

For each experiment, every channel of OPM data was mean corrected and segmented into left- and right-handed blocks. All data were inspected visually, and no trials were rejected. Across the 16 experiments, one axis of one sensor failed in all recordings. During one recording in participant 2, all three axes of that same OPM failed. This sensor was, therefore, excluded from all analyses. This meant that 87 of the 90 channels collected were available for analysis. All three axes of measurement for each OPM were used in the analyses described below unless otherwise stated.

Source localization

A beamformer was applied to left- and right-handed trials separately using custom code written in MATLAB. In each case, data from all 87 OPM channels were filtered to the beta-band (13–30 Hz) using a fourth-order Butterworth filter. Data covariance matrices were generated (separately for each task condition) and regularized using the Tikhonov method with the regularization parameter set at 5% of the maximum eigenvalue of the unregularized matrix. Current sources in the polar and azimuthal orientations were reconstructed. The radial direction was ignored since MEG is relatively insensitive to radially oriented dipoles. The radial and tangential orientations were defined relative to a sphere that best fit the participants' head shape. The beamformer weights were computed using a forward model that characterizes a current dipole in a single-shell conductor[47] implemented in FieldTrip.[48] Based on the two reconstructed, tangential projections

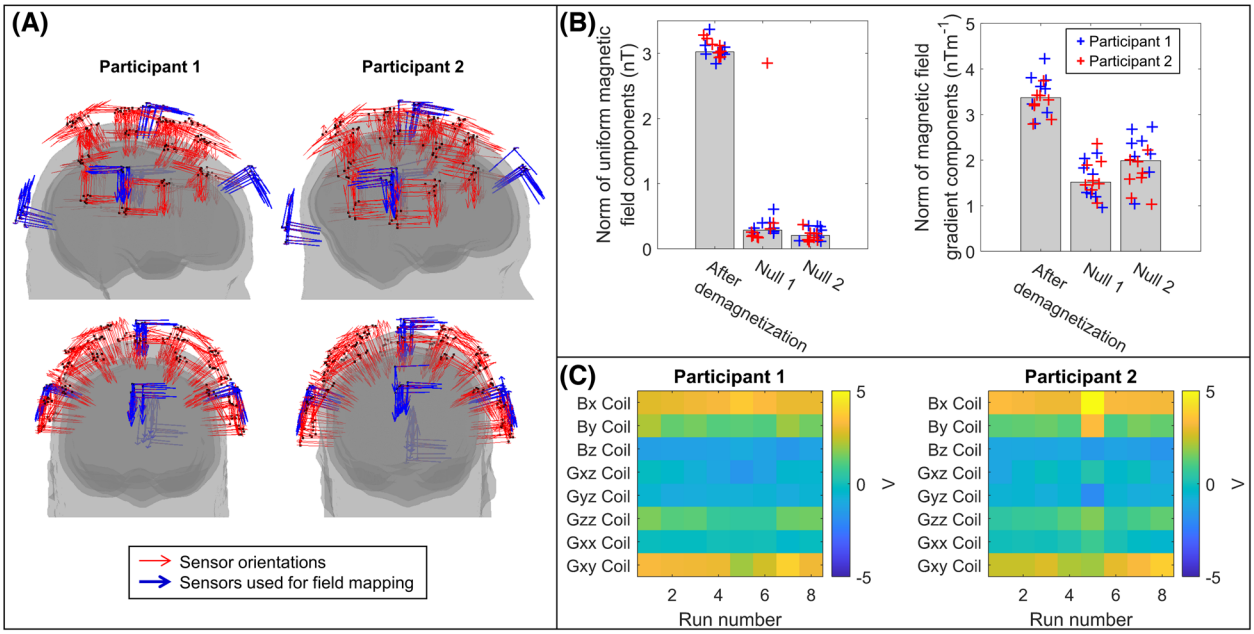

FIGURE 2 Background magnetic field control. (A) Sensor locations, registered to brain anatomy, for each run. Note: Although the helmet was in a slightly different position on the head in each experiment, the sensor positions and orientations are reasonably consistent. The five sensors used in the nulling procedure are shown in blue. (B) The norm of the three uniform magnetic field components, as determined by the model, is shown on the left. Values immediately following demagnetization and after two iterations of nulling are shown. Bars represent the median value across all 16 scans, while the individual data points are shown as blue crosses for participant 1 and red for participant 2. The norm of the five linear magnetic field gradient components is shown on the right. (C) Matrices showing the consistency of the final voltages applied to each of the coils across the eight scans for each participant.

of current, the single orientation of maximum signal amplitude was computed using the method described by Sekihara et al.[49]

A functional image was constructed using a pseudo-T-statistical approach[50] to show the location of current sources exhibiting the maximum beta amplitude modulation between active (1.5 s < t < 3.5 s relative to stimulus onset) and control time windows. The control time window was chosen to coincide with the postmovement beta rebound, whose timing varied between left- and right-handed trials (9 s < t < 11 s and 5.5 s < t < 7.5 s, respectively), since, on average, it took both participants longer to write with their nondominant (left) hand. The brain anatomy was divided into regular 4 mm voxels for computation of the pseudo-T-statistic. For each of the 16 experiments, we calculated two pseudo-T-statistical images showing modulation in beta activity for left- and right-handed writing, respectively.

To assess localization accuracy across runs in detail, these pseudo-T-statistical images were recomputed using 1 mm voxels, and the location (in mm) of the voxel with maximum beta amplitude modulation in the right and left hemispheres for left- and right-handed writing, respectively, was determined for each run. The location of peak activation for each condition was averaged across runs for each participant, and the mean Euclidean distance between this average location and each of the eight individual peak locations for each run was determined.

Visualization of neural activity

To visualize brain activity, we used a "virtual electrode" analysis to assess beta envelope modulation. Beamformer weights for a location of interest were calculated (as used above) and applied to the beta-band filtered OPM data. The Hilbert envelope of the resulting signal was calculated and averaged across trials with the left- and right-handed task conditions analyzed separately. This resulted in a time course of beta modulation throughout the trial.

In addition to the beta envelope, a trial-averaged time-frequency spectrum (TFS) was computed to show the evolution of oscillatory activity during the trial. To do this, reconstructed time courses (using beamformer weights calculated in the broad band) were filtered in a series of overlapping frequency bands, and the Hilbert envelope was computed for each band. Envelopes were then averaged over trials and concatenated in frequency to generate the TFS. TFS data were computed independently for both task conditions (i.e., left- and right-handed writing) in each of the 16 experiments.

Connectivity analysis

In addition to activity, we aimed to investigate functional connectivity specifically by examining: networks of brain regions that work in

concert during the handwriting task, how those networks differ between left- and right-handed writing, and whether these networks differ between individuals.

To compute a whole-brain connectome, a brain parcellation was performed. For each participant, the brain anatomy was segmented into 78 cortical regions according to the automated anatomical labeling (AAL) atlas.[51] Connectivity was estimated using amplitude envelope correlation, applied within the brain parcellation. A time course of beta-band activity at the center of mass of each AAL region was extracted using the beamformer approach described above. This resulted in 78 regional time courses. Connectivity was assessed between every possible pair of regions resulting in 3003 independent functional connectivity measurements. One confound in MEG connectivity estimation is that due to the ill-posed inverse problem, estimates of activity from spatially separate locations are not necessarily independent; rather, the signal from one region can leak into a neighboring region. Thus, for each region pair, we applied a pairwise orthogonalization whereby the beta-band time course from region A was regressed from region B. This technique has been shown to effectively mitigate signal leakage.[52,53] Following this, the envelope of beta oscillations was computed using a Hilbert transform and downsampled to 10 Hz. The Pearson correlation between envelope time courses was used as a metric of functional connectivity. Sequential application of this procedure for all possible region pairs resulted in a 78 × 78 connectome matrix with diagonal symmetry. These matrices were derived independently for left- and right-handed writing—resulting in 32 independently computed connectomes for each run in each participant.

Differences between left- and right-handed writing

As an initial test of the system, we aimed to show a difference between left- and right-handed writing. To this end, we undertook two separate statistical tests. First, we tested the hypothesis that beta modulation measured in the left and right sensory cortices would differ between task conditions. We reconstructed beta envelopes (as performed above) in both left and right sensory cortices (defined according to the AAL atlas) for all eight experiments in both participants. The magnitude of beta modulation was quantified as the difference in amplitude between an active and control window. Relative to stimulus onset for right-handed writing, the active window was defined as $2\text{ s} < t < 4\text{ s}$, and the control window was defined as $5\text{ s} < t < 7\text{ s}$. These values were changed to $4\text{ s} < t < 6\text{ s}$ for the active window and $8\text{ s} < t < 10\text{ s}$ for the control window in left-handed trials to account for slower writing. This process resulted in 32 measurements per participant (i.e., eight runs with estimates in two locations for the two conditions). We carried out independent Wilcoxon rank sum tests contrasting beta modulation between conditions for each location. We controlled for multiple comparisons using Bonferroni correction. This test was carried out independently for both participants.

Second, we tested the hypothesis that connectivity would differ between task conditions. Here, we used two metrics: whole-brain connectivity, which is the sum of all 3003 elements in the connectivity matrix, and connectivity strength in the right sensory cortex, which is the sum of the 77 values of connectivity between the right sensory AAL region and all other regions. For both measures, we calculated eight values per condition, per participant. For each participant, we independently tested for a significant difference in connectivity using the Wilcoxon rank sum test. Again, multiple comparisons were controlled using Bonferroni correction. As a post-hoc visualization, we averaged connectome matrices for both conditions and calculated the difference matrix (i.e., left-handed writing minus right-handed writing). The resulting matrix was visualized using a "glass brain".

Measuring robustness across runs

Neural fingerprinting assumes that every person's brain activity is unique, and consequently, a particular individual can be recognized from their brain imaging data. Based on this principle, we reasoned that—assuming our scanner provides high-fidelity data—the functional signatures (both activity and connectivity) derived would exhibit greater similarity within participants compared to between participants. This hypothesis was tested quantitatively.

Given eight experiments, we are able to calculate 28 within-participant comparisons per participant (i.e., 1 to 2; 1 to 3; 2 to 3, and so on) equaling 56 comparisons in total. Similarly, we are able to compute 64 possible comparisons between participants (i.e., 1 to 1; 1 to 2; 2 to 1, and so on). We could, therefore, test the hypothesis that the 56 within-participant comparisons would, on average, be larger than the 64 between-participant comparisons. These comparisons were quantified using the Pearson correlation coefficient for:

1. T-statistical images. An affine transformation was applied to register all the pseudo-T-statistical images to the Montreal Neurological Institute standard brain. Following this, comparisons were made by vectorizing the 3D functional images and computing the Pearson correlation.
2. Connectomes. The connectome matrices derived for each experiment were vectorized, and Pearson correlation was used to quantify similarity across experiments. (Note: only data above the leading diagonal were used for correlation.)
3. Time-frequency spectra. TFS for the left and right sensorimotor cortices were concatenated and vectorized. The Pearson correlation coefficient was used to quantify similarity across experiments.

These quantitative comparison measures were made independently for the two task conditions. For each of the three comparisons, the 64 values representing between-participant correlations and the 56 values corresponding to the within-participant correlations were averaged separately. The difference in mean values was then calculated as between-participant minus within-participant, meaning that we expected a negative value. To test statistically, we used a Monte Carlo method. An empirical null distribution was generated by randomly permuting the 120 correlation values and generating two new (sham) groups of 64 (between-participant) and 56 (within-participant) values.

A (sham) difference metric was then computed. This process was repeated for 100,000 random permutations to generate a null distribution, and the real value (with true group labels) was compared to the null distribution.

Triaxial reconstruction

As a final analysis, we tested the hypothesis that reconstruction of the MEG data using all three axes of measurement would be advantageous when compared to reconstruction using only radial components. To this end, we assessed the signal-to-noise ratio (SNR) of all signals at the channel level and statistically compared the best radially and tangentially oriented channels. SNR was measured for right-handed writing only as the signal difference between the active and control windows and divided by the standard deviation of the signal in the active window. As before, the active window was defined as $2\text{ s} < t < 4\text{ s}$ and the control window as $5\text{ s} < t < 7\text{ s}$, relative to stimulus onset. This gave eight measures of SNR per participant for every channel (radial and tangential). As a proxy for the total useful signal acquired across the array, SNR values were summed across channels, and the ratio of total triaxial SNR to total radial SNR was calculated. Additionally, we tested for a significant difference in SNR between the radial and tangential channels with the highest SNR, respectively, by using a nonparametric Wilcoxon rank sum test.

Finally, to assess whether triaxial reconstruction could better remove sources of external interference, we reconstructed brain activity in the 78 AAL regions using both the triaxial data (as described above) and radial-only data. The beamformer parameters were identical in each case. We aimed to assess whether a known artifact generated at 16.6 Hz by nearby environmental effects (e.g., an air conditioning unit) could be better suppressed by the beamformer when using triaxial compared to single-axis data. In order to visualize these reconstructed data, a TFS approach was undertaken in which data were reconstructed within 1.5-Hz-wide overlapping frequency bands in the 13–30 Hz range.

RESULTS

Background magnetic field compensation and participant movement

Figures 2B and C show the results of background magnetic field nulling. In Figure 2B, the left-hand chart shows the norm of the three spatially homogeneous components of the magnetic field immediately following demagnetization (left bar) and after two iterations of nulling are applied (center and right bars). The height of the bars represents the median field value across all 16 experiments, and the crosses show data from each experiment independently (participant 1 in blue and participant 2 in red). As shown, the nulling procedure reduces the median ($\pm$ standard deviation) field from 3.0 ± 0.1 nT to 0.2 ± 0.1 nT. The right-hand chart shows an equivalent measure for the five linear gradients of the magnetic field, which were reduced from $3.4 \pm 0.4\ \text{nTm}^{-1}$ to $2.0 \pm 0.5\ \text{nTm}^{-1}$. This reduction in the background magnetic field is key to enabling participant movement. The stability of the background fields between experiments and participants is also apparent in these data. Note that the initial and final fields are similar across experiments, with the exception of run 5 in participant 2 whereby the first nulling iteration failed. This is despite variations in the required head movements to sample the field between the two participants. Repeatability is also highlighted in Figure 2C, which shows the voltages applied to each of the eight coils across the eight runs in each participant. Here, the final voltages applied are similar across all experiments and demonstrate that not only the background field magnitudes but also the spatial components that define these fields were consistent over time.

Figure 3 shows the head movement data acquired for both participants during the handwriting task. In Figure 3A, the upper plot shows a visualization of the direction and scale of movement. To perform the task, participants tended to translate forward (in x) and rotate to look downward (rotation about z). The scale of this movement is shown in the lower panel of Figure 3A, which represents trial-averaged rotations and translations for both participants; solid lines show left-handed writing, and dashed lines show right-handed writing. The separate colors (blue, orange, and yellow) show translation along or rotation about the x-, y-, and z-axes, respectively. Figure 3B shows example rotation and translation data across a single representative experiment (in participant 2), while the table in Figure 3C shows the maximum movements made in all 16 experiments. It is noteworthy that the scale of movement (up to ~5 cm translation and 10° rotation) is such that it could not be carried out inside a conventional MEG scanner. Although conventional MEG scanners can cope with small head movements via post-hoc correction, the scale of movement shown here would cause the participants to hit their heads on the helmet (i.e., the movement would be physically curtailed). This will be addressed further in the Discussion.

Differences between left- and right-handed writing

Figure 4A shows the spatial signature of beta-band modulation for both participants, averaged across the eight experiments. The leftmost panel (red overlay) shows left-handed writing; the center panel (blue overlay) shows right-handed writing, and the rightmost panel (green overlay) shows the difference between the two. In all cases, the pseudo-T-statistical images are thresholded at 80% of their maximum value for visualization. Note that despite participant movement throughout acquisition (Figure 3), our system was able to accurately localize beta modulation to the primary sensorimotor areas. Figure 4B shows the time courses of the beta-band envelope extracted from the left and right sensory areas (delineated according to the AAL atlas). In each chart, beta signatures for left- (red) and right-handed (blue) writing are shown. In all cases, beta power loss during movement with a rebound—above baseline—postmovement is clear. This response has been well characterized in previous studies.[39,40] Note that the rebound

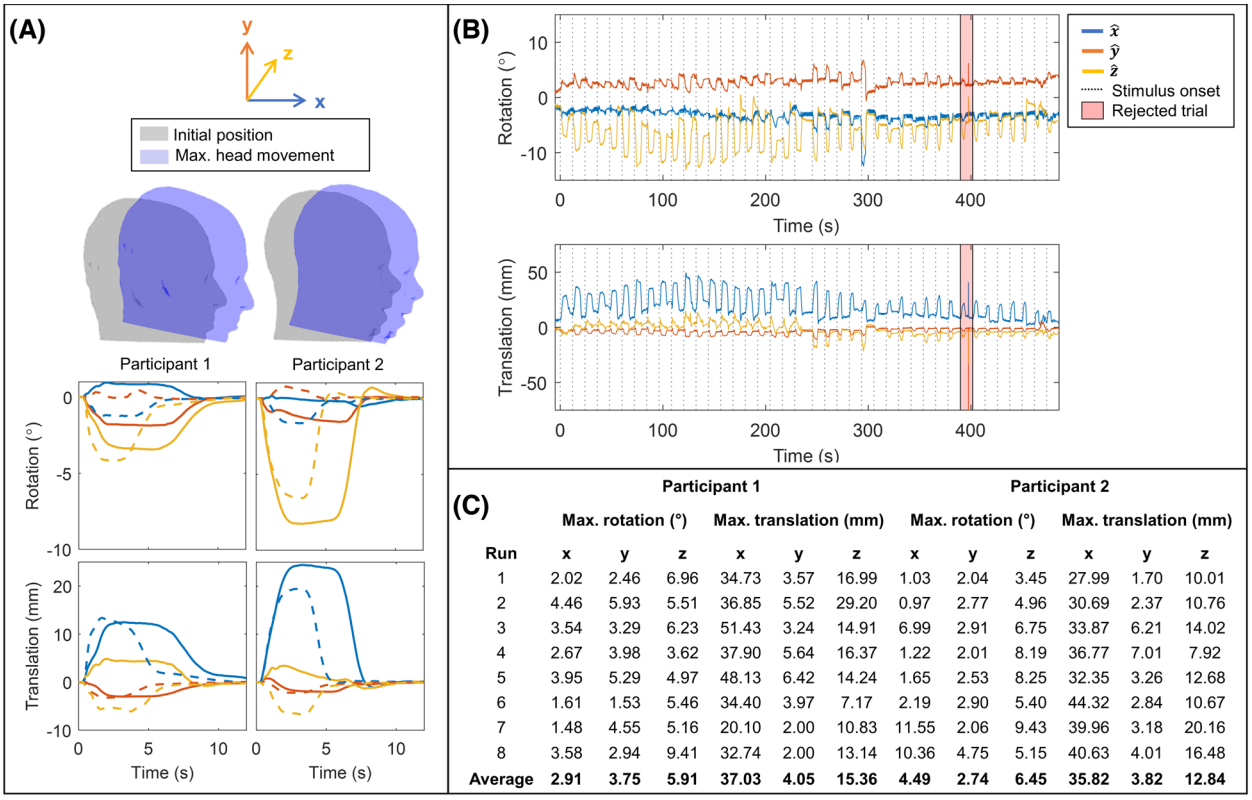

(C)

	Participant 1						Participant 2					
	Max. rotation (°)			Max. translation (mm)			Max. rotation (°)			Max. translation (mm)		
Run	x	y	z	x	y	z	x	y	z	x	y	z
1	2.02	2.46	6.96	34.73	3.57	16.99	1.03	2.04	3.45	27.99	1.70	10.01
2	4.46	5.93	5.51	36.85	5.52	29.20	0.97	2.77	4.96	30.69	2.37	10.76
3	3.54	3.29	6.23	51.43	3.24	14.91	6.99	2.91	6.75	33.87	6.21	14.02
4	2.67	3.98	3.62	37.90	5.64	16.37	1.22	2.01	8.19	36.77	7.01	7.92
5	3.95	5.29	4.97	48.13	6.42	14.24	1.65	2.53	8.25	32.35	3.26	12.68
6	1.61	1.53	5.46	34.40	3.97	7.17	2.19	2.90	5.40	44.32	2.84	10.67
7	1.48	4.55	5.16	20.10	2.00	10.83	11.55	2.06	9.43	39.96	3.18	20.16
8	3.58	2.94	9.41	32.74	2.00	13.14	10.36	4.75	5.15	40.63	4.01	16.48
Average	**2.91**	**3.75**	**5.91**	**37.03**	**4.05**	**15.36**	**4.49**	**2.74**	**6.45**	**35.82**	**3.82**	**12.84**

FIGURE 3 Participant movement during handwriting task. (A) Upper: Visualization of the maximum head rotation about *z* and maximum translation in *x* for each participant. Their maximum movement is shown in blue, overlaid on the initial position shown in gray. Lower: Trial-averaged rotation (top row) and translation (bottom row), in *x*- (blue), *y*- (orange), and *z*-directions (yellow). Average movement for left-handed writing is given by solid lines, and right-handed writing is shown by dashed lines. On average, participant 2 (right) moved their head more during the task than participant 1 (left). (B) Example time course showing head rotation (upper) and translation (lower) over the course of a scan. The beginning of each trial is marked by a dashed line. The red shaded region indicates a "bad trial," where an artifact is present due to inaccuracy of the optical tracking. (C) Table of maximum rotation and translation values for both participants across all runs.

for left-handed writing is comparatively delayed since participants took longer to write with their nondominant hands.

For both participants, right-handed writing elicited a response dominated by the left motor region, whereas left-handed writing produced a more bilateral response with beta modulation in both the left and right primary sensorimotor regions. This is shown by the functional images in Figure 4A and is also reflected in the time courses in Figure 4B, where the response in the right motor cortex is lower in amplitude for right-handed writing (shown in blue). This lateralization was tested statistically with a summary measure of beta modulation in both left and right sensory cortices compared between task conditions. In participant 1, significantly ($p = 0.0011$; Wilcoxon rank sum test) larger beta modulation was observed in the right motor cortex for left-handed, compared to right-handed writing. There was no significant difference between conditions in the left motor cortex ($p = 0.57$; Wilcoxon rank sum test). In participant 2, in the right motor cortex, we again saw significantly ($p = 0.0002$; Wilcoxon rank sum test) larger beta modulation for left-handed writing. Larger modulation in the left motor cortex was also observed in the case of right-handed writing in this participant ($p = 0.01$; Wilcoxon rank sum test).

Figure 5 shows the results of the functional connectivity analysis. In both participants, whole-head connectivity (i.e., the sum of all elements in the connectivity matrix) was significantly higher for left-handed writing compared to right-handed writing (participant 1; $p = 0.0047$; participant 2; $p = 0.010$; Wilcoxon rank sum test). This is shown in the left-hand panels of Figure 5A, where the bar height represents the mean connectivity across the whole head, and the crosses represent whole-head connectivity from individual experimental runs. The results for participants 1 and 2 are shown in the upper and lower plots, respectively. This effect was amplified when looking at connectivity strength between the right sensorimotor cortex and the rest of the brain (right-hand panels of Figure 5A) where, again, left-handed writing resulted in significantly higher connectivity compared to right-handed writing (participant 1; $p = 0.0047$; participant 2; $p = 0.0006$; Wilcoxon rank sum test).

Figure 5B shows the spatial signature of the connectivity differences. The matrices depict connectivity differences (left-handed writing minus right-handed writing) for both participants. The top 15% of connections that differ between conditions are overlaid on a glass brain for visualization. It is evident that differences are centered on

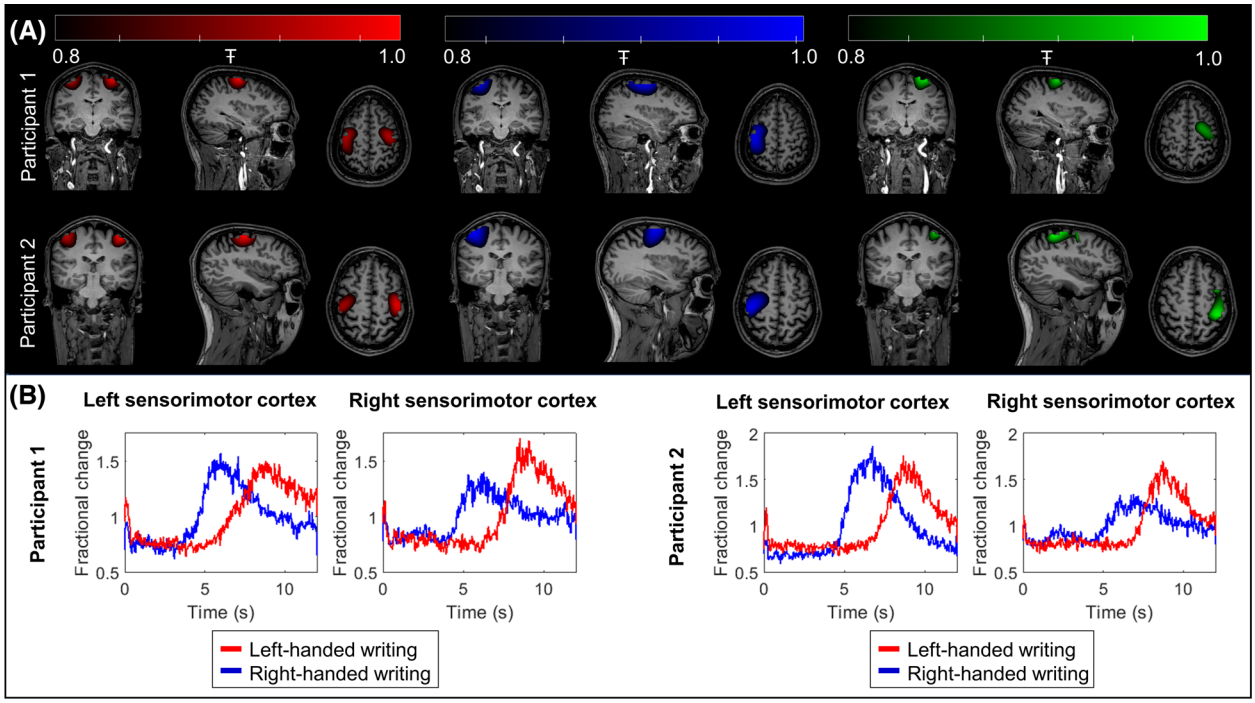

FIGURE 4 Brain function during left- and right-handed writing. (A) Pseudo-T-statistical images, averaged across runs, thresholded at 80% of the maximum value, and overlaid on anatomical MRI. Activity during left-handed trials is shown in red (left panel), right-handed trials shown in blue (center panel), and the difference shown in green (right panel). Images for participant 1 are shown on the top row and participant 2 on the bottom row. For right- (dominant) handed writing, activity is dominant in the left motor region, whereas for left-handed writing, a bilateral response is apparent. (B) The amplitude envelope of beta-band activity in left and right sensorimotor cortices. Data from participant 1 are shown to the left, and participant 2 are shown on the right. For each participant, the graph to the left shows the left sensory cortex, and the plot to the right shows the right sensory cortex. In all cases, the blue traces show average (across runs) beta envelope modulation for right-handed writing, and red shows the same for left-handed writing.

bilateral connections in the motor network with significantly increased connectivity in the case of left-handed writing.

Measuring robustness across runs

Figure 6A shows pseudo-T-statistical images for each of the eight experimental runs for both participants. Note the high degree of consistency across runs. Quantitatively, for the left sensorimotor cortex (during right-handed writing), the mean Euclidean distance between the average location of peak beta amplitude modulation across all runs and each individual peak location within a run was 4 ± 2 mm for participant 1 and 5 ± 2 mm for participant 2. Equivalent values derived in the right sensorimotor cortex for left-handed writing were 4 ± 2 mm for participant 1 and 3 ± 1 mm for participant 2.

Figure 6B shows the connectome matrices that were also derived independently from each run. In both cases, we show the case only for left-handed writing. As with the images in Figure 6A, the connectomes are similar across runs—though there are notable differences between the two participants. These findings are formalized in the bar charts in panels C and D, which show correlation values both within- and between-participants for right-handed writing. In all cases, the bars show the mean values, while each individual data point is shown by the crosses. For the pseudo-T-statistical images, the correlation within participants was 0.93 ± 0.03 (mean ± standard deviation), and this was reduced to 0.76 ± 0.03 for the between-participant correlation. For the connectomes, the correlation within participants was 0.71 ± 0.06 falling to 0.53 ± 0.09 between participants. In both cases, the difference was significant according to our Monte Carlo metric. For the time-frequency spectra, an equivalent analysis failed to show a significant difference for within- and between-participant correlations.

Triaxial reconstruction

Finally, Figure 7 shows the difference between single-axis (radial) and triaxial data. Figure 7A shows a topographical representation of SNR at the channel level. Three separate maps show the cases for the radial and two tangential measurements; the orientations of the tangential measurements are defined by the OPM and helmet geometries. For participant 1, the best radially oriented channel had a mean SNR (across runs) of 6.7 ± 2.5, and the best tangentially oriented channel had an SNR of 5.8 ± 1.7. For participant 2, the best radially oriented channel had a mean SNR of 7.7 ± 2.4, and the best tangentially oriented channel had an SNR of 6.8 ± 1.0; however, there was no significant difference shown for either participant (Wilcoxon rank sum test). The

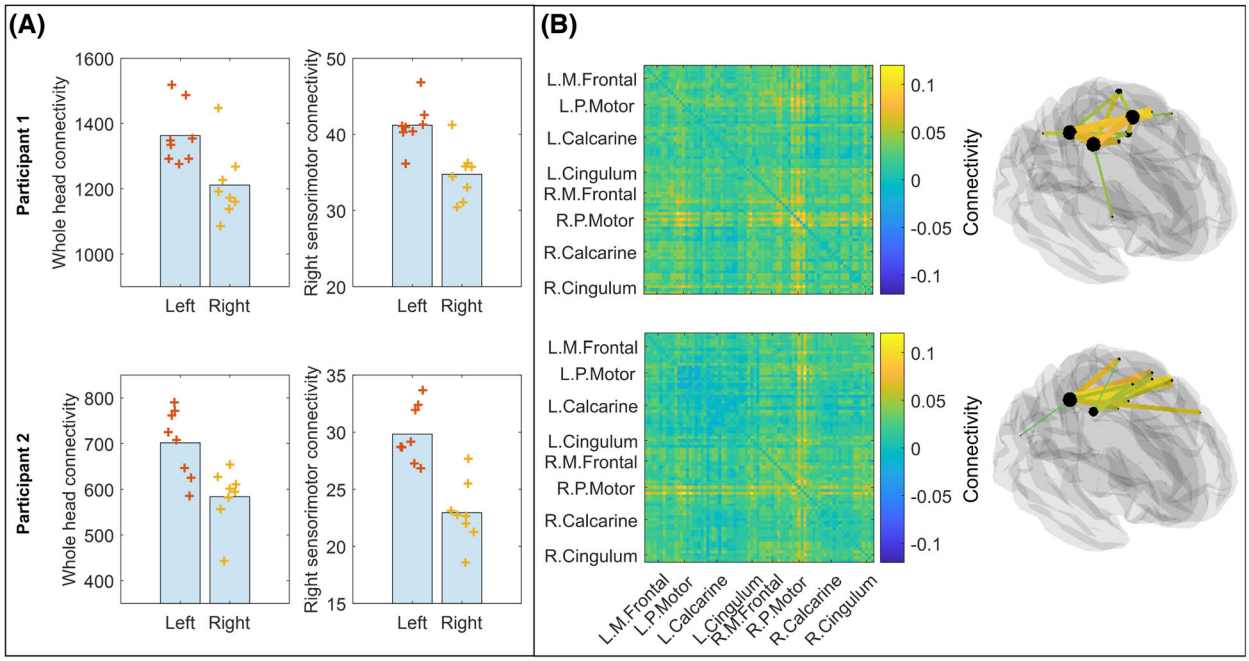

FIGURE 5 Functional connectivity. (A) Left: Whole-brain connectivity in the beta-band, as measured during left- and right-handed trials. Results for participant 1 are shown above and participant 2 below. Right: Connectivity strength in right sensorimotor cortex measured during left- and right-handed writing. For both measures, whole head and right sensorimotor cortex connectivity is significantly higher when using the left (nondominant) hand. (B) Left: Matrix representation showing the difference in connectivity across the 78 AAL regions between left- and right-handed writing. Right: Glass brain visualization of a connectome for participant 1 (above) and participant 2 (below) showing the top 15% of connections. Differences are centered on the right motor cortex, and mostly interhemispheric connections are involved.
Abbreviations: L. Calcarine, left calcarine sulcus; L. Cingulum, left cingulum; L.M. Frontal, left medial frontal cortex; L.P. Motor, left parietal motor cortex; R. Calcarine, right calcarine sulcus; R. Cingulum, right cingulum; R.M. Frontal, right medial frontal cortex; R.P. Motor, right parietal cortex.

mean signal from these channels is shown in Figure 7B; tangential channels are shown in red and radial channels in blue. When summing total SNR across the array, triaxial recording offered a 2.2 ± 0.2 improvement when compared to radial-only recording for participant 1. The ratio was 2.07 ± 0.04 for participant 2.

The laboratory in which the recordings were made exhibits a known, intermittent 16.6 Hz interference source, which is likely an air-conditioning fan. This artifact was clearly visible in 8 of the 16 recordings (four runs in each participant) based on power spectral density analysis of the raw data. For the purposes of this analysis, only those eight recordings were analyzed. Figure 7C shows an example of TFS reconstructed for beta-band data in the left precuneus and the left primary sensory cortex. Representative data are shown from participant 2. The TFS on the right shows a triaxial beamformer reconstruction, while the TFS on the left depicts radial-only reconstruction. Note the clear presence of the 16.6 Hz artifact when single-axis data are used for reconstruction. This result is further characterized in Figure 7D, which shows the interference ratio. The interference ratio is defined as the difference in power spectral density between 16.6 Hz (the artifact) and its neighboring frequencies (15.5 and 17.7 Hz), divided by the power spectral density at the neighboring frequencies. Results are shown at the channel level and for both beamformer reconstructions. The bars show the mean value, while the black crosses show either individual OPM channels for the channel level or individual brain regions for the beamformer reconstructions. Data are shown independently for each participant and for all runs where the artifact was apparent. Note that the magnitude of the artifact is largest at the channel level. It is reduced by beamforming even when only using single-axis data, but it is most effectively attenuated by triaxial reconstruction. This is in agreement with theoretical insights reported previously.[32]

DISCUSSION

Technical considerations

The viability of our OPM-MEG system is demonstrated by the level of robustness of the results. The reproducibility achieved across runs was encouraging given the eight distinct experiments for each participant (data acquired across 3 days) and the extent of the head movements made by both participants throughout. In all runs, high-fidelity metrics of beta modulation were observed, with localization identifying sensorimotor cortices with a high degree of accuracy. Quantitatively, the discrepancy in the peak locations in sensorimotor cortices between experimental runs was of order 4 mm—indicating a high degree of spatial robustness. Furthermore, differences in sensorimotor network activity and connectivity were demonstrated between left-handed and

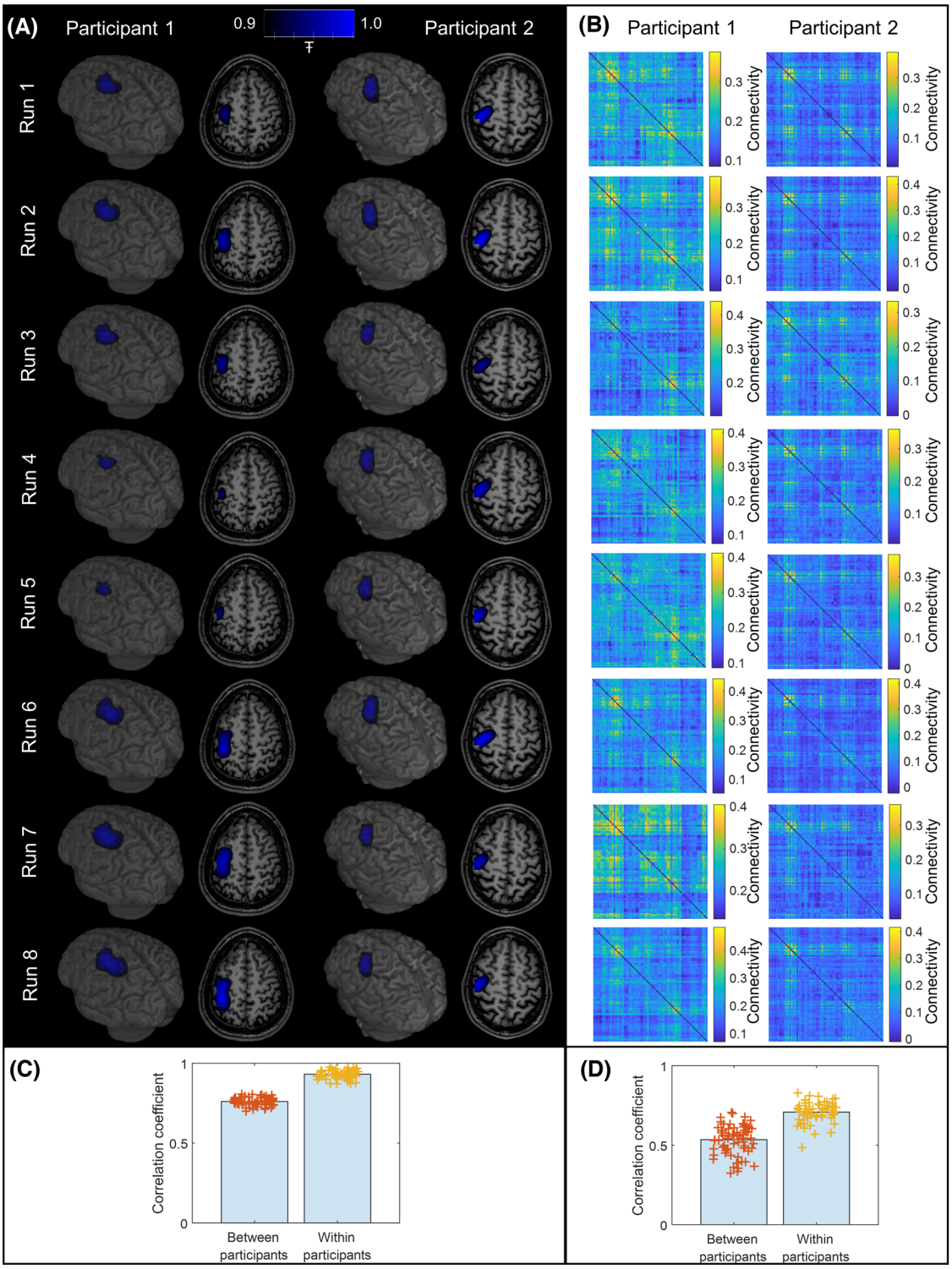

FIGURE 6 Neural fingerprinting. (A) Pseudo-T-statistical images for right-handed writing in both participants were derived independently for all eight runs of the paradigm and overlaid on their brain anatomy. (B) Connectome matrices for right-handed writing, again, were derived independently for all eight runs of the paradigm. (C) Fingerprinting analysis for the pseudo-T-statistical images given in (A), showing within- and between-participant correlations. The bars indicate the mean correlation value, and the crosses show the individual data points. (D) Equivalent to (C) for the connectome matrices shown in (B). Differences are significant in both (C) and (D) according to our Monte Carlo-based statistical test.

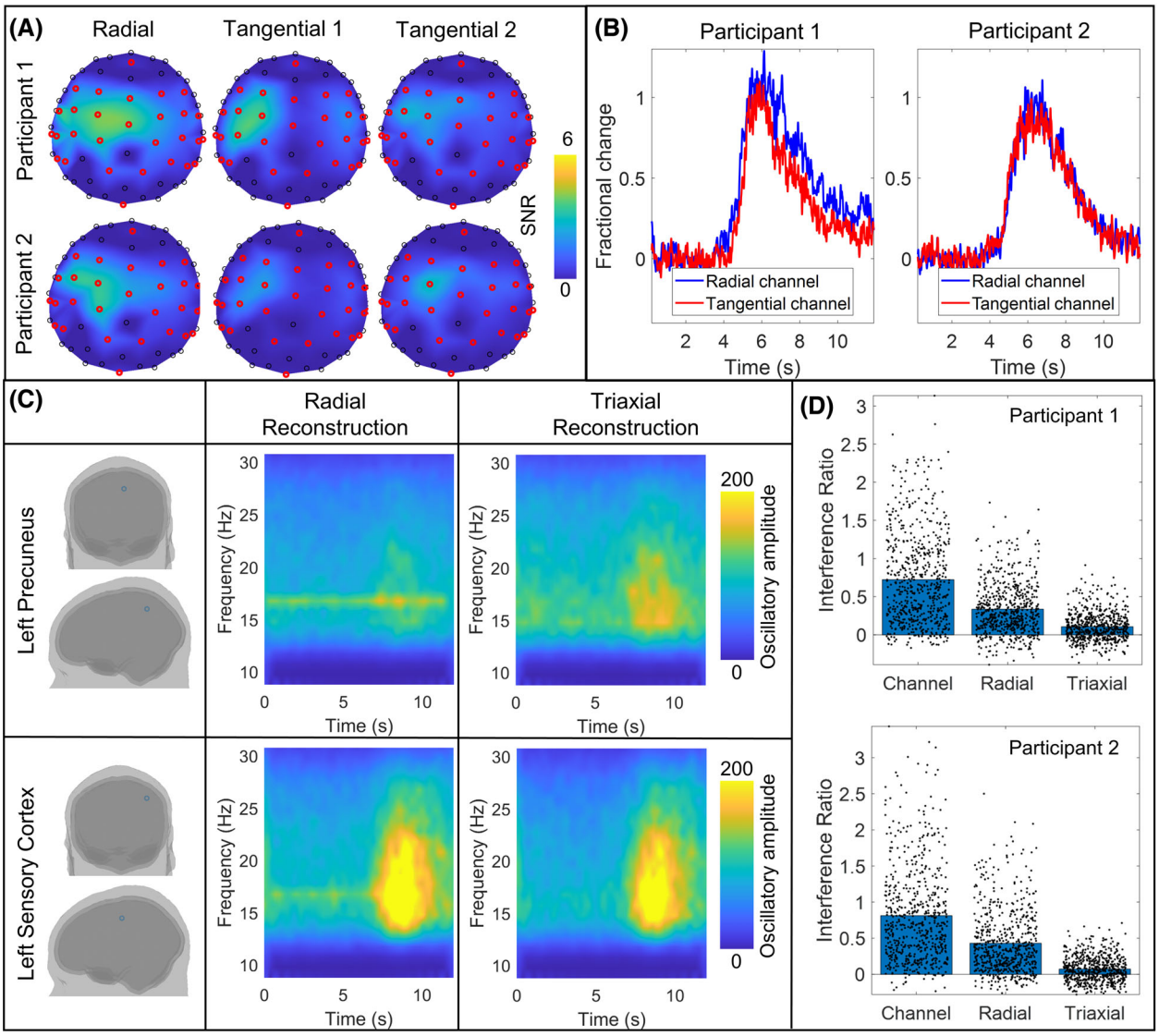

FIGURE 7 Triaxial reconstruction. (A) Topographical maps of SNR for the radial and two tangential measurements at the channel level for right-handed writing in both participants. (B) Time courses of the beta-band envelope were measured at the radial (blue) and tangential (red) channels with the largest SNR. (C) TFS reconstructed for beta-band data from participant 2. Reconstructions were generated for two brain regions—the left precuneus (upper panel) and left primary sensory cortex (lower panel). The left column shows the spatial locations for the reconstruction; the center column shows radial reconstruction, while the right column shows the triaxial reconstruction. (D) Interference ratio (the ratio of the size of the interference spike, to the background [brain] activity) for both participants. The left bar shows the case for channel-level data (the crosses indicate individual channels and runs). The center and right bars show the two different beamformer reconstructions (crosses indicate individual brain regions and runs).

right-handed writing. Those differences were in strong agreement with existing literature (see below). This is again indicative of the fidelity of the acquired data. Within-participant correlation of the pseudo-T-statistical images (another indicator of spatial accuracy) was 93%, and the within-participant correlation of the connectomes, which is a marker of both spatial and temporal signal acuity, was 71%. It is also noteworthy that for both pseudo-T-statistical images and connectome matrices, within-participant correlations were significantly greater than between-participant measures. These correlations demonstrated that the differences between individuals were larger than the differences across runs in the same participant—in accordance with results reported previously.[54] We interpret this as an additional marker of robustness. Overall, the evidence points to our 90-channel system offering an excellent means to interrogate brain electrophysiology during a naturalistic task. However, while repeatability was high across runs, it was not perfect. It is unknown whether the remaining discrepancies are due to instrumental instability, genuine differences in brain activity between runs (due to, e.g., the time of day and fatigue), or a mixture of the two.

Precise control of the background magnetic field is a critical factor in successful OPM-MEG operation. This is because in the SERF regime, which our sensors exploit, OPM output is only linear with the applied

field around zero-field. If background magnetic fields begin to increase, the effective sensor gain is diminished (i.e., for the same change in the field, the sensor output will be lower). Prior to field nulling, but after demagnetization, the background field in the MSE was ~3 nT (Figure 2B). This is much lower than the ambient field found in most MSEs used for MEG where we might expect fields between 10 and 70 nT. However, even at 3 nT, we estimate that if a 90° rotation of the head (hence a 90° rotation of the OPMs) was carried out, some sensors would experience a gain change of ~3.8%. Such changes are known to affect the quality of MEG reconstruction.[13] However, following nulling, the background field was reduced to 0.2 nT meaning an equivalent 90° rotation would generate only a 0.018% gain change. For the scale of a movement carried out during our handwriting paradigm (~5 cm translation and ~10° rotation—see Figure 3), sensor gain changes would have been of order 0.2% had experiments been carried out with no nulling. However, with nulling, these gain changes were reduced to a maximum of ~0.0005%. In sum, the nulling procedure, coupled with dynamic stabilization, which keeps the background field stable over the duration of the experiment, ensures that the OPM output remains linear—providing a faithful representation of the magnetic field even in the face of large participant movements. This is a critical feature of our system. An important consideration is that while nulling resulted in a 0.2 nT remnant magnetic field on average, in many instances, better performance was achieved, with the best being 0.1 nT. The differences in performance between runs are not yet understood but may relate to the accuracy of tracking, small movements of the reference array, or the calibration accuracy of the coil system. In principle, if such errors can be corrected, there is no fundamental reason why background fields cannot be driven even lower; while this would have relatively little impact on gain changes, which are already negligible, it will further reduce low-frequency artifact caused by movement and hence elevate SNR.

Our array was constructed using triaxial sensors. This contrasts with most conventional MEG systems and many OPM-MEG systems,[34,45] which measure only the radial component of neuromagnetic field or field gradient. There are numerous advantages to the triaxial measurement that should be explored. First, triaxial sensors generate three times more measurements compared to a single-axis system. This does not equate to three times more signal since, in the tangential axes, the magnitude of the field from the brain is smaller in comparison to the radial axes.[12,31,32] Nevertheless, experimental measurements (Figure 7) showed that triaxial recording offered twice the total useful signal (summed SNR across the array) compared to single- (radial) axis recordings. On average, the highest SNR was 6.3 for tangentially orientated sensors compared to 7.2 for radially oriented sensors. The fact that the tangential measure was not significantly smaller than the radial measure is likely the result of variability across experiments in signals at the channel level due largely to the different positions of the helmet for each run. Nevertheless, the comparable SNR shows that a useful signal is detected in the tangential axes, and this additional signal will offer significant benefits for source localization.[32] Importantly, though not shown explicitly here, when a limited sampling array is used, the uniformity of coverage is also improved by triaxial measurement[31,33]—a finding that is of critical importance when imaging infants using scalp-mounted sensors.

Second, triaxial sampling enables better separation of magnetic fields originating from inside the head (the MEG signal) from fields originating outside (interference). This, in turn, enables improved rejection of external interference. This finding is not new. The previous work[55] demonstrated that the addition of tangentially oriented SQUID sensors to a conventional system enabled the better separation of interference sources from the MEG signal. Likewise, our own work has theoretically shown how beamforming can be used to exploit the additional information on interfering magnetic fields provided by a triaxial array.[32] Here, this effect was investigated experimentally via single-axis and triaxial beamformer reconstruction of the same data. Such analysis is, to an extent, confounded because of the total number of sensors and orientation sensitivity changes. Nevertheless, the data given in Figure 7 demonstrate how the effect of a known source of external interference on MEG data can be made negligible by the use of triaxial reconstruction. This is an extremely important consideration for OPM-MEG system design. Conventional MEG systems are often formed from gradiometers, which measure the rate of change of magnetic field over space rather than the absolute field value. In the simplest form, gradiometers measure the field change between a radially oriented coil close to the head and another radially oriented coil around 5 cm away. The second coil will measure similar interference, which tends to be spatially uniform but will be less sensitive to the field from the brain, which decays rapidly with radial distance. The result is an overall metric that retains the brain signal but rejects interference. It is possible to construct a similar system of gradiometers based on OPMs[34] and thus control interference in the same way. However, the need for distal sensors would make an OPM helmet bulky, and wearable devices would likely become impractical. A different scheme may use planar gradiometers where the field gradient is measured tangentially rather than radially. Indeed, this has been demonstrated successfully;[7] however, the physical size of the gradiometers then becomes an issue, and either array density is compromised (i.e., fewer planar gradiometers can be arranged on the head) or the baseline (the distance over which gradient is measured) becomes small, limiting depth sensitivity. For these reasons, control of background interference with OPMs is challenging, and the use of conventional gradiometric solutions poses problems, particularly if we wish to maintain wearability. Triaxial sensitivity and the advantages that it brings thus represents a significant and viable method of interference rejection. Importantly, while here we show this effect via beamforming, there are many other interference rejection metrics (e.g., Ref. 56) that would likely benefit from the additional information provided by triaxial measurements.

In addition to the above considerations, there are important technical advantages for a triaxial OPM. First, since triaxial sensitivity enables measurement of the full field vector, a *complete and unambiguous calibration* of the sensor, including its gain and orientation sensitivity, can be carried out. Specifically, three separate pulses of the magnetic field can be applied using the on-sensor coils. For example, any signal generated on the *y*-axis measurement from an *x*-axis pulse

can then be characterized and corrected in software. This orthogonalization implemented in the present sensors means that the OPM will provide a true estimation of not only field magnitude but also direction. This calibration can be used to eliminate crosstalk both between sensors (i.e., perturbations in measurements at one sensor due to the presence of a neighboring sensor) and crosstalk between axes within the same sensor—a significant advantage compared to single- or dual-axis sensing. Finally, triaxial sensitivity is essential for closed-loop operation in practical use. Unlike solid-state vector magnetometers, OPM sensitivity, calibration, and directionality in the *z*-direction depend not only on the magnetic field in the *z*-direction but equally strongly on the magnetic field in the *x*- and *y*-directions (cross-axis projection errors[57]). With triaxial sensitivity, a closed-loop operation can stabilize the internal magnetic field of an OPM in all three directions,[58] thereby increasing the dynamic range, stabilizing the sensor gain, and making OPMs tolerant to changes in the magnetic field in any direction.

This said, rather than use closed-loop operation on all sensors individually, we chose to control the linearity of the response by using the biplanar coils and dynamic stabilization. This nulls the background magnetic field across the OPM array as a whole, ensures a linear response, and negates the need for closed-loop operation.

OPM-MEG is still in development, and there are several limitations of the current system that should be acknowledged. First, brain coverage in the current system was limited because only 30 triaxial OPMs were available. However, there is no reason why we cannot increase the number of sensors to provide whole-brain coverage. Indeed, previous work[45,54] showed that an OPM-MEG system with 50 radial-only channels performed well compared to a state-of-the-art cryogenic system. We strongly believe that a similar number of triaxial sensors would give both whole-brain coverage and better performance. Second, the noise floor of OPMs is currently higher than the noise floor of SQUIDs. Therefore, future work on sensitivity may facilitate further improvements in results. Miniaturized OPMs are still a recent development, and their performance has improved significantly over recent years; there is no fundamental reason that OPMs cannot surpass the sensitivity of SQUIDs. Indeed, it is likely that improved lasers may offer a direct route to this goal. Third, a significant challenge is the heat generated by the sensors during operation. In the current system, a judicious helmet design kept the temperature on the scalp comfortable. However, as systems move toward higher numbers of sensors, greater amounts of heat will dissipate with the potential to become uncomfortable for the participant. Future OPM-MEG systems may then require active cooling within the OPM helmet.[59] Finally, although our magnetic field compensation approach successfully provided a low-field environment, the location of the nulled volume was at the center of the room and around $0.5 \times 0.5 \times 0.5$ m^3 in volume. This means that while head movements can be carried out with minimal effect on sensor operation, larger movements (e.g., a participant walking) remain prohibited. The development of new "reconfigurable" coils to generate nulled volumes at any location inside the MSE,[60] and a drive to a similarly low remnant field, therefore, remains a critical area of development.

Neuroscientific findings

This study was conducted with the aim of evaluating the fidelity of our OPM-MEG system rather than to investigate the neural substrates underlying handwriting. Nevertheless, our findings warrant some discussion. We measured fluctuations in beta activity that were localized to primary sensory and motor cortices during handwriting. As might be expected, when writing with the dominant hand, beta modulation was lateralized with the strongest in the contralateral cortex. However, a more bilateral response was observed when writing with the nondominant, left hand—a finding that was significant in both participants independently. A secondary finding showed increased bilateral sensorimotor connectivity during left-handed, compared to right-handed, writing. Spatial analysis showed increased interhemispheric connectivity between the left and right motor regions, which is consistent with the idea that a bilateral network of brain areas was recruited to perform the task with the nondominant hand. These observations are in strong agreement with previous literature. For example, in an early functional magnetic resonance imaging (fMRI) study, Kim et al.[61] showed a hemispheric asymmetry in the activation of the motor cortex during simple movements. Likewise, Singh and colleagues[62] used fMRI to show that in right-handed participants, ipsilateral activation was significantly greater when participants carried out a task with their nondominant, compared to their dominant, hand. While these studies report the blood oxygenation level-dependent (BOLD) hemodynamic response, which is distinct from the neurophysiological response measured in MEG, there is a known link between beta oscillations and BOLD;[63] therefore, we would expect similar asymmetries to be apparent in beta modulation.

Handwriting itself is a complex procedure that evokes activity across a number of brain areas. Here, we studied the sensorimotor network, which is integrally involved but not specific to handwriting. A meta-analysis performed by Planton et al.[64] demonstrated the involvement of a much larger network, including the left superior frontal sulcus, middle frontal gyrus, left intraparietal sulcus, superior parietal area, and right cerebellum. All of these brain areas were said to be writing-specific. Other areas include those associated with linguistic processes, such as the posterior/inferior temporal cortex. Our study was limited by coverage since only 30 sensors were available. We, therefore, chose to focus on the left and right motor regions. In addition, we focused primarily on beta-band oscillations, which are well known to be the dominant rhythm within the sensorimotor system—although other brain rhythms are also known to be associated with motor control.[65] For this reason, future studies of this type of paradigm should employ a sensor array that facilitates whole-head coverage to increase sensitivity to other regions and look to investigate both oscillatory modulation and connectivity across a broader range of frequencies.

Finally, we note the potential of OPM-MEG to measure brain function during naturalistic tasks. Importantly, handwriting has been carried out across a variety of scanning environments, including positron emission tomography,[64] fMRI,[64] and conventional MEG,[65]

which shows that it is possible to carry out tasks of this nature even in a restricted scanning environment. However, as demonstrated by data in Figure 3, *natural* handwriting involves movements of the head that would be extremely challenging to carry out in conventional systems. For example, in fMRI, participants are typically supine with movement severely restricted, and spin history effects can modulate the BOLD signal acquired over time. Participant movement is also often, but not always, physically restricted by the presence of a dedicated head radiofrequency coil. In conventional MEG, any motion of the participant relative to the fixed sensor array causes changes in signal amplitude, SNR, and field topography. As with fMRI, algorithms to correct such artifacts are available (e.g., Refs. 56, 65–71). But even with movement compensation, successful MEG measurement relies on the participant's head remaining inside the helmet and places a hard limit on permitted head movements. Figure 3 demonstrates that the scale of movement evoked by our handwriting task could not have been carried out in a conventional MEG scanner without the participant's head coming into contact with the helmet. Conversely, OPM-MEG has enabled a scale of movement in which natural handwriting can be achieved. Moreover, these results pave the way for more expansive paradigms enabling a greater degree of head movement, which has the potential to facilitate a new generation of neuroscientific study.

CONCLUSION

OPM-MEG is an emerging functional imaging technique offering greater flexibility to design new naturalistic neuroscientific paradigms and scan cohorts of individuals who struggle to comply with conventional imaging environments. In addition, it promises high sensitivity and spatial resolution since sensors require no cryogenic cooling and can be positioned closer to the brain than the SQUID-based sensors used in conventional MEG. However, the technology is new, and the optimum design for a viable OPM-MEG system is far from settled. Here, we have constructed and demonstrated a novel 90-channel OPM-MEG system based on triaxial OPM sensors operated in an optimized low-field environment. Results show that our background magnetic field compensation reduced the field inside the MSE to a level of around 0.2 nT, enabling participant movement with minimal effect on sensor operation. Further, in agreement with theoretical studies, our triaxial array offered not only high-fidelity reconstruction of electrophysiological function (i.e., peak activation in sensorimotor cortices localized within ∼4 mm across repeat scans) but also significant advantages for characterization and rejection of external interference compared to what would be achieved with single-axis (radial) OPMs. We were able to record data during a naturalistic handwriting paradigm with results showing significant differences in the spatiotemporal profile of activity and connectivity for left-handed and right-handed writing. These results are in strong agreement with previous studies. Overall, our study highlights the unique potential of OPM-MEG as a high-performance method for functional neuroimaging.

ACKNOWLEDGMENTS

We express our sincere thanks to Edyta Kolodziejczuk and Holly Schofield for their work on early versions of the neural fingerprinting analyses used here. This work was supported by an Engineering and Physical Sciences Research Council (EPSRC) Healthcare Impact Partnership grant (EP/V047264/1) and an Innovate UK germinator award (grant number 1003346). We also acknowledge support from the UK Quantum Technology Hub in Sensing and Timing, funded by EPSRC (EP/T001046/1), a Wellcome Collaborative Award in Science (203257/Z/16/Z and 203257/B/16/Z), and the National Institutes of Health (grant number R01EB028772). Sensor development was made possible by funding from the National Institutes of Health (R44MH110288). Funding from EPSRC and the Medical Research Council (MRC) [EP/L016052/1] provided a Ph.D. studentship for M.R. via the Oxford Nottingham Biomedical Imaging Centre for Doctoral Training.

AUTHOR CONTRIBUTIONS

M.R. contributed to the study conceptualization, data collection, data analysis, data interpretation, and writing and review of the paper. M.J.B. contributed to the study conceptualization, data analysis, data interpretation, and writing and review of the paper. E.B. and N.H. contributed to the study conceptualization, data collection, data interpretation, and paper review. R.H. contributed to data analysis, data interpretation, and paper review. J.O., N.R., J.L., and L.R. contributed to data collection and paper review. R.B. contributed to the study conceptualization and paper review. V.S. contributed to study conceptualization, data collection, and paper review.

COMPETING INTERESTS

E.B. and M.J.B. are directors of Cerca Magnetics Limited, a spin-out company whose aim is to commercialize aspects of OPM-MEG technology. E.B., M.J.B., R.B., N.H., and R.H. hold founding equity in Cerca Magnetics Limited, and R.B., N.H., and R.H. sit on the scientific advisory board. E.B. is on the scientific advisory board of MYndSpan Ltd. The authors are involved in U.K. patent application numbers GB2015427.4, GB2106961.2, and GB2108360.5; all of which relate to OPM-MEG. V.S. is the founding director of QuSpin Inc., a commercial entity selling OPMs. J.O. is an employee of QuSpin. V.S. and J.O. are involved in U.S. patent number US10775450B1, which relates to triaxial OPMs.

PEER REVIEW

The peer review history for this article is available at: https://publons.com/publon/10.1111/nyas.14890.

REFERENCES

1. Cohen, D. (1968). Magnetoencephalography: Evidence of magnetic fields produced by alpha-rhythm currents. *Science*, *161*, 784–786.
2. Cohen, D. (1972). Magnetoencephalography: Detection of the brains electrical activity with a superconducting magnetometer. *Science*, *175*, 664–666.
3. Hamalainen, M., Hari, R., Ilmoniemi, R. J., Knuutila, J., & Lounasmaa, O. V. (1993). Magnetoencephalography: Theory, instrumentation, and applications to non-invasive studies of the working human brain. *Reviews of Modern Physics*, *65*, 413–497.

4. Baillet, S. (2017). Magnetoencephalography for brain electrophysiology and imaging. *Nature Neuroscience*, *20*, 327–339.
5. Tierney, T. M., Holmes, N., Mellor, S., López, J. D., Roberts, G., Hill, R. M., Boto, E., Leggett, J., Shah, V., Brookes, M. J., Bowtell, R., & Barnes, G. R. (2019). Optically pumped magnetometers: From quantum origins to multi-channel magnetoencephalography. *Neuroimage*, *199*, 598–608.
6. Boto, E., Holmes, N., Leggett, J., Roberts, G., Shah, V., Meyer, S. S., Muñoz, L. D., Mullinger, K. J., Tierney, T. M., Bestmann, S., Barnes, G. R., Bowtell, R., & Brookes, M. J. (2018). Moving magnetoencephalography towards real-world applications with a wearable system. *Nature*, *555*(7698), 657.
7. Hill, R. M., Boto, E., Holmes, N., Hartley, C., Seedat, Z. A., Leggett, J., Roberts, G., Shah, V., Tierney, T. M., Woolrich, M. W., Stagg, C. J., Barnes, G. R., Bowtell, R., Slater, R., & Brookes, M. J. (2019). A tool for functional brain imaging with lifespan compliance. *Nature Communications*, *10*, 4785.
8. Seymour, R. A., Alexander, N., Mellor, S., O'neill, G. C., Tierney, T. M., Barnes, G. R., & Maguire, E. A. (2021). Using OPMs to measure neural activity in standing, mobile participants. *Neuroimage*, *244*, 118604.
9. Feys, O., Corvilain, P., Aeby, A., Sculier, C., Holmes, N., Brookes, M., Goldman, S., Wens, V., & De Tiège, X. (2021). On-scalp optically pumped magnetometers vs. cryogenic magnetoencephalography for diagnostic evaluation of epilepsy in school-aged children. *Radiology*, *304*, 429–434.
10. Boto, E., Meyer, S. S., Shah, V., Alem, O., Knappe, S., Kruger, P., Fromhold, T. M., Lim, M., Glover, P. M., Morris, P. G., Bowtell, R., Barnes, G. R., & Brookes, M. J. (2017). A new generation of magnetoencephalography: Room temperature measurements using optically-pumped magnetometers. *Neuroimage*, *149*, 404–414.
11. Boto, E., Bowtell, R., Krüger, P., Fromhold, T. M., Morris, P. G., Meyer, S. S., Barnes, G. R., & Brookes, M. J. (2016). The benefits of atomic magnetometers for MEG: A simulation study. *PLoS One*, *11*, e0157655.
12. Iivanainen, J., Stenroos, M., & Parkkonen, L. (2017). Measuring MEG closer to the brain: Performance of on-scalp sensor arrays. *Neuroimage*, *147*, 542–553.
13. Nugent, A. C., Benitez Andonegui, A., Holroyd, T., & Robinson, S. E. (2022). On-scalp magnetocorticography with optically pumped magnetometers: Simulated performance in resolving simultaneous sources. *Neuroimage Reports*, *2*, 100093.
14. Happer, W. (1972). Optical pumping. *Review of Modern Physics*, *44*, 169.
15. Kastler, A. (1973). The Hanle effect and its use for the measurements of very small magnetic fields. *Nuclear Instruments and Methods*, *110*, 259–265.
16. Allred, J. C., Lyman, R. N., Kornack, T. W., & Romalis, M. V. (2002). High-sensitivity atomic magnetometer unaffected by spin-exchange relaxation. *Physical Review Letters*, *89*(13), Article Number: 130801.
17. Cohen-Tannoudji, C., Dupont-Roc, J., Haroche, S., & Laloë, F. (1970). Diverses résonances de croisement de niveaux sur des atomes pompés optiquement en champ nul I. théorie. *Revue De Physique Appliquee*, *5*, 95.
18. Alem, O., Benison, A. M., Barth, D. S., Kitching, J., & Knappe, S. (2014). Magnetoencephalography of epilepsy with a microfabricated atomic magnetrode. *Journal of Neuroscience*, *34*(43), 14324–14327.
19. An, K., Shim, J. H., Kwon, H., Lee, Y.-H., Yu, K.-K., Kwon, M., Chun, W. Y., Hirosawa, T., Hasegawa, C., Iwasaki, S., Kikuchi, M., & Kim, K. (2021). Detection of the 40-Hz auditory steady-state response with optically pumped magnetometers. bioRxiv 2021.10.01.462598; https://doi.org/10.1101/2021.10.01.462598
20. Borna, A., Carter, T. R., Colombo, A. P., Jau, Y.-Y. U., Mckay, J., Weisend, M., Taulu, S., Stephen, J. M., & Schwindt, P. D. D. (2020). Non-invasive functional-brain-imaging with an OPM-based magnetoencephalography system. *PLoS One*, *15*, e0227684.
21. Borna, A., Carter, T. R., Goldberg, J. D., Colombo, A. P., Jau, Y.-Y. U., Berry, C., Mckay, J., Stephen, J., Weisend, M., & Schwindt, P. D. D. (2017). A 20-channel magnetoencephalography system based on optically pumped magnetometers. *Physics in Medicine and Biology*, *62*(23), 8909–8923.
22. Griffith, W. C., Knappe, S., & Kitching, J. (2010). Femtotesla atomic magnetometry in a microfabricated vapor cell. *Optics Express*, *18*, 27167–27172.
23. Iivanainen, J., Zetter, R., Grön, M., Hakkarainen, K., & Parkkonen, L. (2019). On-scalp MEG system utilizing an actively shielded array of optically-pumped magnetometers. *Neuroimage*, *194*, 244–258.
24. Iivanainen, J., Zetter, R., & Parkkonen, L. (2019). Potential of on-scalp MEG: Robust detection of human visual gamma-band responses. *Human Brain Mapping*, *41*, 150–161.
25. Johnson, C., Schwindt, P. D. D., & Weisend, M. (2010). Magnetoencephalography with a two-color pump-probe, fiber-coupled atomic magnetometer. *Applied Physics Letters*, *97*(24), 243703.
26. Johnson, C. N., Schwindt, P. D., & Weisend, M. (2013). Multi-sensor magnetoencephalography with atomic magnetometers. *Physics in Medicine & Biology*, *58*(17), 6065–6077.
27. Kamada, K., Sato, D., Ito, Y., Natsukawa, H., Okano, K., Mizutani, N., & Kobayashi, T. (2015). Human magnetoencephalogram measurements using newly developed compact module of high-sensitivity atomic magnetometer. *Japanese Journal of Applied Physics*, *54*(2), Article number 026601.
28. Kominis, I. K., Kornack, T. W., Allred, J. C., & Romalis, M. V. (2003). A subfemtotesla multichannel atomic magnetometer. *Nature*, *422*(6932), 596–599.
29. Xia, H., Ben-Amar Baranga, A., Hoffman, D., & Romalis, M. V. (2006). Magnetoencephalography with an atomic magnetometer. *Applied Physics Letters*, *89*, 211104.
30. Shah, V., Doyle, C., & Osborne, J. (2020). *Zero field parametric resonance magnetometer with triaxial sensitivity*. Quspin Inc.
31. Marhl, U., Sander, T., & Jazbinšek, V. (2022). Simulation study of different OPM-MEG measurement components. *Sensors*, *22*, 3184.
32. Brookes, M. J., Boto, E., Rea, M., Shah, V., Osborne, J., Holmes, N., Hill, R. M., Leggett, J., Rhodes, N., & Bowtell, R. (2021). Theoretical advantages of a triaxial optically pumped magnetometer magnetoencephalography system. *Neuroimage*, *236*, 118025.
33. Boto, E., Shah, V., Hill, R. M., Rhodes, N., Osborne, J., Doyle, C., Holmes, N., Rea, M., Leggett, J., Bowtell, R., & Brookes, M. J. (2022). Triaxial detection of the neuromagnetic field using optically pumped magnetometry: Feasibility and application in children. *Neuroimage*, *252*, 119027.
34. Nardelli, N. V., Perry, A. R., Krzyzewski, S. P., & Knappe, S. A. (2020). A conformal array of microfabricated optically-pumped first-order gradiometers for magnetoencephalography. *EPJ Quantum Technology*, *7*, 11.
35. Holmes, N., Leggett, J., Boto, E., Roberts, G., Hill, R. M., Tierney, T. M., Shah, V., Barnes, G. R., Brookes, M. J., & Bowtell, R. (2018). A bi-planar coil system for nulling background magnetic fields in scalp mounted magnetoencephalography. *Neuroimage*, *181*, 760–774.
36. Holmes, N., Tierney, T. M., Leggett, J., Boto, E., Mellor, S., Roberts, G., Hill, R. M., Shah, V., Barnes, G. R., Brookes, M. J., & Bowtell, R. (2020). Balanced, bi-planar magnetic field and field gradient coils for field compensation in wearable magnetoencephalography. *Scientific Reports*, *9*, 14196.
37. Rea, M., Holmes, N., Hill, R. M., Boto, E., Leggett, J., Edwards, L. J., Woolger, D., Dawson, E., Shah, V., Osborne, J., Bowtell, R., & Brookes, M. J. (2021). Precision magnetic field modelling and control for wearable magnetoencephalography. *Neuroimage*, *241*, 118401.
38. Roberts, G., Holmes, N., Alexander, N., Boto, E., Leggett, J., Hill, R. M., Shah, V., Rea, M., Vaughan, R., Maguire, E. A., Kessler, K., Beebe, S., Fromhold, M., Barnes, G. R., Bowtell, R., & Brookes, M. J. (2019). Towards magnetoencephalography in a virtual reality environment. *Neuroimage*, *199*, 408–417.

39. Salmelin, R., & Hari, R. (1994). Spatiotemporal characteristics of sensorimotor neuromagnetic rhythms related to thumb movement. *Neuroscience*, *60*(2), 537–550.
40. Jasper, H., & Penfield, W. (1949). Electrocorticograms in man: Effect of voluntary movement upon the electrical activity of the precentral gyrus. *Archiv Für Psychiatrie Und Nervenkrankheiten*, *183*(1), 163–174.
41. Finn, E. S., Shen, X., Scheinost, D., Rosenberg, M. D., Huang, J., Chun, M. M., Papademetris, X., & Constable, R. T. (2015). Functional connectome fingerprinting: Identifying individuals using patterns of brain connectivity. *Nature Neuroscience*, *18*(11), 1664–1671.
42. Da Silva Castanheira, J., Orozco Perez, H. D., Misic, B., & Baillet, S. (2021). Brief segments of neurophysiological activity enable individual differentiation. *Nature Communications*, *12*(1), 5713.
43. Sareen, E., Zahar, S., Van De Ville, D., Gupta, A., Griffa, A., & Amico, E. (2021). Exploring MEG brain fingerprints: Evaluation, pitfalls, and interpretations. *Neuroimage*, *240*, 118331.
44. Altarev, I., Babcock, E., Beck, D., Burghoff, M., Chesnevskaya, S., Chupp, T., Degenkolb, S., Fan, I., Fierlinger, P., Frei, A., Gutsmiedl, E., Knappe-Grüneberg, S., Kuchler, F., Lauer, T., Link, P., Lins, T., Marino, M., Mcandrew, J., Niessen, B., … Zechlau, T. (2014). A magnetically shielded room with ultra low residual field and gradient. *Review of Scientific Instruments*, *85*(7), 075106.
45. Hill, R. M., Boto, E., Rea, M., Holmes, N., Leggett, J., Coles, L. A., Papastavrou, M., Everton, S. K., Hunt, B. A. E., Sims, D., Osborne, J., Shah, V., Bowtell, R., & Brookes, M. J. (2020). Multi-channel whole-head OPM-MEG: Helmet design and a comparison with a conventional system. *Neuroimage*, *219*, 116995.
46. Zetter, R., Iivanainen, J., & Parkkonen, L. (2019). Optical co-registration of MRI and on-scalp MEG. *Scientific Reports*, *9*, 5490.
47. Nolte, G. (2003). The magnetic lead field theorem in the quasi-static approximation and its use for magnetoencephalography forward calculation in realistic volume conductors. *Physics in Medicine & Biology*, *48*, 3637–3652.
48. Oostenveld, R., Fries, P., Maris, E., & Schoffelen, J. M. (2011). FieldTrip: Open source software for advanced analysis of MEG, EEG, and invasive electrophysiological data. *Computational Intelligence and Neuroscience*, *2011*, 156869.
49. Sekihara, K., Nagarajan, S. S., Poeppel, D., & Marantz, A. (2004). Performance of an MEG adaptive-beamformer source reconstruction technique in the presence of additive low-rank interference. *Ieee Transactions on Bio-Medical Engineering*, *51*, 90–99.
50. Vrba, J., & Robinson, S. E. (2001). Signal processing in magnetoencephalography. *Methods*, *25*(2), 249–271.
51. Tzourio-Mazoyer, N., Landeau, B., Papathanassiou, D., Crivello, F., Etard, O., Delcroix, N., Mazoyer, B., & Joliot, M. (2002). Automated anatomical labeling of activations in SPM using a macroscopic anatomical parcellation of the MNI MRI single-subject brain. *Neuroimage*, *15*, 273–289.
52. Brookes, M. J., Woolrich, M. W., & Barnes, G. R. (2012). Measuring functional connectivity in MEG: A multi-variate approach insensitive to linear source leakage. *Neuroimage*, *63*, 910–920.
53. Hipp, J. F., Hawellek, D. J., Corbetta, M., Siegel, M., & Engel, A. K. (2012). Large-scale cortical correlation structure of spontaneous oscillatory activity. *Nature Neuroscience*, *15*(6), 884–890.
54. Boto, E., Hill, R. M., Rea, M., Holmes, N., Seedat, Z. A., Leggett, J., Shah, V., Osborne, J., Bowtell, R., & Brookes, M. J. (2021). Measuring functional connectivity with wearable MEG. *Neuroimage*, *230*, 117815.
55. Nurminen, J., Taulu, S., Nenonen, J., Helle, L., Simola, J., & Ahonen, A. (2013). Improving MEG performance with additional tangential sensors. *IEEE Transactions on Biomedical Engineering*, *60*, 2559–2566.
56. Taulu, S., Simola, J., & Kajola, M. (2005). Applications of the signal space separation method. *Ieee Transactions on Signal Processing*, *53*, 3359–3372.
57. Borna, A., Iivanainen, J., Carter, T. R., McKay, J., Taulu, S., Stephen, J., & Schwindt, P. D. D. (2022). Cross-axis projection error in optically pumped magnetometers and its implication for magnetoencephalography systems. *Neuroimage*, *247*, 118818.
58. Yan, Y., Lu, J., Zhang, S., Lu, F., Yin, K., Wang, K., Zhou, B., & Liu, G. (2022). Three-axis closed-loop optically pumped magnetometer operated in the SERF regime. *Optics Express*, *30*(11), 18300–18309.
59. Pang, M., Huang, Z., Wu, H., Ding, Z., & Han, B.. Thermal analysis of wearable OPM-MEG array system for auditory evoked experiments. *IEEE Sensors*, *22*, 4514–4523.
60. Holmes, N., Rea, M., Hill, R. M., Boto, E., Stuart, A., Leggett, J., Edwards, L. J., Rhodes, N., Shah, V., Osborne, J., Fromhold, T. M., Glover, P., Montague, P. R., Brookes, M. J., & Bowtell, R. (2021). Naturalistic hyperscanning with wearable magnetoencephalography. https://doi.org/10.1101/2021.09.07.459124
61. Kim, S.-G. I., Ashe, J., Hendrich, K., Ellermann, J. M., Merkle, H., Uğurbil, K., & Georgopoulos, A. P. (1993). Functional magnetic resonance imaging of motor cortex: Hemispheric asymmetry and handedness. *Science*, *261*, 615–617.
62. Singh, L. N., Higano, S., Takahashi, S., Kurihara, N., Furuta, S., Tamura, H., Shimanuki, Y., Mugikura, S., Fujii, T., Yamadori, A., Sakamoto, M., & Yamada, S. (1998). Comparison of ipsilateral activation between right and left handers: A functional MR imaging study. *Neuroreport*, *9*, 1861–1866.
63. Hall, E. L., Robson, S. E., Morris, P. G., & Brookes, M. J. (2014). The relationship between MEG and fMRI. *Neuroimage*, *102*, 80–91.
64. Planton, S., Jucla, M., Roux, F.-E., & Démonet, J. F. (2013). The "handwriting brain": A meta-analysis of neuroimaging studies of motor versus orthographic processes. *Cortex*, *49*(10), 2772–2787.
65. Saarinen, T., Kujala, J., Laaksonen, H., Jalava, A., & Salmelin, R. (2020). Task-modulated corticocortical synchrony in the cognitive-motor network supporting handwriting. *Cerebral Cortex*, *30*(3), 1871–1886.
66. Larson, E., & Taulu, S. (2017). The importance of properly compensating for head movements during MEG acquisition across different age groups. *Brain Topography*, *30*, 172–181.
67. Messaritaki, E., Koelewijn, L., Dima, D. C., Williams, G. M., Perry, G., & Singh, K. D. (2017). Assessment and elimination of the effects of head movement on MEG resting-state measures of oscillatory brain activity. *Neuroimage*, *159*, 302–324.
68. Nenonen, J., Nurminen, J., Kičić, D., Bikmullina, R., Lioumis, P., Jousmäki, V., Taulu, S., Parkkonen, L., Putaala, M., & Kähkönen, S. (2012). Validation of head movement correction and spatiotemporal signal space separation in magnetoencephalography. *Clinical Neurophysiology*, *123*(11), 2180–2191.
69. Stolk, A., Todorovic, A., Schoffelen, J.-M., & Oostenveld, R. (2013). Online and offline tools for head movement compensation in MEG. *Neuroimage*, *68*, 39–48.
70. Taulu, S., & Simola, J. (2006). Spatiotemporal signal space separation method for rejecting nearby interference in MEG measurements. *Physics in Medicine & Biology*, *51*(7), 1759.
71. Wehner, D. T., Hämäläinen, M. S., Mody, M., & Ahlfors, S. P. (2008). Head movements of children in MEG: Quantification, effects on source estimation and compensation. *Neuroimage*, *40*, 541–550.

How to cite this article: Rea, M., Boto, E., Holmes, N., Hill, R., Osborne, J., Rhodes, N., Leggett, J., Rier, L., Bowtell, R., Shah, V., & Brookes, M. J. (2022). A 90-channel triaxial magnetoencephalography system using optically pumped magnetometers. *Ann NY Acad Sci*., 1–18. https://doi.org/10.1111/nyas.14890

Chapter 6

Naturalistic hyperscanning with wearable MEG

bioRxiv, 2021, 459124

Naturalistic hyperscanning with wearable magnetoencephalography

Niall Holmes[1]*, Molly Rea[1], Ryan M. Hill[1], Elena Boto[1], Andrew Stuart[2], James Leggett[1], Lucy J. Edwards[1], Natalie Rhodes[1], Vishal Shah[3], James Osborne[3], T. Mark Fromhold[2], Paul Glover[1], P. Read Montague[4], Matthew J. Brookes[1] and Richard Bowtell[1].

[1]Sir Peter Mansfield Imaging Centre, School of Physics and Astronomy, University of Nottingham, University Park, Nottingham, NG7 2RD, U.K.

[2]School of Physics and Astronomy, University of Nottingham, University Park, Nottingham, NG7 2RD, U.K.

[3]QuSpin Inc., 331 South 104th Street, Suite 130, Louisville, 80027, Colorado, U.S.A.

[4]Fralin Biomedical Research Institute, Department of Physics, Virginia Tech, Roanoke, 24016, Virginia, U.S.A.

Abstract

The evolution of human cognitive function is reliant on complex social interactions which form the behavioural foundation of who we are. These social capacities are subject to dramatic change in disease and injury; yet their supporting neural substrates remain poorly understood. Hyperscanning employs functional neuroimaging to simultaneously assess brain activity in two individuals and offers the best means to understand the neural basis of social interaction. However, present technologies are limited, either by poor performance (low spatial/temporal precision) or unnatural scanning environment (claustrophobic scanners, with interactions via video). Here, we solve this problem by developing a new form of hyperscanning using wearable magnetoencephalography (MEG). This approach exploits quantum sensors for MEG signal detection, in combination with high-fidelity magnetic field control – afforded by a novel "matrix coil" system – to enable simultaneous scanning of two freely moving participants. We demonstrate our approach in a somatosensory task and an interactive ball game. Despite large and unpredictable subject motion, sensorimotor brain activity was delineated clearly in space and time, and correlation of the envelope of neuronal oscillations between people was demonstrated. In sum, unlike existing modalities, wearable-MEG combines high fidelity data acquisition and a naturalistic setting, which will facilitate a new generation of hyperscanning.

1. Introduction

Human social interaction is at the core of healthy neurodevelopment. From tactile stimulation to the evolution of language, from information transfer to social development, how we interact with others shapes everything from our abilities and skills to our personalities. However, relatively little is known about the neural underpinnings of these interactions. The simultaneous recording of functional brain imaging data from multiple people (hyperscanning) offers a powerful tool to probe brain activity underlying social interaction (Hari et al., 2015; Hari and Kujala, 2009). However, the available functional imaging technology places severe limitations on experimental design, participant experience, and data quality (Czeszumski et al., 2020). We aim to address these issues by developing a fundamentally new technique for hyperscanning, offering high performance, and the opportunity for naturalistic social interactions.

Functional magnetic resonance imaging (fMRI) offers assessment of brain activity with high spatial resolution, but the requirement that participants be enclosed and motionless in a noisy scanner makes natural interactions during hyperscanning impossible. Whilst MRI can be adapted to scan two people simultaneously (Lee et al., 2012; Renvall et al., 2020), this results in a claustrophobic environment which offers limited possibilities for experimental design. Most fMRI hyperscanning studies (King-Casas et al., 2005; Montague et al., 2002) have used separate scanners connected via video, but this also imposes barriers to natural interaction. In addition, the latency and longevity of the haemodynamic signal makes it challenging to assess brain dynamics.

In contrast, functional near infrared spectroscopy (fNIRS) (Ferrari and Quaresima, 2012) and electroencephalography (EEG) (Lopes da Silva, 2013) are wearable technologies that can be deployed in real-life settings (Dikker et al., 2017; Leong et al., 2017; Reindl et al., 2018), enabling more naturalistic hyperscanning. However, fNIRS suffers poor spatial resolution and (like fMRI) is limited to haemodynamic measurement. EEG, via assessment of scalp-level electrical potentials, directly measures brain electrophysiology and consequently has excellent temporal resolution, but suffers from poor spatial resolution and is sensitive to artefacts from non-neuronal sources of electrical activity, especially muscles during participant movement (Muthukumaraswamy, 2013).

Magnetoencephalography (MEG) measures the magnetic fields generated by neuronal currents (Cohen, 1968), providing direct assessment of electrophysiology. Unlike EEG, MEG has high spatial precision (Baillet, 2017; Hämäläinen et al., 1993) and lower sensitivity to non-neuronal artefact (Boto et al., 2019). However, MEG systems use cryogenically cooled superconducting quantum interference devices (SQUIDs) (Cohen, 1972) housed in magnetically shielded rooms (MSRs) to gain sufficient sensitivity to measure the neuromagnetic field. Low temperatures mean sensors are positioned in a fixed array, 2 – 3 cm from the scalp (to provide thermal insulation). So, like MRI scanners, MEG systems are cumbersome and static; only one person can be scanned at once, participants must remain

motionless, and performance is limited by sensor proximity. Nevertheless, the potential for hyperscanning has been demonstrated using two MEG systems sited in the same MSR (Hirata et al., 2014), or geographically displaced systems connected via video (Baess et al., 2012; Zhdanov et al., 2015). Sequential dual-brain imaging studies have also been performed (Levy et al., 2021, 2017) with participants viewing videos of social interaction.

In sum, hyperscanning experiments can be carried out with existing technology, and such studies are beginning to provide unique insights into how the human brain mediates social interaction (Czeszumski et al., 2020). However, current instrumentation is limited either by its performance (EEG/fNIRS) or the unnatural scanning environment it provides (MEG/fMRI). The development of new technology which can scan two people during *live naturalistic interaction*, and provide *high spatiotemporal resolution, artefact free, data* could transform this field.

Recently, 'wearable' MEG has been developed through the use of optically pumped magnetometers (OPMs) (Boto et al., 2018). OPMs are sensitive magnetic field sensors that *do not require cryogenics*. These devices have enabled the design of flexible MEG sensor arrays which can be placed closer to the scalp, and adapted to the requirements of individual studies and participants. Increased proximity to the scalp improves sensitivity and spatial resolution beyond that which is achieved using cryogenic MEG (Boto et al., 2016; Iivanainen et al., 2017). In addition, the lightweight nature of OPMs has enabled the development of wearable systems which allow participants to move during recordings. This motion tolerance, coupled with provision of high-fidelity data, offers an ideal platform for hyperscanning.

However, to achieve sensitivity to the MEG signal, OPM-MEG requires a strict zero magnetic field environment (Allred et al., 2002). Further, OPMs are vector magnetometers meaning any movement of a sensor through a non-zero background field will generate artefacts that mask brain activity and can saturate sensor outputs. These constraints mean OPM-MEG experiments involving participant motion not only require an MSR, but also 'active' magnetic shielding in the form of electromagnetic coils which cancel any residual magnetic field experienced by the array (Borna et al., 2020; Holmes et al., 2019, 2018; Iivanainen et al., 2019). Such shielding systems have been shown to allow participant motion during MEG studies (Boto et al., 2018; Holmes et al., 2018). This has enabled the recording of brain activity in individual participants undertaking naturalistic tasks (Boto et al., 2018) and exploring virtual reality environments (Roberts et al., 2019), as well as the investigation of cognitive function (Tierney et al., 2018), cerebellar (Lin et al., 2019) and hippocampal (Barry et al., 2019; Tierney et al., 2021) activity, functional connectivity (Boto et al., 2021) and epilepsy (Vivekananda et al., 2020) using a lifespan compliant system (Hill et al., 2019). Such studies demonstrate the power of OPM-MEG as a neuroscientific tool. Nevertheless, active shielding has, until now, only enabled movements within a pre-specified volume at the centre of an MSR and present OPM-MEG systems could not be deployed for hyperscanning.

Here, we describe the technical developments required to overcome this limitation, thus allowing the first OPM-MEG hyperscanning experiments to be performed. The key enabling advance is the 'matrix-coil' system. Unlike previous active magnetic shielding systems, this allows accurate field control anywhere within the volume surrounded by the coil set. Moreover, by positioning two spatially separated zero-field regions over OPM arrays worn by interacting participants, we provide the environment needed for the collection of high-quality MEG data in two-person experiments. In what follows, we describe the matrix coil and provide examples of its use in both hyperscanning and single-participant experiments.

2. Results

Two-person touching task

We first explored the capabilities of OPM-MEG hyperscanning by conducting a simple, guided, two-person touch experiment. Each participant wore an OPM-MEG helmet containing 16 OPMs placed over left sensorimotor cortex. Each OPM is a small integrated unit incorporating a heated cell containing a vapor of rubidium-87 atoms, a 795-nm wavelength diode laser tuned to the D1 transition of rubidium, and a photodetector. Following optical pumping, the rubidium atoms are insensitive to photons of the polarised laser light at zero magnetic field and thus the intensity of the light which passes through the cell to the photodetector is at a maximum. Changes in the magnetic field experienced by the cell result in a decrease in the measured laser intensity as photons are absorbed by the atoms (Dupont-Roc et al., 1969; Shah and Wakai, 2013). This means the photodetector signal can be used as a sensitive measure of magnetic field. Our OPM-MEG system uses arrays of QuSpin Inc. (Louisville, Colorado, USA) Zero Field Magnetometers, which each have a dynamic range of ±5 nT, a noise-floor of <10 fT/√Hz, and a bandwidth of 0-130 Hz (Shah et al., 2018). The OPMs were located on the scalp using 3D printed helmets and a co-registration procedure (Boto et al., 2017; Hill et al., 2020) provided information about the sensor locations relative to brain anatomy.

The experimental setup is shown in Figure 1a. Two participants stood either side of a table, ~65 cm apart. The matrix coil was used to null remnant magnetic field inside the MSR, at the locations of both helmets (thus allowing natural movement for both participants). Upon hearing an audio cue, participant 1 (female, right-handed, age 30, height 172 cm) reached over the table with their right hand and stroked the back of the right hand of participant 2 (male, right-handed, age 25, height 182 cm). Upon a second (different) audio cue, the roles were reversed. Trials were defined as either 'odd' (participant 1 touches participant 2) or 'even' (participant 2 touches participant 1). The sequence was repeated 30 times (60 trials total) with an inter-trial interval of 5 seconds. The movements of the two OPM-MEG helmets were tracked using an optical tracking system.

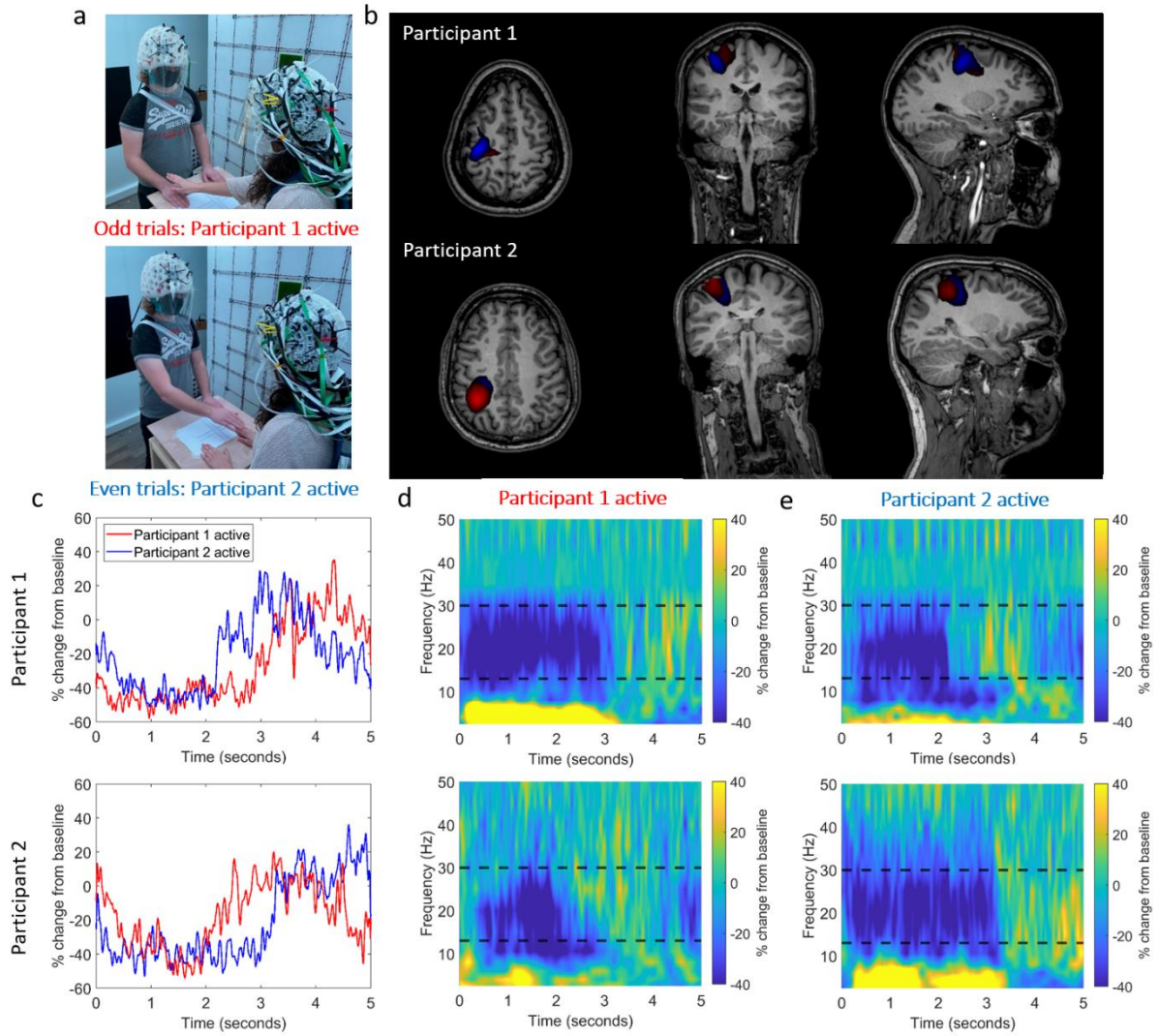

Figure 1: OPM-MEG data collected during a two-person naturalistic touching experiment. *a) Two participants stood either side of a table. In odd numbered trials, participant 1 strokes the right hand of participant 2, with their right hand. In even numbered trials, the roles are reversed. b) Beamformer images show the spatial signature of beta band modulation (thresholded to 80% of the maximum value). The odd trials (participant 1 active) are shown in red and the even trials (participant 2 active) are shown in blue. The spatial pattern suggests activity in the sensorimotor regions. (Note there is a large overlap so the blue overlay is partially obscured). c) Timecourse showing the trial averaged envelope of beta oscillations, extracted from left sensorimotor cortex (peak in the beamformer images). Data from participants 1 and 2 are shown in the top and bottom rows respectively. In both cases, the red trace shows data recorded when participant 1 was touching participant 2. The blue trace shows data recorded when participant 2 was touching participant 1. d) Time-frequency spectra of activity in left sensorimotor cortex. Data were recorded when participant 1 was active. Upper plot shows data from participant 1, lower plot shows data from participant 2. The black dashed lines show the beta band. e) Equivalent to (d) but data shown for when participant 2 was active.*

We hypothesised that beta band (13 – 30 Hz) modulation, as a result of the motor control or sensory response, would be observable in the primary sensorimotor regions. To test this, a beamformer approach (Vrba and Robinson, 2001) tuned to the beta band, was used to derive images of oscillatory modulation during the task. We also performed time-frequency analysis to show modulation of neural oscillations at the location of maximum beta modulation. Figure 1b shows beamformer images contrasting the task (0.5 s < t < 2 s) and control (3 s < t < 4.5 s) time windows. Figures 1c-e show the temporal dynamics of oscillatory power at the peak voxel location. Despite the large head movements which participants made as they reached across the table (maximum translations from the starting position in any one trial were 16 mm and 24 mm, for participants 1 and 2 respectively, the maximum rotations were 3.0° and 7.9° - see supplementary material) the expected task induced reduction in beta amplitude was observed. In each case, the active participant (i.e. the one performing the touch) showed a reduction in beta power that commenced earlier and persisted longer than that seen in the passive participant. This experiment demonstrates that high-quality OPM-MEG hyperscanning data can be obtained using our system, even in the presence of movements.

Two-person ball game

To further demonstrate the system's capabilities, we aimed to show that OPM-MEG hyperscanning can be used to measure brain activity whilst two players hit a table-tennis ball back and forth to one another. Unlike our guided touch task, which where we expected temporally smooth head movements, we expected this task to generate movements that were quicker and more unpredictable. Despite such movement (maximum translations from the starting position in any one trial were 50.0 mm and 64.8 mm, for participants 1 and 2 respectively, the maximum rotations were 17.0° and 17.4°) we hypothesised that the matrix coil system would reduce the remnant field sufficiently to enable collection of useful data; we expected to observe a decrease in beta power in left motor cortices during the task.

The experimental setup is shown in Figure 2a. Participant 1 (see above) and Participant 3 (male, right-handed, age 41, height 188 cm) undertook this experiment. The participants stood ~80 cm apart, each holding a table-tennis bat in their right hand. The remnant magnetic field was nulled using the matrix coil system at the locations of both helmets. An audio cue signalled the participants to begin playing the game, after 5 seconds a second cue signalled the participants to stop the rally and rest for 7 seconds. This process was repeated 25 times and movement of the helmets during the experiment was recorded. Data were processed using a beamformer to derive an image showing the spatial signature of beta modulation between task (2 s < t < 4 s) and control (10 s < t < 12 s) windows. A time frequency spectrum was also extracted from the peak of the beamformer image. Figure 2b shows the beamformer images overlaid on an anatomical MRI. The spatial signature suggests activation in the motor cortex as expected. Figure 2c shows the time-frequency dynamics of oscillatory power, revealing a reduction in the amplitude of beta activity during the task. In addition to overall beta modulation (i.e. the difference

between playing the game and resting) we also expected that, following each strike of the ball, a small amplitude increase in beta power should occur; assuming consistent timings, we expected this effect should alternate between participants (e.g. we expect a peak in activity for participant 1, and a trough in participant 2 just after participant 1 has hit the ball). Analysis was performed to probe the presence of this relationship. Figure 2d shows beta envelopes from both participants; data in the 3 s to 6.5 s time window were extracted and are shown inset in Figure 2e (blue for participant 1, red for participant 2). Autocorrelations of the two timecourses were computed and compared with their cross-correlation (Figure 2e). These data reveal the beta envelopes evolve in anti-correlation, with a lag of ~0.6 s between participants. This direct observation of the correlation of the amplitude envelope of oscillatory brain activity in two participants carrying out a single task highlights the power of hyperscanning.

Matrix coils

OPM-MEG hyperscanning was made possible by our matrix coil, which acts to reduce the strength and spatial variation of the magnetic field surrounding the OPM arrays. This is critical since, to obtain the sensitivity required for MEG, OPMs must be operated at zero-field (Allred et al., 2002; Happer and Tam, 1977; Savukov and Romalis, 2005) requiring sensors to be screened from all sources of static and dynamic magnetic fields. This is achieved, in part, by operating inside MSRs constructed from multiple layers of high magnetic permeability material (mu-metal). However, the presence of the mu-metal leaves a remnant field which can be several 10's of nanotesla (Boto et al., 2018; Hämäläinen et al., 1993; Holmes et al., 2018), meaning that active compensation using electromagnetic coils, which generate an equal and opposite magnetic field to that experienced by the array, is necessary.

1) OPMs typically feature 'on-sensor' coils, which can compensate local static magnetic fields experienced by the OPM, up to ±50 nT. Data are then measured relative to this offset within a narrow dynamic range of around ±5 nT. However, since this compensating field is set at the start of a MEG recording, any subsequent movement of an OPM with respect to the background field induces a change in the measured magnetic field, which affects the data in three main ways: In the worst case, a field shift >5 nT will saturate sensor outputs so that no data can be collected (Holmes et al., 2018; Iivanainen et al., 2019).

2) Even if field shifts are smaller than the dynamic range, the accuracy of measured data is affected by a change in sensor gain; such changes can be as large as 5% for a 1.5 nT field offset (Boto et al., 2018); this nonlinearity causes a significant degradation of data fidelity.

3) Even in cases where a change in field does not cause appreciable modulation of sensor gain, the artefacts caused by rotating the sensor in a field, or translating it in a field gradient, can mask brain activity (e.g. in a 5 nT field, a rotation of just 1° would cause an artefact of ~90 pT, which is ~100 times larger than a typical evoked signal at the scalp (Boto et al., 2017)).

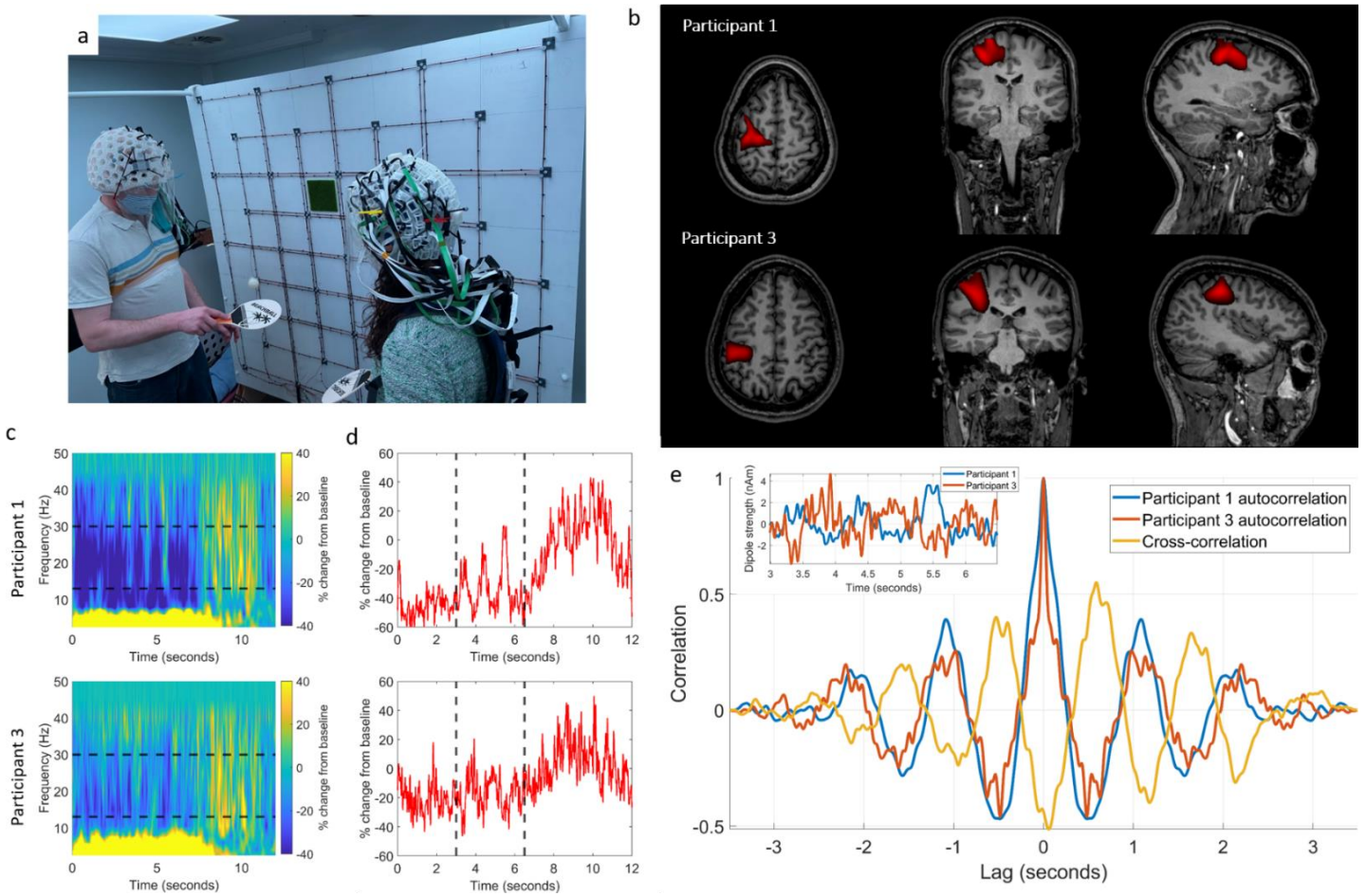

Figure 2: OPM-MEG data collected during a two-person ball game. *a) Two participants each held a table-tennis bat in their right hand and hit the ball back and forth to each other; a 5 s rally was followed by 7 s rest. b) Beamformer images of beta band modulation between task and rest (thresholded to 80% of the maximum value). The spatial pattern suggests beta power reduction in the sensorimotor regions during the rally. c) Time-frequency spectrograms, extracted from left sensorimotor cortex, for participant 1 (top) and participant 3 (bottom). Black dashed lines show the beta band. d) Timecourses of the envelope of beta band activity (again participant 1 top, and participant 3 bottom). Data suggest anti-correlation between 3 and 6.5 seconds (marked with black dashed lines). e) Inset: the timecourses extracted in the 3 – 6.5 second window and overlaid. Main: comparison of the autocorrelations of the two extracted timecourses (blue/red) with their cross-correlation (yellow) reveals anticorrelation with a lag of ~0.6 s between the participants' brain activity.*

For these reasons, creating a zero magnetic field environment is crucial for enabling OPM operation.

To address these issues, we developed a system of matrix coils, comprising two 1.6 x 1.6 m^2 planes, each containing 24, individually controllable, square coils. Each coil has a square side length of 38 cm and is formed of 10 turns of copper wire. A regular 4 x 4 grid of these coils is wound onto each plane along with an overlapping (to allow finer field control in off-axis directions) 3 x 3 grid of coils (excluding the central coil), as shown in Figure 3a. The coil planes were separated by 150 cm and positioned such that the centre of the coil array was at a height of 130 cm from the floor, with the array spanning a height range of 50 to 210 cm. By measuring the remnant magnetic field inside the MSR experienced by each OPM (projected along its sensitive axes) in the helmet, along with a calibration matrix containing the magnetic field generated per unit current, at each OPM, by each of the 48 matrix coils, we can compute the coil currents that will optimally null the magnetic field experienced by the array. This data-driven approach is easily extended to two separate arrays, and provides a low field environment for OPM-MEG experiments which can be readily adapted to the requirements of different paradigms. Participants are required to remain still during the nulling process, but the nulled volumes can be placed at any location between the coils, meaning that an experiment can be carried-out with a single participant standing or seated, or with multiple participants.

To demonstrate the effectiveness of the coils, the two-person experiments, described above, were repeated without the coils activated. We expected that the strength and spatial variation of the magnetic field over the helmet would increase when the coils were switched off, such that the artefacts generated by movements would obfuscate the neural response.

Figure 3a shows the distribution of coil currents required to cancel the magnetic field experienced by the OPMs in the two helmets during the ball game task (the colour of each coil represents the amplitude of the applied current). Figures 3b and 3c show the level of field cancellation achieved over each helmet, for the guided touch and ball game tasks respectively. In both cases, the mean and standard deviation of the absolute values of the remnant magnetic fields, reported by the nulling sensors are shown. During the touch task the remnant field decreased from 3.3 ± 1.8 nT to 0.48 ± 0.44 nT (a factor of 6.9) for participant 1 and from 4.1 ± 2.2 nT to 0.43 ± 0.40 nT (a factor of 9.5) for participant 2. During the two-person ball game the field decreased from 3.8 ± 2.8 nT to 1.6 ± 1.3 nT (a factor of 2.4) for participant 1 and from 5.7 ± 2.9 nT to 2.0 ± 1.2 nT (a factor of 2.9) for participant 3.

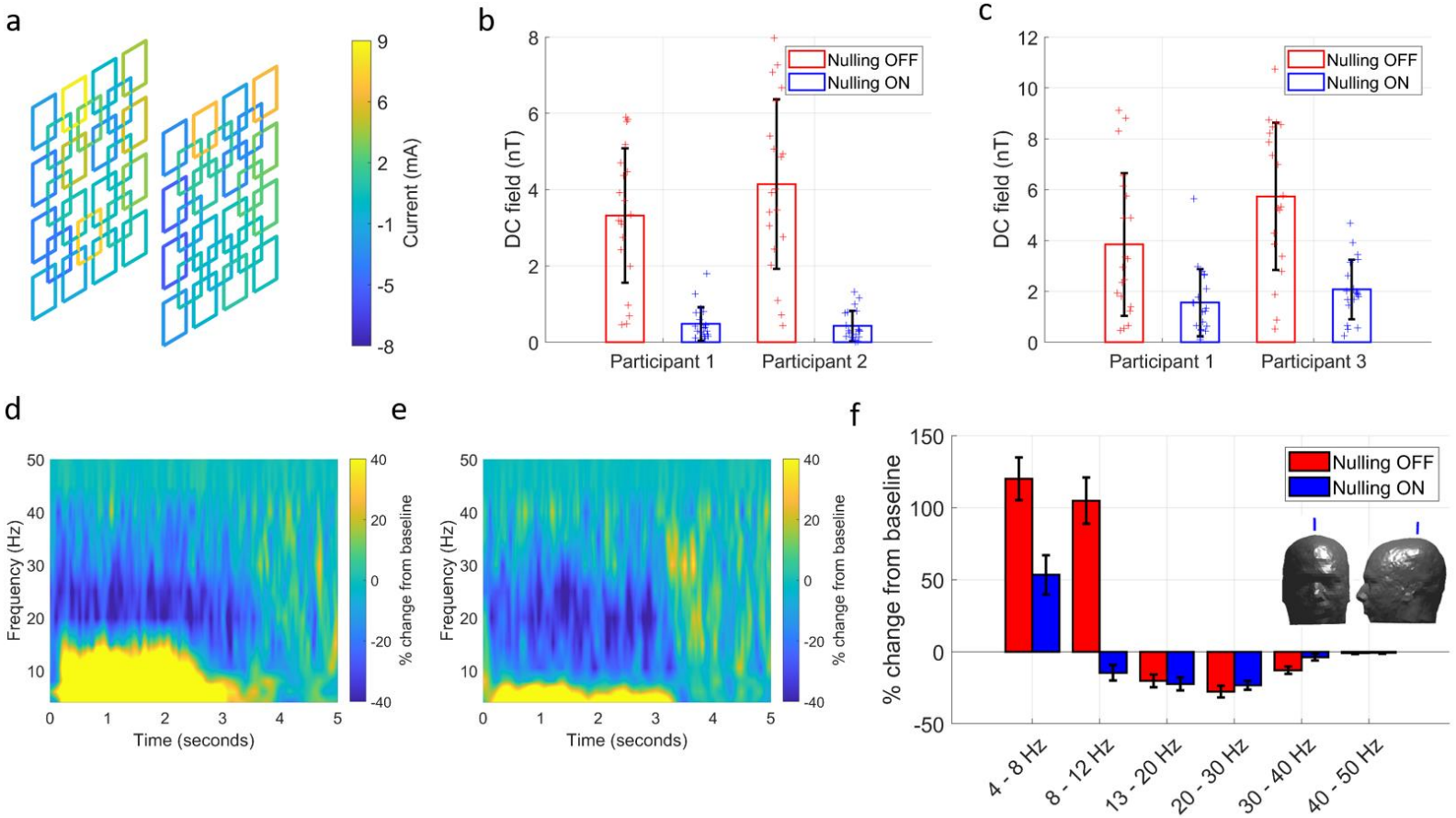

Figure 3: The matrix coil system and its effects on the background magnetic field and data quality. *a) The 48-coil bi-planar matrix coil system. The current in each coil is individually controlled to generate the required field in order to cancel the remnant magnetic field inside the MSR. The current distribution shown was used during the two-person ball game. b) The strength of the DC field, reported by the 48 total field measurements from 24 OPMs (12 per participant), with and without the matrix coils active, during the two-person touch task. The error bars show standard error across sensors. c) Equivalent to (b) for the 2 person ball game. d/e) Sensor-level time-frequency spectra of a single OPM over the sensorimotor cortex of participant 2, during the touching task. Data are recorded without (d) and with (e) matrix coils active. Note how data, particularly in the 10-15 Hz band, are corrupted with artefact when the remnant field is not compensated. f) Comparison of task-induced oscillatory change across all frequencies, with (blue) and without (red) field nulling. Values represent percentage change from baseline. Again, results show that movement artefact masks alpha desynchronisation. Inset images show the location of the sensor.*

To further demonstrate the effectiveness of the matrix coil system, we undertook a sensor level analysis. Figures 3d-e show trial averaged time frequency spectrograms from an OPM placed over the left motor cortex of participant 2, during the touching experiment (even trials). Panel d shows the case when the matrix coils were inactive and panel e shows equivalent data, from the same sensor, when the matrix coil system was used. with the system inactive, large positive changes from baseline spectral density extend across the alpha and beta bands. However, these become negative changes (reflecting the genuine task induced response) when the coil is activated. This degradation is caused by movements of the array through the non-zero remnant field. When activated, the matrix coil reduces the size of the artefacts, revealing the expected response. Figure 3f shows a comparison of the percentage change from baseline of measured oscillatory amplitude, in six key frequency bands, during the task (0.5 to 2 seconds). Mean values are shown, and error bars represent standard error over trials. Most strikingly, alpha desynchronisation is masked when the matrix coil system is not active. These effects show the need for magnetic field compensation during OPM-MEG experiments and highlight the performance and adaptability of the matrix coils.

Solo demonstrations

To further demonstrate the effectiveness of the matrix coil system we conducted a series of ball-game experiments on a single participant (participant 2). 37 OPMs were spread over the helmet to obtain whole-head coverage. On receipt of an audio cue, the participant was instructed to bounce the table-tennis ball on the bat for 10 seconds, until a second audio cue instructed them to rest for 5 seconds. This process was repeated 40 times. The experiment was repeated with and without the matrix coil system activated. Movement of the helmet was recorded. To show the flexibility afforded by the matrix coil system, the participant conducted the task in three different positions: standing, seated on a chair at the centre of the coil, and seated on the floor.

The results show the expected decrease in beta oscillatory power in the left motor cortex during the periods when the participant was bouncing the table-tennis ball. Figures 4a-c show results for the standing, seated on a chair and seated on the floor condition, respectively. For each case, (i) shows the position of the participant during the task, (ii) shows beamformer images of beta modulation contrasting task (2 – 4 s) and rest (8 – 10 s), demonstrating activation of the motor cortices and (iii) shows the degree of DC magnetic field cancellation achieved at each position. (iv) shows the task induced (percentage) change from baseline of oscillatory amplitude in six key frequency bands in data from a single sensor sited over the left motor cortex. These indicate that the alpha band modulation was again obscured without field nulling. We also note the consistency of the field nulling and artefact reduction achieved at each of the three helmet locations.

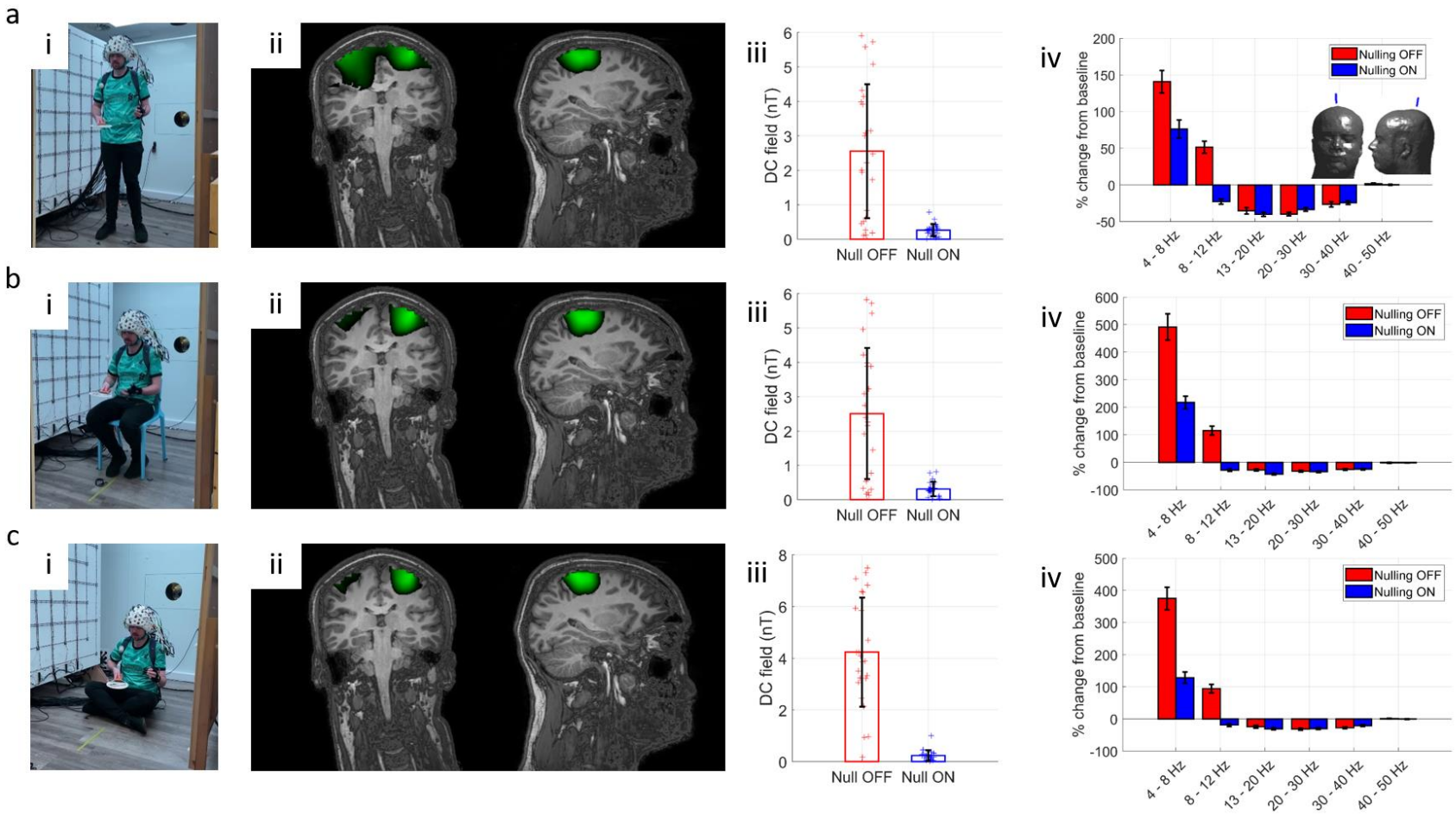

Figure 4: OPM-MEG data collected at various locations in the MSR, enabled by use of the matrix coils. *The three rows show results for cases where the participant was stood up (a), sat on a chair (b) and sat on the floor (c), highlighting the wide range of scanning options afforded by matrix coils. i) Photos of a participant in each position. ii) Beamformer images showing the spatial signature of beta modulation (thresholded to 70% of the maximum value). The spatial pattern suggests activity in the sensorimotor regions when the participant bounces the ball on the bat. Note here all data are taken from the experiment where the matrix coils were active. iii) Bar charts showing the strength of the remnant DC magnetic field, with (blue) and without (red) nulling. iv) Task induced (percentage) change from baseline of neural oscillations in 6 key frequency bands (sensor-level results). As previously, movement artefact masks alpha desynchronisation. Inset shows the chosen sensor location.*

3. Discussion

Brain stimulation in functional imaging is often provided by artificial controlled events, which take place in restrictive, claustrophobic environments. Whilst useful, such experiments are of limited utility for understanding of how the human brain works in its native surroundings. Multi-modal stimuli, such as audio-visual footage and immersive (real or virtual) environments are now routinely deployed to investigate brain function during spontaneous, interactive events which more closely mimic real-life. Such naturalistic settings are crucial for collecting ecologically valid neuroscientific data; indeed it has been postulated that the evolution of the human brain is closely linked to a need for complex social interactions (Dunbar, 1998). For this reason, the importance of developing neuroimaging platforms that can interrogate brain function in naturalistic settings, is paramount. To date, the necessary technology to image brain function has been lacking either in performance or viability. Our work, for the first time, introduces a hyperscanning platform capable of direct detection of electrophysiological responses, with millisecond temporal and millimetre spatial precision, during natural, live interactions.

Our method was enabled by two technological advances, OPMs and matrix coils. Small and lightweight OPMs facilitate the high-precision measurement of magnetic fields generated by neuronal current. Unlike conventional MEG detectors, OPMs do not require cryogenic cooling and so can be placed closer to the head surface, improving data fidelity. Moreover, their lightweight nature allows sensors to move with the head. The flexibility of OPM-MEG has been clearly demonstrated here; an OPM array originally designed for a single participant was split across two helmets allowing simultaneous MEG data acquisition in two people. Accurate knowledge of sensor locations coupled with source analysis allows the derivation of functional images and interrogation of the time-frequency evolution of electrical activity. The synchronised nature of the recordings enables precise analysis of the relative timings of responses across participants. The second critical element of our system is the matrix coil system, which produces the zero-field environment in which the OPMs must be operated. The zero magnetic field requirement of OPMs is a significant barrier to producing wearable MEG systems which tolerate movement. OPMs have a low dynamic range and movement (even in an OPM-optimised MSR with a remnant field of a few nT) can render them inoperable. In addition, a changing field at the sensor induced by participant motion can generate marked changes in OPM sensor gain. Most importantly, movement generates large artefacts which obscure the neuromagnetic field. The use of the matrix coil ensured that OPMs remained operational and minimised gain changes in experiments. Further, motion induced artefacts were minimised; to an extent that, in the absence of matrix coil nulling, the expected alpha event related desynchronisation was completely masked by movement artefact – but recovered with the coil activated.

To demonstrate the adaptability of the matrix coil, we also performed single-person OPM-MEG recordings of a participant standing, seated on a chair and seated on the floor. The robustness of the

spatial signature and temporal dynamics of the reconstructed neuronal activity highlights the utility of the system. It is significant that traditional Helmholtz or bi-planar coil designs are formed from fixed current paths which generate a known magnetic field within a prespecified volume. Such a design enables participant head movement within that volume but does not allow the nulled volume to be moved around the MSR. The matrix approach allows the coil to 're-design itself', altering the current distribution in response to the location of the participant. This allows participants to be positioned anywhere between the coils, and even facilitates the creation of two separate nulled volumes, which is essential for hyperscanning. The modular nature of the matrix coil system also makes its design and construction simple compared to winding the intricate wire paths required by distributed coils systems: complexity is shifted to the coil amplifier and field control systems. Importantly, the data-driven field cancellation approach accounts for any helmet position, coil layout and the magnetic field distortions due to the presence of mu-metal, readily adapting to any size or shape of MSR.

There are some limitations of the present system to consider. Results showed that the performance of the matrix coil system during the two-person ball game was not as good as that during the guided touch or individual person paradigms. This is due to the increased separation of the two participants (required to hit the ball) which pushed the helmets worn by the participants to the edges of the coil planes. Consequently, fewer unit coils were available to contribute to the nulling and so performance was limited. During the standing experiments, the relative heights of the participants and their proximity to the upper-most section of coils had a similar effect. However, this limitation could be readily solved by expanding the coil array. In fact, extension of coil placement onto all six faces of the MSR would enable a wider variety of magnetic fields to be produced, increasing the range of possible experimental setups. Other extensions to our system include enabling the coil control software to account for low-frequency changes in the remnant magnetic field of the room (by imposing feedback controllers on the OPMs' sensitive outputs, updating the coil calibration matrix either via optical tracking and calculation or by applying known oscillating currents to each coil). This would allow participant translations away from the initial nulled volume, paving the way for high-fidelity MEG acquisition in ambulatory participants.

The demonstrations presented in this paper show how hyperscanning can lead to novel findings. For example, our ball game paradigm reveals correlation of brain activity in two interacting participants. Nevertheless, these are simple demonstrations that only hint at the possibilities for OPM-MEG hyperscanning. Previous work has shown myriad possibilities: An excellent example is interactions between babies and their parents - indeed, past studies have employed EEG hyperscanning to show how the brains of a mother and baby demonstrate oscillatory synchronisation during normal social interactions, and that features of social interaction (e.g. eye contact) modulate the level of synchronisation (Leong et al., 2017). This prior work demonstrated the power of hyperscanning, but it

was based upon technology that is limited (EEG is highly motion sensitive, spatial resolution is limited (particularly in infants where electrical potentials are distorted by the fontanelle) and high frequencies (beta and gamma oscillations) are disrupted by artefact). The OPM-MEG technology we have developed overcomes these limitations. Similarly, it offers possibilities for new clinical investigations, for example of social interaction in disorders such as autism.

Ultimately, a true understanding of the brain, and the many disorders that affect it, will only come through the ability to assess naturalistic function. Social interaction is a cornerstone of human development, and so understanding brain function during naturalistic interaction is a critical step along this path. OPM-MEG technology offers a means to do this, with an adaptable scanner equally able to scan one person or two people, using the same instrumentation, providing high fidelity measurements of brain activity. OPM-MEG using matrix coil technology thus has the potential to become the method of choice for future multi-person neuroimaging studies.

4. Methods

OPM-MEG system

The OPM MEG system used here (excepting the matrix coils) is described in detail by Hill et al. (Hill et al., 2020); here we outline briefly its main features. The system (shown schematically in Figure 5) is housed inside a MSR which is optimised for OPM operation (MuRoom, Magnetic Shields Limited, Kent UK). The MSR features 4 layers of mu-metal and 1 layer of copper, along with demagnetisation coils (Altarev et al., 2015; Voigt et al., 2013). The typical remnant magnetic fields and field gradients at the centre of the room are of order 2 nT and 2 nT/m, respectively. Note however that for the experiments carried out here, the head was not positioned at the centre of the room and the remnant fields are consequently larger, as can be seen in Figure 4.

Up to 50, second generation, QuSpin Inc. (Colorado, USA) zero-field magnetometers are available for array formation (see Tierney et al. (Tierney et al., 2019) for a review of OPM physics and Osborne et al. (Shah et al., 2018) for specific details of the QuSpin sensor). The OPMs were mounted inside 3D-printed, rigid scanner-casts which allow co-registration of OPM positions and orientations to anatomical MRI's (whole-head MRI scans were generated using a 3 T Philips Ingenia system, running an MPRAGE sequence, at an isotropic spatial resolution of 1 mm) of the participants' heads (Boto et al., 2017; Hill et al., 2020; Zetter et al., 2019). OPMs were configured to record the component of magnetic field which is radial to the surface of the head. OPM data were sampled at 1,200 Hz using a series of National Instruments (NI, Texas, USA) NI-9205 16-bit analogue to digital converters interfaced with LabVIEW (NI, Texas, USA). Since all the OPMs are sampled and controlled using the same equipment, no additional timing signals or hardware are required to synchronise the data collected from the two helmets. Participant movements were tracked using a OptiTrack V120:Duo (NaturalPoint Inc., Corvalis,

USA) optical tracking system which provides sub-1-millimetre and sub-1-degree precision optical tracking of multiple rigid bodies at a sample rate of 120 Hz. Two cameras, each with an array of 15 infrared (IR) LEDs, are used to illuminate IR reflective markers and the combined coordinates of multiple markers are used to form a rigid body tracking with 6 degrees of freedom (x, y and z translations, pitch, yaw and roll rotations).

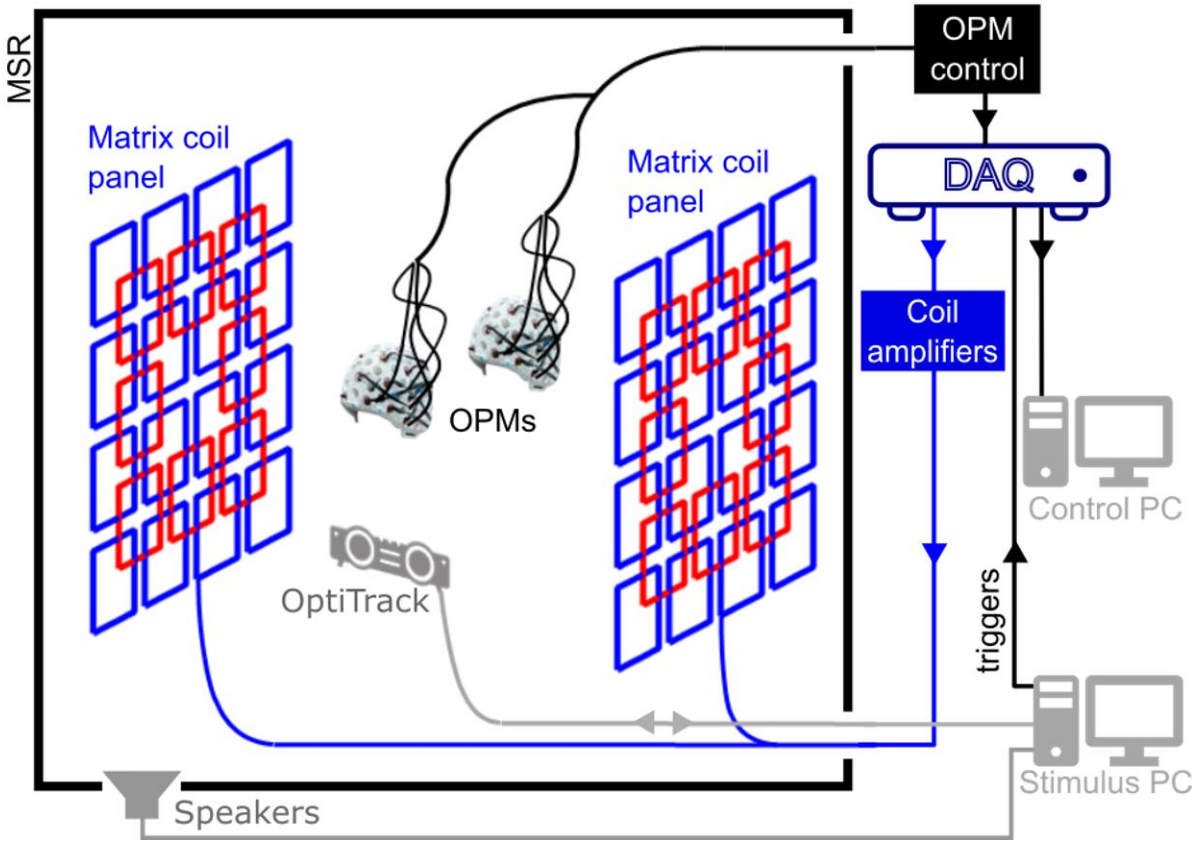

Figure 5: OPM-MEG system schematic. *The system is housed in a magnetically shielded room (MSR). OPMs are interfaced with a series of data acquisition devices. Data from the OPMs are used to drive the matrix coil field nulling process, before a MEG recording begins. Optical tracking of the helmets is performed to monitor motion during a session. Instruction is passed to the participants via auditory cues controlled using a separate stimulus PC.*

Matrix coils

Our aim was to develop a system that produces a magnetic field, equal in magnitude but opposite in direction to the remnant magnetic field within target volume(s) inside the MSR, thereby nulling the field. Matrix-coil systems feature an array of small, simple, unit coils positioned around the participant. Superposition of the magnetic field generated by multiple coils, each carrying an independently controllable current, enables the production of arbitrary patterns of magnetic field variation within a selected target volume (Garda and Galias, 2014; Juchem et al., 2010). Similar multi-coil shimming systems have been developed for MRI (Juchem et al., 2015, 2011). Our matrix coil system was

constructed using a bi-planar design, with each plane containing 24 square coils (square side length 38 cm). The coils are arranged on a 4 x 4 grid with an overlapping 3 x 3 grid in which the central coil is omitted (Figure 3a). Each coil was wound by hand using 10 turns of 0.56 mm diameter copper wire, tightly wrapped around a series of plastic guides attached to a wooden structure (coil resistance ~2 Ω, coil inductance ~160 μH). The two planes are sited on either side of the participant(s), separated by 150 cm.

Each unit coil is connected to a single output of a 48-channel, low-noise, voltage amplifier that was designed and constructed in-house. This is interfaced to three NI-9264 16-bit, digital to analogue converters (DACs) that are controlled using LabVIEW. The voltages applied at the amplifier input range between ±10 V (least significant bit (lsb) voltage = 20 V/2^{16} = 0.305 mV). The maximum electrical current in the coil is tuned by an additional series resistance, which in this setup was 1.2 kΩ, chosen such that the magnetic field noise generated by the coils was beneath the noise floor of the OPMs. The coil driver current noise at this resistance is <10 nA/√Hz in the 1-100 Hz band, we estimate this translates to <20 fT/√Hz noise in the field from all 48 coils at the centre of the planes (see supplementary material), for comparison, the OPM noise floor is <10 fT/√Hz in this frequency range so the two are comparable. The maximum current which can be applied to each coil is ±8.33 mA, and the lsb current is 2.54 μA.

To null the remnant magnetic field inside the MSR during a MEG experiment we employed a data-driven approach. If the magnetic field measured by the n^{th} OPM in an array of N sensors due to unit current in the m^{th} coil in a set of M (= 48) matrix coils is written as db_n/dI_m, we can form a (N x M) coil calibration matrix, $\boldsymbol{A}$, from the full set of values. The field nulling problem can then be described using the following matrix equation:

$$\begin{bmatrix} db_1/dI_1 & db_1/dI_2 & \cdots & db_1/dI_M \\ db_2/dI_1 & db_2/dI_2 & \cdots & db_2/dI_M \\ \vdots & \vdots & \ddots & \vdots \\ db_N/dI_1 & db_N/dI_2 & \cdots & db_N/dI_M \end{bmatrix} \begin{bmatrix} I_1 \\ I_2 \\ \vdots \\ I_M \end{bmatrix} = - \begin{bmatrix} b_1 \\ b_2 \\ \vdots \\ b_N \end{bmatrix}, \quad (1)$$

$$\boldsymbol{Ax} = -\boldsymbol{b}. \quad (2)$$

where the (M x 1) column vector $\boldsymbol{x}$ contains the currents applied to each coil and the (N x 1) column vector $\boldsymbol{b}$ characterises the magnetic field to be cancelled. $\boldsymbol{b}$ is formed using the DC field values measured at the sensors, the negative sign is used to ensure the calculated currents null the magnetic field measured by the array.

The coil currents required to minimise the sum of squares of the measured magnetic field values can be found by identifying the negative of the Moore-Penrose pseudo-inverse matrix of $\boldsymbol{A}$,

$$\boldsymbol{x} = -(\boldsymbol{A}\boldsymbol{A}^T)^{-1}\boldsymbol{A}^T\boldsymbol{b}. \quad (3)$$

To minimise the power dissipated by the system, and ensure the solution is physically realisable, the matrix $\boldsymbol{A}\boldsymbol{A}^T$ can be regularised prior to inversion by addition of a matrix $\alpha\boldsymbol{I}$ where $\boldsymbol{I}$ is the identity matrix of the same dimensions as $\boldsymbol{A}\boldsymbol{A}^T$ and α is a regularisation parameter i.e.

$$\boldsymbol{x} = -(\boldsymbol{A}\boldsymbol{A}^T + \alpha\boldsymbol{I})^{-1}\boldsymbol{A}^T\boldsymbol{b}. \quad (4)$$

To keep the coil currents within the allowed bounds, equation [4] is cast as a feed-forward controller: coil currents are incrementally updated, based on the OPM field measurements at each timepoint i, and the currents applied at the preceding time point as

$$\boldsymbol{x}^i = \boldsymbol{x}^{i-1} - G(\boldsymbol{A}\boldsymbol{A}^T + \alpha\boldsymbol{I})^{-1}\boldsymbol{A}^T\boldsymbol{b}^i. \quad (5)$$

The gain coefficient G is empirically set to produce a stable reduction of the measured fields towards zero on a timescale of a few seconds.

This approach can readily be adapted to changes in the number and shape of the unit coils and flexibly incorporates multiple sensor arrays. However, it only considers the field values at the sensor positions and as a result, unwanted deviations in magnetic field could occur between target points. Coil calibration data for populating the matrix, $\boldsymbol{A}$, can be collected in a variety of ways depending on the available sensing technology e.g. by pulsing each coil in turn or by applying a known sinusoidal current to each coil. Values could also be calculated based on known sensor positions, coil design and geometry of the MSR.

The nulling procedure described above was implemented in LabVIEW. Participants were instructed to remain still whilst a 5 V (4.16 mA), 100 ms pulse was applied to each coil in turn. The change in field experienced by each OPM was measured by interfacing the OPMs with LabVIEW and operating the sensors in their field-zeroing mode. In this mode, QuSpin OPMs can measure the DC magnetic field experienced by the cell (along two orthogonal directions) with a dynamic range of ±50 nT (Shah et al., 2018; Shah and Hughes, 2015). The field zeroing procedure is generally carried out prior to OPM gain calibration when an experiment is performed, providing measurements of the offset magnetic fields required to produce the zero-field environment in the sensor cell. The regularisation parameter α (in Eq. [5]) was set to 1% of the maximum singular value of the matrix $\boldsymbol{A}\boldsymbol{A}^T$. The feed-forward controller gain was set to 0.1 with a time step of 100 ms.

The time needed for the calibration process scales with the number of coils and takes around 1 minute to complete for the 48-coil system. The final coil currents were held constant during the experiments, i.e. no dynamic tracking of changes in magnetic field was applied (we note the magnetic field drift in our MSR is on the order of 200 pT over 10 minutes). The LabVIEW program stores the magnetic field values reported by each sensor prior to calibration, along with the coil calibration matrix, the final voltages applied to each coil and the final magnetic field values.

Data acquisition

All data were collected by the authors. Participants provided written informed consent for all experiments. All studies were approved by the University of Nottingham's Faculty of Medicine and Health Sciences Research Ethics Committee. Additional guidelines to mitigate the risk of transmission of COVID-19 were adhered to by all participants and experimenters: participants wore face masks and visors during the two-person experiments as can be seen in Figures 1 and 2. Audio cues to structure the experiment were single beeps, generated by MATLAB (MathWorks, CA, USA), and played through speakers placed inside waveguides in the top corners of the MSR. MATLAB was also used to generate a trigger signal at the same time as the audio cues which was recorded along with the OPM data for synchronisation.

Guided touch task

For the two-person touching task, each participant wore an array of 16 OPMs mounted in a 3D-printed scanner-cast. Participant 1 (female, aged 30, height 172 cm) wore a scanner-cast which was custom-made for their head based on an anatomical MRI (Chalk Studios, London, UK) meaning that co-registration of the positions and orientations of the OPMs with respect to the participant's brain was known(Boto et al., 2017). Participant 2 (male, aged 25, height 182 cm) wore a rigid, additively manufactured generic scanner-cast (Added Scientific Limited, Nottingham, UK) which was designed to fit an average adult head-shape (Hill et al., 2020). The co-registration of OPM sensors to the anatomy of participant 2 was performed by using 3D structured light scans combined with the known structure of the generic helmet (Hill et al., 2020; Zetter et al., 2019). The positions and orientations of the OPMs used in the experiments for each participant are shown in Figure 6, with the sensors used for field nulling highlighted. Sensors were arranged to cover the left hemisphere with additional sensors placed at the front, back and right sides of the head to extend the region of space over which fields were considered in the nulling process. During the experiment, each participant was instructed to reach over and stroke the right hand of the other participant with their right hand, following an audio cue. The audio cue repeated every 5 seconds and the active participant alternated between trials. Each participant conducted 30 active trials.

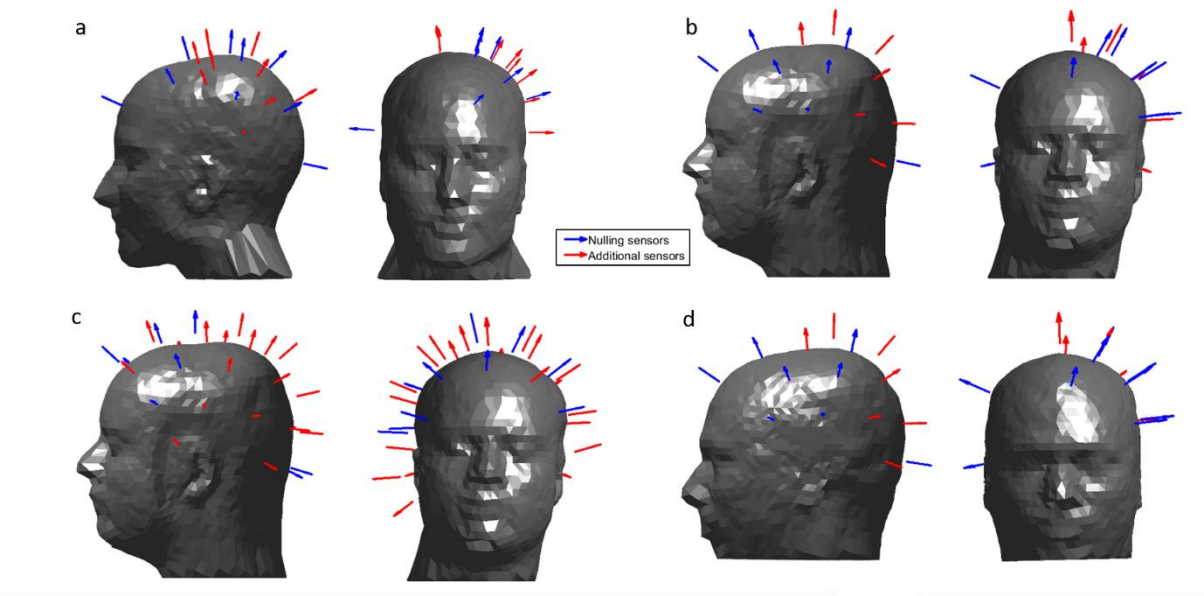

Figure 6: The position and orientation of the OPMs used in each experiment. *Sensors which were used to inform the field nulling are shown in blue and additional sensors are shown in red. During the hyperscanning experiments, sensors were concentrated over the left sensorimotor cortex, with additional sensors placed at the right and the front of the head, to inform the nulling process. Coverage was extended over both hemispheres for the solo ball game. a) Sensor layout for participant 1 during the two-person touch and ball game tasks. b) Sensor layout for participant 2 during the two-person touching task. c) Sensor layout for participant 2 during the solo ball-game task (note coverage of both hemispheres). d) Sensor layout for participant 3 during the two-person ball game.*

Ball game task

During the two-person ball game experiment, participant 1 again wore an individualised scanner cast, whilst participant 3 (and male, aged 41, height 188 cm) wore a generic 3D printed helmet (co-registration as above). The participants were instructed to hit a table-tennis ball back and forth to each other for 5 seconds, following an audio cue. A second audio cue instructed the participants to stop their rally and rest for 7 seconds. This was repeated 25 times. Movement of the two helmets was again tracked using the OptiTrack camera system throughout the experiment. Each Hyperscanning task was repeated twice, with and without the matrix coils active (the participants were not blinded to this condition). Trials where the ball was dropped were noted and excluded from data analysis (two dropped balls in each condition).

Solo experiments

For the solo MEG experiments, a single participant (participant 2) wore the generic scanner-cast containing 37 OPMs distributed over the entire head. During the experiment, the participant was instructed to bounce a table-tennis ball on the bat for 10 seconds following an audio cue. A second audio cue instructed the participants to stop and rest for 5 seconds. This was repeated 40 times.

Recordings were made while the participant stood up at the centre of the coil planes, then sat on a chair and finally sat on the floor of the MSR. The entire process was repeated with and without the matrix coils active. All trials were complete successfully without dropping a ball.

Field nulling

In the hyperscanning experiments, measurements of the amplitude of two field components from 10 OPMs operating in field zeroing mode housed in the scanner-casts of each participant (i.e. the matrix $\boldsymbol{A}$ contains values from 20 OPMs giving $N = 40$ measurements in total) were used as inputs to the LabVIEW-based field nulling program described above. The 10 sensors on each helmet that were used for the nulling process, included the additional sensors sited at the front, back and right-hand sides of the head, as well as seven sensors sited over the left side of the head. Participants were asked to remain still whilst the system was calibrated and instructed to keep their feet planted throughout the experiment to avoid translating their heads away from the nulled volume.

During the solo experiments, The two field components measured by 12 OPMs ($N = 24$ total measurements) operating in field zeroing mode were used as inputs to the field nulling program. Field nulling sensors were chosen such that they spanned the full volume of the head and are highlighted in Figure 6.

OPM settings

All OPM data were collected at a sample rate of 1,200 Hz using the equipment described earlier. Once the matrix coil currents had been set, the OPMs were field zeroed and calibrated using the QuSpin software. The OPMs were then set to their 0.33x gain mode (voltage to magnetic field conversion factor 0.9 V/nT) in which their dynamic range is ±5 nT. The default gain setting has a lower dynamic range of ±1.5 nT (2.7 V/nT) which was not used here as the outputs would have quickly saturated when participants moved during the nulling-off experiments.

Data analysis

All code for analysis was custom written by the authors using MATLAB.

Source reconstruction

A beamformer approach was used to generate the images shown in Figures 1, 2 and 5. An estimate of the neuronal current dipole strength, $\hat{Q}_\theta(t)$, at time t and a position and orientation θ in the brain is formed via a weighted sum of the measured data as

$$\hat{Q}_\theta(t) = \boldsymbol{w}_\theta^T \boldsymbol{m}(t) \tag{6}$$

where $\boldsymbol{m}(t)$ is a vector containing the magnetic field measurements recorded by all OPMs and $\boldsymbol{w}_\theta$ is a weights vector tuned to θ. The weights are chosen such that

$$\min\left[\hat{Q}_\theta^2\right] \text{s.t.} \boldsymbol{w}_\theta^T \boldsymbol{L}_\theta = 1 \quad (7)$$

where $\boldsymbol{L}_\theta$ is the forward field vector containing the solutions to the MEG forward problem for a unit dipole at θ. The optimal weights vector is expressed as

$$\boldsymbol{w}_\theta^T = [\boldsymbol{L}_\theta^T \{\boldsymbol{C} + \mu \boldsymbol{I}\}^{-1} \boldsymbol{L}_\theta]^{-1} \boldsymbol{L}_\theta^T \{\boldsymbol{C} + \mu \boldsymbol{I}\}^{-1} \quad (8)$$

where $\boldsymbol{C}$ is the sensor data covariance matrix. Inversion of the covariance matrix is aided by Tikhonov regularisation (i.e. by addition of the identity matrix scaled by regularisation parameter μ)**.**

To compute the weights vectors for each experiment, the entire dataset was filtered to the beta band (13 – 30 Hz) and used to compute the covariance matrix. The regularisation parameter μ was set to 0.01 times the leading singular value of the covariance matrix. The forward field vector was calculated using a multi-sphere head model and the current dipole approximation (Sarvas, 1987).

Images of activation show the pseudo-T-statistical contrast between data recorded in active and control windows. Specifically, two covariance matrices were computed for the active and control periods, C_a and C_c respectively, and the pseudo-T-statistical contrast, at θ, calculated as

$$\text{Ŧ}_\theta = \frac{\boldsymbol{w}_\theta^T \boldsymbol{C}_a \boldsymbol{w}_\theta - \boldsymbol{w}_\theta^T \boldsymbol{C}_c \boldsymbol{w}_\theta}{2\boldsymbol{w}_\theta^T \boldsymbol{C}_c \boldsymbol{w}_\theta}. \quad (9)$$

Pseudo-T-statistics were computed at the vertices of a regular 4 mm grid spanning the whole brain. This grid of Ŧ values was then thresholded to a percentage of the maximum value and overlaid onto the anatomical MRI of each participant. In the touch experiment the Ŧ values were thresholded to 80% of the maximum value for each condition. The active period was 0.5 to 2 seconds and the control period was 3 to 4.5 seconds. In the two-person ball game the active period was 2 to 4 seconds and the control period was 10 to 12 seconds. In the single-person ball game the Ŧ values were thresholded to 70% of the maximum value, the active period was 2 to 4 seconds and the control period was 8 to 10 seconds.

For each experiment, the location of the voxel with largest pseudo-T-statistic was determined for each participant. The signal from this peak location was reconstructed to form a 'virtual electrode' timecourse (using Equation 6), with beamformer weights calculated in the broad-band (1–150 Hz).

The time-frequency spectra were generated by filtering this timecourse sequentially into overlapping frequency bands. For each band, the Hilbert envelope was calculated before segmenting and averaging over trials and concatenating in the frequency domain. The mean envelope in the beta band was computed using the virtual electrode timecourse filtered to the beta band (13–30 Hz).

Sensor-level analysis

Similar analysis was performed to generate the sensor level time-frequency spectra shown in Figure 3d and 3e. The bar charts comparing change from baseline activity in Figure 3f and 4abc (iv) were computed using contrasting active and control periods, as above, and non-overlapping frequency bands.

Correlating activity

Correlation of brain activity (Figure 2e) was computed using the 3-6.5 s window of the beta band filtered virtual electrode average trial timecourse. The normalised, unbiased, autocorrelation and cross-correlation of the two timecourses were computed for a maximum lag of 3.5 s (i.e. the full duration of the data segment).

Acknowledgements: We express our sincere thanks to collaborators at the Wellcome Centre for Human Neuroimaging, University College London, UK for extremely helpful discussions and ongoing support. We also thank Magnetic Shields Limited who designed and constructed our OPM-optimised magnetically shielded room. This work was supported by the UK Quantum Technology Hub in Sensing and Timing, funded by the Engineering and Physical Sciences Research Council (EPSRC) (EP/T001046/1), a Wellcome Collaborative Award in Science (203257/Z/16/Z and 203257/B/16/Z) and National Institutes of Health grant R01EB028772.

Data and code availability statement: The raw sensor-level data collected in this work (without associated MRIs) will be made publicly available.

Author contributions: The study was designed and conceived by N.H., M.R., T.M.F., P.R.M., M.J.B. and R.B. Experimental equipment was developed by N.H., M.R., R.M.H., A.S., and P.G. Experiments were performed and analysed by N.H., M.R., R.M.H., E.B., J.L., L.J.E., and N.R. All authors contributed to interpreting the results and writing the manuscript.

The authors declare the following competing interests: V.S. is the founding director of QuSpin Inc., the commercial entity selling OPM magnetometers. J.O. is an employee of QuSpin. E.B. and M.J.B. are directors of Cerca Magnetics Limited, a spin-out company whose aim is to commercialise aspects of OPM-MEG technology. E.B., M.J.B., R.B., N.H. and R.H. hold founding equity in Cerca Magnetics Limited. N.H, P.G, M.J.B., and R.B. declare that they have a patent pending to the UK Government Intellectual Property Office (Application No. GB2109459.4) regarding the active magnetic shielding systems described in this work.

References

Allred JC, Lyman RN, Kornack TW, Romalis M V. 2002. High-Sensitivity Atomic Magnetometer Unaffected by Spin-Exchange Relaxation. *Phys Rev Lett*. doi:10.1103/physrevlett.89.130801

Altarev I, Fierlinger P, Lins T, Marino MG, Nießen B, Petzoldt G, Reisner M, Stuiber S, Sturm M, Taggart Singh J, Taubenheim B, Rohrer HK, Schläpfer U. 2015. Minimizing magnetic fields for precision experiments. *J Appl Phys*. doi:10.1063/1.4922671

Baess P, Zhdanov A, Mandel A, Parkkonen L, Hirvenkari L, Mäkelä JP, Jousmäki V, Hari R. 2012. MEG dual scanning: A procedure to study real-time auditory interaction between two persons. *Front Hum Neurosci* **6**:1–7. doi:10.3389/fnhum.2012.00083

Baillet S. 2017. Magnetoencephalography for brain electrophysiology and imaging. *Nat Neurosci*. doi:10.1038/nn.4504

Barry DN, Tierney TM, Holmes N, Boto E, Roberts G, Leggett J, Bowtell R, Brookes MJ, Barnes GR, Maguire EA. 2019. Imaging the human hippocampus with optically-pumped magnetoencephalography. *Neuroimage* **203**. doi:10.1016/j.neuroimage.2019.116192

Borna A, Carter TR, Colombo AP, Jau YY, McKay J, Weisend M, Taulu S, Stephen JM, Schwindt PDD. 2020. Non-invasive functional-brain-imaging with an OPM-based magnetoencephalography system. *PLoS One* **15**:1–24. doi:10.1371/journal.pone.0227684

Boto E, Bowtell R, Krüger P, Fromhold TM, Morris PG, Meyer SS, Barnes GR, Brookes MJ. 2016. On the potential of a new generation of magnetometers for MEG: A beamformer simulation study. *PLoS One* **11**. doi:10.1371/journal.pone.0157655

Boto E, Hill RM, Rea M, Holmes N, Seedat ZA, Leggett J, Shah V, Osborne J, Bowtell R, Brookes MJ. 2021. Measuring functional connectivity with wearable MEG. *Neuroimage* **230**. doi:10.1016/j.neuroimage.2021.117815

Boto E, Holmes N, Leggett J, Roberts G, Shah V, Meyer SS, Muñoz LD, Mullinger KJ, Tierney TM, Bestmann S, Barnes GR, Bowtell R, Brookes MJ. 2018. Moving magnetoencephalography towards real-world applications with a wearable system. *Nature* **555**:657–661. doi:10.1038/nature26147

Boto E, Meyer SS, Shah V, Alem O, Knappe S, Kruger P, Fromhold TM, Lim M, Glover PM, Morris PG, Bowtell R, Barnes GR, Brookes MJ. 2017. A new generation of magnetoencephalography: Room temperature measurements using optically-pumped magnetometers. *Neuroimage*. doi:10.1016/j.neuroimage.2017.01.034

Boto E, Seedat ZA, Holmes N, Leggett J, Hill RM, Roberts G, Shah V, Fromhold TM, Mullinger KJ, Tierney TM, Barnes GR, Bowtell R, Brookes MJ. 2019. Wearable neuroimaging: Combining and contrasting magnetoencephalography and electroencephalography. *Neuroimage* **201**. doi:10.1016/j.neuroimage.2019.116099

Cohen D. 1972. Magnetoencephalography: Detection of the brain's electrical activity with a superconducting magnetometer. *Science (80-)*. doi:10.1126/science.175.4022.664

Cohen D. 1968. Magnetoencephalography: Evidence of magnetic fields produced by alpha-rhythm currents. *Science (80-)*. doi:10.1126/science.161.3843.784

Czeszumski A, Eustergerling S, Lang A, Menrath D, Gerstenberger M, Schuberth S, Schreiber F, Rendon ZZ, König P. 2020. Hyperscanning: A Valid Method to Study Neural Inter-brain Underpinnings of Social Interaction. *Front Hum Neurosci* **14**:1–17. doi:10.3389/fnhum.2020.00039

Dikker S, Wan L, Davidesco I, Kaggen L, Oostrik M, McClintock J, Rowland J, Michalareas G, Van Bavel JJ, Ding M, Poeppel D. 2017. Brain-to-Brain Synchrony Tracks Real-World Dynamic Group Interactions in the Classroom. *Curr Biol* **27**:1375–1380. doi:10.1016/j.cub.2017.04.002

Dunbar RIM. 1998. The social brain hypothesis. *Evol Anthropol* **6**:178–190. doi:10.1002/(SICI)1520-6505(1998)6:5<178::AID-EVAN5>3.0.CO;2-8

Dupont-Roc J, Haroche S, Cohen-Tannoudji C. 1969. Detection of very weak magnetic fields (10–9gauss) by 87Rb zero-field level crossing resonances. *Phys Lett A* **28**:638–639. doi:10.1016/0375-9601(69)90480-0

Ferrari M, Quaresima V. 2012. A brief review on the history of human functional near-infrared spectroscopy (fNIRS) development and fields of application. *Neuroimage* **63**:921–935. doi:10.1016/j.neuroimage.2012.03.049

Garda B, Galias Z. 2014. Tikhonov regularization and constrained quadratic programming for magnetic coil design problems. *Int J Appl Math Comput Sci*. doi:10.2478/amcs-2014-0018

Hämäläinen M, Hari R, Ilmoniemi RJ, Knuutila J, Lounasmaa O V. 1993. Magnetoencephalography theory, instrumentation, and applications to noninvasive studies of the working human brain. *Rev Mod Phys* **65**:413–497. doi:10.1103/RevModPhys.65.413

Happer W, Tam AC. 1977. Effect of rapid spin exchange on the magnetic-resonance spectrum of alkali vapors. *Phys Rev A*. doi:10.1103/PhysRevA.16.1877

Hari R, Henriksson L, Malinen S, Parkkonen L. 2015. Centrality of Social Interaction in Human Brain Function. *Neuron* **88**:181–193. doi:10.1016/j.neuron.2015.09.022

Hari R, Kujala M V. 2009. Brain basis of human social interaction: From concepts to brain imaging. *Physiol Rev* **89**:453–479. doi:10.1152/physrev.00041.2007

Hill RM, Boto E, Holmes N, Hartley C, Seedat ZA, Leggett J, Roberts G, Shah V, Tierney TM, Woolrich MW, Stagg CJ, Barnes GR, Bowtell RR, Slater R, Brookes MJ. 2019. A tool for functional brain imaging with lifespan compliance. *Nat Commun*. doi:10.1038/s41467-019-12486-x

Hill RM, Boto E, Rea M, Holmes N, Leggett J, Coles LA, Papastavrou M, Everton SK, Hunt BAE, Sims D, Osborne J, Shah V, Bowtell R, Brookes MJ. 2020. Multi-channel whole-head OPM-MEG: Helmet design and a comparison with a conventional system. *Neuroimage*. doi:10.1016/j.neuroimage.2020.116995

Hirata M, Ikeda T, Kikuchi M, Kimura T, Hiraishi H, Yoshimura Y, Asada M. 2014. Hyperscanning MEG for understanding mother-child cerebral interactions. *Front Hum Neurosci* **8**:1–6. doi:10.3389/fnhum.2014.00118

Holmes N, Leggett J, Boto E, Roberts G, Hill RM, Tierney TM, Shah V, Barnes GR, Brookes MJ, Bowtell R. 2018. A bi-planar coil system for nulling background magnetic fields in scalp mounted magnetoencephalography. *Neuroimage*. doi:10.1016/j.neuroimage.2018.07.028

Holmes N, Tierney TM, Leggett J, Boto E, Mellor S, Roberts G, Hill RM, Shah V, Barnes GR, Brookes MJ, Bowtell R. 2019. Balanced, bi-planar magnetic field and field gradient coils for field compensation in wearable magnetoencephalography. *Sci Rep*. doi:10.1038/s41598-019-50697-w

Iivanainen J, Stenroos M, Parkkonen L. 2017. Measuring MEG closer to the brain: Performance of on-scalp sensor arrays. *Neuroimage* **147**:542–553. doi:10.1016/j.neuroimage.2016.12.048

Iivanainen J, Zetter R, Grön M, Hakkarainen K, Parkkonen L. 2019. On-scalp MEG system utilizing an actively shielded array of optically-pumped magnetometers. *Neuroimage*. doi:10.1016/j.neuroimage.2019.03.022

Juchem C, Nixon TW, McIntyre S, Boer VO, Rothman DL, De Graaf RA. 2011. Dynamic multi-coil shimming of the human brain at 7 T. *J Magn Reson*. doi:10.1016/j.jmr.2011.07.005

Juchem C, Nixon TW, McIntyre S, Rothman DL, Graaf RAD. 2010. Magnetic field modeling with a set of individual localized coils. *J Magn Reson*. doi:10.1016/j.jmr.2010.03.008

Juchem C, Umesh Rudrapatna S, Nixon TW, de Graaf RA. 2015. Dynamic multi-coil technique (DYNAMITE) shimming for echo-planar imaging of the human brain at 7 Tesla. *Neuroimage*. doi:10.1016/j.neuroimage.2014.11.011

King-Casas B, Tomlin D, Anen C, Camerer CF, Quartz SR, Montague PR. 2005. Getting to know you: Reputation and trust in a two-person economic exchange. *Science (80-)* **308**:78–83. doi:10.1126/science.1108062

Lee RF, Dai W, Jones J. 2012. Decoupled circular-polarized dual-head volume coil pair for studying two interacting human brains with dyadic fMRI. *Magn Reson Med*. doi:10.1002/mrm.23313

Leong V, Byrne E, Clackson K, Georgieva S, Lam S, Wass S. 2017. Speaker gaze increases information coupling between infant and adult brains. *Proc Natl Acad Sci U S A* **114**:13290–13295. doi:10.1073/pnas.1702493114

Levy J, Goldstein A, Feldman R. 2017. Perception of social synchrony induces mother-child gamma coupling in the social brain. *Soc Cogn Affect Neurosci* **12**:1036–1046. doi:10.1093/scan/nsx032

Levy J, Lankinen K, Hakonen M, Feldman R. 2021. The integration of social and neural synchrony: A case for ecologically valid research using MEG neuroimaging. *Soc Cogn Affect Neurosci* **16**:143–152. doi:10.1093/scan/nsaa061

Lin C-H, Tierney TM, Holmes N, Boto E, Leggett J, Bestmann S, Bowtell R, Brookes MJ, Barnes GR, Miall RC. 2019. Using optically-pumped magnetometers to measure magnetoencephalographic signals in the human cerebellum. *J Physiol*. doi:10.1113/jp277899

Lopes da Silva F. 2013. EEG and MEG: Relevance to neuroscience. *Neuron* **80**:1112–1128. doi:10.1016/j.neuron.2013.10.017

Montague PR, Berns GS, Cohen JD, McClure SM, Pagnoni G, Dhamala M, Wiest MC, Karpov I, King RD, Apple N, Fisher RE. 2002. Hyperscanning: Simultaneous fMRI during linked social interactions. *Neuroimage* **16**:1159–1164. doi:10.1006/nimg.2002.1150

Muthukumaraswamy SD. 2013. High-frequency brain activity and muscle artifacts in MEG/EEG: A review and recommendations. *Front Hum Neurosci*. doi:10.3389/fnhum.2013.00138

Reindl V, Gerloff C, Scharke W, Konrad K. 2018. Brain-to-brain synchrony in parent-child dyads and the relationship with emotion regulation revealed by fNIRS-based hyperscanning. *Neuroimage* **178**:493–502. doi:10.1016/j.neuroimage.2018.05.060

Renvall V, Kauramäki J, Malinen S, Hari R, Nummenmaa L. 2020. Imaging Real-Time Tactile Interaction With Two-Person Dual-Coil fMRI. *Front Psychiatry* **11**:1–11. doi:10.3389/fpsyt.2020.00279

Roberts G, Holmes N, Alexander N, Boto E, Leggett J, Hill RM, Shah V, Rea M, Vaughan R, Maguire EA, Kessler K, Beebe S, Fromhold M, Barnes GR, Bowtell R, Brookes MJ. 2019. Towards OPM-MEG in a virtual reality environment. *Neuroimage* **199**. doi:10.1016/j.neuroimage.2019.06.010

Sarvas J. 1987. Basic mathematical and electromagnetic concepts of the biomagnetic inverse problem. *Phys Med Biol*. doi:10.1088/0031-9155/32/1/004

Savukov IM, Romalis M V. 2005. Effects of spin-exchange collisions in a high-density alkali-metal vapor in low magnetic fields. *Phys Rev A - At Mol Opt Phys*. doi:10.1103/PhysRevA.71.023405

Shah V, Hughes JK. 2015. Method for detecting zero-field resonance. US 20150212168 A1.

Shah V, Osborne J, Orton J, Alem O. 2018. Fully integrated, standalone zero field optically pumped magnetometer for biomagnetism. *Steep Dispers Eng Opto-Atomic Precis Metrol XI* 51. doi:10.1117/12.2299197

Shah VK, Wakai RT. 2013. A compact, high performance atomic magnetometer for biomedical applications. *Phys Med Biol*. doi:10.1088/0031-9155/58/22/8153

Tierney TM, Holmes N, Mellor S, López JD, Roberts G, Hill RM, Boto E, Leggett J, Shah V, Brookes MJ, Bowtell R, Barnes GR. 2019. Optically pumped magnetometers: From quantum origins to multi-channel magnetoencephalography. *Neuroimage* **199**. doi:10.1016/j.neuroimage.2019.05.063

Tierney TM, Holmes N, Meyer SS, Boto E, Roberts G, Leggett J, Buck S, Duque-Muñoz L, Litvak V, Bestmann S, Baldeweg T, Bowtell R, Brookes MJ, Barnes GR. 2018. Cognitive neuroscience using wearable magnetometer arrays: Non-invasive assessment of language function. *Neuroimage* **181**:513–520. doi:10.1016/j.neuroimage.2018.07.035

Tierney TM, Levy A, Barry DN, Meyer SS, Shigihara Y, Everatt M, Mellor S, Lopez JD, Bestmann S, Holmes N, Roberts G, Hill RM, Boto E, Leggett J, Shah V, Brookes MJ, Bowtell R, Maguire EA, Barnes GR. 2021. Mouth magnetoencephalography: A unique perspective on the human hippocampus. *Neuroimage* **225**. doi:10.1016/j.neuroimage.2020.117443

Vivekananda U, Mellor S, Tierney TM, Holmes N, Boto E, Leggett J, Roberts G, Hill RM, Litvak V, Brookes MJ, Bowtell R, Barnes GR, Walker MC. 2020. Optically pumped magnetoencephalography in epilepsy. *Ann Clin Transl Neurol* **7**:397–401. doi:10.1002/acn3.50995

Voigt J, Knappe-Grüneberg S, Schnabel A, Körber R, Burghoff M. 2013. Measures to reduce the residual field and field gradient inside a magnetically shielded room by a factor of more than 10. *Metrol Meas Syst*. doi:10.2478/mms-2013-0021

Vrba J, Robinson SE. 2001. Signal processing in magnetoencephalography. *Methods*. doi:10.1006/meth.2001.1238

Zetter R, Iivanainen J, Parkkonen L. 2019. Optical Co-registration of MRI and On-scalp MEG. *Sci Rep* **9**:1–9. doi:10.1038/s41598-019-41763-4

Zhdanov A, Nurminen J, Baess P, Hirvenkari L, Jousmäki V, Mäkelä JP, Mandel A, Meronen L, Hari R, Parkkonen L. 2015. An internet-based real-time audiovisual link for dual MEG recordings. *PLoS One* **10**:1–15. doi:10.1371/journal.pone.0128485

Chapter 7

A lightweight MSR with active shielding

Scientific Reports, Volume 12, 2022, 13561

scientific reports

Check for updates

OPEN

A lightweight magnetically shielded room with active shielding

Niall Holmes[1]✉, Molly Rea[1], James Chalmers[2], James Leggett[1], Lucy J. Edwards[1], Paul Nell[2], Stephen Pink[2], Prashant Patel[2], Jack Wood[2], Nick Murby[2], David Woolger[2], Eliot Dawson[3], Christopher Mariani[3], Tim M. Tierney[4], Stephanie Mellor[4], George C. O'Neill[4], Elena Boto[1], Ryan M. Hill[1], Vishal Shah[5], James Osborne[5], Rosemarie Pardington[6], Peter Fierlinger[7], Gareth R. Barnes[4], Paul Glover[1], Matthew J. Brookes[1] & Richard Bowtell[1]

Magnetically shielded rooms (MSRs) use multiple layers of materials such as MuMetal to screen external magnetic fields that would otherwise interfere with high precision magnetic field measurements such as magnetoencephalography (MEG). Optically pumped magnetometers (OPMs) have enabled the development of wearable MEG systems which have the potential to provide a motion tolerant functional brain imaging system with high spatiotemporal resolution. Despite significant promise, OPMs impose stringent magnetic shielding requirements, operating around a zero magnetic field resonance within a dynamic range of ± 5 nT. MSRs developed for OPM-MEG must therefore effectively shield external sources and provide a low remnant magnetic field inside the enclosure. Existing MSRs optimised for OPM-MEG are expensive, heavy, and difficult to site. Electromagnetic coils are used to further cancel the remnant field inside the MSR enabling participant movements during OPM-MEG, but present coil systems are challenging to engineer and occupy space in the MSR limiting participant movements and negatively impacting patient experience. Here we present a lightweight MSR design (30% reduction in weight and 40–60% reduction in external dimensions compared to a standard OPM-optimised MSR) which takes significant steps towards addressing these barriers. We also designed a 'window coil' active shielding system, featuring a series of simple rectangular coils placed directly onto the walls of the MSR. By mapping the remnant magnetic field inside the MSR, and the magnetic field produced by the coils, we can identify optimal coil currents and cancel the remnant magnetic field over the central cubic metre to just |B|= 670 ± 160 pT. These advances reduce the cost, installation time and siting restrictions of MSRs which will be essential for the widespread deployment of OPM-MEG.

Low magnetic field environments, such as magnetically shielded rooms (MSRs), with minimal disturbances from external sources are needed for precision experiments, including the search for the electric dipole moment of fundamental particles[1], and biomagnetic recordings, such as magnetoencephalography (MEG)[2]. MEG is a non-invasive functional brain imaging technique which measures magnetic fields generated by neuronal currents[3]. Inverse modelling is applied to these measured fields to reconstruct the underlying neuronal activity with excellent spatial (~ 3 mm) and temporal (~ 1 ms) resolution[2,4], offering a unique and non-invasive window into the function of the human brain[5]. However, the neuromagnetic field is on the order of 100 s of femtotesla (fT) at the scalp and so is easily masked by interfering sources. A MSR is therefore a critical component of a MEG system[2].

State-of-the-art MEG scanners use a fixed array of superconducting quantum interference devices (SQUIDs). As these sensors must be cooled to liquid helium temperatures, the geometry of a SQUID-MEG MSR is largely governed by the requirement that a cryogenic dewar be sited within the shield. However, recent developments in quantum technologies have led to MEG systems based on optically pumped magnetometers (OPMs)[6–8]. Commercially available OPMs (such as those provided by QuSpin Inc. (Louisville, Colorado, USA) and FieldLine Inc. (Boulder, Colorado, USA)) are small, integrated, magnetic field sensors which exploit the quantum properties of alkali metals[9,10]. These sensors can be mounted into a wearable helmet which allows participants to move

[1]Sir Peter Mansfield Imaging Centre, School of Physics and Astronomy, University of Nottingham, University Park, Nottingham NG7 2RD, UK. [2]Magnetic Shields Limited, Headcorn Road, Staplehurst, Tonbridge, Kent TN12 0DS, UK. [3]Cerca Magnetics Limited, Headcorn Road, Staplehurst, Tonbridge, Kent TN12 0DS, UK. [4]Wellcome Centre for Human Neuroimaging, UCL Institute of Neurology, London WC1N 3AR, UK. [5]QuSpin Inc., 331 South 104th Street, Suite 130, Louisville, CO 80027, USA. [6]Young Epilepsy, St. Piers Lane, Lingfield, Surrey RH7 6PW, UK. [7]Department of Physics, Technical University Munich, 85748 Garching, Germany. ✉email: niall.holmes@nottingham.ac.uk

during MEG studies[11]. To attain the level of sensitivity required to measure MEG signals (signals of interest in the 1–100 Hz range, sensitivity of < 15 fT/√Hz required) OPMs are operated around a zero magnetic field resonance, within a narrow dynamic range of ± 5 nT[12] and a bandwidth of 0–130 Hz. MSRs for OPM-MEG must therefore screen magnetic interference from sources within this frequency range, whilst also providing an environment in which magnetic fields are < 1 nT in magnitude and the gradients in the field are < 1 nT/m. This performance is required over a volume large enough to contain both the head and the sensor array during the expected range of participant movements, such that any change in field (either induced by an external source, or via rotation/translation of a sensor during participant movement) does not send any OPM outside its dynamic range.

In contrast to SQUID-MEG, wearable OPM-MEG can be carried out using a wide range of MSR shapes and sizes. As well as fixed cuboidal shields, cylindrical shields that can be easily relocated have been used where space is limited (though such designs largely prohibit participant motion)[7]. To realise the full potential of OPM-MEG and enable widespread deployment, MSRs must be optimised to provide the magnetic environment required for OPM operation whilst addressing key concerns such as the cost, weight, comfort and architectural impact of the shield.

Passive shielding of magnetic fields is achieved by enclosing experiments within multiple layers of a material with a high magnetic permeability. A commonly used material is MuMetal, which is a nickel–iron alloy of very high permeability (μ_r can be greater than 200,000 following a heat treatment to enlarge material grain). The flux-shunting mechanism shields low frequency (DC to 10 Hz) magnetic fields by diverting flux lines into the MuMetal where they follow the MuMetal around the shielded region and exit on the other side of the enclosure[13]. To screen high frequency (10 Hz to MHz) magnetic fields, a material with a high electrical conductivity is also used (e.g. copper or aluminium). Eddy-currents in the material induce a magnetic field which deflects the imposed field[13]. Current commercially available shielded rooms which are optimised for OPM-MEG employ four layers of MuMetal, and one layer of copper. As a result, these MSRs are heavy (> 10 tonnes), with strict siting requirements and a need for substantial building work. This coupled with long manufacturing and installation times makes further innovation in MSR design highly desirable.

Although a high shielding factor (the ratio of the magnetic field strength of the interfering source measured with and without the shield) can be achieved when screening external sources, the ferromagnetic nature of MuMetal means MSRs often have a remnant, internal magnetic field of around 10–30 nT[14]. Demagnetisation coils can be incorporated into the MuMetal walls of the MSR to reduce the remnant field so, if a decaying sinusoidal current is applied to these coils, the metal is driven around its $B-H$ curve towards a point of zero magnetisation[15,16]. The remnant magnetic field is then reduced to a level which depends on material choices (e.g. layer thickness, layer spacing and material permeability), and engineering imperfections (such as access holes, doors and joints between MuMetal panels). A field strength of around 2–5 nT is typically achieved[17].

To compensate the remnant field further (and enable participant movement in OPM-MEG) active magnetic shielding is employed where electromagnetic coils are used to generate a magnetic field which is equal in magnitude, but opposite in direction, to the remnant field. Tri-axial Helmholtz coils, or similar systems, can be used to generate known magnetic fields in all orientations and compensate for remnant field and field gradients[8], but these designs are ill-suited for use with human subjects as they enclose participants in an uncomfortable setting. Our previous work demonstrated the first motion-tolerant OPM-MEG studies, using bi-planar 'fingerprint' coils. These coils are produced using MRI gradient coil design methods which restricted the coil windings to two large planes (1.6×1.6 m^2 square planes separated by 1.5 m). These can be placed on either side of a participant, allowing easy access[18]. Such systems occupy space inside the MSR, and field cancellation is limited to a small ($0.4 \times 0.4 \times 0.4$ m^3) volume at the centre of the space between the coil planes. Furthermore, although the coils in these systems are typically designed to generate a distinct homogeneous uniform field or field gradient over a desired volume, the produced fields interact with the MuMetal walls of the MSR leading to a change in the expected field strength per unit current and a distortion of the spatial variation of the magnetic field, making accurate cancellation challenging if interactions are not accounted for at the design stage[19–21]. It is of course desirable to move coil wirepaths closer to the walls of the MSR to maximise the available space inside, though this increases the strength of the interaction with the MuMetal.

Here we describe the design, construction, operation and performance of a passively and actively magnetically shielded room—with internal dimensions $2.4 \times 2.4 \times 2.4$ m^3—which makes significant steps towards overcoming the challenges outlined above. The light MSR is formed from two layers of MuMetal and one layer of copper, with reduced layer spacings compared to previous designs. Demagnetisation coils are incorporated into the MuMetal layers. To improve the shielding efficiency of the lighter MSR, we developed a new multi-coil active shielding system, the 'window coil', featuring a series of 27 rectangular coils. The coil dimensions and positions were optimised, accounting for interaction with MuMetal walls of the MSR, and the constructed coils placed directly onto the MSR's walls to maximise the available space in the MSR, and significantly improve the experience of participants in MEG experiments. By mapping the strength and spatial variation of the magnetic field produced by each coil, and also mapping the remnant magnetic field, appropriate coil currents were identified to generate a superposition of magnetic field patterns from all 27 coils that cancels the remnant field over a large ($1 \times 1 \times 1$ m^3) volume inside the MSR. The shielding performance of the MSR was validated by measuring shielding factors over a range of frequencies using controlled magnetic fields. Example OPM sensor noise data in the empty MSR were also collected to verify its suitability for biomagnetic recordings.

Methods

Magnetically shielded room. The MSR described here was installed at Young Epilepsy (Lingfield, Surrey, UK) a charity for children and young adults with epilepsy. The MSR was designed for use by an OPM-MEG system (Cerca Magnetics Limited, Kent, UK) in epilepsy research. As well as ensuring magnetic performance,

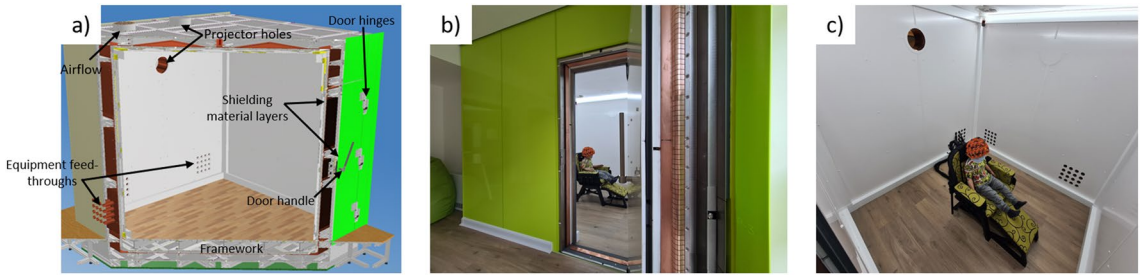

Figure 1. The Light MuRoom magnetically shielded room. (**a**) Computer model of the Light MuRoom, cross-section revealing framework and layer structure. (**b**) Photograph of the exterior of the participant facing side of the MSR. (**c**) Photograph of the interior of the MSR with wearable OPM-MEG system mounted on a plastic mannequin.

aesthetic considerations were important to create a comfortable scanning environment for young patients and their families.

MSR design. Magnetic Shields Limited (MSL, Kent, UK) designed and constructed the lightweight MSR (The Light MuRoom) which comprises two layers (outer and inner layers) of 1.5 mm thick MuMetal, and one layer (middle layer) of 4 mm-thick copper. This is a significant reduction in the amount of shielding material compared to existing OPM-optimised MSRs such as the MSL standard MuRoom[22] at the Sir Peter Mansfield Imaging Centre, University of Nottingham (UoN) which features two outer layers of 1.5 mm thick MuMetal, two inner layers of 1 mm thick MuMetal and one middle layer of 6 mm copper. The modifications to the standard MuRoom design result in a 40% reduction in MuMetal and 33% reduction in copper reduces the total weight of the MSR by around 30% to ~ 7 tonnes. The material cost and the required installation time are also decreased.

To allow for construction within laboratory and non-laboratory environments where space is constrained, the total distance between the inner and outer layers was also reduced. The standard MuRoom has an internal volume (x,y,z) (y is the vertical direction) of $3 \times 2.4 \times 3$ m^3, and an external volume of $3.7 \times 3.4 \times 4.0$ m^3 whereas the Light MuRoom has a usable internal volume of $2.4 \times 2.4 \times 2.4$ m^3 and an external volume of approximately $2.8 \times 3 \times 2.8$ m^3; a reduction of between 40 and 60% in the total wall thickness along the different dimensions of the MSR. The spacing between the outer MuMetal and copper layer is ~ 0.1 m, and the spacing between the copper and inner MuMetal layer is ~ 0.02 m.

The MSR was constructed from MuMetal and copper panels mounted onto an aluminium framework which was placed on an anti-vibrational layer on a poured concrete base. The largest MuMetal panels were 1.11×0.55 m^2 and the largest copper panels were 0.76×0.76 m^2. This was an approximately 20% reduction in area compared to the 1.23×0.61 m^2 MuMetal panels and a 40% reduction compared to the 1×1 m^2 copper panels used in the UoN MuRoom. A reduction in MuMetal panel size improves production efficiency, as more panels can undergo heat treatment in a single run, reducing fabrication time and costs. Smaller panels are also easier to handle during installation. The MuMetal shielding panels in the outer layer were arranged at 90° in plane rotation to those on the inner layer to minimise flux leakage. The MSR door comprises three hinges and features a lever-style handle. An emergency release mechanism allows access to the MSR in under twenty seconds in the unlikely event of a failure of the standard locking mechanism, critical to obtain patient access in the event of a seizure. LED lighting was placed along the edges of the MSR to ensure minimal DC field shifts at the centre of the room.

Consultation sessions were held with the health professionals and patient groups who would use the MSR to determine how to provide a comfortable scanning environment. The MSR was sunk into the floor, so that participants do not have to climb a step upon entry. Building works were carried out post-installation so that the front side of the MSR is a continuation of the room in which it is situated, rather than a separate entity. To the participant, only the front wall of the MSR is visible; a separate room behind the wall contains the rear of the MSR and is used for housing equipment. Furthermore, the flooring in the waiting lobby was the same floor as in the MSR. These elements create a calm environment for a recording. An annotated computer-generated model and photographs of the constructed MSR are shown in Fig. 1.

Demagnetisation. Magnetisation of MuMetal increases over time due to external field fluctuations such as those manifested by the Earth's magnetic field. This effect is exacerbated by opening and closing the door of the MSR due to the magnetic domains within the material moving through, and aligning with, the Earth's field. To generate a repeatable MuMetal magnetisation, demagnetisation coils were wound around each face of the inner and outer layers of MuMetal, with windings balanced on either side of the layers[16]. The coils of the two layers were connected in series with each other. Currents were applied to the coils via a digital to analogue converter (DAC) on a National Instruments (NI, Austin, Texas, USA) BNC-6212 digital acquisition (DAQ) unit which outputs to an AE Techron (Elkhart, Indiana, USA) 7226 power amplifier that was connected to one side of a Bel (Lynbrook, New York, USA) 530-SU-7.5 signal transformer (to remove any DC offset). The other side of the transformer was connected to the demagnetisation coils. A linearly decaying sinusoidal signal is generated by interfacing the DAQ with a LabVIEW (NI) program. The optimal waveform parameters (frequency = 9.5 Hz, peak current ~ 1.5 A, decaying for 60 s) were found empirically by measuring the magnetic field before and after demagnetisation with a Bartington (Mag-13, Bartington Instruments, Witney, UK) triaxial fluxgate magnetom-

eter. Demagnetisation is performed every time the door is opened, and the amplifier circuit is switched off prior to any measurements to avoid interference.

The vertical component of the remnant magnetic field magnitude post demagnetisation (measured using the fluxgate magnetometer at the centre of the MSR and at the corners of a $0.4 \times 0.4 \times 0.4$ m^3 volume, prior to any active magnetic shielding) was 4.84 ± 0.39 nT (mean and standard deviation, max/min value of 4.34/5.70 nT, shielding of Earth's magnetic field by a factor of ~ 10,000). For comparison, the standard MuRoom achieves a remnant field < 2 nT at UoN[22]. Additional active magnetic shielding was developed to further compensate the remnant field (see "Results" section).

Shielding factor measurements. To quantify the performance of the MSR, shielding factor measurements were taken by applying known magnetic fields over a range of frequencies pre- and post-installation, using the fluxgate magnetometer interfaced with a Bartington Spectramag-6 24-bit DAQ to record data. Pre-installation, a square, 5-turn, electromagnetic coil (side length 3.3 m offset, 500 mm from the planned location of the exterior walls, produced field oriented vertically from floor to ceiling) was set up around the perimeter of the MuRoom foundations in the floor. The coil was driven with sinusoidal waveforms at frequencies of 0.01, 0.1, 1, 10, and 100 Hz using an AE Techron 7226 power amplifier. Waveforms were generated using custom Python software and outputted by a NI USB-6212 DAQ. A coil current of approximately 2 A pk--pk generated a sinusoidal magnetic field with an amplitude of 20 μT pk--pk at the centre of the coil at each frequency. Field amplitudes were measured at a point corresponding to the internal centre-point of the MuRoom post-construction. Once the MSR installation was complete, the coil was rebuilt, and the magnetic field measurements were repeated. Amplitudes of the AC signals were taken from a fast Fourier transform of the recorded data. The ratios of the field values measured with and without the MSR were used to estimate the shielding factor of the MSR.

Window coil active magnetic shielding system. To reinforce the effects of the passive shielding and demagnetisation coils, we developed an active magnetic shielding system which we refer to as the 'window coil'. The window coil set was parameterised, and an approach adapted from MRI multi-coil shimming systems[23,24] was used to optimise coil parameters within the constraints set by the MSR geometry and the driving electronics[25].

Coil design. The window coil system comprises six sets of four, square, electromagnetic unit-coils, each formed of twenty turns of wire, arranged with four-fold symmetry on a single face of the MSR. The coil arrangement on each MSR face is characterised by three parameters:

- L_c, the square-side-length of each unit coil in the window coil,
- O, the offset of the centre of each square unit coil from the centre of the window coils,
- H, the offset of the centre of the window coil from the centre of the MuMetal wall in the vertical (y-direction).

The coil sets are centred in the horizontal (x and z) dimensions of each wall, as outlined in Fig. 2a. For ease of manufacturing, the same values of the O and L_c parameters were used for all walls of the MSR. To inform the choice of an optimal set of coil parameters, we conducted a simulation study to investigate the ability of a range of different coil designs to produce a desired magnetic field over a series of 'target points' within the MSR.

The magnetic field at a target point $\boldsymbol{r_n}(x, y, z)$ produced by a square unit coil m (from a set of $M = 24$ unit coils), when carrying a unit current, is denoted by $\boldsymbol{b_m}(\boldsymbol{r_n})$. The total magnetic field, $\boldsymbol{B}(\boldsymbol{r_n})$ at this target point from all coils in the system, with the m^{th} coil carrying a current i_m (from $m = 1$ up to coil $m = M$), is the vector sum of all coil contributions i.e.

$$\boldsymbol{B}(\boldsymbol{r_n}) = \sum_{m=1}^{M} i_m \boldsymbol{b_m}(\boldsymbol{r_n}). \tag{1}$$

Expanding the calculation over multiple target points allows for the creation of a linear algebra equation that can be used to find the optimal coil currents. In the form $\boldsymbol{Ai} = \boldsymbol{b_t}$ we define a 'forward field' matrix $\boldsymbol{A}$, a 'target field' vector $\boldsymbol{b_t}$ and a coil current vector $\boldsymbol{i}$. The forward field matrix contains the magnetic field components B_x, B_y and B_z generated by a unit current in each coil evaluated at each of $n = 1$ to N total target field points, and so has dimensions $3N$ rows by M columns. The target field vector $\boldsymbol{b_t}$ has dimensions $3N$ rows by 1 column and the current vector $\boldsymbol{i}$ has dimensions M rows by 1 column. The forward field matrix is calculated using the coil parameters, and the target field vector is pre-defined, so we wish to find the current vector which appropriately maps the forward field matrix to the target field vector. To ensure that the coil currents for a given set of parameters are physically manageable, we minimise the norm $||\boldsymbol{Ai} - \boldsymbol{b_t}||_2^2$ subject to the constraints that the upper and lower bound (ub and lb) of the allowed values of any component i_m of the vector $\boldsymbol{i}$ is $lb \leq i_m \leq ub$ with the bounds defined by the specifications of the coil driving electronics. The problem is formed as

$$\min_{\boldsymbol{i}} \; ||\boldsymbol{Ai} - \boldsymbol{b_t}||_2^2 \text{ subject to } lb \leq i_m \leq ub. \tag{2}$$

To obtain a solution for $\boldsymbol{i}$ we use constrained quadratic programming[25] casting the minimisation in the form

$$\min_{\boldsymbol{i}}\left(\frac{1}{2}\boldsymbol{i}^T(\boldsymbol{A}^T\boldsymbol{A})\boldsymbol{i} + \left(-\boldsymbol{A}^T\boldsymbol{b_t}\right)^T\boldsymbol{i}\right) \text{ subject to } lb \leq i_m \leq ub \tag{3}$$

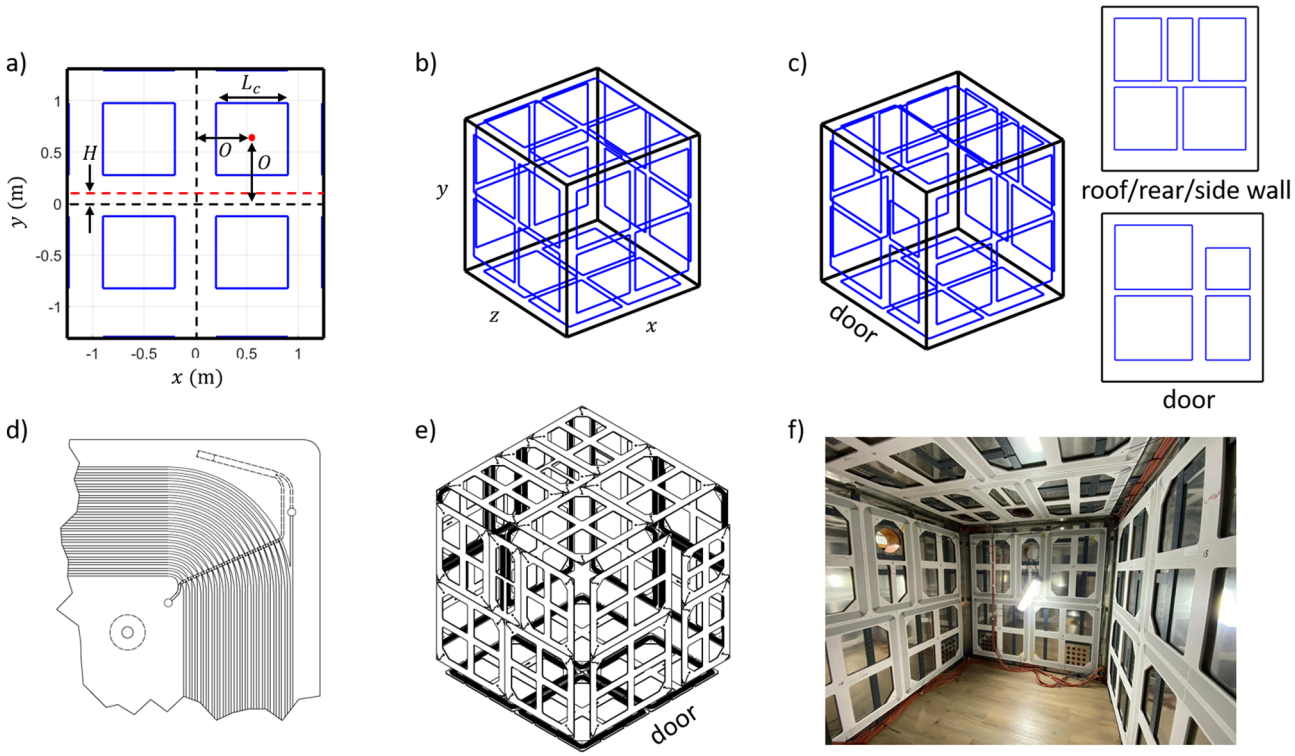

Figure 2. The window coil active magnetic shielding system. (**a**) Parameterisation of the window coil. Four square coils are arranged with four-fold symmetry on each face. The coil square side length, offset from the centre of the window and offset in the vertical axis are shared between all faces. Coil parameters are optimised to produce known components of magnetic field over the central cubic metre of the MSR. (**b**) Final optimised window coil featuring 24 identical square coils. This structure is challenging to engineer due to the need to incorporate the access door and projection ports in 3/6 walls. (**c**) Adapted design accounts for geometry of the MSR and features 27 coils. (**d**) Drawing of the corner of a single coil panel. To accommodate 20 turns of wire in each coil, a series of grooves are arranged in a spiral pattern into which copper wire is placed. The conductor return path is also shown. (**e**) Final model of the window coil featuring all panels. (**f**) Photograph of installed coil panels (floor coils hidden beneath the flooring and door coils hidden by angle of photograph) taken prior to cladding.

where the superscript $\boldsymbol{A}^T$ denotes the matrix transpose.

The proximity of the coil to the walls of the MSR means that the magnetic fields produced by the interaction of the coils with the MuMetal walls need to be accounted for when designing a high-performance active-shielding system. These interactions have been investigated previously and can be evaluated using a set of virtual mirror currents produced via reflection of the coil wirepaths in the walls of the MSR[19,26,27]. Recursive reflections of the reflected wirepaths are applied to ensure that the boundary conditions are correctly fulfilled, such that tangential field components are zero on the internal surface formed by the walls of the MSR. To ensure that the magnetic fields produced by the simulated coil designs reflect the real-world case, the effects of interactions up to third order reflections are incorporated into the forward field matrix. We assumed that the coils are displaced from each wall of the MSR by 0.02 m when calculating the position of the reflected elements. The vector sum of the magnetic field produced by each of the reflected elements at each target point forms the magnetic field value $\boldsymbol{b_m}(\boldsymbol{r_n})$ which is incorporated into the forward field matrix $\boldsymbol{A}$.

To optimise coil parameters within this framework we first identified the range of window-coils which could be formed, as each parameter characterising the coils has a maximum value bounded by the dimensions of the MSR. The presence of demagnetisation cabling, cladding panels and flooring reduces the final usable volume onto which we can mount coil panels to $(l_x, l_y, l_z) = (2.20\text{x}2.40\text{x}2.20)\text{m}^3$ (coordinate system defined in Fig. 2a,b, y is the vertical direction from floor to ceiling). As we wish for all window coils to share the same parameters, this restricts the permissible values of L_c to $L_c < \frac{l_x}{2}$. For a given value of L_c the values of O are then restricted to $O < \frac{l_x}{2} - \frac{L_c}{2}$. We then restrict H for a given value of L_c and O such that only the window coils on the xy and zy walls of the MSR have a non-zero H, whose values are restricted to $H < \frac{l_y}{2} - \frac{L_c}{2} - O$.

For a given set of coil parameters, we find the current vectors which best generate ten different target field vectors: the three uniform field components and (to ensure the magnetic field gradients are well balanced, with symmetry arising from $\nabla \cdot \boldsymbol{B} = 0$ and, in the current free region enclosed by the target points, $\nabla \times \boldsymbol{B} = 0$) 7 (linear) field gradient components (four longitudinal gradients and three transverse gradients were used, see complete list in Online Appendix 1). For each combination of coil parameters, and each of the 10 field components, fc, a value of the quality of the solution $Q_{fc} = ||\boldsymbol{Ai} - \boldsymbol{b_t}||_2^2$ is calculated. As optimal coil parameters are

likely to be different for different field components, a final combined quality value, F, is calculated from the 10 individual values, $F = \sum_{fc=1}^{10} \sqrt{Q_{fc}^2}$.

The coil parameters which minimise the value of F are found using MATLAB (Mathworks, Natick, MA, USA). The MATLAB constrained minimisation function *fmincon* varies the values of L_c, O and H according to the constraints above (no negative values of H were considered). The magnetic field from each unit coil was calculated using the Biot-Savart law where the field calculated for a unit current was multiplied by 20 to account for 20 turns of wire. The target field strength for each component was set to 5 nT and 5 nT/m for the magnetic field and magnetic field gradient components respectively. In each case, the target field is calculated over a regular 0.05 m resolution cubic grid ($N = 9261$ target points in total) which spans a volume of $1 \times 1 \times 1$ m^3 at the centre of the usable portion of the room. The MATLAB optimisation toolbox features a constrained quadratic programming function *quadprog* which was used to solve Eq. (3) and obtain the optimal current vectors to produce each field component for each coil design with currents bound to $-0.1\text{A} \leq i_m \leq +0.1\text{A}$. The optimal coil parameters were found to be $L_c = 1\text{m}$, $O = 0.55\text{m}$ and $H = 0.08\text{m}$. This design is shown in Fig. 2b.

Design iteration. In practice, the MSR design features several 'no-go' areas on the inner walls such as the sites of waveguides for equipment cabling, holes for visual projection and a large access door for participants and experimenters. The location of these features makes the optimised coil design (Fig. 2b) challenging to realise. The optimal parameters were therefore used as a guide to adapt the design to accommodate the no-go regions on the surface of the Light MuRoom structure. Figure 2c shows the adapted coil design. No changes were made on the floor and the right-hand wall. Holes for visual projection were present on the left-hand wall, the rear wall and the ceiling, meaning the coil design on these walls was adapted to feature five coils instead of four. Two rectangular coils were placed either side of the projector hole and a smaller rectangular coil was placed around the projector hole. On the door face, four coils were used with two extended up to the edge of the door whilst two smaller coils were added to the door itself. The 27-coil design was shown to slightly increase (indicating poorer performance) the final quality factor by 2%. Figure 3 shows simulated contours over the target points for an example uniform field (B_z, Fig. 3a), a longitudinal field gradient ($dB_x/dx = -dB_y/dy$, Fig. 3b) and a transverse field gradient ($dB_x/dz = dB_z/dx$, Fig. 3c). The magnetic field at each target point in the field map was normalised to the target field or field gradient strength (5 nT or 5 nT/m) to show deviation from field or gradient uniformity over the target points. We note the high uniformity of the uniform field component, < 3% deviation over the $1 \times 1 \times 1$ m^3 volume. This degrades to > 20% deviation for the longitudinal gradient (Fig. 3b) and > 30% deviation for the transverse gradient (Fig. 3c). Contours of the remaining field and gradient components are shown in Online Appendix 1.

Coil construction. Each coil panel was constructed by laying 0.65 mm diameter insulated copper wire into 3 mm grooves machined into 10-mm-thick plastic panels. The grooves were arranged in a spiral pattern for ease of construction that accommodated 20-turns with the average coil side length across turns corresponding to the optimal coil parameters, as shown in Fig. 2d. Figure 2e-f shows the panel layout. The spiral pattern has minimal effect on the produced field at the centre of the MSR compared to the rectangular wirepaths used in simulation. The coil resistance and inductance vary according to panel size, but the maximum values were 4.99 Ω and 1.25 mH respectively. The panels were mounted onto the walls of the MSR and connected to a junction box which is in turn connected to an electronics cabinet. The electronics cabinet contains nine QuSpin Inc. low-noise voltage drivers (http://quspin.com/low-noise-coil-driver/). Each driver controls three coils and each channel was configured to provide up to ± 68 mA current from an input voltage of ± 10 V. The input voltages to the coil drivers are supplied by a series of National Instruments NI-9264 16-bit DACs which are controlled by a NI-cDAQ-9174 DAQ and LabVIEW.

Field nulling. To null the remnant magnetic field, we employed the method described by Rea et al.[28] which uses optical tracking of a moving array of magnetic field sensors to generate a spherical harmonic model of the magnetic field in the MSR[29]. We mounted two triaxial fluxgate magnetometers (Bartington Mag-13MSL100—low-noise variant with ± 100 μT dynamic range, accuracy < 1 nT, noise < 6 pTrms/√Hz at 1 Hz) along with a set of five infrared reflective markers, onto a plastic stand attached to a plastic stick, as shown in Fig. 4a. Four optical tracking cameras (OptiTrack Flex 13, NaturalPoint Inc., Corvallis, Oregon, USA) were placed in the top corners of the room as shown in Fig. 4b. The cameras track the position of the reflective markers and use the combined coordinates of a series of markers (Fig. 4a) that are fixed with respect to each other (forming a rigid body) to infer six degrees-of-freedom tracking (translation and rotation) of the rigid body with sub-millimetre and sub-1-degree precision.

The fixed positions of the sensitive volumes of the fluxgate sensors with respect to the centre of mass of the rigid body were measured, allowing combination of the optical tracking data with the magnetometer data to produce an accurate fit to a model of the magnetic field. Fluxgate data were collected at 1200 Hz using a NI-9205 16-bit analogue to digital converter (ADC) interfaced with LabVIEW. Optical tracking data were collected at 120 Hz using the OptiTrack Motive software platform interfaced with MATLAB via the Motive NatNet SDK (V3.1). The magnetometer data were low-pass filtered at 10 Hz and down-sampled to 120 Hz to match the sample rate of the optical tracking system. The optical tracking data were also low-pass filtered at 10 Hz. A trigger signal was used to synchronise the two recordings. Both data streams were corrected to reflect the changes in magnetic field and in sensor position and orientation relative to the first timepoint. We chose a third-order spherical harmonic magnetic field model featuring three uniform fields, five field gradients and seven curvature

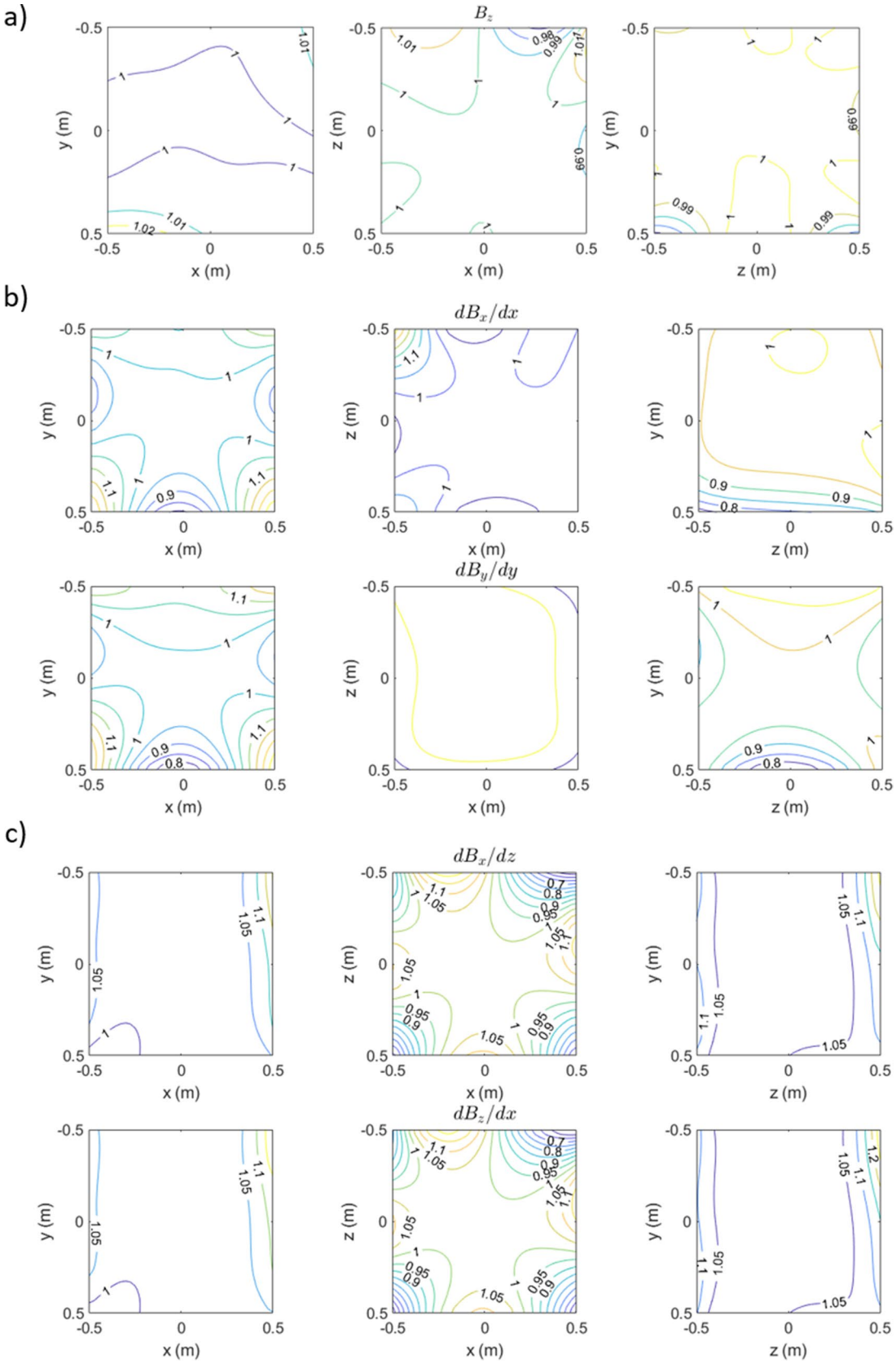

Figure 3. Simulated magnetic field components produced by the window coil active magnetic shielding system. Contours of the magnetic field variation for (**a**) a uniform magnetic field B_z, (**b**) a longitudinal field gradient $dB_x/dx = -dB_y/dy$ and (**c**) a transverse field gradient $dB_x/dz = dB_z/dx$. All contours are shown in three planes (arranged from left to right): z = 0 m |x|, |y| < 0.5 m, y = 0 m |x|, |z| < 0.5 m and x = 0 m |z|, |y| < 0.5 m respectively. The field values at each target point are normalised to the target field or field gradient strength (of 5 nT or 5 nT/m) to show deviation from uniformity. Contours of the remaining magnetic field components are shown in Online Appendix 1.

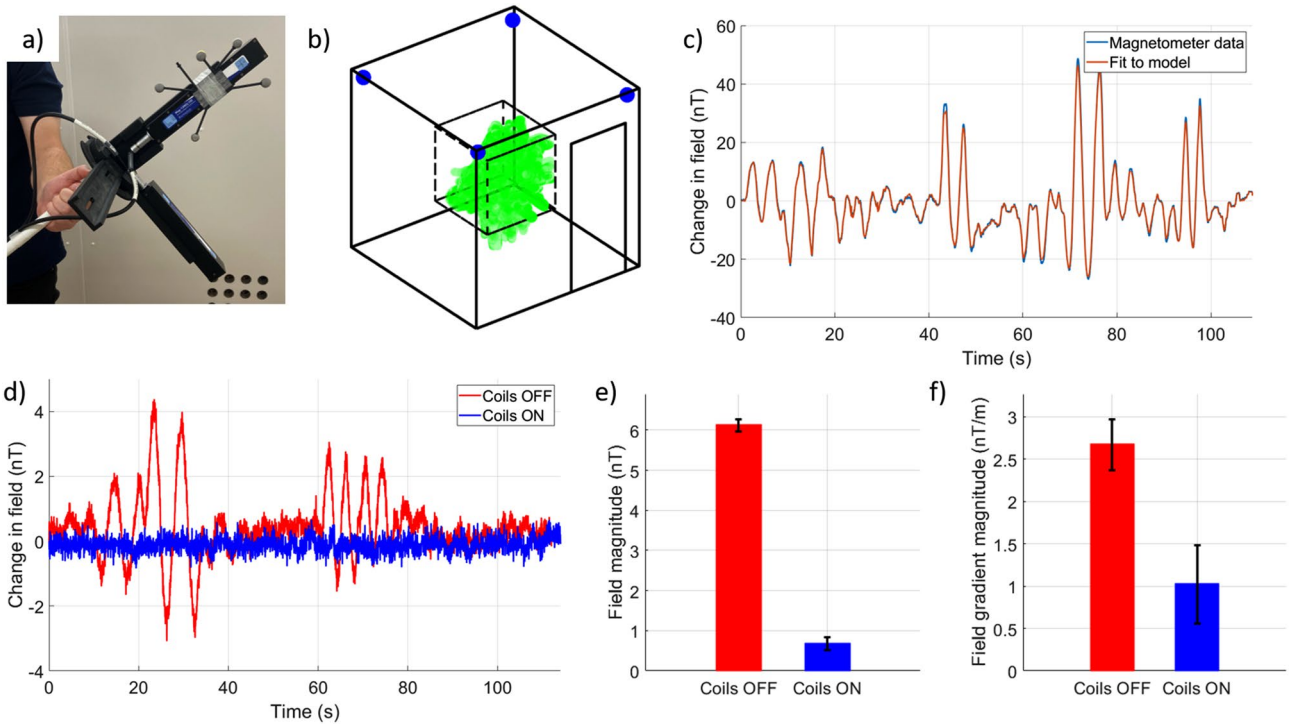

Figure 4. Active compensation of the remnant magnetic field using a field mapping method. (**a**) Two triaxial fluxgate magnetometers attached to a plastic stick. A series of five infrared reflective markers are also attached to the stick allowing optical tracking of the position and orientation of the sensors within the MSR. (**b**) Schematic of the field mapping setup. The tracking cameras are mounted in the corners of the MSR and highlighted in blue. The dashed black volume shows the central cubic metre volume within which the stick was moved. The green highlighted marks show the path which the fluxgate magnetometers followed during the field mapping process, covering most of the central cubic metre of the MSR. (**c**) Magnetometer data from a single component of one triaxial sensor measured when a single coil was activated. By combining the data from all magnetometers with the optical tracking data a spherical harmonic model can be used to approximate the strength and spatial variation of the field produced by each coil. (**d**) The red trace shows the magnetic field measured by one magnetometer in the MSR with all coils switched off. The magnetic field model of each coil was used to calculate coil voltages which produce the required nulling field. Once voltages had been applied, the mapping was performed again. The blue trace shows the magnetometer data after nulling where similar sensor translations and rotations produce little to no change in the measured field. (**e**) Field mapping and nulling was repeated 8 times. The bar chart shows a consistent remnant field following demagnetisation and a consistent reduction in the RMS magnitude of the three uniform field components found by the model when the compensation is applied. (**f**) A similar reduction is seen in the RMS magnitude of the five field gradient components.

(varying with the square of distance) terms (all terms listed in Table 2), such that the method returns a total of fifteen fit coefficients which describe the relative strength of each spherical harmonic component in the model.

To use the field mapping coefficients to select window coil currents for field nulling, we first mapped the remnant magnetic field (after demagnetisation of the room) over the central cubic metre of the MSR, by performing a series of rotations and translations of the fluxgate magnetometers. This process takes approximately 2 min. The same set of rotations and translations were performed for producing all field maps. An example of the mapped volume is shown in Fig. 4b. We then applied 5 V to a single coil using the DACs and mapped the field again. An example fit to the magnetic field generated by one coil is shown in Fig. 4c. By subtracting the coefficients found for the remnant field from those found when the coil was energised and dividing by 5, we obtain the change in each component of our magnetic field model that is generated by a unit of applied voltage. By repeating for all 27 coils we could construct a coil calibration matrix, which describes the change in each field component generated by a unit voltage applied to each coil. The pseudo-inverse of this matrix can then be used to identify the coil voltages which best produce the field required to cancel the remnant field. The correlation coefficient between our model fit and the measured data was > 0.98 for each coil, suggesting a good model and accurate coil calibration values. The calibration stage takes ~ 1 h to complete but is only performed once.

We investigated the performance of the field mapping and nulling method by first demagnetising the MSR, then mapping the remnant magnetic field and calculating the coil voltages required to cancel this magnetic field. Once these nulling voltages had been applied, we then re-mapped the magnetic field inside the MSR, expecting to see a decrease in the changes in magnetic field experienced by the fluxgates as they move through the same path. The nulling was repeated eight times to assess the repeatability of both the demagnetisation process and the level of field cancellation that was achievable.

Frequency/Hz	Shielding factor
0 (DC)	10,331 (4.84 nT, calculated relative to a nominal 50 μT vertical field)
0.01	158
0.1	237
1	1230
10	9757
100	8065

Table 1. Shielding factors of the MSR at different frequencies measured with a fluxgate magnetometer.

Uniform field components	Field strength (nT) coils OFF	Field strength (nT) coils ON	Ratio
$B_x(\hat{\boldsymbol{x}})$	−0.99 ± 0.18	0.14 ± 0.23	7.1
$B_y(\hat{\boldsymbol{y}})$	−4.09 ± 0.17	−0.44 ± 0.13	9.3
$B_z(\hat{\boldsymbol{z}})$	4.45 ± 0.15	−0.38 ± 0.24	11.7
Field gradient components	**Field strength (nT/m) coils OFF**	**Field strength (nT/m) coils ON**	**Ratio**
$y\hat{\boldsymbol{x}} + x\hat{\boldsymbol{y}}(\frac{dB_x}{dy} = \frac{dB_y}{dx})$	−1.22 ± 0.24	0.37 ± 0.60	3.3
$z\hat{\boldsymbol{x}} + x\hat{\boldsymbol{z}}(\frac{dB_x}{dz} = \frac{dB_z}{dx})$	1.05 ± 0.31	−0.29 ± 0.44	3.6
$z\hat{\boldsymbol{y}} + y\hat{\boldsymbol{z}}(\frac{dB_y}{dz} = \frac{dB_z}{dy})$	2.05 ± 0.40	0.02 ± 0.43	102.5
$-x\hat{\boldsymbol{x}} - y\hat{\boldsymbol{y}} + 2z\hat{\boldsymbol{z}}(-\frac{dB_x}{dx} - \frac{dB_y}{dy} = 2\frac{dB_z}{dz})$	−0.12 ± 0.16	−0.04 ± 0.16	3.0
$x\hat{\boldsymbol{x}} - y\hat{\boldsymbol{y}}(\frac{dB_x}{dx} = -\frac{dB_y}{dy})$	−0.18 ± 0.32	0.13 ± 0.61	1.4
Curvature components	**Field strength (nT/m²) coils OFF**	**Field strength (nT/m²) coils ON**	**Ratio**
$6xy\hat{\boldsymbol{x}} + 3(x^2 - y^2)\hat{\boldsymbol{y}}$	0.49 ± 0.16	0.08 ± 0.45	6.1
$3(x^2 - y^2)\hat{\boldsymbol{x}} - 6xy\hat{\boldsymbol{y}}$	0.09 ± 0.16	0.37 ± 0.26	0.2
$yz\hat{\boldsymbol{x}} + xz\hat{\boldsymbol{y}} + xy\hat{\boldsymbol{z}}$	0.9 ± 1.9	−1.4 ± 2.4	0.6
$2xz\hat{\boldsymbol{x}} - 2yz\hat{\boldsymbol{y}} + (x^2 - y^2)\hat{\boldsymbol{z}}$	−0.47 ± 0.74	−0.27 ± 0.97	1.7
$-2xy\hat{\boldsymbol{x}} + (4z^2 - x^2 - 3y^2)\hat{\boldsymbol{y}} + 8yz\hat{\boldsymbol{z}}$	−0.15 ± 0.12	−0.25 ± 0.20	0.6
$(4z^2 - 3x^2 - y^2)\hat{\boldsymbol{x}} - 2xy\hat{\boldsymbol{y}} + 8xz\hat{\boldsymbol{z}}$	−0.03 ± 0.15	−0.11 ± 0.20	0.3
$-6xz\hat{\boldsymbol{x}} - 6yz\hat{\boldsymbol{y}} + (6z^2 - 3x^2 - 3y^2)\hat{\boldsymbol{z}}$	−0.19 ± 0.16	0.02 ± 0.20	9.5

Table 2. Model fit coefficients before and after nulling for fifteen field components in the spherical harmonic model. Values quoted are the mean and standard deviation over eight repeat measurements. $\hat{\boldsymbol{x}}, \hat{\boldsymbol{y}}, \hat{\boldsymbol{z}}$ denote the Cartesian unit vectors.

Results

MSR performance. Table 1 shows the measured shielding factors of the MSR at a range of frequencies within the OPM bandwidth.

Window coil performance and repeatability. The maximum translation of the centre of mass of the optical tracking markers from the centre of the mapped volume was (x,y,z) (0.32 ± 0.08 m, 0.50 ± 0.06 m, 0.44 ± 0.06 m) and (0.30 ± 0.04 m, 0.48 ± 0.04 m, 0.41 ± 0.06 m) before and after nulling respectively (mean ± standard deviation of the 8 repeats). The maximum rotation of the centre of mass of the optical tracking markers about the origin in the x,y,z axes was (50 ± 10°, 28 ± 3°, 40 ± 10°) and (50 ± 10°, 28 ± 5°, 40 ± 10°). The consistency of movement suggests changes in the magnetic field model are due to a change in the magnetic field of the MSR. Timecourses of field variation measured by one of the magnetometers before and after field nulling are shown in Fig. 4d. A clear reduction in the size of artefacts during sensor movement is shown when the coils are active. Figure 4e shows a decrease in the magnitude of the three uniform components of the spherical harmonic model from $|\boldsymbol{B}| = 6.13 \pm 0.15$ nT to $|\boldsymbol{B}| = 0.67 \pm 0.16$ nT (mean ± standard deviation of the 8 repeats) before and after the coil voltages were applied. Figure 4f shows a decrease in the magnitude of the five field gradient components from $|\boldsymbol{G}| = 2.67 \pm 0.30$ nT/m to $|\boldsymbol{G}| = 1.02 \pm 0.46$ nT/m. Table 2 summarises the change in each of the fifteen components in the spherical harmonic model, reduction is observed in all uniform field and gradient components. Although an increase in some curvature components is observed their strength is ~ 1 nT/m², and the variation with the square of distance means these terms have minimal impact on the field at the noise level of the fluxgate sensors. The average standard deviation (σ) of the six individual timecourses of fluxgate data used to generate the model fits reduced from $\sigma = 0.84 \pm 0.15$ to $\sigma = 0.24 \pm 0.02$ nT before and after field nulling respectively. The average correlation coefficient (r) across the 6 magnetometer channels reduced from $r = 0.96 \pm 0.02$ to $r = 0.45 \pm 0.09$ before and after field nulling. The reduction of the correlation coefficient suggests that the magnetic field is compensated to the noise level of the fluxgates; i.e. little artefact remains in the

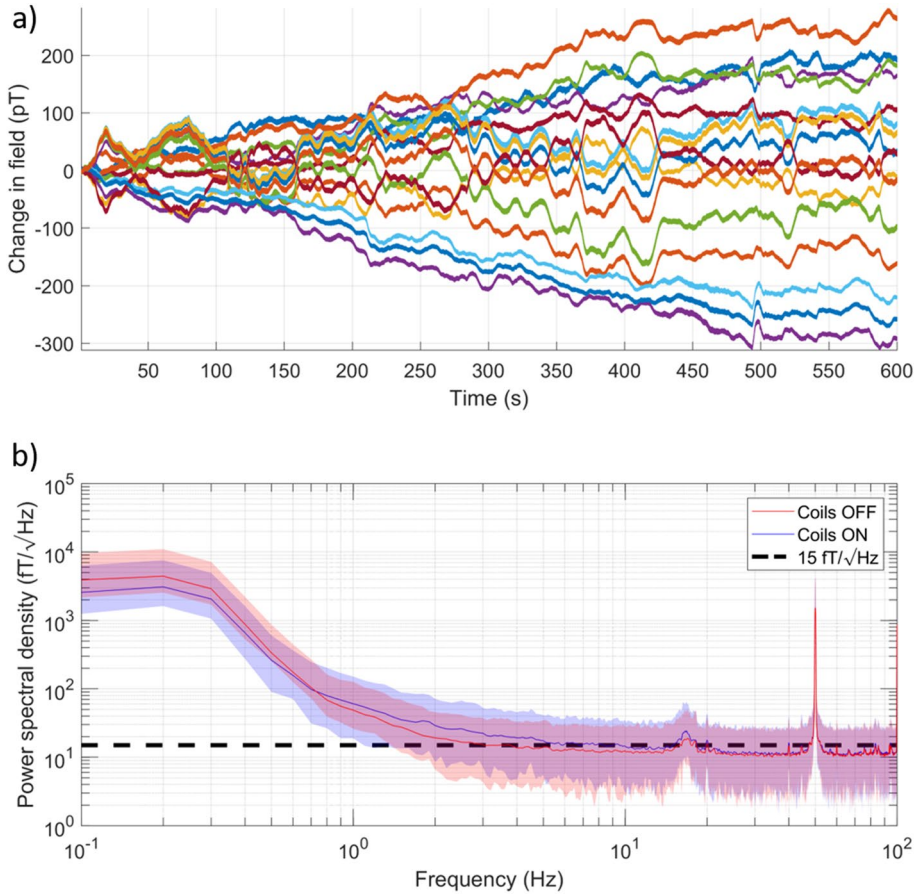

Figure 5. OPM data taken in the Light MuRoom. (**a**) Timecourses of the change in magnetic field experienced by eight dual-axis OPMs (16 total channels) which were placed at the centre of the empty MSR with the window coil system switched on. Each OPM was configured to measure two components of magnetic field. Over 10 min the change in field is ~ 300 pT indicating good shielding performance and a quiet magnetic environment. (**b**) Mean and range (shaded) of the power spectral density of the data collected from the OPMs with and without the window coil system active. The black dashed line indicates 15 fT/√Hz. Data suggests that the MSR is a suitable environment for OPM-MEG, and that the coil system does not add additional magnetic field noise.

data which correlates with sensor translations and rotations. These results show that the window coil and field mapping method allow effective compensation of the remnant magnetic field inside the MSR.

OPM verification. Eight QuSpin Zero Field Magnetometers (QZFM, 3rd Generation, Dual-axis variant, sensitivity < 15 fT/√Hz in 3–100 Hz band) were placed at the centre of the room. The MSR was demagnetised prior to the recordings. The QZFMs were each configured to measure two components of magnetic field. Data were recorded for 10 min at 1200 Hz using a NI-9205 ADC. As the coil voltages found in the previous experiments used < 1% of the DACs' dynamic range, a 2 kΩ resistor was added in series to each coil so that 30% of the dynamic range could be used. This additional resistance also reduces the current noise which is translated into magnetic field noise inside the MSR. Two recordings were taken: with, and without, the window coil system switched on. Figure 5a shows timecourse data recorded from these sensors during the experiment with the window coil switched on. Figure 5b shows the power spectral density of the data for both cases, analysed by using a flat-top window and segmenting data into 10 s chunks, prior to computing the power spectral density using MATLAB's periodogram function and then averaging the results. The mean PSD is plotted as a solid line (blue/red for the coils on/off) and the range across all channels is noted by the shaded areas. The data show low-frequency field drifts of ~ 300 pT in 10 min. The mean noise level within the frequency bands of interest for neuronal oscillations, (with/without the window coil switched on respectively) were: delta (0.5–4 Hz) 43/38 fT/√Hz, theta (4–8 Hz) 16/13 ft/√Hz, alpha (8–12 Hz) 14/13 fT/√Hz, beta (13–30 Hz) 14/12 fT/√Hz and gamma (30–100 Hz) 12/11 fT/√Hz. The range across sensors is comparable for the two conditions. This performance is likely to provide a suitable environment for OPM-MEG recordings.

Discussion

Lightweight MSRs, which can be easily sited, are crucial for the widespread deployment of OPM-MEG systems. The design process here involved halving the number of MuMetal layers, reducing the layer spacing and reducing the thickness of the copper compared to an existing OPM-optimised MSR. Each change will have a negative impact on the shielding factor of the MSR but Table 1 demonstrates that despite these changes, high shielding factors are achieved which provide performance that is sufficient to obtain usable OPM data (Fig. 5). We note that the MSR was located at a site with minimal magnetic disturbances, it remains to be seen if this performance would be suitable for a more challenging environment such as a city-centre or hospital setting without additional techniques, such as operating the coils in a constant feedback loop with fixed reference sensors to cancel low-frequency field changes. The rate of change of field that can be generated by driving a coil of inductance L and efficiency η with drive voltage V is given by $dB/dt = \eta V/L$. Setting η to the maximum field per unit current required by any of the 27 coils to generate a uniform B_x -field at the centre of the MSR of 4.6 nT/mA, we find that a rate of field change of 3.5 nT/ms can be achieved with $V = 1$ V. Since $\left|\frac{d\boldsymbol{B}}{dt}\right| \propto \omega|\boldsymbol{B}|$ for a sinusoidal waveform, this allows the generation of a field of more than 5 nT in amplitude even at 100 Hz, which is more than adequate for field cancellation in the frequency range that is relevant for MEG. At higher frequencies (> 1 kHz) the coupling between the magnetic field generated by the coils and the MuMetal shows significant frequency dependence, producing variations in the strength, phase and spatial variation of the fields. Although dynamic operation of the coils would focus on low-frequency effects, operation at higher frequency could be possible via precise modelling of the MuMetal interaction for different frequency regimes or adaptive algorithms could be employed during constant feedback processes. Optimising the copper layer to improve shielding at higher frequencies could also be used to further improve the shielding factor measurements and enable deployment of the MSR in noisier settings.

Electromagnetic coil systems for compensation of the remnant magnetic field of a MSR have formed a key area of development for OPM-based MEG. Previous work has involved the design and construction of bi-planar[14,19] and Helmholtz-coil systems[8], each featuring a series of distinct coils that generate known components of magnetic field or field gradient. The compensation of magnetic fields, and low-frequency field drifts, to the sub nT levels required for sensor operation has been achieved over small volumes which span head-mounted arrays of OPMs undergoing limited movements. The incorporation of interactions of produced fields with the MuMetal walls of the MSR has been shown to improve the quality of the field patterns produced by such coils[21], potentially providing more accurate field nulling. Coil design techniques and open-source packages have been developed for a variety of shield and coil geometries[20,30]. However, the elaborate wirepaths and multiple coil layers required by these systems lead to a complex manufacturing and installation process. The limited spatial extent of region encompassed by previous coil solutions (e.g. two 1.6×1.6 m^2 planes separated by 1.5 m) has had significant impact on the usable region of the MSR, limiting the extent to which a comfortable scanning environment can be achieved.

The window coil system, and field compensation methods we have described have three key advantages over existing techniques: (1) Manufacturing is simplified, with square/rectangular coils that can be flexibly placed on the inner surface of the MSR. (2) Coil calibration and operation is data-driven, accounting for any field imperfections that cannot be accurately modelled. (3) Coils can be configured to produce magnetic fields within a user-defined volume, effectively 're-designing' themselves to adapt to their environment. This flexibility presents unique opportunities. The large compensation volume described here allows for a wide range of participant motion, but coils could also be tuned to compensate smaller volumes such as the OPM-MEG helmet. By continually monitoring head position with optical tracking cameras, and combining field modelling with the data collected by the OPM sensors in the MEG helmet, the coils could feasibly be operated in a constant feedback mode to continually update the location of the shielded volume, a further advantage of a multi-coil system. The OPMs would also be sensitive to the residual field that the fluxgates are unable to detect, thus improving the performance of the field nulling. Dynamic stabilisation in this way would remove the low-frequency 'drifts' present in the OPM data shown in Fig. 5a. These advances could enable experiments which required ambulatory motion—a key step towards realising the full potential of OPM-MEG.

Data and code availability

All data generated or analysed during this study are included in this published article and its supplementary information files.

Received: 31 January 2022; Accepted: 25 July 2022
Published online: 09 August 2022

References

1. Sachdeva, N. *et al.* New Limit on the Permanent Electric Dipole Moment of Xe 129 Using He 3 Comagnetometry and SQUID Detection. *Phys. Rev. Lett.* **123**, 143003 (2019).
2. Hämäläinen, M., Hari, R., Ilmoniemi, R. J., Knuutila, J. & Lounasmaa, O. V. Magnetoencephalography theory, instrumentation, and applications to noninvasive studies of the working human brain. *Rev. Mod. Phys.* **65**, 413–497 (1993).
3. Cohen, D. Magnetoencephalography: Evidence of magnetic fields produced by alpha rhythm currents. *Science* **161**, 784–786 (1968).
4. Baillet, S. Magnetoencephalography for brain electrophysiology and imaging. *Nat. Neurosci.* https://doi.org/10.1038/nn.4504 (2017).
5. Gross, J. Magnetoencephalography in cognitive neuroscience: A primer. *Neuron* **104**, 189–204 (2019).
6. Boto, E. *et al.* Moving magnetoencephalography towards real-world applications with a wearable system. *Nature* **555**, 657–661 (2018).

7. Borna, A. *et al.* Non-invasive functional-brain-imaging with an OPM-based magnetoencephalography system. *PLoS ONE* **15**, 1–24 (2020).
8. Iivanainen, J., Zetter, R., Grön, M., Hakkarainen, K. & Parkkonen, L. On-scalp MEG system utilizing an actively shielded array of optically-pumped magnetometers. *Neuroimage* https://doi.org/10.1016/j.neuroimage.2019.03.022 (2019).
9. Dupont-Roc, J., Haroche, S. & Cohen-Tannoudji, C. Detection of very weak magnetic fields (10–9gauss) by 87Rb zero-field level crossing resonances. *Phys. Lett. A* **28**, 638–639 (1969).
10. Shah, V. K. & Wakai, R. T. A compact, high performance atomic magnetometer for biomedical applications. *Phys. Med. Biol.* https://doi.org/10.1088/0031-9155/58/22/8153 (2013).
11. Shah, V., Osborne, J., Orton, J. & Alem, O. Fully integrated, standalone zero field optically pumped magnetometer for biomagnetism. *Steep Dispers. Eng. Opto-Atomic Precis. Metrol.* https://doi.org/10.1117/12.2299197 (2018).
12. Allred, J. C., Lyman, R. N., Kornack, T. W. & Romalis, M. V. High-sensitivity atomic magnetometer unaffected by spin-exchange relaxation. *Phys. Rev. Lett.* https://doi.org/10.1103/physrevlett.89.130801 (2002).
13. Hoburg, J. F. Principles of quasistatic magnetic shielding with cylindrical and spherical shields. *IEEE Trans. Electromagn. Compat.* https://doi.org/10.1109/15.477342 (1995).
14. Holmes, N. *et al.* A bi-planar coil system for nulling background magnetic fields in scalp mounted magnetoencephalography. *Neuroimage* https://doi.org/10.1016/j.neuroimage.2018.07.028 (2018).
15. Voigt, J., Knappe-Grüneberg, S., Schnabel, A., Körber, R. & Burghoff, M. Measures to reduce the residual field and field gradient inside a magnetically shielded room by a factor of more than 10. *Metrol. Meas. Syst.* https://doi.org/10.2478/mms-2013-0021 (2013).
16. Altarev, I. *et al.* Minimizing magnetic fields for precision experiments. *J. Appl. Phys.* https://doi.org/10.1063/1.4922671 (2015).
17. Altarev, I. *et al.* A magnetically shielded room with ultra low residual field and gradient. *Rev. Sci. Instrum.* https://doi.org/10.1063/1.4886146 (2014).
18. Roberts, G. *et al.* Towards magnetoencephalography in a virtual reality environment. *Neuroimage* https://doi.org/10.1016/j.neuroimage.2019.06.010 (2019).
19. Holmes, N. *et al.* Balanced, bi-planar magnetic field and field gradient coils for field compensation in wearable magnetoencephalography. *Sci. Rep.* https://doi.org/10.1038/s41598-019-50697-w (2019).
20. Zetter, R. *et al.* Magnetic field modeling with surface currentsL: Part II: Implementation and usage of bfieldtools. *J Appl Phys.* **128**, 063905 (2020).
21. Packer, M. *et al.* Optimal inverse design of magnetic field profiles in a magnetically shielded cylinder. *Phys. Rev. Appl.* **14**, 1 (2020).
22. Hill, R. M. *et al.* Multi-channel whole-head OPM-MEG: Helmet design and a comparison with a conventional system. *Neuroimage* https://doi.org/10.1016/j.neuroimage.2020.116995 (2020).
23. Juchem, C., Green, D. & De Graaf, R. A. Multi-coil magnetic field modeling. *J. Magn. Reson.* https://doi.org/10.1016/j.jmr.2013.08.015 (2013).
24. Juchem, C., Umesh Rudrapatna, S., Nixon, T. W. & de Graaf, R. A. Dynamic multi-coil technique (DYNAMITE) shimming for echo-planar imaging of the human brain at 7 Tesla. *Neuroimage* https://doi.org/10.1016/j.neuroimage.2014.11.011 (2015).
25. Garda, B. & Galias, Z. Tikhonov regularization and constrained quadratic programming for magnetic coil design problems. *Int. J. Appl. Math. Comput. Sci.* https://doi.org/10.2478/amcs-2014-0018 (2014).
26. Juhas, A., Pekari, N. & Toepfer, H. Magnetic field of rectangular current loop with sides parallel and perpendicular to the surface of high-permeability material. *SJEE* **11**, 701–717 (2014).
27. Qinjie, C. *et al.* Optimization of a Coil system for generating uniform magnetic fields inside a cubic. *Energies* **11**, 608 (2018).
28. Rea, M. *et al.* Precision magnetic field modelling and control for wearable magnetoencephalography. *Neuroimage* **241**, 118401 (2021).
29. Mellor, S. J. *et al.* Magnetic Field Mapping and Correction for Moving OP-MEG. *IEEE Trans. Biomed. Eng.* **97**, 243703 (2021).
30. Kutschka, H., Doeller, C. F., Haueisen, J. & Maess, B. Magnetic field compensation coil design for magnetoencephalography. *Sci. Rep.* https://doi.org/10.1038/s41598-021-01894-z (2021).

Acknowledgements

This work was supported by an Innovate UK Collaborative R&D grant (Light MuRoom, Ref: 104604), the UK Quantum Technology Hub in Sensing and Timing, funded by the Engineering and Physical Sciences Research Council (EPSRC) (EP/T001046/1) and a Wellcome Collaborative Award in Science (203257/Z/16/Z and 203257/B/16/Z).

Author contributions

The study was designed and conceived by N.H., D.W., T.M.T., R.P., G.R.B., M.J.B. and R.B. Experiments were performed and analysed by N.H., M.R., J.C., L.J.E., J.L., P.P., J.W., and N.M. All authors contributed to the design, construction and installation of the facility, interpreting results and writing the manuscript.

Competing interests

D.W. is the managing director of Magnetic Shields Limited, the company which designed and constructed the magnetically shielded room described in this work. J.C., P.N., S.P., P.P., J.W., and N.M. are employees of Magnetic Shields Limited. P.F. receives compensation as a scientific advisor to Magnetic Shields Limited. E.B. D.W. and M.J.B. are directors of Cerca Magnetics Limited, a spin-out company whose aim is to commercialise aspects of OPM-MEG technology. Cerca products include magnetically shielded rooms for biomagnetic measurements from Magnetic Shields Limited. E.B., M.J.B., R.B., N.H. and R.H. hold founding equity in Cerca Magnetics Limited and R.B., N.H. and R.H. sit on the scientific advisory board. E.D. and C.M. are employees of Cerca Magnetics Limited. V.S. is the founding director of QuSpin Inc., a commercial entity selling the OPM magnetometers used in this work. J.O. is an employee of QuSpin Inc. R.P. is the Director of Integrated Care at Young Epilepsy, the charity where the magnetically shielded room described in this work was installed. N.H, J.C., D.W., P.G, M.J.B., and R.B. declare that they have a patent pending to the UK Government Intellectual Property Office (Application No. GB2109459.4) regarding the active magnetic shielding systems described in this work. The remaining authors, M.R., J.L., L.J.E., T.M.T., S.M., G.C.O and G.R.B., declare no competing interests.

Additional information

Supplementary Information The online version contains supplementary material available at https://doi.org/10.1038/s41598-022-17346-1.

Correspondence and requests for materials should be addressed to N.H.

Summary and outlook

This thesis had two primary aims:

1. **To develop techniques to more accurately map and compensate the background magnetic field inside a MSR, using existing coil systems for active magnetic shielding.**
2. **To demonstrate new, multi-coil active magnetic shielding systems that enable flexibility in participant positioning within the MSR.**

The first aim was addressed in Chapters 4 and 5, which describe the development and application of an improved magnetic field mapping approach for compensation of the background magnetic field in OPM-MEG using a bi-planar, distributed coil system. In Chapter 4, remnant magnetic fields of <300 pT were achieved, with gradients ~1 nTm^{-1}, facilitating a reduction in low frequency (0—2 Hz) motion artefacts by a factor of 5. Such precise magnetic field control enabled detection of a visual steady-state evoked response with 6 Hz stimulation during continuous head movements, and represents a substantial step forward in the capability of OPM-MEG to measure low frequency effects, such as delta and theta oscillations.

Further application of the technique, in Chapter 5, allowed us to map motor function to the contralateral motor cortex during left- or right-handed writing with 4 mm accuracy. The robustness of the approach was also demonstrated by the repeatability of this source reconstruction and of magnetic field compensation to ~200 pT across the sixteen experiments. The nature of this handwriting paradigm involved repeated, naturalistic head movements of up to 5 cm and 10°, which are not possible using conventional MEG scanning technologies.

The second aim of this thesis was addressed in Chapters 6 and 7, using two distinct multi-coil active shielding systems. In Chapter 6, a bi-planar 'matrix' coil system was used to enable magnetic field compensation over an OPM array located anywhere between the coil planes, achieving residual magnetic fields between 0.23 and 2.0 nT depending on the helmet position. The flexibility in participant positioning afforded by this system was demonstrated by consistency in reconstruction of motor function during a bat-and-ball task when the participant was standing, seated, and sat on the floor of the MSR. Additionally, the matrix coil enabled the first OPM-MEG hyperscanning experiments to be performed, simultaneously mapping sensorimotor function in two interacting participants during a touch task and observing correlated beta-band dynamics as they bat a ball back and forth in a tennis task.

Chapter 7 described the integration of a multi-coil active magnetic shielding system into the walls of a lightweight MSR. This 'window' coil system provides an open and comfortable scanning environment while facilitating magnetic field compensation to ~700 pT over a large, 1 m^3 central volume. This result is comparable to that obtained by high performance MSRs (Altarev et al., 2014; Voigt et al., 2013), yet achieved with fewer, thinner layers of material. Thus, the Light MuRoom with integrated active shielding goes a long way to lessening the installation time, material and construction costs, and siting restrictions that represent perhaps the most significant barrier to widespread uptake of OPM-MEG.

Future work

Precision magnetic field control

Since the work described in Chapters 4 and 5 was conducted, we have further refined our background magnetic field control technique by improving cable management and optimising magnetic field gradient compensation via the bi-planar coils in software. Figure 8.1 shows the outcome of six repeat experiments in which the background magnetic field was nulled to <50 pT, and gradient components to ~500 pTm^{-1}. Such high-performance magnetic field compensation will ensure an OPM remains operational during large rotations and translations of the sensor, with minimal gain errors, thus facilitating a large range of participant motion while preserving the accuracy of subsequent source reconstructions. In such residual magnetic fields, the resulting motion artefacts will also be minimised, further improving OPM-MEG data quality, particularly at low frequencies. This is especially relevant in the study of young children, who are likely to move more during scan and whose neural oscillations are typically slower than those of adults (Saby and Marshall, 2012), such that the frequencies of motion artefacts overlap more substantially with the neuromagnetic signals of interest.

The application of precision magnetic field control could conceivably enable a myriad of exciting neuroscientific studies. For example, a similar study to that described in Chapter 5 could be performed in children as they learn to write, enabling the development of the language network to be examined. In

a clinical setting, such field control techniques could allow patients with epilepsy to be scanned during a seizure (known as the ictal phase), such that the associated uncontrolled movements have minimal impact on data quality. This has the potential to improve estimation of the seizure onset zone compared to the use of conventional MEG technologies, which rely upon measurements during interictal (between seizure) activity generated instead by the irritative zone (Rosenow and Lüders, 2001).

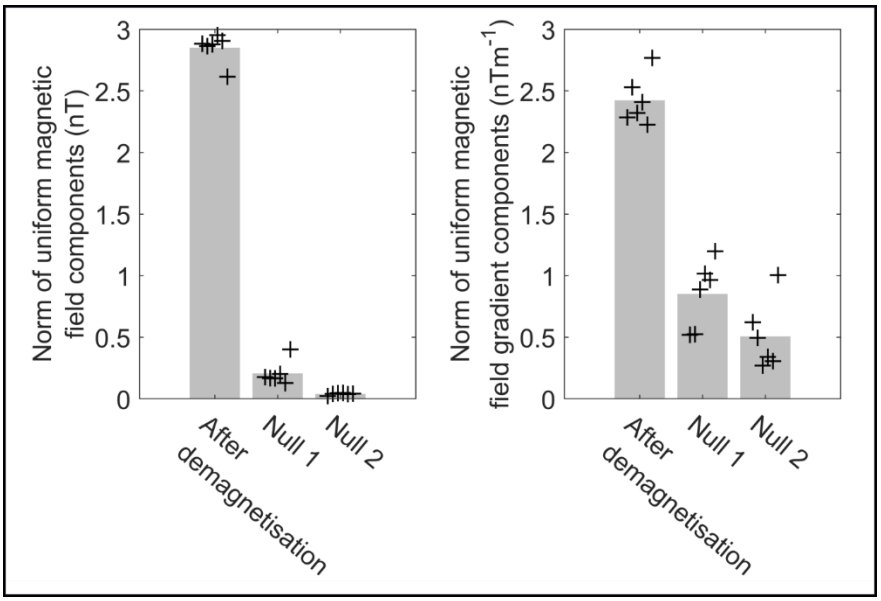

Figure 8.1 – Latest precision magnetic field control results. *Remnant magnetic fields <0.05 nT are achieved after two iterations of field mapping and compensation, with gradient components ~0.5 nTm^{-1}. The norm of the uniform magnetic field components or magnetic field gradient components are shown in the left and right panels respectively, with individual data points shown for 6 repeat experiments, and the average value given by the bars.*

The nature of the bi-planar, distributed coil system meant that magnetic field compensation was applied over a fixed, 40 cm^3 central volume. Translation of the technique to more adaptable multi-coil shielding systems, such as those described in Chapters 6 and 7, would enable precision magnetic field control to be applied across an OPM array positioned anywhere within the region bounded by the coils. However, since the magnetic field and gradient components generated by each coil over the desired volume were determined *a priori* for use in the coil calibration matrix, scaling this approach up for compensation using 48 unit coils over a reconfigurable region would likely be both time consuming and computationally intensive. Furthermore, the reference measurements required to facilitate dynamic stabilisation of changes in the background magnetic field over time restrict this approach to some fixed volume, i.e., precision magnetic field control could be applied with the participant standing and the reference sensors positioned nearby, but the participant must remain in the same location throughout an experiment. In order to facilitate ambulatory motion, real-time magnetic field compensation, without the use of reference measurements, would be a more appropriate solution.

Multi-coil active magnetic shielding

Conceivably, real-time magnetic field compensation could be implemented for a freely moving participant using multi-coil active shielding, by combining instantaneous magnetic field measurements using OPMs mounted in a rigid helmet with sensor position and orientation information gleaned from optical tracking. As before, the magnetic field measured by each OPM could be fit to the spherical harmonic model and the optimal coil currents calculated to compensate the remnant magnetic field across the OPM array. An instantaneous coil calibration matrix would be required to do this on a moving participant, which could be computed using the Biot-Savart law given the simple geometry of the unit coils. Advantages of such a method would be the incorporation of interactions between the magnetic fields generated by the coils with the MuMetal walls in a data-driven approach and removing the need for spatially separated reference measurements. However, this approach would be computationally intensive and thus present a challenge to implement, since real-time magnetic field compensation would have to be low latency in order to maintain sensor operation and minimise sensor gain changes during free movement.

Chapter 6 described the prototype matrix coil system consisting of 48 unit coils mounted on two planes. At the time of writing, work is underway to integrate a 96 coil system into the walls of the MSR at the Sir Peter Mansfield Imaging Centre, University of Nottingham (see Figure 8.2). This multi-coil system will facilitate control of the background magnetic field anywhere within the inner dimensions of our MSR and allow access to a full range of participant motion for future OPM-MEG studies. For example, with sufficient control of the background magnetic field, a participant could walk freely around the room, or an infant crawl on the floor, during a scan. Hence neurodevelopmental studies could be performed as a child learns to walk, and the breakdown of brain-to-body interactions could be assessed in elderly people prone to falling or those with Parkinson's disease, as they try to initiate movement in the 'up and go' test (Mathias et al., 1986; Richardson, 1991). Furthermore, hyperscanning could be performed to study interactions between a parent and child, akin to that performed in EEG and fNIRS (Reindl et al., 2018; Wass et al., 2018) yet exploiting the improved spatiotemporal resolution and sensitivity offered by MEG. This could lead to a greater understanding of how our brains process social interaction, how children learn from a parental figure, and how these effects may differ in childhood disorders.

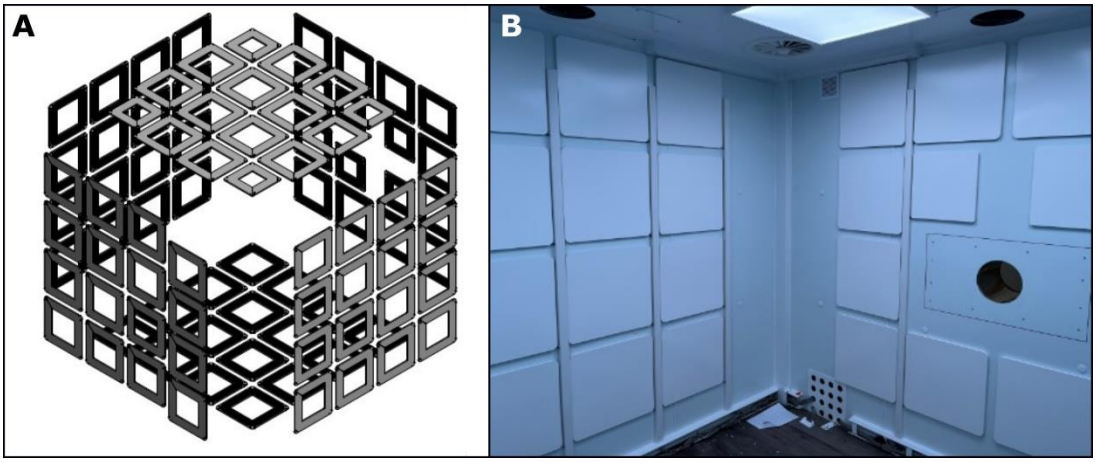

Figure 8.2 – Integrated matrix coil system for active magnetic shielding. *A) Model of 96 unit coils for integration into the walls of the OPM-optimised MSR at the University of Nottingham. B) Photograph of wall-mounted coil installation.*

Closed-loop operation of triaxial OPMs

While active shielding systems such as those described in this thesis control the global magnetic environment across an OPM array, closed-loop operation presents an accompanying or perhaps alternative solution, by maintaining a local zero-field environment across the vapour cell of each individual sensor. As discussed in Section 3.1, viable closed-loop operation requires the OPMs to have triaxial sensitivity. Therefore, at the time of writing this is an emerging approach with great potential for enabling flexibility in participant positioning and movement in OPM-MEG that should be explored in future work.

Concluding remarks

Of the available functional brain imaging modalities, MEG arguably provides the most insight into neural activity in health and disease, offering high spatial and temporal resolution via non-invasive recordings. While whole-head, SQUID-based MEG systems became commercially available in the mid-1990s, relatively few changes to hardware and data collection had occurred since, meaning participant motion remained restricted. A fortuitous combination of advances in quantum technologies, microfabrication and miniaturisation techniques, as well as passive and active magnetic shielding, has led to the development of wearable MEG in recent years.

Broadly, the aim of this thesis was to expand the range of participant motion possible during OPM-MEG and provide an open and comfortable scanning environment. Precise control of background magnetic fields beyond previous efforts, via a technique that can be easily incorporated into scanning protocol and carried out by the participant, paves the way for many novel applications both neuroscientific and clinical. The introduction of multi-coil systems has enabled a greater range of

motion during scanning, and it is now conceivable that scanning individuals during ambulatory motion will be possible with OPM-MEG in the near future.

However, OPM-MEG is still in its early years, and as such the approach is not yet as robust and reliable as is required for routine clinical deployment. OPM-MEG technology is yet to acquire regulatory approval, and scanning protocols need to be optimised and streamlined, particularly for use in infants or those with cognitive impairment. However, work in this thesis and beyond shows that there are no unnavigable barriers to widespread deployment of OPM-MEG as a neuroscientific and clinical tool that offers high quality data, adaptability to any age group and free movement during scanning. For almost a century, EEG has been the cornerstone of clinical neurophysiology, but as OPM-MEG continues to develop, so does its potential to supersede EEG as the fundamental neuroscientific tool used to improve the lives of many people living with the most severe neurological conditions.

References

Ahlfors, S.P., Ilmoniemi, R.J., Hämäläinen, M.S., 1992. Estimates of visually evoked cortical currents. Electroencephalogr. Clin. Neurophysiol. 82, 225–236. https://doi.org/10.1016/0013-4694(92)90172-E

Alem, O., Sander, T.H., Mhaskar, R., Leblanc, J., Eswaran, H., Steinhoff, U., Okada, Y., Kitching, J., Trahms, L., Knappe, S., 2015. Fetal magnetocardiography measurements with an array of microfabricated optically pumped magnetometers. Phys. Med. Biol. 60, 4797–4811. https://doi.org/10.1088/0031-9155/60/12/4797

Allred, J.C., Lyman, R.N., Kornack, T.W., Romalis, M. V., 2002. High-sensitivity atomic magnetometer unaffected by spin-exchange relaxation. Phys. Rev. Lett. 89, 1308011–1308014. https://doi.org/10.1103/physrevlett.89.130801

Altarev, I., Babcock, E., Beck, D., Burghoff, M., Chesnevskaya, S., Chupp, T., Degenkolb, S., Fan, I., Fierlinger, P., Frei, A., Gutsmiedl, E., Knappe-Grüneberg, S., Kuchler, F., Lauer, T., Link, P., Lins, T., Marino, M., McAndrew, J., Niessen, B., Paul, S., Petzoldt, G., Schläpfer, U., Schnabel, A., Sharma, S., Singh, J., Stoepler, R., Stuiber, S., Sturm, M., Taubenheim, B., Trahms, L., Voigt, J., Zechlau, T., 2014. A magnetically shielded room with ultra low residual field and gradient. Rev. Sci. Instrum. 85. https://doi.org/10.1063/1.4886146

Ang, K.H., Chong, G., Li, Y., 2005. PID control system analysis, design, and technology. IEEE Trans. Control Syst. Technol. 13, 559–576. https://doi.org/10.1109/TCST.2005.847331

Åström, K.J., Hägglund, T., 1995. PID Controllers: Theory, Design, and Tuning, 2nd ed. ISA - The Instrumentation, Systems and Automation Society.

Attwell, D., Laughlin, S.B., 2001. An energy budget for signaling in the grey matter of the brain. J. Cereb. Blood Flow Metab. https://doi.org/10.1097/00004647-200110000-00001

Baillet, S., 2017. Magnetoencephalography for brain electrophysiology and imaging. Nat. Neurosci. https://doi.org/10.1038/nn.4504

Baker, A.P., Brookes, M.J., Rezek, I.A., Smith, S.M., Behrens, T., Smith, P.J.P., Woolrich, M., 2014. Fast transient networks in spontaneous human brain activity. Elife. https://doi.org/10.7554/eLife.01867

Bardeen, J., Cooper, L.N., Schrieffer, J.R., 1957. Microscopic theory of superconductivity. Phys. Rev. https://doi.org/10.1103/PhysRev.106.162

Barratt, E.L., Tewarie, P.K., Clarke, M.A., Hall, E.L., Gowland, P.A., Morris, P.G., Francis, S.T., Evangelou, N., Brookes, M.J., 2017. Abnormal task driven neural oscillations in multiple sclerosis: A visuomotor MEG study. Hum. Brain Mapp. 38, 2441–2453. https://doi.org/10.1002/hbm.23531

Bassett, D.S., Yang, M., Wymbs, N.F., Grafton, S.T., 2015. Learning-induced autonomy of sensorimotor systems. Nat. Neurosci. 18, 744–751. https://doi.org/10.1038/nn.3993

Batie, M., Bitant, S., Strasburger, J.F., Shah, V., Alem, O., Wakai, R.T., 2018. Detection of Fetal Arrhythmia by Using Optically Pumped Magnetometers. JACC Clin. Electrophysiol. 4, 284–287. https://doi.org/10.1016/j.jacep.2017.08.009

Bell, W.E., Bloom, A.L., 1961. Optically driven spin precession. Phys. Rev. Lett. https://doi.org/10.1103/PhysRevLett.6.280

Bell, W.E., Bloom, A.L., 1957. Optical detection of magnetic resonance in alkali metal vapor. Phys. Rev. https://doi.org/10.1103/PhysRev.107.1559

Berger, H., 1929. Über das Elektrenkephalogramm des Menschen. Arch. Psychiatr. Nervenkr. 87, 527–570. https://doi.org/10.1007/BF01797193

Bison, G., Wynands, R., Weis, A., 2003. A laser-pumped magnetometer for the mapping of human cardiomagnetic fields. Appl. Phys. B Lasers Opt. 76, 325–328. https://doi.org/10.1007/s00340-003-1120-z

Biswal, B., Zerrin Yetkin, F., Haughton, V.M., Hyde, J.S., 1995. Functional connectivity in the motor cortex of resting human brain using echo-planar mri. Magn. Reson. Med. 34, 537–541. https://doi.org/10.1002/mrm.1910340409

Bloch, F., 1953. The principle of nuclear induction. Science (80-.). 118, 425–430. https://doi.org/10.1126/science.118.3068.425

Bloch, F., 1946. Nuclear Induction. Phys. Rev. 70, 460–474. https://doi.org/10.1103/PhysRev.70.460

Bork, J., Hahlbohm, H., Klein, R., 2001. The 8-layered magnetically shielded room of the PTB: Design and construction.

Borna, A., Carter, T.R., Colombo, A.P., Jau, Y.Y., McKay, J., Weisend, M., Taulu, S., Stephen, J.M., Schwindt, P.D.D., 2020. Non-invasive functional-brain-imaging with an OPM-based magnetoencephalography system. PLoS One. https://doi.org/10.1371/journal.pone.0227684

Borna, A., Carter, T.R., Goldberg, J.D., Colombo, A.P., Jau, Y.Y., Berry, C., McKay, J., Stephen, J., Weisend, M., Schwindt, P.D.D., 2017. A 20-channel magnetoencephalography system based on optically pumped magnetometers. Phys. Med. Biol. https://doi.org/10.1088/1361-6560/aa93d1

Borna, A., Iivanainen, J., Carter, T.R., McKay, J., Taulu, S., Stephen, J., Schwindt, P.D.D., 2022. Cross-Axis projection error in optically pumped magnetometers and its implication for magnetoencephalography systems. Neuroimage 247, 118818. https://doi.org/10.1016/j.neuroimage.2021.118818

Boto, E., 2019. Wearable magnetoencephalography. University of Nottingham.

Boto, E., Bowtell, R., Krüger, P., Fromhold, T.M., Morris, P.G., Meyer, S.S., Barnes, G.R., Brookes, M.J., 2016. On the potential of a new generation of magnetometers for MEG: A beamformer simulation study. PLoS One 11, 1–24. https://doi.org/10.1371/journal.pone.0157655

Boto, E., Hill, R.M., Rea, M., Holmes, N., Seedat, Z.A., Leggett, J., Shah, V., Osborne, J., Bowtell, R., Brookes, M.J., 2021. Measuring functional connectivity with wearable MEG. Neuroimage. https://doi.org/10.1016/j.neuroimage.2021.117815

Boto, E., Holmes, N., Leggett, J., Roberts, G., Shah, V., Meyer, S.S., Muñoz, L.D., Mullinger, K.J., Tierney, T.M., Bestmann, S., Barnes, G.R., Bowtell, R., Brookes, M.J., 2018. Moving magnetoencephalography towards real-world applications with a wearable system. Nature 555, 657–661. https://doi.org/10.1038/nature26147

Boto, E., Meyer, S.S., Shah, V., Alem, O., Knappe, S., Kruger, P., Fromhold, T.M., Lim, M., Glover, P.M., Morris, P.G., Bowtell, R., Barnes, G.R., Brookes, M.J., 2017. A new generation of magnetoencephalography: Room temperature measurements using optically-pumped magnetometers. Neuroimage 149, 404–414. https://doi.org/10.1016/j.neuroimage.2017.01.034

Boto, E., Shah, V., Hill, R.M., Rhodes, N., Osborne, J., Doyle, C., Holmes, N., Rea, M., Leggett, J., Bowtell, R., Brookes, M.J., 2022. Triaxial detection of the neuromagnetic field using optically-pumped magnetometry: feasibility and application in children. Neuroimage 252, 119027. https://doi.org/10.1016/J.NEUROIMAGE.2022.119027

Breakspear, M., Williams, L.M., Stam, C.J., 2004. A Novel Method for the Topographic Analysis of Neural Activity Reveals Formation and Dissolution of “Dynamic Cell Assemblies,” Journal of Computational Neuroscience.

Brenner, D., Lipton, J., Kaufman, L., Williamson, S.J., 1978. Somatically Evoked Magnetic Fields of the Human Brain. Science (80-.). 199, 81–83. https://doi.org/10.1126/SCIENCE.199.4324.81

Brookes, M.J., Boto, E., Rea, M., Shah, V., Osborne, J., Holmes, N., Hill, R.M., Leggett, J., Rhodes, N., Bowtell, R., 2021. Theoretical advantages of a triaxial optically pumped magnetometer magnetoencephalography system. Neuroimage 236. https://doi.org/10.1016/j.neuroimage.2021.118025

Brookes, M.J., Wood, J.R., Stevenson, C.M., Zumer, J.M., White, T.P., Liddle, P.F., Morris, P.G., 2011. Changes in brain network activity during working memory tasks: A magnetoencephalography study. Neuroimage. https://doi.org/10.1016/j.neuroimage.2010.10.074

Broser, P.J., Knappe, Svenja, Kajal, D.-S., Noury, N., Alem, Orang, Shah, V., Braun, C., Broser P J Broser, P.J., Knappe, S, Alem, O, Kajal, D., 2018. Optically Pumped Magnetometers for Magneto-Myography to Study the Innervation of the Hand. IEEE Trans. NEURAL Syst. Rehabil. Eng. 26. https://doi.org/10.1109/TNSRE.2018.2871947

Budker, D., Romalis, M., 2007. Optical magnetometry. Nat. Phys. https://doi.org/10.1038/nphys566

Cao, F., An, N., Xu, W., Wang, W., Yang, Y., Xiang, M., Gao, Y., Ning, X., 2021. Co-registration Comparison of On-Scalp Magnetoencephalography and Magnetic Resonance Imaging. Front. Neurosci. 15, 995. https://doi.org/10.3389/fnins.2021.706785

Carlson, J.W., Derby, K.A., Hawryszko, K.C., Weideman, M., 1992. Design and evaluation of shielded gradient coils. Magn. Reson. Med. 26, 191–206. https://doi.org/10.1002/MRM.1910260202

Celozzi, S., Araneo, R., Lovat, G., 2008. Appendix B: Magnetic Shielding, in: Electromagnetic Shielding. https://doi.org/10.1002/9780470268483.app2

Churchill, J.D., Tharp, J.A., Wellman, C.L., Sengelaub, D.R., Garraghty, P.E., 2004. Morphological correlates of injury-induced reorganization in primate somatosensory cortex. https://doi.org/10.1186/1471-2202-5-43

Cimatti, Z., Schwartz, D.P., Bourdain, F., Meunier, S., Bleton, J.-P., Vidailhet, M., Renault, B., Garnero, L., 2007. Time-frequency analysis reveals decreased high-frequency oscillations in writer’s cramp. Brain 130, 198–205. https://doi.org/10.1093/brain/awl259

Cohen-Tannoudji, C., Dupont-Roc, J., Haroche, S., Laloë, F., 1970. Diverses résonances de croisement de niveaux sur des atomes pompés optiquement en champ nul. I. Théorie. Rev. Phys. Appliquée 5, 95–101. https://doi.org/10.1051/rphysap:019700050109500

Cohen, D., 1972. Magnetoencephalography: Detection of the brain's electrical activity with a superconducting magnetometer. Science (80-.). 175, 664–666. https://doi.org/10.1126/science.175.4022.664

Cohen, D., 1968. Magnetoencephalography: Evidence of magnetic fields produced by alpha-rhythm currents. Science (80-.). 161, 784–786. https://doi.org/10.1126/science.161.3843.784

Cohen, D., 1967. A shielded facility for low-level magnetic measurements. J. Appl. Phys. 38, 1295–1296. https://doi.org/10.1063/1.1709590

Coussens, T., Abel, C., Gialopsou, A., Bason, M.G., James, T.M., Orucevic, F., Kruger, P., 2021. Modular optically-pumped magnetometer system.

Curio, G., 1995. Neuromagnetic recordings of evoked and injury-related activity in the peripheral nervous system. Biomagn. Fundam. Res. Clin. Appl. Amsterdam Elsevier Sci. 709–714.

Dale, M.W., Morley, G.W., 2017. Medical applications of diamond magnetometry: commercial viability.

Dang, H.B., Maloof, A.C., Romalis, M. V., 2010. Ultrahigh sensitivity magnetic field and magnetization measurements with an atomic magnetometer. Appl. Phys. Lett. https://doi.org/10.1063/1.3491215

De Pasquale, F., Della Penna, S., Snyder, A.Z., Lewis, C., Mantini, D., Marzetti, L., Belardinelli, P., Ciancetta, L., Pizzella, V., Romani, G.L., Corbetta, M., 2010. Temporal dynamics of spontaneous MEG activity in brain networks. Proc. Natl. Acad. Sci. U. S. A. 107, 6040–6045. https://doi.org/10.1073/PNAS.0913863107/SUPPL_FILE/PNAS.200913863SI.PDF

Dupont-Roc, J., Haroche, S., Cohen-Tannoudji, C., 1969. Detection of very weak magnetic fields (10-9 gauss) by 87Rb zero-field level crossing resonances. Phys. Lett. A 28, 638–639. https://doi.org/10.1016/0375-9601(69)90480-0

Elzenheimer, E., Laufs, H., Schulte-Mattler, W., Schmidt, G., 2020. Magnetic Measurement of Electrically Evoked Muscle Responses with Optically Pumped Magnetometers. IEEE Trans. Neural Syst. Rehabil. Eng. 28, 756–765. https://doi.org/10.1109/TNSRE.2020.2968148

Engel, A.K., Gerloff, C., Hilgetag, C.C., Nolte, G., 2013. Intrinsic Coupling Modes: Multiscale Interactions in Ongoing Brain Activity. Neuron 80, 867–886. https://doi.org/10.1016/J.NEURON.2013.09.038

Engel, J., Lopes da Silva, F., 2012. High-frequency oscillations - Where we are and where we need to go. Prog. Neurobiol. https://doi.org/10.1016/j.pneurobio.2012.02.001

Fedele, T., Scheer, H.J., Burghoff, M., Curio, G., Körber, R., 2015. Ultra-low-noise EEG/MEG systems enable bimodal non-invasive detection of spike-like human somatosensory evoked responses at 1 kHz. Physiol. Meas. 36, 357–368. https://doi.org/10.1088/0967-3334/36/2/357

Fourcault, W., Romain, R., Le Gal, G., Bertrand, F., Josselin, V., Le Prado, M., Labyt, E., Palacios-Laloy, A., 2021. Helium-4 magnetometers for room-temperature biomedical imaging: toward collective operation and photon-noise limited sensitivity. Opt. Express 29, 14467. https://doi.org/10.1364/oe.420031

Fox, P.T., Raichle, M.E., 1984. Stimulus rate dependence of regional cerebral blood flow in human striate cortex, demonstrated by positron emission tomography. J. Neurophysiol. 51, 1109–1120. https://doi.org/10.1152/jn.1984.51.5.1109

Fries, P., 2005. A mechanism for cognitive dynamics: Neuronal communication through neuronal coherence. Trends Cogn. Sci. 9, 474–480. https://doi.org/10.1016/j.tics.2005.08.011

Gaetz, W., Rhodes, E., Bloy, L., Blaskey, L., Jackel, C.R., Brodkin, E.S., Waldman, A., Embick, D., Hall, S., Roberts, T.P.L., 2020. Evaluating motor cortical oscillations and age-related change in autism spectrum disorder. Neuroimage 207, 116349. https://doi.org/https://doi.org/10.1016/j.neuroimage.2019.116349

Gascoyne, L.E., Brookes, M.J., Rathnaiah, M., Katshu, M.Z.U.H., Koelewijn, L., Williams, G., Kumar, J., Walters, J.T.R., Seedat, Z.A., Palaniyappan, L., Deakin, J.F.W., Singh, K.D., Liddle, P.F., Morris, P.G., 2021. Motor-related oscillatory activity in schizophrenia according to phase of illness and clinical symptom severity. NeuroImage Clin. 29, 102524. https://doi.org/10.1016/j.nicl.2020.102524

Gerlach, W., Stern, O., 1922. Der experimentelle Nachweis der Richtungsquantelung im Magnetfeld. Zeitschrift für Phys. 1922 91 9, 349–352. https://doi.org/10.1007/BF01326983

Geselowitz, D.B., 1967. On Bioelectric Potentials in an Inhomogeneous Volume Conductor. Biophys. J. 7, 1–11. https://doi.org/10.1016/S0006-3495(67)86571-8

Golay, M.J.E., 1958. Field homogenizing coils for nuclear spin resonance instrumentation. Rev. Sci. Instrum. 29, 313–315. https://doi.org/10.1063/1.1716184

Goldman, D.E., 1943. Potential, impedance, and rectification in membranes. J. Gen. Physiol. 27, 37–60. https://doi.org/10.1085/jgp.27.1.37

Griffith, W.C., Knappe, S., Kitching, J.E., 2010. Femtotesla atomic magnetometry in a microfabricated vapor cell. Opt. Express 18 26, 27167–27172.

Gross, J., Baillet, S., Barnes, G.R., Henson, R.N., Hillebrand, A., Jensen, O., Jerbi, K., Litvak, V., Maess, B., Oostenveld, R., Parkkonen, L., Taylor, J.R., van Wassenhove, V., Wibral, M., Schoffelen, J.M., 2013. Good practice for conducting and reporting MEG research. Neuroimage. https://doi.org/10.1016/j.neuroimage.2012.10.001

Gruetter, R., 1993. Automatic, localized in vivo adjustment of all first- and second-order shim coils. Magn. Reson. Med. 29, 804–811. https://doi.org/10.1002/mrm.1910290613

Gu, W., Ru, X., Li, D., He, K., Cui, Y., Sheng, J., Gao, J.H., 2021. Automatic coregistration of MRI and on-scalp MEG. J. Neurosci. Methods 358, 109181. https://doi.org/10.1016/j.jneumeth.2021.109181

Hadamard, J., 1902. Sur les problems aux derivees patielles et leur signification physique.

Hämäläinen, M., Hari, R., Ilmoniemi, R.J., Knuutila, J., Lounasmaa, O. V., 1993. Magnetoencephalography theory, instrumentation, and applications to noninvasive studies of the working human brain. Rev. Mod. Phys. 65, 413–497. https://doi.org/10.1103/RevModPhys.65.413

Hämäläinen, M.S., Ilmoniemi, R.J., 1994. Interpreting magnetic fields of the brain: minimum norm estimates. Med. Biol. Eng. Comput. 1994 321 32, 35–42. https://doi.org/10.1007/BF02512476

Hämäläinen, M.S., Sarvas, J., 1989. Realistic Conductivity Geometry Model of the Human Head for Interpretation of Neuromagnetic Data. IEEE Trans. Biomed. Eng. 36, 165–171. https://doi.org/10.1109/10.16463

Hämäläinen, M.S., Sarvas, J., 1987. Feasibility of the homogeneous head model in the interpretation of neuromagnetic fields. Phys. Med. Biol. 32, 91–97. https://doi.org/10.1088/0031-9155/32/1/014

Hammond, P., 1960. Electric and magnetic images. Proc. IEE - Part C Monogr. 107, 306-313(7).

Handler, W.B., Harris, C.T., Scholl, T.J., Parker, D.L., Goodrich, K.C., Dalrymple, B., Van Sass, F., Chronik, B.A., 2014. New head gradient coil design and construction techniques. J. Magn. Reson. Imaging 39, 1088–1095. https://doi.org/10.1002/jmri.24254

Hansen, P., Kringelbach, M., Salmelin, R., 2010. MEG: An introduction to methods, MEG: An Introduction to Methods. https://doi.org/10.1093/acprof:oso/9780195307238.001.0001

Happer, W., 1972. Optical pumping. Rev. Mod. Phys. 44, 169–249. https://doi.org/10.1103/RevModPhys.44.169

Hari, R., Karhu, J., Hämäläinen, M., Knuutila, J., Salonen, O., Sams, M., Vilkman, V., 1993. Functional Organization of the Human First and Second Somatosensory Cortices: a Neuromagnetic Study. Eur. J. Neurosci. 5, 724–734. https://doi.org/10.1111/j.1460-9568.1993.tb00536.x

Hari, R., Salmelin, R., 2012. Magnetoencephalography: From SQUIDs to neuroscience. Neuroimage 20th Anniversary Special Edition. Neuroimage. https://doi.org/10.1016/j.neuroimage.2011.11.074

Hermundstad, A.M., Bassett, D.S., Brown, K.S., Aminoff, E.M., Clewett, D., Freeman, S., Frithsen, A., Johnson, A., Tipper, C.M., Miller, M.B., Grafton, S.T., Carlson, J.M., 2013. Structural foundations of resting-state and task-based functional connectivity in the human brain. Proc. Natl. Acad. Sci. U. S. A. 110, 6169–6174. https://doi.org/10.1073/pnas.1219562110

Hidalgo-Tobon, S.S., 2010. Theory of gradient coil design methods for magnetic resonance imaging. Concepts Magn. Reson. Part A Bridg. Educ. Res. 36, 223–242. https://doi.org/10.1002/cmr.a.20163

Hill, R.M., 2020. Design and fabrication for next generation magnetoencephalography. University of Nottingham.

Hill, R.M., Boto, E., Holmes, N., Hartley, C., Seedat, Z.A., Leggett, J., Roberts, G., Shah, V., Tierney, T.M., Woolrich, M.W., Stagg, C.J., Barnes, G.R., Bowtell, R.R., Slater, R., Brookes, M.J., 2019. A tool for functional brain imaging with lifespan compliance. Nat. Commun. https://doi.org/10.1038/s41467-019-12486-x

Hill, R.M., Boto, E., Rea, M., Holmes, N., Leggett, J., Coles, L.A., Papastavrou, M., Everton, S.K., Hunt, B.A.E., Sims, D., Osborne, J., Shah, V., Bowtell, R., Brookes, M.J., 2020. Multi-channel whole-head OPM-MEG: Helmet design and a comparison with a conventional system. Neuroimage.

https://doi.org/10.1016/j.neuroimage.2020.116995

Hill, R.M., Devasagayam, J., Holmes, N., Boto, E., Shah, V., Osborne, J., Safar, K., Worcester, F., Mariani, C., Dawson, E., Woolger, D., Bowtell, R., Taylor, M.J., Brookes, M.J., 2022. Using OPM-MEG in contrasting magnetic environments. Neuroimage 253, 119084. https://doi.org/10.1016/j.neuroimage.2022.119084

Hobson, P.J., Vovrosh, J., Stray, B., Packer, M., Winch, J., Holmes, N., Hayati, F., McGovern, K., Bowtell, R., Brookes, M.J., Bongs, K., Fromhold, T.M., Holynski, M., 2022. Bespoke magnetic field design for a magnetically shielded cold atom interferometer. Sci. Reports 2022 121 12, 1–12. https://doi.org/10.1038/s41598-022-13979-4

Hoburg, J.F., 1995. Principles of Quasistatic Magnetic Shielding with Cylindrical and Spherical Shields. IEEE Trans. Electromagn. Compat. https://doi.org/10.1109/15.477342

Holmes, N., Leggett, J., Boto, E., Roberts, G., Hill, R.M., Tierney, T.M., Shah, V., Barnes, G.R., Brookes, M.J., Bowtell, R., 2018. A bi-planar coil system for nulling background magnetic fields in scalp mounted magnetoencephalography. Neuroimage 181, 760–774. https://doi.org/10.1016/j.neuroimage.2018.07.028

Holmes, N., Tierney, T.M., Leggett, J., Boto, E., Mellor, S., Roberts, G., Hill, R.M., Shah, V., Barnes, G.R., Brookes, M.J., Bowtell, R., 2019. Balanced, bi-planar magnetic field and field gradient coils for field compensation in wearable magnetoencephalography. Sci. Rep. https://doi.org/10.1038/s41598-019-50697-w

Hounsfield, G.N., 1973. Computerized transverse axial scanning (tomography): I. Description of system. Br. J. Radiol. 46, 1016–1022. https://doi.org/10.1259/0007-1285-46-552-1016

Huang, M.X., Mosher, J.C., Leahy, R.M., 1999. A sensor-weighted overlapping-sphere head model and exhaustive head model comparison for MEG. Phys. Med. Biol. 44, 423–440. https://doi.org/10.1088/0031-9155/44/2/010

Huang, M.X., Theilmann, R.J., Robb, A., Angeles, A., Nichols, S., Drake, A., D'Andrea, J., Levy, M., Holland, M., Song, T., Ge, S., Hwang, E., Yoo, K., Cui, L., Baker, D.G., Trauner, D., Coimbra, R., Lee, R.R., 2009. Integrated imaging approach with MEG and DTI to detect mild traumatic brain injury in military and civilian patients. J. Neurotrauma 26, 1213–1226. https://doi.org/10.1089/neu.2008.0672

Iivanainen, J., Stenroos, M., Parkkonen, L., 2017. Measuring MEG closer to the brain: Performance of on-scalp sensor arrays. Neuroimage. https://doi.org/10.1016/j.neuroimage.2016.12.048

Iivanainen, J., Zetter, R., Grön, M., Hakkarainen, K., Parkkonen, L., 2019. On-scalp MEG system utilizing an actively shielded array of optically-pumped magnetometers. Neuroimage 194, 244–258. https://doi.org/10.1016/j.neuroimage.2019.03.022

Jaklevic, R.C., Lambe, J., Silver, A.H., Mercereau, J.E., 1964. Quantum Interference Effects in Josephson Tunneling. Phys. Rev. Lett. 12, 159–160. https://doi.org/10.1103/PhysRevLett.12.159

Jensen, O., Kaiser, J., Lachaux, J.P., 2007. Human gamma-frequency oscillations associated with attention and memory. Trends Neurosci. 30, 317–324. https://doi.org/10.1016/J.TINS.2007.05.001

Jensen, O., Mazaheri, A., 2010. Shaping functional architecture by oscillatory alpha activity: Gating by inhibition. Front. Hum. Neurosci. 4, 186. https://doi.org/10.3389/fnhum.2010.00186

Jöbsis, F.F., 1977. Noninvasive, infrared monitoring of cerebral and myocardial oxygen sufficiency and circulatory parameters. Science (80-.). 198, 1264–1267. https://doi.org/10.1126/science.929199

Johnson, C., Schwindt, P.D.D., Weisend, M., 2010. Magnetoencephalography with a two-color pump-probe, fiber-coupled atomic magnetometer. Appl. Phys. Lett. https://doi.org/10.1063/1.3522648

Johnson, C.N., Schwindt, P.D.D., Weisend, M., 2013. Multi-sensor magnetoencephalography with atomic magnetometers. Phys. Med. Biol. https://doi.org/10.1088/0031-9155/58/17/6065

Jones, S.R., 2016. When brain rhythms aren't 'rhythmic': implication for their mechanisms and meaning. Curr. Opin. Neurobiol. https://doi.org/10.1016/j.conb.2016.06.010

Josephson, B.D., 1962. Possible new effects in superconductive tunnelling. Phys. Lett. 1, 251–253. https://doi.org/10.1016/0031-9163(62)91369-0

Juchem, C., Nixon, T.W., McIntyre, S., Boer, V.O., Rothman, D.L., De Graaf, R.A., 2011. Dynamic multi-coil shimming of the human brain at 7 T. J. Magn. Reson. 212, 280–288. https://doi.org/10.1016/J.JMR.2011.07.005

Juchem, C., Nixon, T.W., McIntyre, S., Rothman, D.L., De Graaf, R.A., 2010. Magnetic field homogenization of the human prefrontal cortex with a set of localized electrical coils. Magn. Reson. Med. 63, 171–180. https://doi.org/10.1002/mrm.22164

Kaltiainen, H., Helle, L., Liljeström, M., Renvall, H., Forss, N., 2018. Theta-Band Oscillations as an Indicator of Mild Traumatic Brain Injury. Brain Topogr. 31, 1037–1046. https://doi.org/10.1007/s10548-018-0667-2

Kamada, K., Sato, D., Ito, Y., Natsukawa, H., Okano, K., Mizutani, N., Kobayashi, T., 2015. Human magnetoencephalogram measurements using newly developed compact module of high-sensitivity atomic magnetometer. Jpn. J. Appl. Phys. https://doi.org/10.7567/JJAP.54.026601

Kastler, A., 1973. The Hanle effect and its use for the measurements of very small magnetic fields. Nucl. Instruments Methods 110, 259–265. https://doi.org/https://doi.org/10.1016/0029-554X(73)90698-8

Kastler, A., 1951. Méthodes optiques d'étude de la résonance magnétique. Physica 17, 191–204. https://doi.org/https://doi.org/10.1016/0031-8914(51)90058-4

Kelly, H.W.K., 1946. Degaussing. Nature. https://doi.org/10.1038/157646a0

Kinahan, P.E., Rogers, J.G., 1989. Analytic 3D image reconstruction using all detected events. IEEE Trans. Nucl. Sci. 36, 964–968. https://doi.org/10.1109/23.34585

Knappe, S., Sander, T.H., Kosch, O., Wiekhorst, F., Kitching, J., Trahms, L., 2010. Cross-validation of microfabricated atomic magnetometers with superconducting quantum interference devices for biomagnetic applications. Appl. Phys. Lett. https://doi.org/10.1063/1.3491548

Kominis, I.K., Kornack, T.W., Allred, J.C., Romalis, M. V., 2003. A subfemtotesla multichannel atomic magnetometer. Nature. https://doi.org/10.1038/nature01484

Kornack, T.W., 2005. A Test of CPT and Lorentz Symmetry Using a K-3He Co-magnetometer. Princeton University.

Korvenoja, A., Wikström, H., Huttunen, J., Virtanan, J., Laine, P., Aronen, H.J., Seppäläinen, A.-M., llmoniemi, R.J., 1995. Activation of ipsilateral primary sensorimotor cortex by median nerve stimulation. Neuroreport 6.

Kowalczyk, A.U., Bezsudnova, Y., Jensen, O., Barontini, G., 2021. Detection of human auditory evoked brain signals with a resilient nonlinear optically pumped magnetometer. Neuroimage 226. https://doi.org/10.1016/J.NEUROIMAGE.2020.117497

Kutschka, H., Doeller, C.F., Haueisen, J., Maess, B., 2021. Magnetic field compensation coil design for magnetoencephalography. Sci. Reports 2021 111 11, 1–12. https://doi.org/10.1038/s41598-021-01894-z

Larson, E., Taulu, S., 2017. The Importance of Properly Compensating for Head Movements During MEG Acquisition Across Different Age Groups. Brain Topogr. 30, 172–181. https://doi.org/10.1007/s10548-016-0523-1

Lauterbur, P.C., 1973. Image Formation by Induced Local Interactions: Examples Employing Nuclear Magnetic Resonance. Nature 242, 190–191. https://doi.org/10.1038/242190a0

Lin, C.H., Tierney, T.M., Holmes, N., Boto, E., Leggett, J., Bestmann, S., Bowtell, R., Brookes, M.J., Barnes, G.R., Miall, R.C., 2019. Using optically pumped magnetometers to measure magnetoencephalographic signals in the human cerebellum. J. Physiol. 597, 4309–4324. https://doi.org/10.1113/JP277899

Lopes da Silva, F., 2013. EEG and MEG: Relevance to neuroscience. Neuron. https://doi.org/10.1016/j.neuron.2013.10.017

López, M.E., Cuesta, P., Garcés, P., Castellanos, P.N., Aurtenetxe, S., Bajo, R., Marcos, A., Delgado, M.L., Montejo, P., López-Pantoja, J.L., Maestú, F., Fernandez, A., 2014. MEG spectral analysis in subtypes of mild cognitive impairment. Age (Omaha). 36, 1095–1112. https://doi.org/10.1007/s11357-014-9624-5

Luckhoo, H., Hale, J.R., Stokes, M.G., Nobre, A.C., Morris, P.G., Brookes, M.J., Woolrich, M.W., 2012. Inferring task-related networks using independent component analysis in magnetoencephalography. Neuroimage 62, 530–541. https://doi.org/10.1016/J.NEUROIMAGE.2012.04.046

MacKert, B.M., Curio, G., Burghoff, M., Trahms, L., Marx, P., 1998. Magnetoneurographic 3D localization of conduction blocks in patients with unilateral S1 root compression. Electroencephalogr. Clin. Neurophysiol. Mot. Control 109, 315–320. https://doi.org/10.1016/S0924-980X(98)00024-1

Mager, A.J., 1970. Magnetic Shields. IEEE Trans. Magn. 6, 67–75. https://doi.org/10.1109/TMAG.1970.1066714

Mäkelä, J.P., Hari, R., 1987. Evidence for cortical origin of the 40 Hz auditory evoked response in man. Electroencephalogr. Clin. Neurophysiol. 66, 539–546. https://doi.org/10.1016/0013-4694(87)90101-5

Mandal, P.K., Banerjee, A., Tripathi, M., Sharma, A., 2018. A comprehensive review of magnetoencephalography (MEG) studies for brain functionality in healthy aging and Alzheimer's disease (AD). Front. Comput. Neurosci. https://doi.org/10.3389/fncom.2018.00060

Mansfield, P., Grannell, P.K., 1973. NMR "diffraction" in solids? J. Phys. C Solid State Phys 6.

Marquetand, J., Middelmann, T., Dax, J., Baek, S., Sometti, D., Grimm, A., Lerche, H., Martin, P., Kronlage, C., Siegel, M., Braun, C., Broser, P., 2021. Optically pumped magnetometers reveal fasciculations non-invasively. Clin. Neurophysiol. 132, 2681–2684. https://doi.org/10.1016/J.CLINPH.2021.06.009

Mathias, S., Nayak, U.S., Isaacs, B., 1986. Balance in elderly patients: the "get-up and go" test. Arch. Phys. Med. Rehabil. 67, 387–389.

Mhaskar, R., Knappe, S., Kitching, J., 2012. A low-power, high-sensitivity micromachined optical magnetometer. Appl. Phys. Lett. https://doi.org/10.1063/1.4770361

Muthukumaraswamy, S.D., 2013. High-frequency brain activity and muscle artifacts in MEG/EEG: A review and recommendations. Front. Hum. Neurosci. https://doi.org/10.3389/fnhum.2013.00138

Muthukumaraswamy, S.D., Singh, K.D., Swettenham, J.B., Jones, D.K., 2010. Visual gamma oscillations and evoked responses: Variability, repeatability and structural MRI correlates. Neuroimage 49, 3349–3357. https://doi.org/10.1016/J.NEUROIMAGE.2009.11.045

Nardelli, N. V., Perry, A.R., Krzyzewski, S.P., Knappe, S.A., 2020. A conformal array of microfabricated optically-pumped first-order gradiometers for magnetoencephalography. EPJ Quantum Technol. 2020 71 7, 1–11. https://doi.org/10.1140/EPJQT/S40507-020-00086-4

Nardelli, N. V, Krzyzewski, S.P., Knappe, S.A., 2019. Reducing crosstalk in optically-pumped magnetometer arrays. Phys. Med. Biol. 64, 21NT03. https://doi.org/10.1088/1361-6560/ab4c06

Nenonen, J., Nurminen, J., Kičić, D., Bikmullina, R., Lioumis, P., Jousmäki, V., Taulu, S., Parkkonen, L., Putaala, M., Kähkönen, S., 2012. Validation of head movement correction and spatiotemporal signal space separation in magnetoencephalography. Clin. Neurophysiol. 123, 2180–2191. https://doi.org/10.1016/j.clinph.2012.03.080

Neymotin, S.A., Daniels, D.S., Caldwell, B., McDougal, R.A., Carnevale, N.T., Jas, M., Moore, C.I., Hines, M.L., Hämäläinen, M., Jones, S.R., 2020. Human neocortical neurosolver (HNN), a new software tool for interpreting the cellular and network origin of human MEG/EEG data. Elife 9. https://doi.org/10.7554/eLife.51214

Nolte, G., Bai, O., Wheaton, L., Mari, Z., Vorbach, S., Hallett, M., 2004. Identifying true brain interaction from EEG data using the imaginary part of coherency. Clin. Neurophysiol. 115, 2292–2307. https://doi.org/10.1016/j.clinph.2004.04.029

Ogawa, S., Lee, T.M., Kay, A.R., Tank, D.W., 1990. Brain magnetic resonance imaging with contrast dependent on blood oxygenation. Proc. Natl. Acad. Sci. U. S. A. 87, 9868–9872. https://doi.org/10.1073/pnas.87.24.9868

Öisjöen, F., Schneiderman, J.F., Figueras, G.A., Chukharkin, M.L., Kalabukhov, A., Hedström, A., Elam, M., Winkler, D., 2012. High-T c superconducting quantum interference device recordings of spontaneous brain activity: Towards high-T c magnetoencephalography. Appl. Phys. Lett. 100. https://doi.org/10.1063/1.3698152

Osborne, J., Orton, J., Alem, O., Shah, V., 2018. Fully integrated standalone zero field optically pumped magnetometer for biomagnetism, in: Shahriar, S.M., Scheuer, J. (Eds.), Steep Dispersion Engineering and Opto-Atomic Precision Metrology XI. SPIE, pp. 89–95. https://doi.org/10.1117/12.2299197

Packer, M., Hobson, P.J., Holmes, N., Leggett, J., Glover, P., Brookes, M.J., Bowtell, R., Fromhold, T.M., 2020. Optimal Inverse Design of Magnetic Field Profiles in a Magnetically Shielded Cylinder. Phys. Rev. Appl. https://doi.org/10.1103/physrevapplied.14.054004

Patel, R.L., Zhou, L.Q., Frangeskou, A.C., Stimpson, G.A., Breeze, B.G., Nikitin, A., Dale, M.W., Nichols, E.C., Thornley, W., Green, B.L., Newton, M.E., Edmonds, A.M., Markham, M.L., Twitchen, D.J., Morley, G.W., 2020. Subnanotesla Magnetometry with a Fiber-Coupled Diamond Sensor. Phys. Rev. Appl. 14, 44058. https://doi.org/10.1103/PhysRevApplied.14.044058

Pfeiffer, C., Ruffieux, S., Jonsson, L., Chukharkin, M.L., Kalabukhov, A., Xie, M., Winkler, D., Schneiderman, J.F., 2019. A 7-channel high-T_{c} SQUID-based on-scalp MEG system. IEEE Trans. Biomed. Eng. https://doi.org/10.1109/tbme.2019.2938688

Pfurtscheller, G., Lopes da Silva, F.H., 1999. Event-related EEG/MEG synchronization and desynchronization: Basic principles. Clin. Neurophysiol. https://doi.org/10.1016/S1388-2457(99)00141-8

Pfurtscheller, G., Stancák, A., Neuper, C., 1996. Post-movement beta synchronization. A correlate of an idling motor area? Electroencephalogr. Clin. Neurophysiol. 98, 281–293.

https://doi.org/10.1016/0013-4694(95)00258-8

Rabi, I.I., Zacharias, J.R., Millman, S., Kusch, P., 1938. A New Method of Measuring Nuclear Magnetic Moment. Phys. Rev. 53, 318. https://doi.org/10.1103/PhysRev.53.318

Raichle, M.E., Gusnard, D.A., 2002. Appraising the brain's energy budget. Proc. Natl. Acad. Sci. U. S. A. https://doi.org/10.1073/pnas.172399499

Reindl, V., Gerloff, C., Scharke, W., Konrad, K., 2018. Brain-to-brain synchrony in parent-child dyads and the relationship with emotion regulation revealed by fNIRS-based hyperscanning. Neuroimage 178, 493–502. https://doi.org/10.1016/J.NEUROIMAGE.2018.05.060

Riaz, B., Pfeiffer, C., Schneiderman, J.F., 2017. Evaluation of realistic layouts for next generation on-scalp MEG: Spatial information density maps. Sci. Rep. 7. https://doi.org/10.1038/s41598-017-07046-6

Richardson, S., 1991. The Timed "Up & Go": A Test of Basic Functional Mobility for Frail Elderly Persons. J. Am. Geriatr. Soc. 39, 142–148. https://doi.org/10.1111/j.1532-5415.1991.tb01616.x

Roberts, G., Holmes, N., Alexander, N., Boto, E., Leggett, J., Hill, R.M., Shah, V., Rea, M., Vaughan, R., Maguire, E.A., Kessler, K., Beebe, S., Fromhold, M., Barnes, G.R., Bowtell, R., Brookes, M.J., 2019. Towards OPM-MEG in a virtual reality environment. Neuroimage. https://doi.org/10.1016/j.neuroimage.2019.06.010

Roberts, T.P.L., Khan, S.Y., Rey, M., Monroe, J.F., Cannon, K., Blaskey, L., Woldoff, S., Qasmieh, S., Gandal, M., Schmidt, G.L., Zarnow, D.M., Levy, S.E., Edgar, J.C., 2010. MEG detection of delayed auditory evoked responses in autism spectrum disorders: Towards an imaging biomarker for autism. Autism Res. 3, 8–18. https://doi.org/10.1002/aur.111

Robson, S.E., Brookes, M.J., Hall, E.L., Palaniyappan, L., Kumar, J., Skelton, M., Christodoulou, N.G., Qureshi, A., Jan, F., Katshu, M.Z., Liddle, E.B., Liddle, P.F., Morris, P.G., 2016. Abnormal visuomotor processing in schizophrenia. NeuroImage Clin. 12, 869–878. https://doi.org/10.1016/J.NICL.2015.08.005

Roméo, F., Hoult, D.I., 1984. Magnet field profiling: Analysis and correcting coil design. Magn. Reson. Med. 1, 44–65. https://doi.org/https://doi.org/10.1002/mrm.1910010107

Rondin, L., Tetienne, J.P., Hingant, T., Roch, J.F., Maletinsky, P., Jacques, V., 2014. Magnetometry with nitrogen-vacancy defects in diamond. Reports Prog. Phys. https://doi.org/10.1088/0034-4885/77/5/056503

Rosenow, F., Lüders, H., 2001. Presurgical evaluation of epilepsy. Brain 124, 1683–1700. https://doi.org/10.1093/brain/124.9.1683

Roshen, W.A., 1990. Effect of finite thickness of magnetic substrate on planar inductors. IEEE Trans. Magn. 26, 270–275. https://doi.org/10.1109/20.50553

Saby, J.N., Marshall, P.J., 2012. The utility of EEG band power analysis in the study of infancy and early childhood. Dev. Neuropsychol. https://doi.org/10.1080/87565641.2011.614663

Sander, T.H., Preusser, J., Mhaskar, R., Kitching, J., Trahms, L., Knappe, S., 2012. Magnetoencephalography with a chip-scale atomic magnetometer. Biomed. Opt. Express. https://doi.org/10.1364/boe.3.000981

Sarvas, J., 1987. Basic mathematical and electromagnetic concepts of the biomagnetic inverse problem. Phys. Med. Biol. 32, 11–22. https://doi.org/10.1088/0031-9155/32/1/004

Schweizer, F., 1962. Magnetic shielding factors of a system of concentric spherical shells. J. Appl. Phys. 33, 1001–1003. https://doi.org/10.1063/1.1777151

Schwindt, P.D.D., Lindseth, B., Knappe, S., Shah, V., Kitching, J., Liew, L.A., 2007. Chip-scale atomic magnetometer with improved sensitivity by use of the Mx technique. Appl. Phys. Lett. https://doi.org/10.1063/1.2709532

Sekihara, K., Hild, K.E., Nagarajan, S.S., 2006. A Novel Adaptive Beamformer for MEG Source Reconstruction Effective When Large Background Brain Activities Exist. IEEE Trans. Biomed. Eng. 53. https://doi.org/10.1109/TBME.2006.878119

Seltzer, S.J., 2008. Developments in Alkali-Metal Atomic Magnetometry. Princeton University.

Shah, V., Doyle, C., Osborne, J., 2020. Zero field parametric resonance magnetometer with triaxial sensitivity. US10775450B1.

Shah, V., Hughes, K.J., 2015. Method for detecting zero-field resonance. US9116201B2.

Shah, V., Knappe, S., Schwindt, P.D.D., Kitching, J., 2007. Subpicotesla atomic magnetometry with a microfabricated vapour cell. Nat. Photonics. https://doi.org/10.1038/nphoton.2007.201

Shah, V., Romalis, M. V, 2009. Spin-exchange relaxation-free magnetometry using elliptically polarized light. Phys. Rev. A - At. Mol. Opt. Phys. 80. https://doi.org/10.1103/PhysRevA.80.013416

Shah, V.K., Wakai, R.T., 2013. A compact, high performance atomic magnetometer for biomedical applications. Phys. Med. Biol. 58, 8153–8161. https://doi.org/10.1088/0031-9155/58/22/8153

Sheng, D., Perry, A.R., Krzyzewski, S.P., Geller, S., Kitching, J., Knappe, S., 2017. A microfabricated optically-pumped magnetic gradiometer. Appl. Phys. Lett. https://doi.org/10.1063/1.4974349

Shin, H., Law, R., Tsutsui, S., Moore, C.I., Jones, S.R., 2017. The rate of transient beta frequency events predicts behavior across tasks and species. Elife 6. https://doi.org/10.7554/eLife.29086

Stenroos, M., Hunold, A., Haueisen, J., 2014. Comparison of three-shell and simplified volume conductor models in magnetoencephalography. Neuroimage 94, 337–348. https://doi.org/10.1016/j.neuroimage.2014.01.006

Sun, Z., Schnabel, A., Burghoff, M., Li, L., 2016. Calculation of an optimized design of magnetic shields with integrated demagnetization coils. AIP Adv. 6, 075220. https://doi.org/10.1063/1.4960329

Taulu, S., Simola, J., Kajola, M., 2005. Applications of the signal space separation method. IEEE Trans. Signal Process. 53, 3359–3372. https://doi.org/10.1109/TSP.2005.853302

Taylor, J.M., Cappellaro, P., Childress, L., Jiang, L., Budker, D., Hemmer, P.R., Yacoby, A., Walsworth, R., Lukin, M.D., 2008. High-sensitivity diamond magnetometer with nanoscale resolution. Nat. Phys. 4, 810–816. https://doi.org/10.1038/nphys1075

Ter-Pogossian, M.M., Phelps, M.E., Hoffman, E.J., Mullani, N.A., 1975. A positron-emission transaxial tomograph for nuclear imaging (PETT). Radiology 114, 89–98. https://doi.org/10.1148/114.1.89

Thiel, F., Schnabel, A., Knappe-Grüneberg, S., Stollfuß, D., Burghoff, M., 2007. Demagnetization of magnetically shielded rooms. Rev. Sci. Instrum. 78, 35106. https://doi.org/10.1063/1.2713433

Tierney, T.M., Holmes, N., Mellor, S., López, J.D., Roberts, G., Hill, R.M., Boto, E., Leggett, J., Shah, V., Brookes, M.J., Bowtell, R., Barnes, G.R., 2019. Optically pumped magnetometers: From quantum origins to multi-channel magnetoencephalography. Neuroimage. https://doi.org/10.1016/j.neuroimage.2019.05.063

Tierney, T.M., Holmes, N., Meyer, S.S., Boto, E., Roberts, G., Leggett, J., Buck, S., Duque-Muñoz, L., Litvak, V., Bestmann, S., Baldeweg, T., Bowtell, R., Brookes, M.J., Barnes, G.R., 2018. Cognitive neuroscience using wearable magnetometer arrays: Non-invasive assessment of language function. Neuroimage 181, 513–520. https://doi.org/10.1016/j.neuroimage.2018.07.035

Tierney, T.M., Levy, A., Barry, D.N., Meyer, S.S., Shigihara, Y., Everatt, M., Mellor, S., Lopez, J.D., Bestmann, S., Holmes, N., Roberts, G., Hill, R.M., Boto, E., Leggett, J., Shah, V., Brookes, M.J., Bowtell, R., Maguire, E.A., Barnes, G.R., 2021. Mouth magnetoencephalography: A unique perspective on the human hippocampus. Neuroimage 225. https://doi.org/10.1016/J.NEUROIMAGE.2020.117443

Tierney, T.M., Mellor, S., O'Neill, G.C., Timms, R.C., Barnes, G.R., 2022. Spherical harmonic based noise rejection and neuronal sampling with multi-axis OPMs. Neuroimage 258, 119338. https://doi.org/10.1016/J.NEUROIMAGE.2022.119338

Turner, R., 1993. Gradient coil design: A review of methods. Magn. Reson. Imaging. https://doi.org/10.1016/0730-725X(93)90209-V

Uhlenbeck, G.E., Goudsmit, S., 1926. Spinning Electrons and the Structure of Spectra. Nature 117, 264–265. https://doi.org/10.1038/117264a0

Umbricht, D., Krljesb, S., 2005. Mismatch negativity in schizophrenia: a meta-analysis. Schizophr. Res. 76, 1–23. https://doi.org/10.1016/J.SCHRES.2004.12.002

van Ede, F., Quinn, A.J., Woolrich, M.W., Nobre, A.C., 2018. Neural Oscillations: Sustained Rhythms or Transient Burst-Events? Trends Neurosci. https://doi.org/10.1016/j.tins.2018.04.004

Van Veen, B.D., Buckley, K.M., 1988. Beamforming: a versatile approach to spatial filtering. IEEE ASSP Mag. 5, 4–24. https://doi.org/10.1109/53.665

Van Veen, B.D., Van Drongelen, W., Yuchtman, M., Suzuki, A., 1997. Localization of brain electrical activity via linearly constrained minimum variance spatial filtering. IEEE Trans. Biomed. Eng. 44, 867–880. https://doi.org/10.1109/10.623056

Voigt, J., Knappe-Grüneberg, S., Schnabel, A., Körber, R., Burghoff, M., 2013. Measures to reduce the residual field and field gradient inside a magnetically shielded room by a factor of more than 10. Metrol. Meas. Syst. 20, 239–248. https://doi.org/10.2478/mms-2013-0021

Vrba, J., 2000. Multichannel SQUID Biomagnetic Systems, in: Weinstock, H. (Ed.), Applications of Superconductivity. Springer Netherlands, Dordrecht, pp. 61–138. https://doi.org/10.1007/978-94-017-0752-7_2

Vrba, J., Robinson, S.E., 2001. Signal processing in magnetoencephalography. Methods 25, 249–271. https://doi.org/10.1006/meth.2001.1238

Wass, S. V., Noreika, V., Georgieva, S., Clackson, K., Brightman, L., Nutbrown, R., Covarrubias, L.S., Leong, V., 2018. Parental neural responsivity to infants' visual attention: How mature brains influence immature brains during social interaction. PLoS Biol. 16. https://doi.org/10.1371/journal.pbio.2006328

Wehner, D.T., Hämäläinen, M.S., Mody, M., Ahlfors, S.P., 2008. Head movements of children in MEG: Quantification, effects on source estimation, and compensation. Neuroimage 40, 541–550. https://doi.org/10.1016/j.neuroimage.2007.12.026

Westner, B.U., Lubell, J.I., Jensen, M., Hokland, S., Dalal, S.S., 2021. Contactless measurements of retinal activity using optically pumped magnetometers. Neuroimage 243, 118528. https://doi.org/10.1016/j.neuroimage.2021.118528

Xia, H., Ben-Amar Baranga, A., Hoffman, D., Romalis, M. V., 2006. Magnetoencephalography with an atomic magnetometer. Appl. Phys. Lett. https://doi.org/10.1063/1.2392722

Yoda, K., 1990. Analytical design method of self-shielded planar coils. J. Appl. Phys. 67, 4349–4353. https://doi.org/10.1063/1.344953

Zetter, R., Iivanainen, J., Parkkonen, L., 2019. Optical Co-registration of MRI and On-scalp MEG. Sci. Rep. 9. https://doi.org/10.1038/s41598-019-41763-4

Zetter, R., Mäkinen, A.J., Iivanainen, J., Zevenhoven, K.C.J., Ilmoniemi, R.J., Parkkonen, L., 2020. Magnetic field modeling with surface currents. Part II. Implementation and usage of bfieldtools. J. Appl. Phys. https://doi.org/10.1063/5.0016087

Zhang, R., Xiao, W., Ding, Y., Feng, Y., Peng, X., Shen, L., Sun, C., Wu, T., Wu, Y., Yang, Y., Zheng, Z., Zhang, X., Chen, J., Guo, H., 2020. Recording brain activities in unshielded Earth's field with optically pumped atomic magnetometers. Sci. Adv. 6, 8792–8804. https://doi.org/10.1126/SCIADV.ABA8792/SUPPL_FILE/ABA8792_SM.PDF

Zhang, S., Zhang, K., Zhou, Y., Ye, M., Lu, J., 2022. Triaxial precise magnetic field compensation of a zero-field optically pumped magnetometer based on a single-beam configuration. Opt. Express 30, 24579–24588. https://doi.org/10.1364/OE.464361

Zhang, X., Chen, C. qiao, Zhang, M. kang, Ma, C. yu, Zhang, Y., Wang, H., Guo, Q. qian, Hu, T., Liu, Z. bang, Chang, Y., Hu, K. jia, Yang, X. dong, 2020. Detection and analysis of MEG signals in occipital region with double-channel OPM sensors. J. Neurosci. Methods 346, 108948. https://doi.org/10.1016/J.JNEUMETH.2020.108948

Zimmerman, J.E., Thiene, P., Harding, J.T., 1970. Design and operation of stable rf-biased superconducting point-contact quantum devices, and a note on the properties of perfectly clean metal contacts. J. Appl. Phys. 41, 1572–1580. https://doi.org/10.1063/1.1659074

Zumer, J.M., Scheeringa, R., Schoffelen, J.M., Norris, D.G., Jensen, O., 2014. Occipital Alpha Activity during Stimulus Processing Gates the Information Flow to Object-Selective Cortex. PLoS Biol. 12, e1001965. https://doi.org/10.1371/journal.pbio.1001965